Author:
Duffy, Ryan

Title:
X-ray Gas Belts and Radio Source Feedback in Low-Redshift Radio Galaxies

X-ray Gas Belts and Radio Source Feedback in Low-redshift Radio Galaxies

Ryan Duffy

A thesis submitted to the University of Bristol
in accordance with the requirements of the degree of
Doctor of Philosophy
in the Faculty of Science

Department of Physics,
H.H. Wills Physics Laboratory,
Tyndall Avenue,
Bristol,
BS8 1TL

April 2018

$\sim 35,000$ words

Abstract

This thesis studies how typical nearby radio sources are participating in radio plasma-gas interactions, with a specific emphasis on understanding the occurrence, morphologies and origins of X-ray gas belts, and their impact upon AGN feedback and fuelling. These excesses (belts) are not likely to be normal undistorted group or galaxy atmospheres.

Firstly, I report measurements from an *XMM-Newton* observation of the low-excitation radio galaxy 3C 386. The study focusses on an X-ray-emitting gas belt, which lies between and orthogonal to the radio lobes of 3C 386 and has a mean temperature of 0.94 ± 0.05 keV, cooler than the extended group atmosphere. The gas in the belt shows temperature structure with material closer to the surrounding medium being hotter than gas closer to the host galaxy. I suggest that this gas belt involves a 'buoyancy-driven inflow' of part of the group-gas atmosphere where the buoyant rise of the radio lobes through the ambient medium has directed an inflow towards the relic cold core of the group.

This analysis is then expanded to the full low-redshift 3CRR sample which contains 35 radio galaxies. X-ray gas belts are found to be common among the sample, with 15 sources exhibiting an excess of X-ray emitting counts between the lobes but away from the active nucleus. I use *Chandra* data to investigate the origins of these X-ray belts. I show that all the belts in the sample are primarily composed of thermally emitting gas. In all cases where belt temperature structure can be measured, the outer belt gas is hotter than the inner. It is probable that the belts have a variety of histories including inflow, outflow and mergers. I detect inverse-Compton emission in the plumes of five of the nine FR I radio galaxies in the sample of belted sources, allowing a measurement of magnetic field strength. I find that the amount by which magnetic field strength tends to be lower than the minimum-energy value is similar for FR Is and FR IIs, if minimum energy for both is calculated assuming no protons. Since FR Is in clusters are known to need protons for pressure support with the external medium, these results provide the first evidence that magnetic field strengths are largely oblivious to non-radiating particles in radio galaxy plumes and lobes.

Finally, I use new and archival *Chandra* observations of Cygnus A, totalling $\sim$1.9 Ms, to investigate the distribution and temperature structure of gas lying within the projected extent of the cocoon shock and exhibiting a rib-like structure. I confirm that the X-rays are dominated by thermal emission with an average temperature of around 4 keV, and have discovered an

asymmetry in the temperature gradient, with the southwestern part of the gas cooler than the rest by up to 2 keV. Pressure estimates suggest that the gas is a coherent structure of single origin located inside the cocoon, with a mass of roughly $2 \times 10^{10} M_{\odot}$. I conclude that the gas is debris resulting from disintegration of the cool core of the Cygnus A cluster after the passage of the jet during the early stages of the current epoch of activity. The 4 keV gas now lies on the central inside surface of the hotter cocoon rim. The temperature gradient could result from an offset between the centre of the cluster core and the Cygnus A host galaxy at the switch-on of current radio activity.

Acknowledgements

Foremost, I would like to express my sincere gratitude to my supervisor, Diana Worrall, and my co-supervisor in all but name, Mark Birkinshaw, for all their help and support throughout my PhD. I would especially like to thank Diana, for her continuous patience, help in numerous crises of confidence, and editing of endless manuscripts and abstracts. I am very grateful to have had such an excellent supervisor.

I thank my friends across the country, for providing me with countless nights and weekends filled with camaraderie, escapism, laughter and fun. I also thank my brother, for providing a constant source of encouragement and motivation to better myself, and for greatly improving my ability to debate.

Finally, I thank both my parents for their love and support throughout my life, for showing me the world, and encouraging a passion for science. Words cannot express how truly grateful I am for everything they do for me.

Declaration

I declare that the work in this dissertation was carried out in accordance with the requirements of the University's *Regulations and Code of Practice for Research Degree Programmes* and that it has not been submitted for any other academic award. Except where indicated by specific reference in the text, the work is the candidate's own work. Work done in collaboration with, or with the assistance of, others, is indicated as such. Any views expressed in the dissertation are those of the author.

Ryan Duffy
April 2018

I note here contributions to the work from collaborators, along with any work which has previously been published for each of the individual chapters:

Chapter 2 – *Method* – Elements of the data analysis procedures are adapted from sections in Duffy et al. (2016) and Duffy et al. (2018).

Chapter 3 – *Buoyancy-driven inflow to a relic cold core: the gas belt in radio galaxy 3C 386* – This work has been published in Duffy et al. (2016), and is largely reproduced from the paper. D. M. Worrall, M. Birkinshaw and R. P. Kraft had input in the preparation of the manuscript. D. M. Worrall wrote the proposal to obtain the *XMM-Newton* data.

Chapter 4 – *X-ray gas belts in low-redshift 3CRR radio galaxies* – This chapter is in large parts reproduced from a paper due to be submitted to MNRAS in the near future. D. M. Worrall and M. Birkinshaw had input in the preparation of the manuscript.

Chapter 5 – *The X-ray ribs within the cocoon shock of Cygnus A* – This work has been published in Duffy et al. (2018) and is largely reproduced from the paper. M. W. Wise wrote the proposal to obtain data for the *Chandra* Visionary Project on Cygnus A. D. M. Worrall, M. Birkinshaw, P. E. J. Nulsen, W. G. Mathews, R. A. Perley and M. J. Hardcastle had input in the preparation of the manuscript. Section 5.7 was significantly contributed to by M. Birkinshaw.

Contents

List of Figures

List of Tables

1

Introduction

1.1 Outline

The aim of this thesis is to study how typical nearby ($z \leq 0.1$) radio sources are participating in radio plasma-gas interactions, with a specific emphasis on understanding the occurrence, morphologies and origins of X-ray gas belts, and their impact upon active galactic nuclei (AGN) feedback and fuelling. Nearby radio galaxies are best suited to this task, due to the linear scales which are able to be probed using the current generation of X-ray satellites: the *Chandra* X-ray Observatory and *XMM-Newton*.

This introduction provides a brief history of research into AGN, before discussing the significant morphological features of radio galaxies, along with their primary emission mechanisms, and the emission mechanisms of the ambient media they inhabit. I conclude this chapter by considering AGN feedback, before introducing X-ray gas belts and how they may be connected to this process.

Chapter 2 describes the data analysis procedures and the physics used to uncover the properties of the various structures in each radio source. Chapter 3 describes an in-depth study of the radio galaxy 3C 386 and its gas belt, using *XMM-Newton*. In Chapter 4, I study the belted sources in the low-redshift 3CRR sample using *Chandra*. In Chapter 5, I investigate the non-axisymmetric X-ray gas within the cocoon shock of Cygnus A, before concluding the results of

the work in Chapter 6.

1.2 Active Galaxies

An active area of research in modern astrophysics concerns the processes surrounding and governed by a galaxy's central supermassive black hole (SMBH). In certain cases, the SMBH appears as an AGN, with luminosities ranging from between 10^{33} to 10^{40} W, and their emission spread across the whole electromagnetic spectrum. They are believed to be powered by accreting matter on to a central SMBH, such that the radiation cannot be explained by stars or hot gas permeating through the galaxy, and can exceed the total emission from the rest of the galaxy.

1.2.1 History

Characteristic features of AGN were observed in the early 20th Century, with the jet in M87 described as 'a curious straight ray' (Curtis, 1918), although there was limited understanding of the physical mechanisms responsible. Later, Seyfert (1943) described observations of a few galaxies with bright, point-like nuclei which exhibited broader emission lines than expected, should the motions of stars within the galaxy be responsible. The high velocities measured implied material orbiting around a very high compact mass. The advent of radio interferometry was a catalyst for the advancement of understanding AGN. Interferometer measurements of Cygnus A, first demonstrated that the source was elongated (Hanbury Brown et al., 1952) and then showed two equal, separate components separated by 1.5 arcmin on either side of the optical image (Jennison and Das Gupta, 1953). This morphology proved to be common for extragalactic radio sources. The Third Cambridge Catalogue of Radio Sources (3C) was first compiled from a survey undertaken at 159 MHz (Edge et al., 1959) and was then followed by the revised 3C (3CR) survey at 178 MHz (Bennett, 1962), with many radio sources becoming known by their 3C designation. Allen et al. (1962) compiled a list of bright, unresolved sources from the 3C catalogue with brightness temperatures higher than 10^7 K, indicating a non-thermal origin for these sources. The broad emission lines in the source 3C 273 were shown to be redshifted hydrogen lines by Schmidt (1963), indicating 3C 273 was an extragalactic source, and implying that it was the nuclear region of a galaxy. Sources of this type were dubbed 'quasi-stellar radio sources' or quasars. 3C 273 provided further insight into the nature of AGN when a rocket carrying collimated proportional counters detected X-ray emission coincident with the

source (Bowyer et al., 1970), with X-ray luminosity comparable to its optical luminosity. X-ray emission from these objects is significant as it provides a direct probe of the accretion processes thought to be powering AGN, as the X-rays can penetrate through columns of obscuring dust and gas.

1.2.2 Types of Active Galaxy

As can be inferred from above, AGN typically radiate over a broad range of the electromagnetic spectrum. It is convenient to divide AGN into two classes: radio-loud and radio-quiet. Radio-loud objects exhibit emission from both relativistic jets and the lobes and plumes which the jets inflate. In radio-quiet objects, emission from these structures can be neglected at all wavelengths. AGN of all luminosities reside almost exclusively in massive galaxies, and have distributions of sizes, stellar surface mass densities and concentrations that are similar to those of ordinary early-type galaxies (Kauffmann et al., 2003). The host galaxies of low-luminosity AGN have stellar populations similar to normal galaxies, while high-luminosity AGN have much younger mean stellar ages (Kauffmann et al., 2003).

Within the radio-quiet regime, active galaxies can be classified as low-ionisation nuclear emission-line regions (LINERs), Seyfert galaxies and radio-quiet quasars. LINERs show weak nuclear emission-line regions and no other signatures of AGN emission. Seyfert galaxies were first identified in Seyfert (1943) and can be subdivided into two further classifications: Seyfert 1 and Seyfert 2. Seyfert 1s show strong broad emission lines and are more likely to show low-energy X-ray emission than Seyfert 2s. In general, Seyfert galaxies exhibit optical emission from their nuclei, with their spectra displaying continuum emission, narrow, and occasionally broad emission lines. Radio-quiet quasars exhibit the same features as Seyfert 1s, but have higher luminosities. In terms of their host galaxies, LINERs are older, more massive, less dusty and have higher velocity dispersions than Seyferts (Kewley et al., 2006).

Within the radio-loud regime, active galaxies are classified as radio galaxies, radio-loud quasars and blazars. Radio-loud quasars exhibit the same optical features as radio-quiet quasars, but also display additional emission associated with a radio jet. Blazars are distinguished by rapidly variable, polarised optical, radio and X-ray emission. Radio galaxies are sources which show nuclear and extended radio features, and will be discussed more in depth in Section 1.3 as they are the focus of this work.

It is widely accepted each type of active galaxy described above is the same, and that their

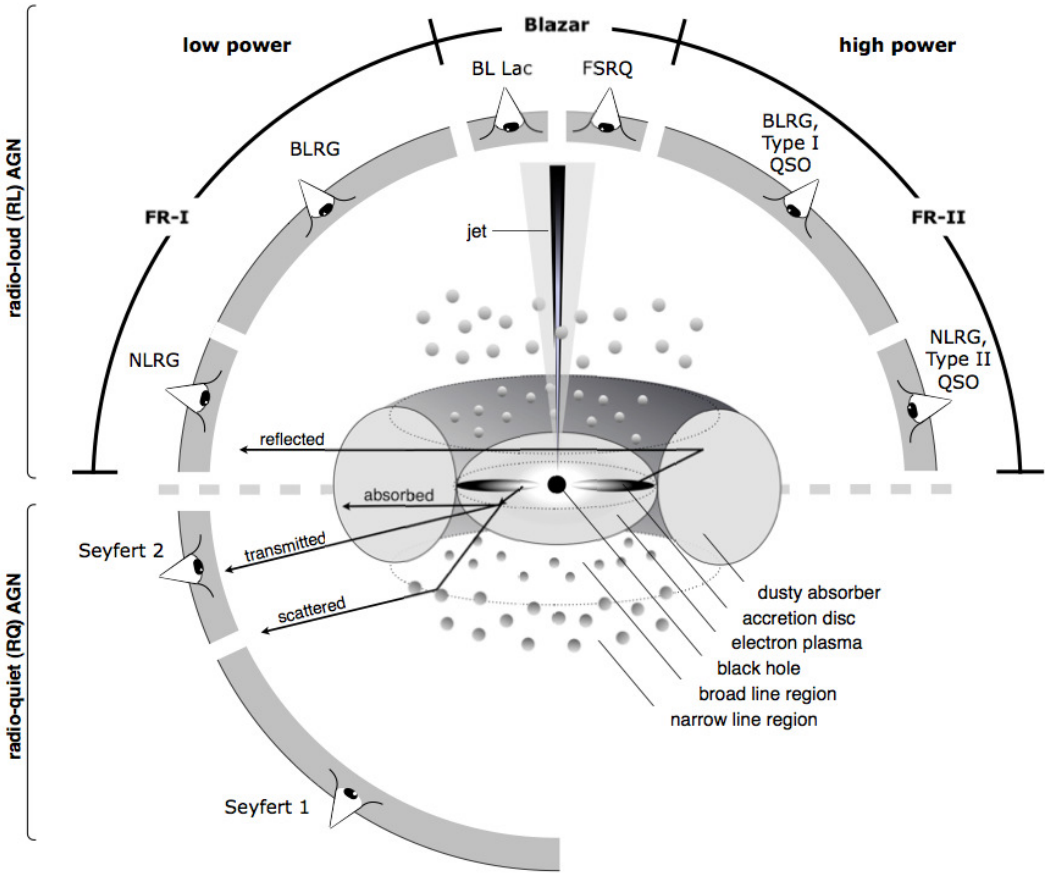

Figure 1.1: Example of a grand unified model. An accreting black hole is surrounded by line-emitting clouds and a dusty, obscuring torus. Radio jets are visible in radio-loud sources. An active galaxy's classification is dependent on the observer's viewing angle. Figure reproduced from Beckmann and Shrader (2012).

properties vary only on the angle at which the source is viewed from the Earth. Attempts to unfiy active galaxies under one model are called 'unification schemes' (Urry and Padovani, 1995), and are illustrated in Figure 1.1. The observational differences are attributed to the angle at which a dusty torus surrounding the central black hole is viewed. The classification into Seyfert 1 and Seyfert 2 is dependent on the visibility of a region of rapidly-moving clouds which produce broad emission lines in the optical and UV ranges. This region is visible in Seyfert 1s, and obscured in Seyfert 2s. Blazars have their spectral energy distributions (SEDs) dominated by a relativistic jet and are understood to be beamed radio-loud galaxies, which are observed directly down the jet. Quasars are viewed at a slightly more inclined angle. The radio jets are collimated outflows of relativistic particles and magnetic field, but it is unclear why some AGN launch jets, while others do not.

1.3 Radio Galaxies

Radio galaxies display a broad range of morphological structures at radio wavelengths, many of which also appear in other wavelengths across the electromagnetic spectrum. The most common features and their general interpretation are described in the following sections.

1.3.1 Core

Radio emission from a compact core usually presents as point source emission at the centre of the radio source, and is usually coincident with an optical nucleus. It represents the partially optically thick base of the jet. If strong nuclear optical line emission is present, the radio galaxy is classified as a High Excitation Radio Galaxy (HERG), and nuclei with weak optical spectral lines are known as Low Excitation Radio Galaxies (LERG). I discuss LERGs and HERGs in greater depth in Section 1.3.5. The spectra of radio cores are almost always flat ($\alpha \approx 0$, where α is the spectral index of synchrotron emission, typically defined as $L(\nu) \propto \nu^{-\alpha}$), and the core's radio luminosity appears to be correlated with the extended radio power, although the scatter is large (Morganti et al., 1995).

1.3.2 Relativistic Jets, Knots and Hotspots

Radio galaxies typically exhibit twin jets of collimated relativistic plasma, which generally propagate in opposite directions. Jets could form when the acceleration and collimation of matter

from the accretion disk is launched due to the magnetic fields of the rotating disk, with the energy originating from accretion power (Blandford and Payne, 1982). Alternatively, a jet could be launched by magnetic field lines which are dragged with the black hole rotation in the ergosphere (Blandford and Znajek, 1977). The energy from this model is extracted from the conversion of the rotational energy of a spinning black hole in the magnetic field into electromagnetic energy. Jets can range in size, from just a few pc in scale, up to even Mpc scales in the most powerful radio galaxies. Their energy is believed to be transported mechanically rather than radiatively, and they are thought to comprise electrons and positrons or protons, and magnetic fields.

Jets can also display knots, which corresponds to bright regions of radio and sometimes X-ray emission. These may be related to internal shocks. More powerful jets terminate in hotspots, which are kpc-scale regions of intense emission. Their spectrum is often flatter than their host lobe, suggesting that hotspots are an observable consequence of jets impacting the ambient medium, producing strong shocks and particle acceleration.

1.3.3 Lobes, Plumes and Cocoons

Jets interacting with their surrounding medium on kpc and Mpc scales give rise to large-scale structures. At the hotspots, particles leak out of the jet to form low density lobes, which expand adiabatically with time. Lobes are large, and frequently roughly symmetric, whereas plumes are similar to lobes, but typically associated with lower-luminosity sources, and tend to be more elongated with less well defined edges and no hotspots. As the lobes and plumes have lower density than their surrounding medium, they rise buoyantly away from the radio source through the ambient medium.

Cocoons are associated with powerful radio galaxies. The jet in these sources is supersonic compared to the ambient medium at large distances from the source, and interacts with the ambient medium resulting in the formation of a terminal shock or hotspot. The shocked plasma streams out of the hotspot and generates a backflow which inflates the cocoon. Vortices are also generated and are advected with the flow and further inflate the cocoon. The cocoon is overpressured with respect to the environment and drives a bow shock into the external medium, leading to the formation of a thick shell of shocked ambient gas. This is seen prominently in sources such as Cygnus A (Smith et al., 2002; Duffy et al., 2018; Snios et al., 2018) and is illustrated schematically in Figure 1.2. The length and width of the cocoon are governed by the jet's power, the internal pressure of the lobes, and the pressure exerted on the cocoon as it moves

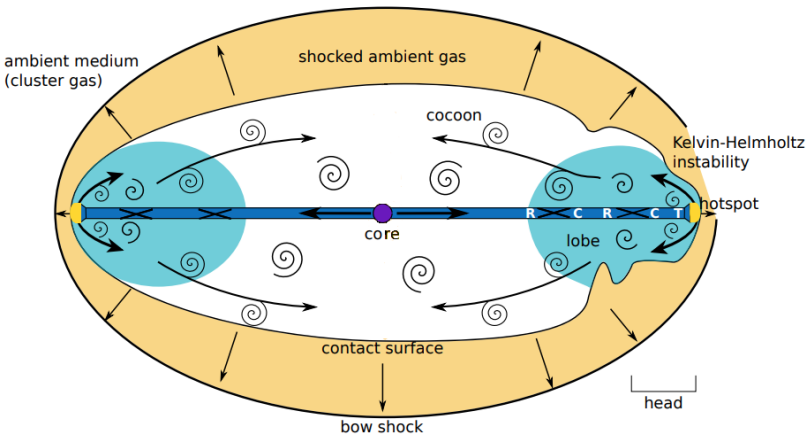

Figure 1.2: Schematic representation of sources which form cocoon shocks. The jet emerges from the accretion disk and passes through regions of rarefaction (R), compression (C) until it is decelerated at the terminal shock (T). Once shocked, the plasma streams out of the hotspot and generates a backflow. Vortices are advected with the flow and inflate the cocoon. Figure taken from Bieri et al. (2016).

through the ambient medium.

1.3.4 Fanaroff-Riley Classification and Dichotomy

Radio galaxies are typically divided into two classes based on the morphology of the radio structure. This is the Fanaroff-Riley classification (Fanaroff and Riley, 1974), which separates centrally-bright sources and edge-bright sources into the FR I and FR II classes, respectively, with a dividing radio luminosity of roughly 5×10^{24} W Hz^{-1} sr^{-1} at 178 MHz. The lower-luminosity FR I sources exhibit broader, bright jets close to the core, which fade with distance into plumes. FR II sources show brighter, collimated jets farther from the core, which end in bright hotspots close to the edge of the lobe, leading to a more edge brightened appearance. The principal morphological differences between the two classes can be seen in Figure 1.3.

The origin of the FR I/FR II dichotomy is unclear, but there are two possible explanations. It could depend on properties intrinsic to the central source, for example how the jet is formed and the jet power or extrinsic properties, such as the environment through which the jet propagates. Aside from differences in radio power and morphology, FR Is and FR IIs are found to occupy different environments. FR Is are typically found in optically luminous giant elliptical galaxies (Ledlow and Owen, 1996), and are more likely to be found in galaxy clusters than FR IIs

(Wing and Blanton, 2011). FR IIs are usually found in less dense environments, preferentially in groups rather than clusters (Zirbel, 1997). As a result of this FR Is may entrain their denser external medium, leading to the eventual deceleration of the jet to transonic speeds (Laing and Bridle, 2002). FR IIs however, more effectively transport energy along their jets, until the bulk kinetic energy is dissipated by a strong shock at the hotspot. In the cores of FR I radio galaxies, correlations between the unabsorbed X-ray, radio and optical fluxes and luminosities suggest that the core emission originates in the base of the jet. In FR II radio galaxies, the core X-ray emission is dominated by absorbed emission, which is likely to originate in an accretion flow (Evans et al., 2006).

The lobes of each type of galaxy could also display fairly significant differences. Hardcastle and Worrall (2000) found that the minimum energy pressures of a sample of X-ray detected FR II galaxies was lower than the external pressure from the ambient medium, suggesting an additional pressure component is required in the lobes. The X-ray emission in these observations, however, could be attributed to the intracluster medium (ICM) as the ROSAT point spread function (PSF) does not enable the separation of any component of any inverse-Compton (iC) emission. *Chandra* and *XMM-Newton* enabled the separation of these components, and X-ray observations have since shown that the estimates of the external pressures are comparable to the pressures at the mid-point of the lobes, at least in FR IIs (Croston et al., 2004; Belsole et al., 2004; Konar et al., 2009; Ineson et al., 2017). This implies that no significant non-radiating proton populations is present in the lobes of FR IIs, although it possible that the entrainment of hot gas plays a role in the particle content of some (Hardcastle and Croston, 2010). Studies of the lobe pressures of FR I sources have found that the iC emission is too low to provide the additional pressure required to balance with the external gas (Croston et al., 2003; Dunn et al., 2005). This has been interpreted as evidence for FR I sources harbouring an energetically dominant proton population, in order for the lobes or plumes to be brought closer to pressure balance with the external environment (Croston et al., 2008b, 2018).

1.3.5 Accretion Mode

The LERGs and HERGs mentioned in Section 1.3.1 have differing accretion rates, with the majority of HERGs having Eddington ratios of $\gtrsim 1\%$ and LERGs with $\lesssim 1\%$ (Mingo et al., 2014; Fernandes et al., 2015), where the Eddington ratio is defined as the source luminosity divided by the Eddington luminosity, where the Eddington luminosity is the maximum luminosity of a

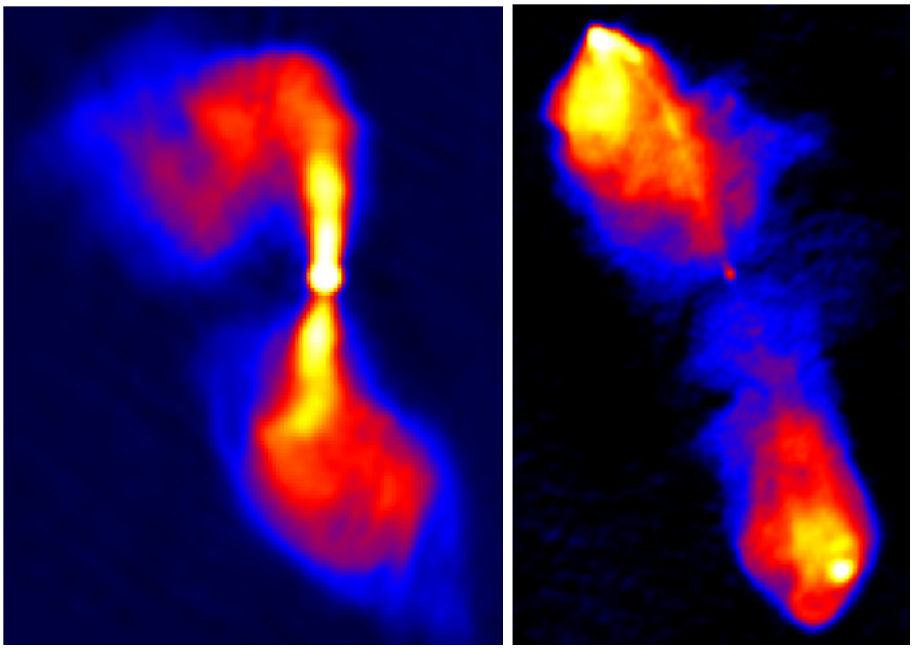

Figure 1.3: *Left:* VLA radio map of the FR I galaxy 3C 272.1 displaying bright jets which fade into plumes. *Right:* VLA radio map of FR II galaxy 3C 98 exhibiting collimated radio jets which terminate at hot spots, encompassed by lobes of radio-emitting plasma.

source in hydrostatic equilibrium. Best and Heckman (2012) also show that LERGs and HERGs have fundamentally different host galaxies, with LERGs being redder, larger and more massive. Bîrzan et al. (2017) found an increase in the occurrence of higher radio luminosity sources at higher redshifts, implying a transition in accretion mode at intermediate redshifts.

The dichotomy in the accretion rate appears to be related to different accretion methods, which are primarily dependent on the source of the accreting gas. HERGs are thought to be fuelled by cold gas which is heated and forms an accretion disk giving rise to radiatively efficient accretion (Shakura and Sunyaev, 1973). This is the standard accretion disk and is formed when the accretion on to the SMBH is close to the Eddington rate, and the opacity of the disk is very high. The model assumes that the disk is in local thermal equilibrium, and thus can radiate its heat efficiently. The accretion gives rise to X-ray emission from the nucleus and infrared radiation from the surrounding dusty torus. The cold gas is channeled into the galaxy centre, with fuel also available for star formation.

It is possible that LERGs are fuelled by hot gas, originating in the IGM/ICM (e.g. Hardcastle et al., 2007; Ineson et al., 2015). In comparison to HERGs, LERGs have a lower accretion rate

and are radiatively inefficient, with an advection dominated accretion flow (ADAF Narayan and Yi 1994). In this scenario, the accretion disk is geometrically extended, similar in shape to a corona rather than a disk, and is very hot. As a result of their low radiative efficiency, ADAFs are much less luminous than standard accretion disks. Spherically symmetric accretion rates of hot gas, also known as Bondi accretion rates (Bondi, 1952), have been shown to correlate well with the jet powers of nearby LERGs (Allen et al., 2006).

1.4 Synchrotron Emission

There are two key emission processes which allow for the study of large-scale radio structures: synchrotron emission and inverse-Compton scattering (iC). Synchrotron radiation is produced by relativistic electrons moving in a magnetic field, and is the dominant non-thermal emission process in radio galaxies. IC emission is produced by the up-scattering of a population of seed photons on relativistic electrons.

1.4.1 Electron energy loss

The equation of motion for a relativistic electron moving in a uniform magnetic field **B** is given by

$$\frac{\mathrm{d}}{\mathrm{d}t}(\gamma m_{\mathrm{e}}\mathbf{v}) = e(\mathbf{v}\times\mathbf{B}) \tag{1.1}$$

where **v** is the velocity vector of an electron of mass m_{e}, charge e and Lorentz factor $\gamma = (1 - \mathbf{v}.\mathbf{v}/c^2)^{-1/2}$. As the electron's acceleration is perpendicular to its velocity (such that $\mathbf{v}.\mathbf{a} = 0$), Equation 1.1 can be rewritten as

$$\gamma m_{\mathrm{e}}\frac{\mathrm{d}\mathbf{v}}{\mathrm{d}t} = e|\mathbf{v}||\mathbf{B}|\sin\theta \tag{1.2}$$

where the pitch angle, θ, is the angle between the direction of motion and the magnetic field. The pitch angle of the particle's orbit is defined by $\tan\theta = v_{\parallel}/v_{\perp}$, where $v_{\parallel}$ and $v_{\perp}$ are the components of the velocity parallel and perpendicular to the magnetic field. This also corresponds to the angle between the vectors **B** and **v**.

Due to the uniform magnetic field, the constant acceleration perpendicular to the velocity vector results in circular motion about the direction of the magnetic field. Equating the acceleration given in Equation 1.2 to the centripetal acceleration and rearranging gives $r_{\rm g}$, the gyroradius of the electron:

$$r_{\rm g} = \frac{\gamma m_{\rm e} |\mathbf{v}| \sin\theta}{e|\mathbf{B}|} \tag{1.3}$$

The corresponding non-relativistc gyrofrequency, $\nu_{\rm g}$ ($\gamma = 1$) of the electron's orbit about the magnetic field direction is:

$$\nu_{\rm g} = \frac{eB}{2\pi m_{\rm e}} \tag{1.4}$$

Larger magnetic fields mean smaller characteristic radii, and therefore larger gyration frequencies. Particles with larger γ correspond to larger intertias, and have larger gyration frequencies.

The rate of energy loss of a charged particle is determined by the relativistic generalisation of the Larmor formula, which describes the power radiated by a point charge as it accelerates:

$$-\left(\frac{dE}{dt}\right) = 2\sigma_{\rm T} c \gamma^2 \beta^2 u_{\rm B} \sin^2\theta \tag{1.5}$$

where $\sigma_{\rm T}$ is the Thomson cross section, and $u_{\rm B}$ is the energy density of the magnetic field. As the Thomson cross section is proportional to $m_{\rm e}^{-2}$, the power emitted by a proton is far less (by a factor of 1836^2) than that of an electron. For a population of electrons with an isotropic distribution of pitch angles, $\langle \sin^2\theta \rangle = \frac{1}{4\pi} \int_0^{4\pi} \sin^2\theta d\Omega = 2/3$, so that the average loss rate for a particle of energy E is

$$-\left(\frac{dE}{dt}\right) = \frac{4}{3}\sigma_{\rm T} c \gamma^2 \beta^2 u_{\rm B} \tag{1.6}$$

1.4.2 Synchrotron spectrum from a single electron

The following is reproduced from Pacholczyk (1970) and Longair (2011) and shows how a single electron can produce a spectrum of synchrotron emission. The spectrum of synchrotron emission is dominated by a characteristic frequency. Unlike in cyclotron emission, the particle is relativistic, so the characteristic frequency does not correspond to its revolution period. Instead,

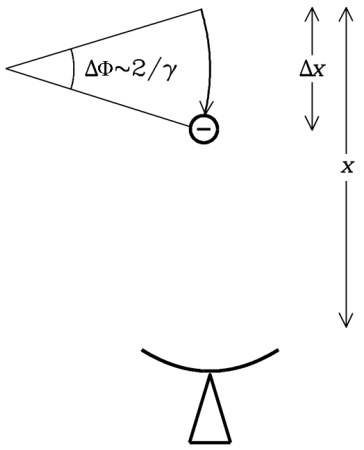

Figure 1.4: Diagram showing the beamed radiation from a single relativistic electron. The observer is shown at the bottom of the image. The beamed radiation is only visible while the electron's velocity within $\pm 1/\gamma$ of the line-of-sight. Diagram reproduced from the NRAO website[1].

it is governed by the fraction of an orbit during which an observer receives radiation. In the frame of the electron, the emitted radiation has a characteristic dipole shape, known as the Larmor dipole pattern, which is dependent on the direction of acceleration. In the electron's frame, the Larmor equation implies a power pattern proportional to $\cos^2\phi'$, with minima at $\pm\pi/2$. In the frame of the observer these minima are seen at much smaller angles: $\sin\theta \approx \frac{1}{\gamma} \approx \phi$ using the small angle approximation as $\frac{1}{\gamma} << 1$.

Relativistic beaming transforms the dipole pattern of radiation in the electron frame into a narrow beam of width $\Delta\phi = \frac{2}{\gamma}$ in the observer's frame. The beamed radiation from the electron is only visible during this time. The duration of the observed pulse, $\Delta t_{\rm p}$, is given in the observer's frame by:

$$\Delta t_{\rm p} = t_2 - t_1 = \frac{\Delta x}{v} + \frac{x - \Delta x}{c} - \frac{x}{c} \tag{1.7}$$

where the first term is the time for the electron to travel the distance Δx, the second term is the light travel time from the electron's position at the end of the pulse to the observer, and the third term is the travel time from the start of the pulse to the observer. As a result:

[1] https://www.cv.nrao.edu/course/astr534/SynchrotronSpectrum.html

$$\Delta t_{\rm p} = \frac{\Delta x}{v}\left(1 - \frac{v}{c}\right) \tag{1.8}$$

This is much less than the time it takes for the electron to move a distance Δx because in the observer's frame, the electron nearly keeps up with the photon it radiates.

In the limit $v \to c$:

$$\left(1 - \frac{v}{c}\right) = \frac{[1-(v/c)][1+(v/c)]}{[1+(v/c)]} = \frac{1 - v^2/c^2}{1+(v/c)} \approx 2\gamma^{-2} \tag{1.9}$$

and so the observed duration of the pulse is then:

$$\Delta t_{\rm p} \approx \frac{1}{2\gamma^2 \omega_{\rm g}} \tag{1.10}$$

This shows that the duration of the pulse observed in the observer's frame of reference is roughly $1/\gamma^2$ shorter than the non-relativistic gyrofrequency. Allowing for the motion of the electron parallel to the magnetic field:

$$\Delta t_{\rm p} = \frac{1}{\gamma^2 \omega_{\rm g} \sin\theta} \tag{1.11}$$

This yields a series of widely spaced narrow pulses, with the observed synchrotron power spectrum given by the Fourier transform of this time series of pulses. The observed frequency for the pulses therefore corresponds to:

$$\Delta\nu \sim (\Delta t_{\rm p})^{-1} \sim \frac{\nu_{\rm g}}{\gamma} \tag{1.12}$$

Although this should not give rise to a continuous spectrum, fluctuations in the electron energy, magnetic field strength or pitch angle can cause frequency shifts larger than $\Delta\nu$, so that it does.

The synchrotron spectrum of a single electron is therefore relatively flat at low frequencies, before it falls off at frequencies above:

$$\nu_{\rm max} = \frac{1}{\Delta t_{\rm p}} \approx \pi\gamma^2 \nu_{\rm g} \sin\theta \propto \gamma^2 B_{\perp} \tag{1.13}$$

This shows there is a tight correspondence between the energy of the electron and the frequency of the observed radiation.

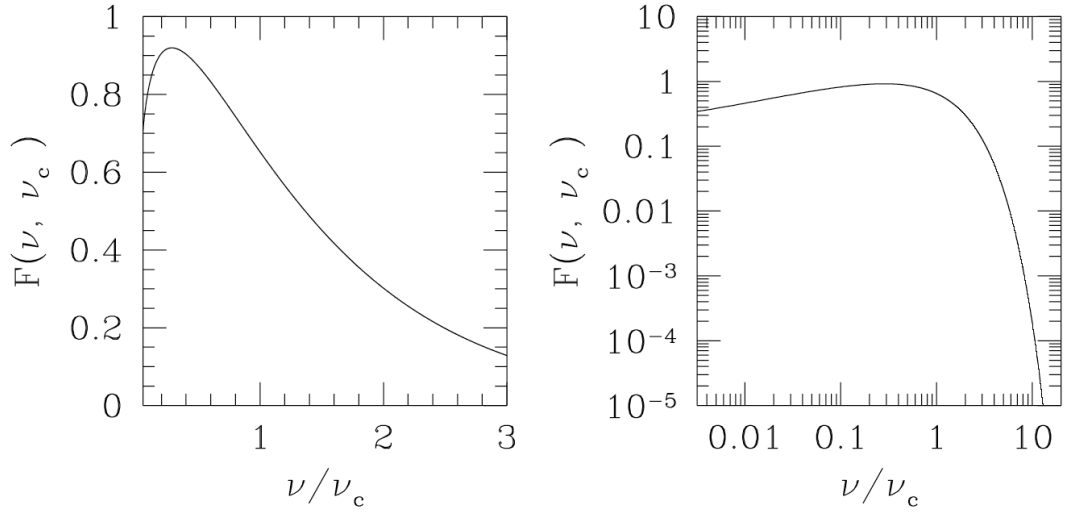

Figure 1.5: The linear and logarithmic forms of the spectral distribution function for synchrotron emission from an electron of Lorentz factor γ, and frequency $\nu_{\rm c}$. Reproduced from Figure 1 of Worrall and Birkinshaw (2006).

The critical frequency of a single electron is defined as

$$\nu_{\rm c} = \frac{3}{2}\nu \sin\theta \tag{1.14}$$

for any pitch angle. As an approximation, $\nu_{\rm c}$ can be used as the frequency of emission, but for the full distribution function it is convenient to define $X = \nu/\nu_{\rm c}$, and then the spectral distribution function is related to frequency through the integral

$$F(\nu, \nu_{\rm c}) = X \int_X^\infty K_{5/3}(\zeta) {\rm d}\zeta \tag{1.15}$$

where $K_{5/3}$ is a modified Bessel function of order 5/3. As can be seen in Figure 1.5, the spectrum peaks at $0.29\nu_{\rm c}$. The spectrum falls exponentially at frequencies above $\nu_{\rm c}$. The turn-down at low frequencies is typically not seen in observations because of synchrotron self-absorption as the source becomes optically thick.

1.4.3 Synchrotron emission from a population of electrons

Rather than a beam of emission from a singular electron, the observer will usually see a superposition of pulses from the population of electrons. These electrons are very unlikely to

be mono-energetic, or in phase. In order to convolve the electron energy distribution with the spectrum from a single electron, it is assumed that the magnetic field is uniform.

From Worrall and Birkinshaw (2006), the luminosity per unit frequency for a number spectrum of electrons $N(E)\mathrm{d}E$ is:

$$L_\nu = 2\pi\sqrt{3}cr_e m_e \nu_\mathrm{g} \sin\theta \int F(\nu, \nu_\mathrm{c}) N(E) \mathrm{d}E \tag{1.16}$$

where r_e is the classical electron radius and m_e is the mass of an electron. Assuming a power law number distribution of electron energies, so $N(E)\mathrm{d}E = \kappa E^{-p}\mathrm{d}E$, where κ is the normalisation of particle spectrum, and an isotropic pitch angle, an analytical result for frequencies between $\gamma_\mathrm{min}^2 \nu_\mathrm{g} < \nu < \gamma_\mathrm{max}^2 \nu_\mathrm{g}$ can be found whereby

$$L_\nu = \kappa \frac{2\pi\, 3^{p/2}}{p+1} c\, r_e\, m_e \sin\theta^{(p+1)/2}\, \nu^{-(p-1)/2}\, \nu_\mathrm{g}^{(p+1)/2}\, \Gamma\left(\frac{p}{4} + \frac{19}{12}\right) \Gamma\left(\frac{p}{4} - \frac{1}{12}\right) \tag{1.17}$$

where r_e and m_e are the radius and mass of an electron, ν_g is the gyrofrequency described in Equation 1.4 and Γ corresponds to the gamma function. If the pitch angle distribution is isotropic, the term in $\sin\theta$ can be replaced by another set of gamma functions, giving:

$$L_\nu = \kappa \frac{2\pi\, 3^{p/2}}{p+1} c\, r_e\, m_e\, \nu^{-(p-1)/2}\, \nu_\mathrm{g}^{(p+1)/2}\, \Gamma\left(\frac{p}{4} + \frac{19}{12}\right) \Gamma\left(\frac{p}{4} - \frac{1}{12}\right) \frac{\sqrt{\pi}\Gamma\left(\frac{p+5}{4}\right)}{2\Gamma\left(\frac{p+7}{4}\right)} \tag{1.18}$$

p is related to the spectral index of synchrotron emission, α, such that $p = 2\alpha + 1$. Substituting this into Equation 1.18, gives:

$$L_\nu = \kappa \frac{2\pi\, 3^{2\alpha+1}}{2\alpha+2} c\, r_e\, m_e\, \nu^{-\alpha}\, \nu_\mathrm{g}^{\alpha+1}\, \Gamma\left(\frac{3\alpha+11}{6}\right) \Gamma\left(\frac{3\alpha+1}{6}\right) \frac{\sqrt{\pi}\Gamma\left(\frac{\alpha+3}{2}\right)}{2\Gamma\left(\frac{\alpha+4}{2}\right)} \tag{1.19}$$

Defining $F(\alpha)$ such that:

$$F(\alpha) = \frac{2\pi\, 3^{2\alpha+1}}{2\alpha+2} \Gamma\left(\frac{3\alpha+11}{6}\right) \Gamma\left(\frac{3\alpha+1}{6}\right) \frac{\sqrt{\pi}\Gamma\left(\frac{\alpha+3}{2}\right)}{2\Gamma\left(\frac{\alpha+4}{2}\right)} \tag{1.20}$$

Then L_ν can be expressed as:

$$L_\nu = F(\alpha)\, \kappa\, \nu^{-\alpha}\, \nu_\mathrm{g}^{(\alpha+1)}\, c\, m_\mathrm{e}\, r_\mathrm{e} \tag{1.21}$$

The spectral index of synchrotron emission is typically defined as $L(\nu) \propto \nu^{-\alpha}$. The spectral shape of synchrotron emission is therefore determined by the spectral distribution of electron energies within a plasma.

1.4.4 Spectral Evolution

From Section 1.4.1, electrons will lose energy at a rate given by Equation 1.6. The radiative lifetime of the electrons is given by:

$$\tau = \frac{E}{-\left(\frac{\mathrm{d}E}{\mathrm{d}t}\right)} \tag{1.22}$$

The evolution of the synchrotron spectrum depends on the injection rate and synchrotron lifetime and is described by the diffusion-loss equation:

$$\frac{\mathrm{d}N(E)}{\mathrm{d}t} = \frac{\mathrm{d}}{\mathrm{d}E}\left[N(E)\left(\frac{\mathrm{d}E}{\mathrm{d}t}\right)\right] + Q(E,t) + D\nabla^2 N(E) \tag{1.23}$$

where $N(E)$ is the particle density, $Q(E,t)$ corresponds to the rate at which particles are injected per unit volume and the final term represents the diffusion of particles away from the source with scalar diffusion coefficient D. This term will be neglected here. In a steady-state system, energy losses are balanced by the addition of new particles ($\mathrm{d}N/\mathrm{d}t = 0$), so in the case where electrons are continuously injected with a spectrum κE^{-p}, Equation 1.23 becomes:

$$\frac{\mathrm{d}}{\mathrm{d}E}\left[N(E)\left(-\frac{\mathrm{d}E}{\mathrm{d}t}\right)\right] = -\kappa E^{-p} \tag{1.24}$$

As $N \to 0$ and $E \to \infty$:

$$N(E) = \frac{\kappa E^{-(p-1)}}{(p-1)\left(-\frac{\mathrm{d}E}{\mathrm{d}t}\right)} \propto E^{-(p+1)} \tag{1.25}$$

High energy electrons for which $\tau << t$ (where t is the age of the source) are subject to synchrotron cooling, and their energy spectrum will be steeper than the initial spectrum. Spectral steepening of α moving from the hotspots towards the source is interpreted as the effect of spectral aging in the lobes. Low energy electrons which have not yet had the time to cool ($\tau << t$) will show a distribution of energies corresponding to the injection spectrum. The energy of the spectral break is related to the lifetime of the source.

1.4.5 Minimum Energy

The total energy emitted by synchrotron radiation depends on both particle and magnetic field energy densities. In order to probe the internal conditions of the lobes, these energy densities have to be separated, but this is impossible with observations of radio flux alone. However, by making assumptions about how the two energy densities combine, it is possible to estimate the lobe conditions required to produce the observed radio flux. One of these is the minimum energy assumption of Burbidge (1956), where the energy densities of particles and magnetic field are assumed to sum to a minimum. This is also close to the assumption of equipartition, where the particles and magnetic field make similar contributions to the total energy.

If non-radiating particles have energy K times that of electrons, the energy density in particles, u_p, can be written as $(1+K)u_{\mathrm{e}^-}$. The energy density in the magnetic field and particles is given by:

$$u_{\mathrm{tot}} = u_B + u_p = \frac{B^2}{2\mu_0} + (1+K)\frac{U_{\mathrm{e}}}{fV} \tag{1.26}$$

where f is the filling factor of particles in the emitting volume V, such that $f \leq 1$. The energy in electrons for a power law distribution of energies if $\alpha \neq 0.5$ is given by:

$$U_{\mathrm{e}} = \int_{E_{\mathrm{min}}}^{E_{\mathrm{max}}} \kappa E^{-p} E \mathrm{d}E = m_{\mathrm{e}}c^2\kappa \int_{\gamma_{\mathrm{min}}}^{\gamma_{\mathrm{max}}} \gamma^{-2\alpha}\mathrm{d}\gamma = m_{\mathrm{e}}c^2\kappa \left(\gamma_{\mathrm{max}}^{1-2\alpha} - \gamma_{\mathrm{min}}^{1-2\alpha}\right)(1-2\alpha)^{-1} \tag{1.27}$$

and by the following if $\alpha = 0.5$:

$$U_{\mathrm{e}} = m_{\mathrm{e}}c^2\kappa\left(\ln\gamma_{\mathrm{max}} - \ln\gamma_{\mathrm{min}}\right) \tag{1.28}$$

Using the definition of the gyrofrequency, L_ν can be written as:

$$L_\nu \propto \kappa B^{\alpha+1}\nu^{-\alpha} \tag{1.29}$$

and then substituting for κ using Equation 1.21 gives:

$$U_{\mathrm{e}} = CL_\nu\nu^\alpha B^{-(\alpha+1)}\left(\gamma_{\mathrm{max}}^{1-2\alpha} - \gamma_{\mathrm{min}}^{1-2\alpha}\right)(1-2\alpha)^{-1} \tag{1.30}$$

where $\alpha \neq 0.5$ and $C = \frac{c}{r_{\mathrm{e}}F(\alpha)}\frac{\nu_{\mathrm{g}}}{B}^{-(\alpha+1)}$. Therefore, the total minimum energy with $\alpha \neq 0.5$ corresponds to a magnetic field strength of:

$$B_{\rm me} = \left[L_\nu \nu^\alpha \frac{C(\alpha+1)}{4\mu_0} \frac{(1+K)}{fV} \frac{(\gamma_{\rm max}^{1-2\alpha} - \gamma_{\rm min}^{1-2\alpha})}{1-2\alpha} \right]^{1/(\alpha+3)} \tag{1.31}$$

and with $\alpha = 0.5$:

$$B_{\rm me} = \left[L_\nu \nu^{0.5} \frac{C(1.5)}{4\mu_0} \frac{(1+K)}{fV} (\ln\gamma_{\rm max} - \ln\gamma_{\rm min}) \right]^{2/7} \tag{1.32}$$

Adopting a sphere of angular radius θ for the emitting volume gives:

$$V = \frac{4}{3}\pi\theta^3 \left[\frac{D_L}{(1+z)^2} \right]^3 \tag{1.33}$$

where D_L corresponds to the luminosity distance of the source. The luminosity density is related to the flux density S_ν by

$$L_\nu = 4\pi S_\nu D_L^2 (1+z)^{\alpha-1} \tag{1.34}$$

Substituting into Equation 1.31, the magnetic field at minimum energy for $\alpha \neq 0.5$ can therefore be given by:

$$B_{\rm me} = \left[3 S_\nu \nu^\alpha (1+z)^{5+\alpha} \frac{C(\alpha+1)}{4\mu_0} \frac{(1+K)}{f\theta^3 D_L} \frac{(\gamma_{\rm max}^{1-2\alpha} - \gamma_{\rm min}^{1-2\alpha})}{1-2\alpha} \right]^{1/(3+\alpha)} \tag{1.35}$$

Substituting $B_{\rm min}$ into Equation 1.26, the total energy density of the system at minimum energy is given by:

$$u_{\rm min} = u_B \frac{(\alpha+3)}{\alpha+1} = u_{\rm p} \frac{(\alpha+3)}{2} \tag{1.36}$$

therefore, approximately, there are roughly equal energies in the magnetic field and relativistic particles as α is usually between 0.5 and 1. A change in this ratio will result in an increase in the total energy and pressure of the source. The energy density is related to the pressure by $P = (\gamma_{\rm s} - 1)u$, where the ratio of specific heats, $\gamma_{\rm s} = 4/3$, for an ultrarelativistic gas, so that the pressure of the system can be expressed as $P = u/3$. The values derived from the minimum energy assumption should be treated as order of magnitude estimates, as there are many scenarios which drive the system away from $u_{\rm min}$. There is also a dependence on $\eta = (1+K)$ and also on the filling factor f. Typically unity is assumed for both f and η (with $K = 0$), in order to estimate a true minimum energy and pressure.

1.4.6 Faraday Rotation and Rotation Measure

Synchrotron radiation is linearly polarised perpendicular to the magnetic field direction projected on to the plane of the sky. The direction of the polarisation may change as the radio emission propagates through the mixed thermal material and fields in the ambient medium or other nearby gaseous structures. The presence of magnetic fields induces different refraction indices for the two circularly polarised components into which linearly polarised radiation can be decomposed. The different propagation speeds of the two components can consequently cause a rotation of the plane of polarisation. This effect is known as Faraday rotation (Faraday, 1846).

For foreground plasma with a wavelength λ, the Faraday rotation is an angle given by:

$$\theta_{\rm F} = {\rm RM}\,\lambda^2 \tag{1.37}$$

where RM is the rotation measure, or the difference between the intrinsic polarisation angle of the emission at the source and after travelling through some of the ambient medium. The RM along a path of length L is (Worrall and Birkinshaw, 2006):

$${\rm RM} = \frac{1}{c}\int_0^L n_{\rm e,th}\nu_{\rm g}r_{\rm e}{\rm cos}\psi{\rm d}z \tag{1.38}$$

where $n_{\rm e,th}$ is the thermal electron density and ψ is the angle of the magnetic field to the line of sight. In SI units,

$${\rm RM} = 8100\int_0^L n_{\rm e,th}B_{\parallel}{\rm d}z \;\;\; {\rm rad\,m^{-2}} \tag{1.39}$$

with the magnetic field line of sight component $B_{\parallel}$ in T, $n_{\rm e,th}$ in ${\rm m}^{-3}$ and the thickness L in pc. To find the rotation measure, mapping in multiple radio frequencies is required, to establish the intrinsic polarisation angle of the source.

1.5 Inverse-Compton Emission

In iC emission, relativistic electrons scatter low energy photons to high energy at the expense of the kinetic energy of the electrons. This process is referred to as inverse-Compton scattering, as the electrons lose energy in this instance, rather than the photons.

1.5.1 Electron energy loss

The following approach is taken from (Longair, 2011), and estimates the power lost by the electron during iC scattering in the observer's frame. In the observer's frame, the energy of a photon and its angle of incidence are given by $h\nu$ and θ respectively. The photon's energy will be far less than that of the relativistic electron's, consequently the Thomson cross-section, σ_{T}, is used to describe the probability of scattering. The power emitted in the electron rest frame (S') is given by

$$-\left(\frac{\mathrm{d}E'}{\mathrm{d}t}\right) = \sigma_{\mathrm{T}} c u'_{\mathrm{rad}} \tag{1.40}$$

where u'_{rad} is the energy density of radiation in the electron's rest frame.

In the electron's rest frame, the incident energy density is boosted by two relativistic Doppler factors. According to the formula for the relativistic Doppler shift, in the rest frame of the electron the energy of the photon becomes:

$$h\nu = h\nu'\gamma(1 + \beta\mathrm{cos}\theta) \tag{1.41}$$

that is, the frequency of the photon is higher in the electron's frame. The second Doppler factor is due to an increased photon arrival rate in the frame of the electron. Correspondingly, their number density is greater by the same factor. If n is the photon number density in the observer's frame then

$$n' = n\gamma(1 + \beta\mathrm{cos}\theta) \tag{1.42}$$

Therefore, the energy density of the incident radiation field in the electron's frame can be expressed as

$$u'_{\mathrm{rad}} = n' h\nu' = u_{\mathrm{rad}}|\gamma(1 + \beta\mathrm{cos}\theta)|^2 \tag{1.43}$$

where the transformation between u'_{rad} and u_{rad} is dependent on the angle between the direction of the photons and the electron velocity.

Assuming the radiation is isotropic in the observer's frame, the total energy in the electron's frame can be found by integrating over the solid angle:

$$u'_{\rm rad} = u_{\rm rad} \int_0^{\pi} \frac{\gamma^2}{2}(1+\beta{\rm cos}\theta)^2 {\rm sin}\theta {\rm d}\theta = \frac{4}{3} u_{\rm rad} \left(\gamma^2 - \frac{1}{4}\right) \tag{1.44}$$

As the rate of loss of energy by the electrons is invariant between inertial frames (such that $({\rm d}E/{\rm d}t) = ({\rm d}E/{\rm d}t)'$), the net energy gained by the photon field is found by subtracting the initial energy contributed by the incident low-energy photons:

$$-\left(\frac{{\rm d}E}{{\rm d}t}\right) = \frac{4}{3}\sigma_{\rm T} c u_{\rm rad} \left(\gamma^2 - \frac{1}{4}\right) - \sigma_{\rm T} c u_{\rm rad} = \frac{4}{3}\sigma_{\rm T} c u_{\rm rad}(\gamma^2 - 1) = \frac{4}{3}\sigma_{\rm T} c \gamma^2 \beta^2 u_{\rm rad} \tag{1.45}$$

This is the net power gained by the radiation field at the expense of the electron. Compared to the corresponding synchrotron power (Equation 1.6), there is a similarity in the energy loss such that:

$$\frac{L_{\rm iC}}{L_\nu} = \frac{u_{\rm rad}}{u_B} \tag{1.46}$$

If relativistic electrons are subjected to both a radiation and magnetic field, then they will emit via both the synchrotron and iC processes. This is not observed if the source becomes optically thick and synchrotron self absorption significantly offsets the synchrotron cooling of the electron population, or if the electron energies are high enough ($\gamma h\nu / m_{\rm e}c^2 \rightarrow 1$) such that the Thomson cross section is no longer applicable (the Klein-Nishina regime). The cross-section in the Klein-Nishina regime is smaller than for Thomson scattering, and as such the electrons scatter less on the photon fields, and therefore cool less than predicted.

1.5.2 The observed inverse-Compton spectrum

In the electron's frame, relativistic aberration causes most of the photons to approach almost head-on. If the incident radiation field in the observer's frame is composed of photons having frequency ν_0, the frequency in the electron frame is given by:

$$\nu'_0 = \nu_0[\gamma(1+\beta{\rm cos}\theta)] \approx \nu_0[\gamma(1+\beta)] \tag{1.47}$$

for small angles where $\theta << 1$. Thomson scattering produces radiation with the same frequency as the seed photons, so the collisions are elastic. Thus, in the frame of the electron the frequencies before and after scattering are equal ($\nu'_0 = \nu'$).

In the observer's frame, relativistic aberration beams the scattered photons in the same direction as the electron's motion. In the observer's frame, the frequency ν of the scattered radiation is given by:

$$\nu = \nu'\gamma(1 + \beta\cos\theta) \approx \nu'\gamma(1 + \beta) \approx \nu_0\gamma^2(1 + \beta)^2 \tag{1.48}$$

In the ultrarelativistic regime, $\beta \to 1$. The maximum energy of the up-scattered radiation in the observer's frame corresponds to a head-on collision, in which the photon is sent back along its path. This is given by

$$h\nu_{\max} = h\nu\gamma^2(1 + \beta^2)^2 \approx 4\gamma^2 h\nu_0 \tag{1.49}$$

The number of photon collisions with a single electron per unit time is

$$\frac{\mathrm{d}N}{\mathrm{d}t} = \frac{\sigma_T c u_{\mathrm{rad}}}{h\nu_0} \tag{1.50}$$

The average energy, $h\bar{\nu}$, of scattered photons is equal to the energy loss per electron divided by the rate of scattering:

$$h\bar{\nu} = \frac{-\frac{\mathrm{d}E}{\mathrm{d}t}}{\frac{\mathrm{d}N}{\mathrm{d}t}} = \frac{4}{3}\beta^2\gamma^2 h\nu_0 \approx \frac{4}{3}\gamma^2 h\nu_0 \tag{1.51}$$

As the maximum frequency is only three times larger than the average frequency, this shows that the iC spectrum is strongly peaked around the average frequency. As a result of Equation 1.51, far-infrared photons with $\nu_0 = 3 \times 10^{12}$ Hz, scattered by electrons with $\gamma = 1000$ will be scattered to X-ray frequencies ($\nu = 3 \times 10^{18}$ Hz, with energy ~ 10 keV). X-ray radiation from iC scattering over the scales associated with radio galaxies is normally produced using the cosmic microwave background (CMB) as seed photons. The full spectrum of iC scattered CMB photons by a power law distribution of electrons results in an intensity spectrum of the scattered radiation of the form:

$$L_{\mathrm{iC}} \propto u_{\mathrm{CMB}}(1 + z)^{3+\alpha}\nu_{\mathrm{CMB}}^{\alpha-1}\nu_{\mathrm{X}}^{-\alpha} \tag{1.52}$$

1.5.3 Inverse-Compton magnetic field

Similarly to Equation 1.52, the radio synchrotron intensity spectrum can be described as:

$$L_{\rm r} \propto u_{\rm B} \nu_{\rm g}^{\alpha-1} \nu_{\rm r} \tag{1.53}$$

As the synchrotron radio emission and X-ray iC emission from the same relativistic electrons have the same spectral shape, the ratio of the observed flux densities in X-rays and radio, $R_{\rm obs}$, is (Harris and Grindlay, 1979):

$$R_{\rm obs} = \frac{S_{\rm X}}{S_{\rm r}} \left(\frac{\nu_{\rm X}}{\nu_{\rm r}} \right)^{\alpha} = (1+z)^{3+\alpha} \frac{u_{\rm CMB}}{u_{\rm B}} \left(\frac{\nu_{\rm CMB}}{\nu_{\rm g}} \right)^{\alpha-1} \tag{1.54}$$

where $S_{\rm X}$ and $S_{\rm r}$ are the X-ray and radio flux densities, $\nu_{\rm X}$ and $\nu_{\rm r}$ are the X-ray and radio frequencies, $u_{\rm CMB}$ and $\nu_{\rm CMB}$ are the values of the CMB energy density and frequency at redshift 0 and $\nu_{\rm g}$ is the non-relativistic gyrofrequency (Equation 1.4). As both the energy density of the magnetic field, $u_{\rm B}$, and $\nu_{\rm g}$ are related to the magnetic field strength ($u_{\rm B} \propto B^2$ and $\nu_{\rm g} \propto B$), $R_{\rm obs} \propto B_{\rm iC}^{-(\alpha+1)}$. Assuming the same spectral index is obtained for both the X-ray and the radio emission, the iC magnetic field, $B_{\rm iC}$, can then be calculated using:

$$B_{\rm iC} = \left[(1+z)^{3+\alpha} \frac{2\mu_0 u_{\rm CMB}}{R_{\rm obs}} \left(\frac{\nu_{\rm CMB} 2\pi\gamma m_{\rm e}}{e} \right)^{\alpha-1} \right]^{1/(1+\alpha)} \tag{1.55}$$

1.5.4 Inverse-Compton Emission in Radio Galaxies

Before the advent of X-ray observatories, the minimum energy condition was used to estimate the internal content and energy of radio lobes. When X-ray observations became more common with the introduction of *ROSAT*, radio and X-ray observations could be combined to lift the degeneracy between magnetic and particle energy densities in the hotspots and extended structures of radio galaxies. The dominant photon field in the lobes is from CMB photons, with a small contribution from synchrotron self-Compton (SSC) (Hardcastle et al., 2002). IC emission from nuclear photons has also been observed in certain cases, such as in 3C 207, which has much stronger X-ray emission near the nucleus than in the rest of the lobes (Brunetti et al., 2002).

IC X-ray emission is typically not detected from FR I lobes, and so their pressures are generally calculated assuming equipartition. The pressure estimates for these sources from equipartition tend to be less than that of the surrounding intracluster medium (ICM) (Hardcastle et al., 1998; Worrall and Birkinshaw, 2000; Dunn et al., 2005), suggesting the presence of a population

of non-radiating particles is required to increase the pressure of the lobe. Hardcastle and Worrall (1999) report observations of half of the Third Cambridge Catalogue of Radio Sources (3CRR) (Laing et al., 1983) with $ROSAT$, reporting a 60% detection rate of X-rays in the lobes of radio sources. Croston et al. (2005) reported a 75% detection of X-rays in the lobes of 33 FR II radio galaxies and quasars, with the measured energy densities consistent with iC scattering of the CMB. FR II lobes show X-ray emission indicative of IC more commonly than FR Is, and when the properties of these lobes are used to model the electron energy density in the lobes, the lobes tend to appear closer to pressure balance with their environment (Kataoka and Stawarz, 2005; Croston et al., 2005; Belsole et al., 2007; Ineson et al., 2017). These results suggest that there is typically no energetically significant proton population in the lobes of FR II radio galaxies (unlike for FR Is), and so iC modelling provides an accurate way of measuring the total energy content of the lobes along with estimating the radio source's jet power.

1.5.5 Synchrotron self-Compton emission

The dominant process for the most powerful hotspots with strong spectral steepening or a synchrotron cut off at radio/optical frequencies is thought to be the synchrotron self-Compton (SSC) process, in which radio photons from the synchrotron process are iC scattered to X-ray energies by synchrotron emitting electrons (Harris et al., 1994; Hardcastle et al., 2004). X-ray measurements of the SSC process in hotspots suggest that magnetic fields in these systems are remarkably close to equipartition, and the hotspot energies are unlikely to be dominated by protons or very low filling factors (Hardcastle et al., 2004).

1.6 Intracluster Medium

The space between the galaxies in clusters of galaxies is filled with a hot ($T \sim 10^6 - 10^8$ K), low density ($n_{\rm e} \sim 10^{-4} - 10^{-2}$ cm^{-3}), diffuse gas known as the intracluster medium (ICM). Its existence was first suggested as early as 1959 (Limber, 1959), although it was first detected with Geiger counters onboard a rocket (Byram et al., 1966). Its high temperature is caused by shocks, whereby the kinetic energy from its deep gravitational potential well is converted to thermal energy during cluster formation. The gas mass of the ICM is roughly 10 times larger than the mass in stars (Gonzalez et al., 2013), and is the primary contributor to the baryonic mass of galaxy clusters, accounting for approximately 10% of the total dark matter dominated

mass (Chiu et al., 2016).

Spectroscopic studies of the ICM utilising observations from *Chandra* and *XMM-Newton* can be used to measure the thermodynamic properties of the gas such as the density, temperature and metallicity. These properties give information about their host cluster, and also the evolution of structure across cosmic time in general (Voit, 2005). Assuming the ICM is in hydrostatic equilibrium and the cluster is spherically symmetric, the total cluster mass can be derived easily (Sarazin, 1986). The distribution of metals within clusters can reveal how and when metals were removed from their stellar systems. Radial profiles of the density and temperature allow for the measurement of other fundamental thermodynamic properties such as the pressure and the entropy. The entropy encodes information about the thermal history of the cluster, especially with regard to mergers and AGN feedback (Ponman et al., 1999).

CMB photons can be scattered off the high energy electrons of the ICM. This leads to a small distortion of the CMB spectrum and boosts the energy of the CMB photons. This effect is called the Sunyaev-Zel'dovich (SZ) effect (Sunyaev and Zeldovich, 1972), and as the signal is independent of redshift, it allows for the detection of high redshift clusters whose X-ray surface brightness would be otherwise too weak for detection.

1.6.1 Thermal Bremsstrahlung

For a primarily hydrogen-composed gas of the temperatures and densities typically found in galaxy clusters, the primary emission process is thermal bremsstrahlung (or free-free) emission. Since the gas temperature is very high, most elements are highly ionised, hence the gas is really a hot plasma. Negatively charged electrons experience an acceleration when they encounter a positively charged ion, and thus emit a photon. As the electrons are slowing down, the gas on the whole loses energy and consequently cools.

The low frequency spectrum for a single electron is given by the following equation (Longair, 2011):

$$I(\omega) = \frac{16Z^2e^6n_i}{3\pi^3c^3m_{\mathrm{e}}^2v}\ln\frac{b_{\max}}{b_{\min}} \tag{1.56}$$

where $b_{\max}$ and $b_{\min}$ correspond to the minimum and maximum impact parameters between the electron and the ion it encounters, Z is the charge of the ion, n_i is the number density of ions, v is the velocity of the electron, m_{e} is the mass of an electron and e is the charge of an electron.

To calculate the spectrum for bremsstrahlung of a thermal plasma at a temperature T, Equation 1.56 needs to be integrated over the impact parameters, and the three-dimensional velocity distribution of particles given by the Maxwell distribution:

$$n_{\rm e}(v)dv = 4\pi n_{\rm e}\left(\frac{m_{\rm e}}{2\pi k_B T}\right)^{3/2} v^2 e^{-\frac{m_{\rm e}v^2}{2k_B T}} dv \tag{1.57}$$

The emissivity, or the energy per unit time, frequency and volume, is then given by:

$$\epsilon_\nu^{\rm ff} = \frac{32\pi e^6}{3m_{\rm e}c^3}\left(\frac{2\pi}{3m_{\rm e}k_B T}\right)^{1/2} Z^2 n_e n_i e^{-\frac{h\nu}{k_B T}} g_{\rm ff} \tag{1.58}$$

where $g_{\rm ff}$ is the Gaunt factor, which corrects for quantum mechanical effects and for the effects of distant collisions. Equation 1.58 predicts that emission from clusters should fall off rapidly at high frequencies, as is observed. The multiplication of density in the equation shows the collisional nature of the process.

To assess the role of cooling in the ICM, the cooling timescale can be defined as:

$$t_{\rm cool} = \frac{\mathrm{d}\,\ln(T)}{\mathrm{d}t}^{-1} \tag{1.59}$$

For temperatures that apply to the ICM in most clusters, the cooling time can be approximated as (Sarazin, 1986):

$$t_{\rm cool} \approx 8.5\times10^{10}\left(\frac{n_{\rm e}}{10^{-3}\,{\rm cm}^{-3}}\right)^{-1}\left(\frac{T}{10^8\,{\rm K}}\right)^{1/2}\ {\rm years} \tag{1.60}$$

However, at temperatures below $\sim$ 2 keV, the line emission from the ICM cannot be ignored (as it is in this approximation). Cooling curves from Figure 5 in Worrall and Birkinshaw (2006) then give more accurate estimates of the cooling time.

1.6.2 Isothermal β-model

Observations of the X-ray emission from groups and clusters of galaxies has shown that the morphologies of the emitting gas are quite varied, and that they can be related to the dynamical state of the system. Forman and Jones (1982) proposed a classification into 'regular' and 'irregular' cluster morphologies. Regular (or relaxed) clusters usually show roughly round, centrally peaked X-ray brightness distributions, which decrease smoothly with distance. Clusters in this classification are thought to be evolved systems which have undergone dynamical relaxation.

If the cluster potential is assumed to be that of a self-gravitating isothermal sphere, then the gas distribution is given by (Cavaliere and Fusco-Femiano, 1978):

$$\eta_\rho = \eta_{\rho 0}\left[1+\left(\frac{r}{r_{\rm cx}}\right)^2\right]^{\frac{-3\beta}{2}} \tag{1.61}$$

where η_ρ corresponds to the proton density, $\eta_{\rho 0}$ corresponds to the central proton density and r corresponds to the distance from the centre. $r_{\rm cx}$ is a measure of the size of the central core, and is fitted so that the projected galaxy density at distance $r_{\rm cx}$ from the cluster centre is one half of the central density. The quantity β controls the fall-off of proton number density with radius and is defined as

$$\beta = \frac{\mu m_{\rm H}\sigma_{\rm r}^2}{k_B T} \tag{1.62}$$

where μ is the mean molecular weight and $\sigma_{\rm r}$ is the radial velocity dispersion characteristic of the mass. Physically, β corresponds to the ratio between the kinetic energy of gravitationally bound galaxies and the thermal energy of the hot gas in the ICM.

The surface brightness profile of the X-ray emission in regular clusters is well described by a similar function:

$$S = S_0\left[1+\left(\frac{r}{r_{\rm cx}}\right)^2\right]^{-3\beta+1/2} \tag{1.63}$$

where S_0 is the central surface brightness.

The integrals needed to computer various cluster quantities, such as the gas and total masses, luminosity and X-ray surface brightness can all be found analytically via integrals of properties derived from the isothermal β-model. For example, the gas mass within the core radius can be found from the following integral:

$$M(r\leq r_{\rm cx}) = \frac{m_{\rm H}}{X}\int_0^{r_{\rm cx}} dr 4\pi r^2 \eta_{\rho 0}\left[1+\left(\frac{r}{r_{\rm cx}}\right)^2\right]^{\frac{-3\beta}{2}} \tag{1.64}$$

where M is the mass and X is the abundance of hydrogen by mass.

With later *ROSAT* data, and now *Chandra* and *XMM-Newton* data, it has now been established that the ICM is not isothermal, but shows decreasing temperature profiles on large scales.

Despite this, the use of the isothermal β-model persists, as it allows for calculation of the main properties of the ICM to first approximation. Additionally, the model fails to reproduce the strongly peaked X-ray surface brightness distribution in some clusters. This peaked emission is sometimes interpreted as emission from the ISM of the central galaxy superimposed on that from the IGM/ICM, or as indication of the presence of a cool core. Fits to the peaked emission can be significantly improved by the use of two different β models, one fitting the central galaxy emission and the other fitting the more large scale ICM emission (e.g. Croston et al., 2008b).

1.6.3 Fluid Instabilities in Radio Galaxies

The interaction of radio structure with with the external medium can lead to fluid instabilities, which can call into question the long term stability of those structures.

a) Kelvin-Helmholtz Instability

Kelvin-Helmholtz (KH) instabilities can occur when there is a velocity difference across the interface between two different fluids. This occurs in radio galaxies between the relativistic radio jet and the surrounding external medium, or between jet backflow and the shocked ambient gas in FR II sources with cocoon shocks. If an instability, or ripple, develops at the interface between the two fluids, the flow over the ripple has to be faster and therefore exerts less pressure and allows the ripple to grow further. This causes the mixing of the two fluids across the boundary, with progressive destruction of collimation and slowing down of the flow (Chandrasekhar, 1961; Gerwin, 1968).

Instability timescales are rather short with respect to the jet propagation timescale, such that the instabilities can effect jets soon after they are launched. Long wavelengths can modulate the morphology of the beam, while short wavelengths give rise to a turbulent cascade that eventually leads to thermal dissipation (Ferrari, 1998).

b) Rayleigh-Taylor Instability

Rayleigh-Taylor (RT) instabilities can occur when a light fluid pushes on a heavy fluid, for example when the lighter radio lobes push on the thermal gas in the ICM. As the lobes are of lower density than their outer environment, the lobes rise buoyantly and sweep up some of the ICM, which can be seen in several sources as enhanced emission at the edges or rims of the

lobes. The RT instabilities should tear the bubble apart in times less than the estimated age of most cavities (Pizzolato and Soker, 2006).

The RT instabilities can however, potentially be suppressed by either magnetic field or several purely dynamical gas effects which arise naturally (Pizzolato and Soker, 2006).

1.7 AGN Feedback

1.7.1 The Cooling Flow Problem

The radiative cooling times (Equation 1.60) in dense gas at the centres of the hot atmospheres which make up clusters are found to be much shorter than their ages and the age of the Universe, with timescales of order 1 Gyr. The gas is initially heated up to 10^7 K by the gravitational collapse which occurs when the clusters form (Fabian, 1994). At the centre of the cluster, the density of the gas is high and its temperature is relatively low, suggesting cooling timescales less than the Hubble time. Where this is the case, a cooling flow should form, in which gas cools and flows inwards in quasi-hydrostatic equilibrium.

The cooling flow should manifest itself observationally with prominent star formation and significant amounts of gas at temperatures less than 2 keV. However, X-ray analysis of clusters has provided evidence that the mass deposition rates of cool gas is much lower than would be expected (Peterson et al., 2001; Hudson et al., 2010) and that estimated star formation rates are much lower than the levels expected from a cooling flow model (O'Dea et al., 2008). This cooling flow problem was noted during some of the earliest X-ray observations of clusters (Cowie and Binney, 1977; Fabian and Nulsen, 1977). This suggests that something is heating the gas in the ICM, preventing the cooling. Energy injection from supernovae is found to be insufficient (Peterson et al., 2003; Voit, 2005), so AGN are typically invoked to provide the additional heating, via AGN feedback. Black holes are though to feedback into their environment via two distinct modes which operate on different scales: the radiative or quasar mode, and the kinetic or jet mode.

1.7.2 Radiative Mode

Quasars accreting at close to the Eddington-limit and radiatively efficiently can display winds and outflows of highly ionised material from the accretion disk, driven by radiation pressure (Veilleux et al., 2005). These galactic winds typically show as wide-angle, galaxy-scale outflows

of gas and dust. They can impact upon a galaxy's evolution by expelling and heating gas from the nucleus, thereby lowering the star formation rate (Wagner et al., 2013), quenching galaxies (Pontzen et al., 2017), shaping galaxy morphology (Dubois et al., 2016) and regulating black hole accretion (Hopkins et al., 2016). Observations suggest that the quasar-driven winds are more important at higher redshifts ($z \geq 2$), where star formation and AGN activity peaks (Leung et al., 2017). More luminous galaxies tend to have formed their stars earlier and over a shorter time span, which could be attributed to the AGN effectively sterilising their hosts via these winds (Hopkins et al., 2006).

1.7.3 Kinetic Mode

The kinetic or radio mode, is where an AGN feeds back into its environment through large-scale, relativistic radio jets. Scheuer (1974) proposed that newly formed radio lobes, inflated in the external medium by radio jets, will drive shocks into the external medium, heating it. The kinetic mode is thought to be responsible for regulating the runaway cluster-gas cooling anticipated by the cooling flow problem. This thesis is focussed on this mode of AGN feedback.

1.7.4 Observational Evidence of Feedback

In the nearby Universe, direct observational evidence for AGN feedback arises from observations of clusters, groups and giant elliptical galaxies, which contain large amounts of hot gas. This discovery was made possible by the current generation of X-ray instruments, with high sensitivity and spatial and spectral resolution, namely the *Chandra* X-ray Observatory and *XMM-Newton*. Data from these instruments showed X-ray cavities or bubbles, embedded within the rich atmospheres of clusters. These cavities present as regions of low surface brightness, as the X-ray emitting gas in them has been displaced by radio plasma. Studies of samples of systems with X-ray cavities found a strong correlation between the mechanical power injected into the hot gas by the AGN through the inflation of the cavities, and the energy required to offset cooling (Bîrzan et al., 2004; Croton et al., 2006; Rafferty et al., 2006). These studies have also found that cavities are common, especially in systems which require heating to prevent catastrophic cooling. X-ray cavities are also thought to play a role in lifting cooling gas from the centre of clusters, which then condenses and forms molecular clouds (McNamara et al., 2016). Alongside this, AGN also potentially inject energy into the ICM by inducing weak shocks and propagating energy via sound and pressure waves (Fabian et al., 2006; Sanders and Fabian, 2007).

There are several issues with these studies. Most of these studies are focussed at redshifts of ≤ 0.3, with very few direct studies of feedback in clusters undertaken at $z > 0.5$, as it is difficult to detect clusters at high redshift. One of the few undertaken is by Hlavacek-Larrondo et al. (2012), who find no evidence for the evolution of cavity properties with redshift (up to $z \sim 0.6$), with outburst powers and energetics similar, and no evidence of bubbles rising farther or lesser distances from the nucleus. Additionally, the rich cluster environments necessary for studies of cavities are not representative of the typical environments of AGN, which are more commonly found in groups and the full range of radio power is not studied. Moreover, many details of AGN feedback are poorly understood. For example it is unclear how energy is transported on large cluster scales.

1.8 X-ray gas belts in radio galaxies

Radio galaxies in group and cluster environments can display prominent, X-ray bright, belt-like gas structures. These gas belts present themselves as enhanced X-ray emission perpendicular to the radio axis, and are often found between the radio lobes, coincident with areas of low radio surface brightness. A bright central 'bar' of X-ray emission showing interactions with the base of the lobes, is a common feature of numerical models of radio galaxies (Hardcastle and Krause, 2013, 2014).

It is presumed that radio jets inject energy into their surrounding environments on both small and large scales, impacting physical processes such as star formation in their galaxies and preventing gas cooling on cluster scales. The physical processes related to the gas belts are therefore important, as the belts may directly impact the fuelling of the central black hole of their host galaxies or help mediate a transfer of energy from AGN to the external medium. As mentioned above, feedback from radio sources is typically studied using cavities expanded in rich cluster environments (Bîrzan et al., 2004, 2008). However, there are limitations to studying feedback using these techniques alone: the environments are not representative of those most frequently inhabited by radio sources and the full range of radio power is not studied. Studying sources with gas belts within a complete sample in combination with the powerful FR II source Cygnus A, allows us to overcome some of these limitations.

It is possible that a gas belt may be formed by the external medium being driven inwards by the expanding radio lobes as has been seen in the studies of 3C 386 (Duffy et al., 2016) presented

in this thesis. Scenarios similar to this have been noted in simulations (Gilkis and Soker, 2012; Hillel and Soker, 2016). This inflowing gas has the potential to provide additional fuel to the AGN, prolonging its current outburst, or beginning a new cycle of radio activity, should some of the gas be delivered to the pc-scale regions around the central black hole. It is also possible that gas belts could form as a result of gas from the cooler interstellar/intergalactic medium (ISM/IGM) being driven outwards from the source, by either the jet or the radio lobes. This has been seen for the gas belt in 3C 35 (Mannering et al., 2013), in which fossil group gas has been driven outwards by the expanding radio lobes. In this scenario, the AGN is robbed of a fuel supply, leading to a cessation of jet activity. Other gas belts have been shown to shape the radio structure, rather than being shaped by it. X-ray bright gas originating from a merger between two galaxies is pushing apart old radio lobes of 3C 442A, and re-energising the radio-emitting plasma (Worrall et al., 2007).

In this thesis, I report the first systematic study of X-ray gas belts in the complete low-redshift 3CRR sample (Laing et al., 1983), along with an in-depth study of the non-axisymmetric X-ray gas (or ribs) within the cocoon shock of Cygnus A in order to categorise the occurrence, morphologies and origins of gas belts, and their impact on AGN feedback and galaxy evolution. Throughout this work I adopt a ΛCDM cosmology with $H_0 = 70$ km s^{-1} Mpc^{-1}, $\Omega_{m0} = 0.3$ and $\Omega_{\Lambda 0} = 0.7$.

2

Method

Throughout this work, *Chandra* and *XMM-Newton* observations are used to probe the physical properties of gas belts along with the lobes and external medium of their host radio galaxies. This work studies sources selected at low-redshift from the 3CRR sample (Laing et al., 1983), along with Cygnus A, the archetypal powerful FRII radio source. The analysis procedures applied are fairly consistent throughout the work and so, an overview of the methods applied consistently across the datasets are discussed in this chapter. I broadly followed the procedures given in the *XMM-Newton* Extended Source Analysis Software Cookbook (Snowden and Kuntz, 2011) for the *XMM-Newton* data, and the science threads on the *Chandra* X-ray Center's website[1] for the *Chandra* data. Differences to the manner in which the methods are applied to different sources are discussed in the relevant chapters.

2.1 Sources studied

2.1.1 The low-redshift 3CRR sample

There are 173 sources in the complete 3CRR sample of radio sources selected at 178 MHz. I select those with $z < 0.1$ for best spatial resolution and sensitivity. This gives a subsample of

[1] `http://cxc.harvard.edu/ciao/threads/index.html`

Source	z	Galactic Absorption (atoms cm^{-2})	FR Class	Optical Type	178 MHz Luminosity (W Hz^{-1} sr^{-1})
3C 35*	0.0677	1.30×10^{21}	II	LERG	9.93×10^{24}
3C 76.1	0.0325	1.06×10^{21}	I	LERG	2.54×10^{24}
3C 98	0.0304	1.29×10^{21}	II	HERG	8.75×10^{24}
3C 192	0.0597	4.19×10^{20}	II	HERG	1.55×10^{25}
3C 272.1	0.0034	2.78×10^{20}	I	LERG	3.1×10^{22}
3C 285	0.0794	1.27×10^{20}	II	HERG	1.52×10^{25}
3C 296	0.0247	1.86×10^{20}	I	LERG	1.43×10^{24}
3C 305	0.0416	1.70×10^{20}	I	HERG	5.5×10^{24}
3C 310	0.0538	3.63×10^{20}	I	LERG	3.3×10^{25}
3C 386*	0.0177	1.81×10^{21}	I	LERG	1.46×10^{24}
3C 388	0.0917	6.32×10^{20}	II	HERG	4.29×10^{25}
3C 442A	0.027	5.07×10^{20}	I	LERG	2.3×10^{24}
4C 73.08	0.0581	2.33×10^{20}	II	HERG	9.94×10^{24}
NGC 6109	0.0295	1.47×10^{20}	I	LERG	1.86×10^{24}
NGC 7385	0.0262	5.06×10^{20}	I	LERG	1.24×10^{24}

Table 2.1: Sources identified as holding belts in 3CRR at $z < 0.1$. Sources marked with a '*' are better described with *XMM-Newton*. Data taken from the online 3CRR catalogue[2].

36 sources, 35 of which are radio galaxies, with 15 containing X-ray bright gas belts. 3CRR is particularly useful as it is a complete flux limited sample of radio-loud galaxies in the Northern Hemisphere with declination $\delta > 10^{\circ}$ and Galactic latitude with $|b| > 10^{\circ}$. Each of these sources has not only high-quality radio maps, but also one or more *Chandra* X-ray observations. By imposing an upper limit on redshift, I ensure that the ~ 0.5 arcsecond resolution of *Chandra* corresponds to a linear scale of better than 1 kpc. The belted sources within the 3CRR sample studied in this work and their properties are detailed in Table 2.1.

In the majority of cases, I analyse *Chandra* observations of these objects. For 3C 386 however, I instead analyse *XMM-Newton* data, and for 3C 35 I make use of the *XMM-Newton* analysis of Mannering et al. (2013).

2.1.2 Cygnus A

Cygnus A is the best known and nearest example of a powerful FRII radio galaxy. The galaxy which hosts Cygnus A is also the dominant galaxy of a 6 keV cluster with mass within 500 kpc in excess of $\sim 2 \times 10^{14} M_{\odot}$ (Arnaud et al., 1984; Smith et al., 2002). The proximity and power

[2] `http://3crr.extragalactic.info/`

of Cygnus A allows in-depth study of interactions between its expanding radio lobes and the surrounding X-ray gas. Within the projected extent of Cygnus A's cocoon shock, surrounding the radio core, lies a region of enhanced X-ray emission with a complex structure. Its location, between the radio lobes and roughly orthogonal to the radio axis, implies that it may be similar in nature to the gas belts visible in the other, lower power sources in the 3CRR sample. The analysis of Cygnus A makes use of almost 2 Ms of X-ray data, taken as part of a *Chandra* Visionary Project on this fascinating source.

2.2 *XMM-Newton*

XMM-Newton's European Photon Imaging Camera (EPIC) is comprised of three telescopes focussing on to a set of three X-ray charged couple device (CCD) arrays. Wolter nested mirrors focus incoming photons on to the three arrays; MOS1, MOS2 (Metal Oxide Semiconductor) and pn. The MOS arrays consist of 7 front-illuminated CCDs of 600 by 600 pixels, while the pn detector consists of 12 CCDs of 64 by 189 pixels. The physical scale of the pixels is 1.1 arcsec for the MOS detectors and 4.1 arcsec for the pn detector. Schematics of each of these detectors are shown in Figure 2.1. The EPIC cameras can perform sensitive imaging observations over the telescope's 30 arcmin field of view between roughly 0.1 and 10 keV (Figure 2.2), with moderate spectral and angular resolution.

2.2.1 Processing

I make use of *XMM-Newton* to study a gas belt in the 3CRR source 3C 386. Data presented in this work are from the EPIC MOS1, MOS2 and pn cameras in full-frame mode. The Observation Data Format (ODF) files were reprocessed using the tasks EMCHAIN for the MOS detectors and EPCHAIN for the pn detector. Up to and including quadruple events (PATTERN 0–12) for the MOS data and single and double events (PATTERN 0–4) were extracted. I make use of the *XMM-Newton* Extended Source Analysis Software procedure (XMM-ESAS) along with the relevant current calibration files (CCF) which contain filter wheel closed (FWC), quiescent particle background (QPB) and soft proton (SP) calibration data.

[3] `https://xmm-tools.cosmos.esa.int/external/xmm_user_support/documentation/uhb/epic.html`

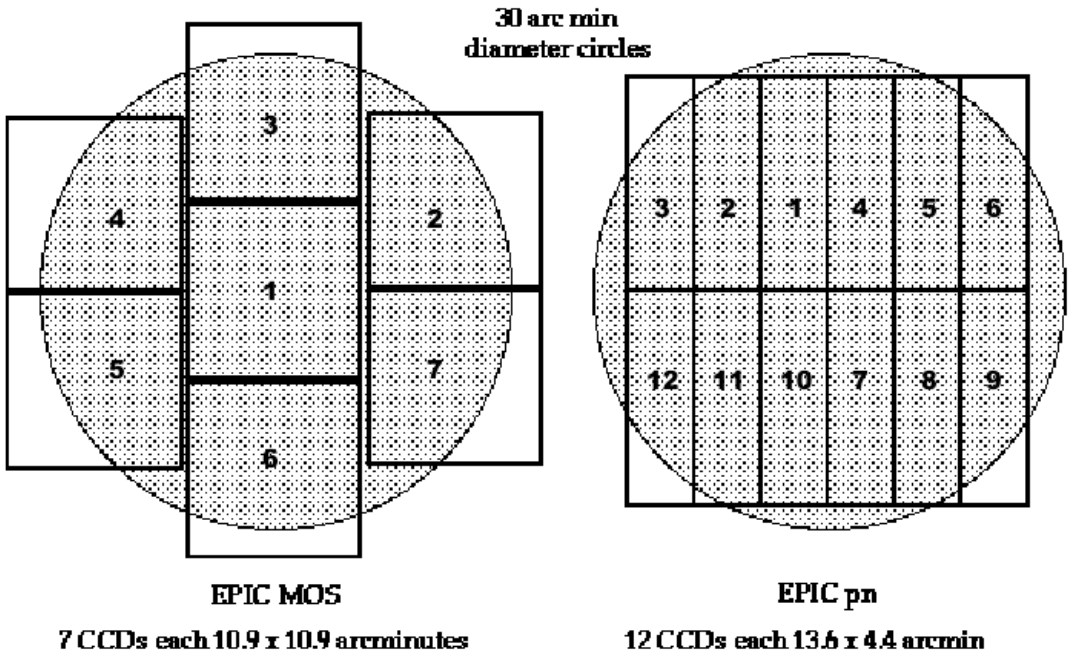

Figure 2.1: A schematic of the EPIC flight focal plane CCD configurations. The layout of MOS1 and MOS2 are shown on the left, with pn on the right. The two MOS cameras are rotated 90 degrees with respect to each other. Reproduced from the *XMM-Newton* User's Handbook[3].

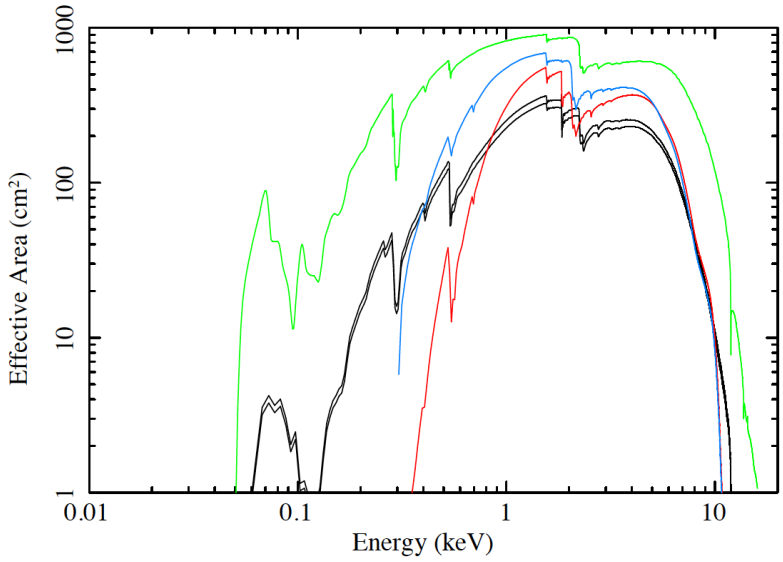

Figure 2.2: Total response efficiency (effective area) against incident photon energy for the *XMM-Newton* and *Chandra* instruments. The black lines correspond to the MOS1 and MOS2 arrays, the green line is the pn detector, the red line corresponds to *Chandra*'s ACIS-I and the blue line corresponds to ACIS-S detectors (Section 2.3).

a) Flare Cleaning

Due to the high variability of solar flares, the SP component of the observation cannot be well removed using background subtraction. Instead, frames which are dominated by high flare count rates must be excluded, reducing the net exposure time. I created a Good Time Intervals (GTI) file using the XMM-ESAS tasks MOS-FILTER and PN-FILTER to generate SP contamination-filtered products for the field of view data. The energy range used in determining the GTI for both the MOS and PN detectors was 2.5-12 keV.

For the MOS1 detector, CCD 3 and CCD 6 were excluded from subsequent processing, as both had previously suffered from micrometeorite damage. In the same strike which damaged CCD 3, CCD 4 sustained collateral damage causing low energy events to dominate towards the high x values in detector coordinates. To avoid entirely excluding CCD 4 from subsequent analysis, I created a histogram of the number of events as a function of the detector's x position (DETX), in order to determine a cutoff for good data. The number of events begins to spike at DETX $\approx$ 9750 and so events registered in pixels with x values above this cutoff are excluded from future analysis (Snowden and Kuntz, 2011).

2.2.2 Spectroscopy

I used the XMM-ESAS task CHEESE, which runs source detection on full-field images and then outputs a mask image of these sources, which is used in excising the sources from images and spectra. The mask was modified to include any additional compact sources apparent by eye which were not detected by the CHEESE task. Following this, the tasks MOS-SPECTRA and PN-SPECTRA were run. These extract spectra from the cleaned event files for a selected region. Finally, the XMM-ESAS processes MOS_BACK and PN_BACK were utilised to create particle background spectra for the relevant regions. The *XMM-Newton* background was sampled away from the source and fitted to models using methods described in Section 2.2.3. Spectra were binned using a minimum of 25 counts per bin, over a range of 0.4-8.5 keV for the MOS detectors and 0.4-7.2 keV for the pn detector.

2.2.3 Modelling the *XMM* background

I reduced the flare-free *XMM-Newton* data using the XMM-ESAS software package. For the primary analysis I chose to model the background, using local background subtraction to check

for consistency. The model background used spectra extracted from a circular off-source region, away from the source and its associated gas belt and group gas. The location of the extraction region differs between detectors in order to avoid chip gaps, but for each it is extracted from an area of blank sky.

The modelled background is preferred to subtracting a local background as it can accommodate variation in background counts across the field of view. Due to this, unless explicitly stated, values quoted in this thesis for 3C 386 will be those measured from fits with modelled background. The local background is simply used as a method of cross checking.

I follow the prescription of Mannering et al. (2013), who in turn followed Snowden and Kuntz (2011), to model the *XMM-Newton* background component. The *XMM-Newton* tasks MOS_BACK and PN_BACK generate model QPB spectra from the FWC observations and unexposed corners of the MOS and pn CCDs, respectively. This quiescent instrumental background is subtracted from data, and then additional components in the *XMM-Newton* background need to be modelled explicitly. Instrumental Al Kα and Si Kα lines were fitted with unabsorbed Gaussians of zero intrinsic widths at line energies of 1.49 keV and 1.75 keV, respectively, for the MOS detectors, whilst only the Al Kα line at 1.49 keV was required for the pn data. The energy range for the pn detector was restricted between 0.4 and 7.2 keV, due to the difficulty in modelling the QPB at high energies for this detector and the large number of instrumental Cu Kα lines present at 7.49 keV and above.

The cosmic X-ray background was modelled by an unabsorbed thermal component representing emission from the heliosphere at $kT \approx 0.1$ keV, a higher temperature ($kT \approx 0.25 - 0.7$ keV) absorbed thermal component representing emission from the hotter halo and intergalactic medium, and an absorbed power law with $\Gamma \approx 1.46$ representing the unresolved background of cosmological sources. I also included a cool, ($kT \approx 0.1$ keV) absorbed thermal component representing emission from the cooler halo, but this was fit with a very small normalisation and was unnecessary (Snowden and Kuntz, 2011). In order to further constrain the cosmic background contribution, a ROSAT All Sky Survey (RASS) spectrum from the HEASARC X-ray Background Tool was also included. The RASS spectral data is available down to 0.1 keV, whilst the lowest energy I have considered for extraction on the *XMM-Newton* instruments is 0.4 keV. The RASS data therefore improves the determination of the X-ray cosmic background at low energies.

Solar Wind Charge Exchange (SWCX) emission, which originates in the heliosphere, contributes a significant fraction of the X-ray background at energies of less than 1 keV. The ions of high charge state in the solar wind interact with neutral atoms, thereby gaining an electron in a highly excited state. This electron decays by emitting X-rays, which produces a background strongly dependent on the solar wind proton flux and heavy ion abundances. I included several SWCX lines in the *XMM-Newton* background model, represented by additional Gaussians at several line energies with zero intrinsic width. These were identified by fitting a model containing the instrumental Gaussian and cosmic X-ray background components, and adding the SWCX at relevant energies to improve the fit.

Data and responses for the three XMM detectors were not combined before spectral fitting. Rather, their data were fitted concurrently to the same models. Between each data set several parameters are held common; these include the energies and widths of each Gaussian used to describe a line, and parameters such as the redshift of the source and the abundances and temperatures of each part of the cosmic X-ray background model.

2.3 *Chandra* X-ray Observatory

Chandra's Advanced CCD Imaging Spectrometer (ACIS) consists of two detector arrays: the I-array, which is composed of 4 CCDs, and the S-array, which is composed of 6 CCDs (see Figure 2.3 for a schematic). Each CCD is 1024 by 1024 pixels, with a pixel size of 0.4920 $\pm$ 0.0001 arcsec. Eight of the ten CCDs are front illuminated, while the remaining two are back-illuminated and more responsive at lower energies. ACIS simultaneously acquires high resolution images and moderate resolution spectra in the energy range roughly between 0.4 and 8.0 keV (see Figure 2.2).

2.3.1 Processing

Except for 3C 386, the 3CRR sources studied in this work (Chapter 4), along with the analysis of the non-axisymmetric gas in Cygnus A uses *Chandra*. Data reduction was performed using the *Chandra* Interactive Analysis of Observations (CIAO) of varying versions dependent on the date of analysis, combined with the then current version of the calibration database (CALDB). Data were reprocessed using the CHANDRA_REPRO script, which automates the recommended

[4] `http://cxc.harvard.edu/proposer/POG/html/chap6.html`

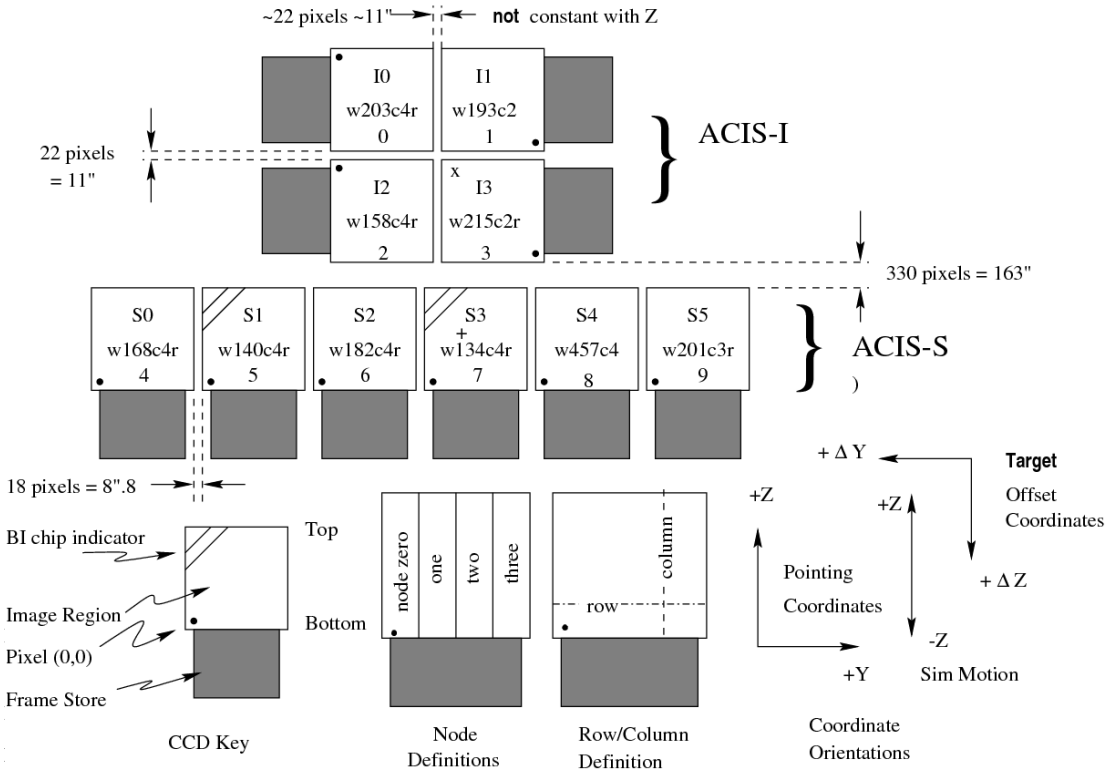

Figure 2.3: A schematic of the ACIS flight focal plane. Figure reproduced from the *Chandra* Proposers' Observatory guide[4].

data processing steps for an observation. CHANDRA_REPRO produces a new bad pixel file by flagging hot pixels (those with an unusually high number of events), afterglow events (resulting from charge deposition from a cosmic ray) and pixels with bad/bright bias (electronic noise in the CCD). The script also produces a level 2 event file by applying the most recent calibrations. When observations were taken in very faint mode (VFAINT) opposed to faint mode, events are graded in the outer ring of a larger pixel island (5×5, opposed to 3×3), in order to better identify large diffuse charged-particle interactions. The event grade is a number which categorises the pattern of pixels whose charge exceeds a certain value. Events of grade 0, 2, 3, 4 or 6 were selected, with other grades rejected as particle events, rather than interactions with X-ray photons. The EDSER sub-pixel algorithm is applied to improve the image quality of sources near the optical axis of the telescope.

After the completion of CHANDRA_REPRO, a background light curve was produced and a DEFLARE was applied using the *lc_clean* algorithm to identify anomalous count rate periods which indicate background flaring. The data are then screened to avoid these times.

2.3.2 Imaging

The CIAO function WAVDETECT was used to identify point sources from a 0.5-7.0 keV exposure corrected image (by correlating the image with mexican hat wavelets). In order to isolate the morphology of the extended emission in the 3CRR sources and consequently identify belt-like emission, all point sources in the field were excluded, excluding the radio cores. CIAO's DMFILTH was used to fill in the gap regions with intensities from the surrounding areas for image display. The image was then divided by the exposure map (over the 0.5-7.0 keV range, using an effective energy of 2.3 keV) in order to correct for the varying effective area across the field of view. The observations were then smoothed using a Gaussian function within ds9. The resulting images are shown in Section 4.4.1.

2.3.3 Spectroscopy

The ACIS X-ray background changes slowly with time and is relatively well understood. It is composed of several components that predominantly affect low X-ray energies: the cosmic X-ray background (dominated by Galactic emission at energies less than 1 keV), cosmic ray events, and strong particle flaring. As the belt emission generally appears far brighter than the surrounding ambient medium, for *Chandra* observations I opted to use a local background,

rather than modelling or using blank sky background. The selection of background regions and associated caveats are described for each source individually in the relevant sections.

X-ray spectra were extracted from each observation using CIAO's SPECEXTRACT, which also generates the associated response files. The response files generated are the Redistribution Matrix File (RMF) and the Ancillary Response File (ARF). The RMF describes the probability that a photon will be detected in a given channel, and the ARF describes the effective area of the telescope as a function of photon energy. A spectral model can then be convolved with the ARF and RMF before being statistically compared to the data.

In several instances sources studied have multiple observations associated with them. This is especially prominent in the analysis of Cygnus A, which makes use of 62 observations. In these cases (unless stated otherwise) COMBINE_SPECTRA was used to sum multiple spectra. This also combines the response files and any associated background files. Spectral fitting was then performed on the combined file.

2.4 On-source Spectral Fitting

On-source emission in this work is usually fit with either a thermal model (Astrophysical Plasma Emission Code (APEC)) or non-thermal (power-law) models, or combinations of the two.

2.4.1 Astrophysical Plasma Emission Code

The APEC model parameterises a hot, collisionally-dominated, optically thin plasma by modelling continuum-emission and line-emission processes.

a) Continuum Emission Processes

The continuum emission processes included are thermal bremsstrahlung, radiative recombination and two-photon emission.

The bremsstrahlung process produces continuum emission when a particle, such as a free electron, is decelerated in the electric field of another charged particle, such as an atomic nucleus. The free electron's loss of kinetic energy results in the emission of a photon to maintain conservation of energy. In a typical hot astrophysical plasma, the bremsstrahlung continuum created by electrons interacting with hydrogen and helium nuclei is often the dominant source of energy loss. This process is described in more detail in Section 1.6.1.

Radiative recombination occurs when an electron collides and recombines with an ion, resulting in the emission of a photon. The energy of the emitted photon will equal the kinetic energy of the newly-recombined electron. This results in the emission of continuum rather than lines, as the values of kinetic energy are not quantised, thus producing a continuous spectrum with defined edges at the binding energies. At low temperatures ($kT \sim 0.1$ keV), the radiative recombination continuum due to the recombination of oxygen ions dominates over the bremsstrahlung contribution.

In two-photon emission, a photon pair are emitted following a single electron transition. This appears as a continuum as the relative energies of the emitted pair of photons is uncertain, but the pair as a whole conserves the transmission energy.

b) Line Emission Processes

The line-emission processes included are one-electron radiative transitions, dielectric recombination satellite lines and inner-shell ionisation.

Emission lines arise from one-electron radiative transitions when an electron drops from an upper to a lower energy state, emitting a photon of a specific frequency.

Dielectric recombination occurs when an electron in a recombines with an ion in an excited state which excites a second electron. This results in a highly excited ion which may autoionise, converting the process into a simple scattering event, or radiatively decay, creating a satellite line, which will be at a slightly longer wavelength than the normal transition from an electron in that energy level.

Inner-shell ionisation results from a photon or electron colliding with and ionising an inner-shell electron. This unstable state is remedied by outer shell electrons falling into the inner shells and emitting photons of specific wavelengths.

2.4.2 Physical Parameters of the Gas Belts

The relative contributions of each of the components described in the previous sections are governed by the temperature, density and metallicity of the plasma. At high densities, spectra are dominated by collisional processes, whereas at low densities, the contribution of collisional de-excitation is minimal and can be ignored, and the radiative processes dominate.

For spectra fit with an APEC model, values for the temperature, kT in keV, the metallicity

in units of $Z_{\odot}$ using the elemental abundances of Anders and Grevesse (1989), and the normalisation are returned. The emission measure, defined in terms of the normalisation as specified within the spectral fitting software XSPEC (Arnaud, 1996), N, is given by

$$10^{14}N = \frac{(1+z)^2 \int n_{\rm e} n_{\rm p} dV}{4\pi D_{\rm L}^2} \tag{2.1}$$

where $D_{\rm L}$ is the luminosity distance in cm, V is the volume in cm^3, and $n_{\rm e}$ and $n_{\rm p}$ are the electron and proton densities in cm^{-3} respectively. With normal cosmic values for element abundances, the proton number density for a region of uniform density is given by

$$n_{\rm p} \approx \sqrt{\frac{10^{14} N 4\pi D_{\rm L}^2}{(1+z)^2 1.18 V}} \tag{2.2}$$

as the electron and proton densities are related by

$$\frac{n_{\rm e}}{n_{\rm p}} = \frac{1+X}{2X} \sim 1.18 \tag{2.3}$$

where X is the mass fraction in hydrogen, which is 0.74 for normal cosmic (assumed solar) abundances. If the proton density is constant over the volume, the pressure can then be found by

$$P = 3.6 \times 10^{-10} n_{\rm p} kT \quad \text{Pa} \tag{2.4}$$

where $n_{\rm p}$ is in units of cm^{-3} and kT is in units of keV (Worrall et al., 2012).

Additionally, I also calculated the entropy index, S, in each region using Equation 2.5 (Ponman et al., 1999). This quantity does not refer directly to thermodynamical entropy. The thermodynamical entropy is proportional to the natural log of this entropy index, plus a constant.

$$S = \frac{kT}{n_{\rm p}^{2/3}} \tag{2.5}$$

The entropy index is of interest in these investigations, as the entropy structure contains information about the thermal history of the gas in groups and clusters, especially with regard to the effect of feedback on the ICM.

2.4.3 Physical Parameters of the Lobes

It is also important to understand the physical properties of the radio lobes, especially the pressure. This can be used to determine whether the lobes have influenced the formation of the gas belt, or vice versa. I use two methods to estimate the pressure within the lobes, the first of which is the minimum energy approximation, discussed in Section 1.4.5. The counts in a radio map can be converted to a radio flux density, S_ν, using the following equation:

$$S_\nu = \text{counts} \times \frac{4\ln(2)}{\pi} \times \frac{\text{CDELT}^2}{\text{BMAJ} \times \text{BMIN}} \tag{2.6}$$

where CDELT is the pixel size in the appropriate axis and BMAJ and BMIN are the major and minor axes of the restoring beam, respectively. The minimum energy magnetic field, $B_{\rm me}$, is then calculated using Equation 1.35, with $\gamma_{\rm min} = 10$ and $\gamma_{\rm max} = 10^5$. The pressure is then a third of the total energy density.

The lobes may not be at minimum energy, so a better estimate of the pressure can be obtained should the lobes produce detectable iC X-ray emission. The spectral extraction regions for the lobes are defined using the radio contours. Should the X-ray emission fit a power law, with the same spectral index α as its radio emission, then the normalisation of the fit at 1 keV can be converted to an X-ray flux density and the iC magnetic field, $B_{\rm iC}$, can be calculated using Equation 1.55.

2.4.4 Physical Parameters of the External Medium

The majority of the physical parameters of the external medium come from β-profiles and APEC fits to some external emission to find the temperature. These are either derived by me or taken from Ineson et al. (2015). Exceptions to this are discussed when relevant. The β-profiles are used to calculate the density of the external medium at the average distance to the base of the lobes from the core. As the gas belts are found between the lobes, this gives an idea of the properties of the external medium at the relevant distance. The same equations applied to the gas belts in Section 2.4.2 are then used to find the pressures and entropies of the ambient medium.

When it is possible to calculate all these values, a complete picture of the dynamics of the radio source and gas belt can be obtained.

3

Buoyancy-driven inflow to a relic cold core: the gas belt in radio galaxy 3C 386

In this chapter, I conduct an in-depth analysis of an *XMM-Newton* observation of 3C 386, which features a bright X-ray gas belt aligned orthogonal to the radio axis, and between the radio lobes. This chapter has been published and is largely reproduced from Duffy et al. (2016).

3.1 Introduction

Radio galaxies fuelled by active galactic nuclei (AGN) inject energy into the surrounding medium and are important sources of heating in galaxy groups and clusters (Scheuer, 1974). Energy transfer via an AGN feedback process is inferred most directly through gas cavities created by jet structures, which are seen frequently at the centres of clusters in the local Universe (McNamara and Nulsen, 2007). Cavities are formed when a radio jet does work on gas, pushing it away from the densest regions of the group or cluster environment. Along with cavities, many galaxies in group environments display prominent belt-like gas structures, which are associated with the central narrowing of radio sources between their radio lobes (Mannering et al., 2013).

Belted sources such as 3C 35, 3C 285 and 3C 442A have previously been studied, with different conclusions as to their origins. For 3C 35, Mannering et al. (2013) interpret the gas belt as fossil-group gas driven outwards by the expanding radio lobes. Hardcastle et al. (2007) refer to the thermal gas which is aligned orthogonal to the radio lobes in 3C 285 as a ridge. They suggest the ridge was present long before radio activity commenced, and only a small fraction of the gas was contributed by merger activity involving 3C 285's host galaxy. In the case of 3C 442A, Worrall et al. (2007) conclude that an active merger is causing the gas of merging galaxies to align orthogonal to, and do work on, the radio lobes.

For the three belted sources studied previously in detail, the gas appears to be either relatively stagnant or to be flowing away from the host galaxy. This could cause a barrier to positive feedback which requires AGN activity and black hole growth to be linked to gas-cooling and star formation, although the mechanisms may assist a negative feedback cycle. Alternatively, it is possible that some belts could result from gas driven inwards towards the AGN. This could potentially cause runaway positive feedback, if gas cooling from the outer atmosphere can reach the pc-scale regions around the central black hole, and provide extra fuel to renew or prolong AGN activity. In this chapter, I add an additional source, 3C 386, to the detailed study of belted sources, using new data from *XMM-Newton*. I present evidence that 3C 386 does indeed exhibit behaviour that is opposite to that seen in the previously studied cases.

3.1.1 3C 386

3C 386 is a low-excitation radio galaxy with an elliptical host which lies around 75 Mpc (z=0.0177) away. It is a 'fat' or 'relaxed double' radio galaxy, and provides an example where the absence of jets and hot spots (Strom et al., 1978) probably indicates little current relativistic particle acceleration (Young et al., 2005). It is a fairly typical relaxed double source, with its lobes containing fine structure including filaments near the edges which may form shells (Leahy and Perley, 1991). It is roughly 210 arcsec$\times$ 290 arcsec in angular size, which corresponds to projected dimensions of 76 kpc $\times$ 105 kpc in the source rest frame. The central region of the host galaxy of 3C 386 appears bright in the optical due to the chance superposition of an F7 type Galactic star (Lynds, 1971; Buttiglione et al., 2009). There are several other optical point sources discernible within a radius of about 30 kpc; some of which may be globular clusters (Madrid et al., 2006).

3C 386's environment is classified as isolated: only two L* galaxies are seen within an

$800h_{75}^{-1}$ kpc radius compared to an expected 0.9 field galaxies (Miller et al., 1999). Mannering (2013) examined 3C 386's environment using *Spitzer* data taken with the Infrared Array Camera (IRAC) and found 13 faint, but plausibly associated galaxies within a 0.5 Mpc radius. Additionally, there are two galaxies with velocities within 500 km s^{-1} of 3C 386's velocity (Miller et al., 2002). A galaxy close in projected distance is two magnitudes fainter than 3C 386's host at 3.6 μm. Mannering (2013) confirms the isolated environmental classification, as potential companions are too small to contribute significant gas and/or too distant to cause major disturbances in 3C 386's gas belt.

Non-detections of 3C 386 in the X-ray were reported for both Einstein and ROSAT (Feigelson and Berg, 1983; Miller et al., 1999), but it was subsequently detected with *Chandra* (Ogle et al., 2010). While Ogle et al. (2010) studied the nucleus, Mannering (2013) investigated several X-ray components associated with 3C 386. Using a 30 ks *Chandra* observation (Obs ID 10232), a rectangular region defining the gas belt indicated a temperature of $kT \approx 1.1$ keV. Ineson et al. (2015) fitted a single component radial profile through the belt and beyond and spectrally fitted all emission in an annulus of radii 2.46 arcsec to 270 arcsec to $kT = 1.05^{+0.18}_{-0.12}$. Mannering (2013) suggests that the gas belt is consistent with a hot gas halo surrounding an isolated field elliptical. They find the belt to be overpressured relative to the surrounding environment by up to an order of magnitude, and notes that its asymmetric morphology suggests an interaction with the radio source in the past. They, however, come to no conclusion regarding the origins of the gas in the belt.

I use a new 92 ks *XMM-Newton* observation to investigate the gas belt in 3C 386.

3.2 XMM-Newton Observation and Data Reduction

3C 386 was observed with *XMM-Newton* for 92 ks on 11-12 September 2013. The data were reprocessed as described in Section 2.2.1, with flare cleaning undertaken as described in section a). Figure 3.1 shows the light curves generated from the observations, with the net exposure times for each detector after the application of GTIs are given in Table 3.1.

Data processing then continued and spectral extractions were performed as described in Section 2.2.2. A Galactic absorption of $N_{\rm H} = 1.81 \times 10^{21}$ cm^{-2} was applied to all spectral components described as 'absorbed'.

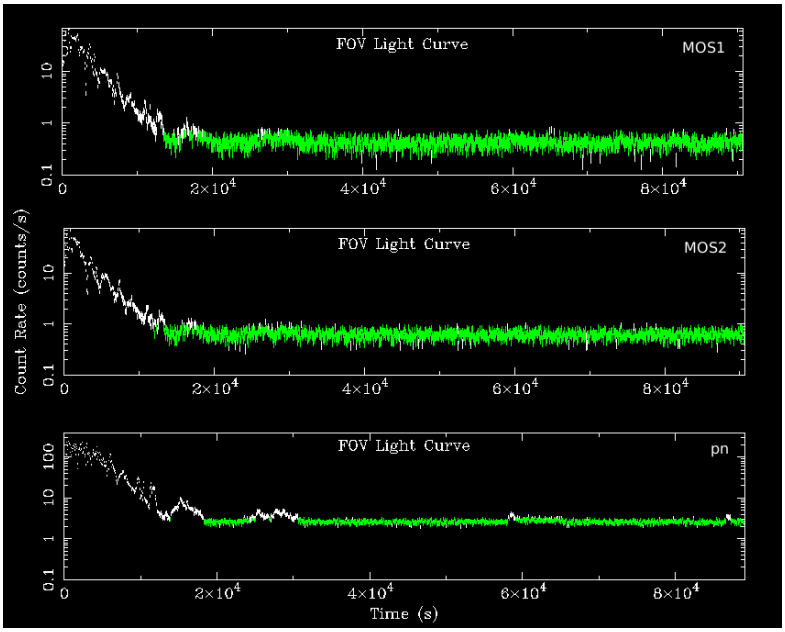

Figure 3.1: Light curves generated from the 3C 386 MOS1, MOS2 and pn observations across the full field of view. The green areas show the acceptable data, whereas the white are frames where flaring dominated and are removed from later processing.

Detector	Duration (ks)	Net exposure (ks)
MOS1	90.7	73.3
MOS2	90.6	73.8
pn	88.1	60.7

Table 3.1: *XMM-Newton* exposure times. The duration refers to the total observation time, whereas the net exposure is the time remaining after the high flare-count-rate frames have been excluded.

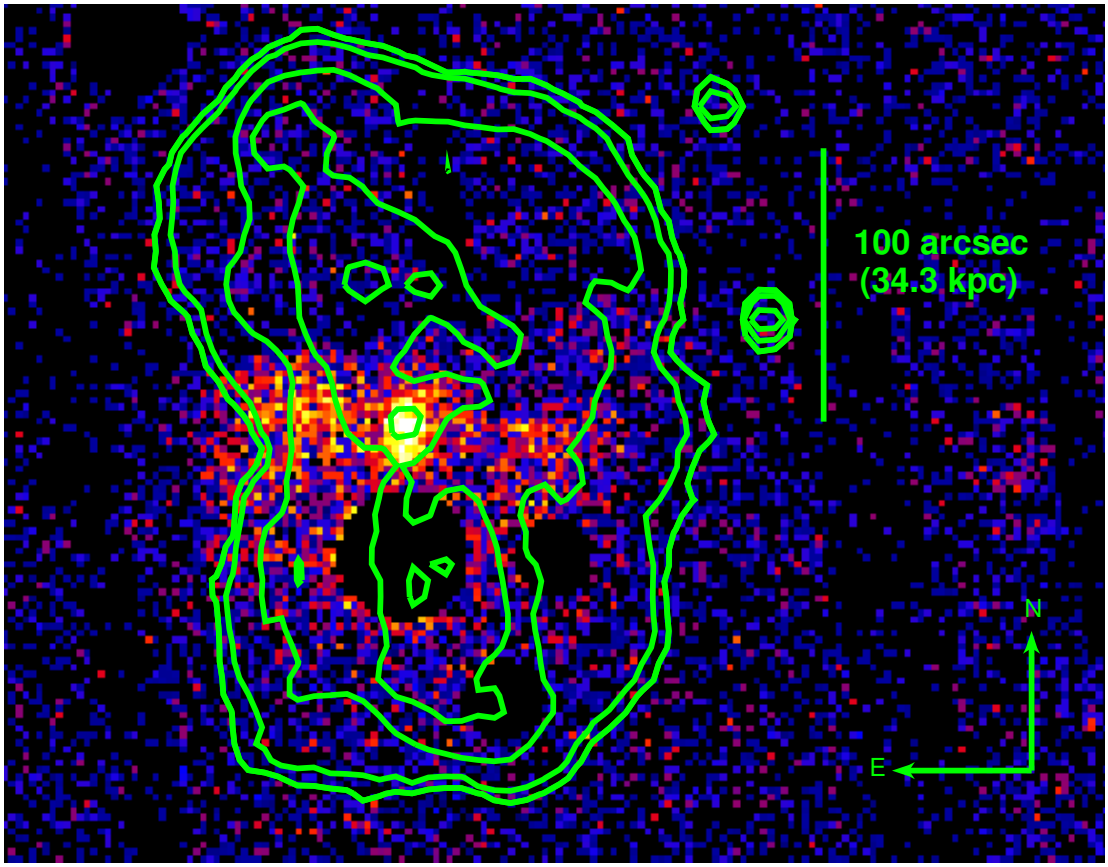

Figure 3.2: Particle background subtracted and exposure corrected MOS and pn combined *XMM-Newton* image between 0.4 and 8.5 keV with 2.5 arcsec pixels. Point sources excluding the AGN nucleus have been excised from the image. Most of the excised sources are uncategorised X-ray sources. Contours are of a 1.4 GHz VLA map 0.2, 1, 5, 10, 15 mJy/beam (5.8 arcsec beam). The radio map is taken from Leahy and Perley (1991).

3.3 X-ray Morphology

Figure 3.2 shows an image of the MOS1, MOS2 and pn data combined using the task COMB, which adds the counts from the three instruments, accounting for differing exposures. The image in Figure 3.2 was background subtracted, to remove the SP and QPB components. Point sources unrelated to the source are excised. Across the centre of the radio source, between the north and south lobes, there is a clear excess of X-ray emission which I describe as the gas belt. The brightening in the centre of this belt corresponds to a superposition of the AGN core and the Galactic F7 star. The slight misalignment between these produces the elliptical shape of the core seen in Figure 3.2. The gas belt extends about 145 arcsec, which corresponds to a projected

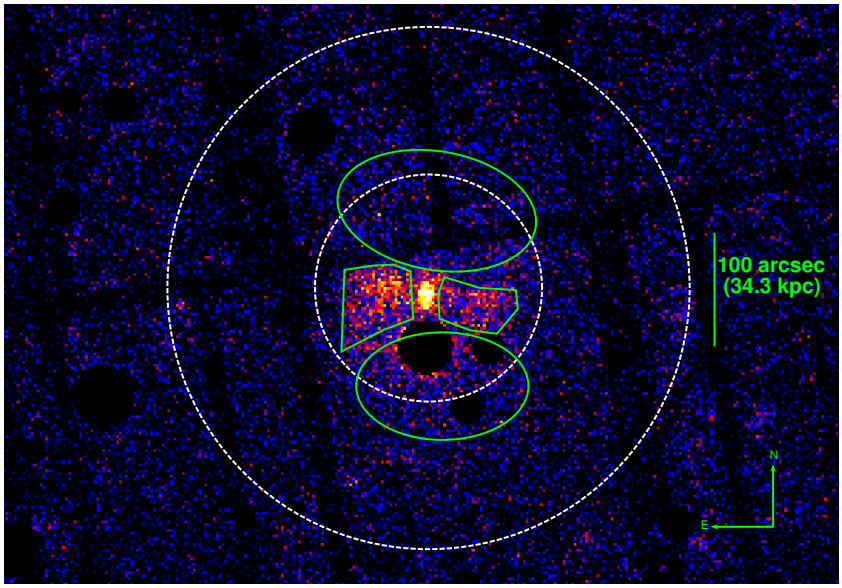

Figure 3.3: Image of 3C 386 with native 2.5 arcsec pixels, with green regions highlighting the extraction region for the gas belt and the north and south lobes and the dashed white region highlighting the extraction region for the extended group emission.

length of 53 kpc in the source rest frame.

A polygonal region for the spectral extraction across the belt was defined by eye (see Figure 3.3). The core was not included in the spectral extraction for the belt.

3.4 Spectroscopy

3.4.1 Background Estimation

The background is modelled as described in Section 2.2.3. The best-fit model for the off-source extraction (Fig. 3.4) has $\chi^2 = 600.4$ for 621 degrees of freedom, with the spectrum shown in Figure 3.4.

3.4.2 Gas Belt

The *XMM-Newton* spectra were extracted from a polygonal region of the gas belt. This region lies orthogonal to the lobes of 3C 386 and is shown in Figure 3.3 superimposed on a combined image from all detectors. Counts from the east and west regions shown in Figure 3.3 were extracted as a single spectrum, in order to model the gas belt as a whole. The spectral data

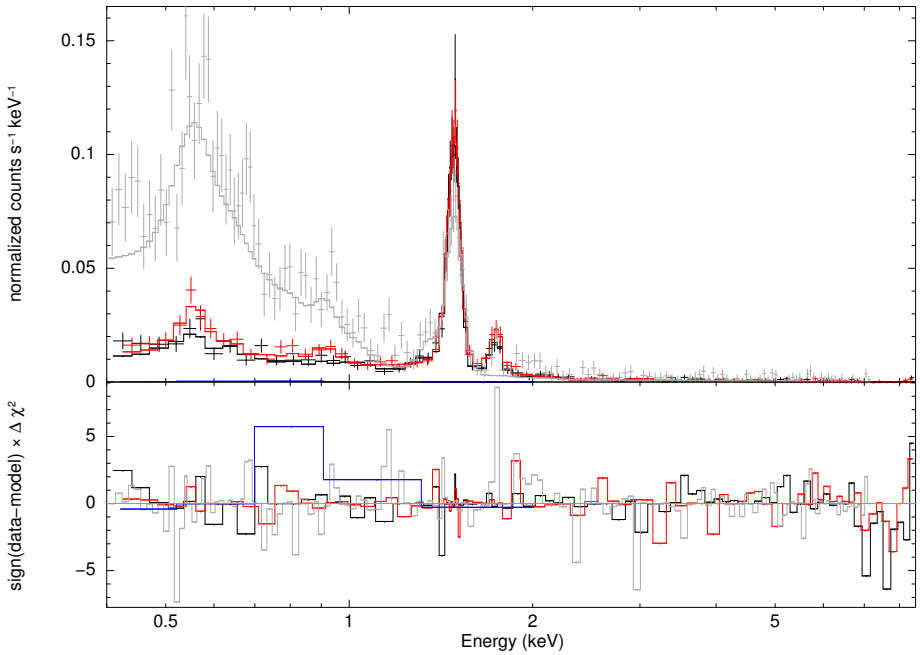

Figure 3.4: *XMM-Newton* spectra extracted from the off-source region, and fit to the background model described in Section 2.2.3. Black, red, and grey correspond to MOS1, MOS2, and pn data, respectively.

	Net count rate (10^{-2} ct s^{-1})			Area (arcmin^2)		
	MOS1	MOS2	pn	MOS1	MOS2	pn
Whole gas belt	0.91±0.04 (88.6%)	0.95±0.04 (89.7%)	3.11±0.08 (87.7%)	1.452	1.443	1.536
Inner belt	0.47 ± 0.03 (91.7%)	0.46 ± 0.03 (92.4%)	1.71 ± 0.06 (89.9%)	0.663	0.619	0.716
Outer belt	0.45 ± 0.03 (87.2%)	0.50 ± 0.03 (88.5%)	1.46 ± 0.06 (85.0%)	0.809	0.838	0.839
North lobe	0.87±0.04 (73.5%)	0.78±0.04 (70.8%)	2.00±0.08 (67.0%)	3.870	3.781	3.273
South lobe	0.82±0.04 (79.9%)	0.69±0.03 (78.5%)	2.14±0.08 (74.0%)	2.558	2.294	2.542
Core	0.23±0.02 (97.2%)	0.25±0.02 (95.7%)	0.93±0.04 (96.0%)	0.113	0.132	0.134
Group gas	3.94±0.10 (59.3%)	3.94±0.10 (58.7%)	8.47±0.21 (51.8%)	32.24	32.92	27.39

Table 3.2: Properties of the regions used in spectral extraction. Net count rates are measured between 0.4-8.5 keV for the MOS1 and MOS2 detectors, and between 0.4-7.2 keV for the pn detector. The net counts refer to the source, instrumental lines, SWCX, SP and CXB emission, minus the QPB background which is removed from the data prior to fitting. The percentages indicate the net source counts over total counts in the region. Area is the net solid angle of the selected region, excluding chip gaps, damaged CCDs and background sources.

counts for each detector are given in Table 3.2. The *XMM-Newton* background is modelled as described in Section 2.2.3. The line energies and widths of the instrumental and SWCX lines determined as in Section 2.2.3 were frozen for the on-source fits, with only the normalisations of the lines allowed to vary.

Details from all fits related to the gas belt are given in Table 3.3. The gas belt *XMM-Newton* data fit a single absorbed Astrophysical Plasma Emission Code (APEC) model (Smith et al., 2001), with a fixed metal abundance of $0.3Z_{\odot}$, of temperature $0.94^{+0.04}_{-0.05}$ keV. APEC predicts spectra for collisionally ionised plasma in the optically thin limit. The data were also fitted with an absorbed power law, giving a reasonable but statistically poorer fit and a photon index of $\Gamma = 2.33 \pm 0.11$. A combination of an absorbed APEC and power-law fit finds a consistent gas temperature of $0.90^{+0.06}_{-0.09}$ keV. In each case, across the entire gas belt, there is good agreement between the parameters obtained from the model background fits and those obtained with a subtracted local background.

a) Gas Belt Temperature Structure

In an effort to establish the mechanism by which the belt was shaped, I further divide the belt region shown in Figure 3.3, into two smaller sub-regions. The sub-regions are shown in Figure 3.5, and are labelled as 'inner' and 'outer' regions corresponding to their position within the belt. Both inner and outer regions were fitted with the same models as the whole gas belt. When fitted to an APEC model, the temperature of the inner gas belt was found to be $0.73^{+0.08}_{-0.11}$ keV whilst the outer belt was found to have a temperature of $1.72^{+0.56}_{-0.36}$ keV.

Assuming the gas belt is a disk viewed side on, there would be some outer belt material in the line of sight in front and behind the inner region of the belt. To compensate for this and gain a more realistic measurement of the temperature of the inner belt, I fitted an APEC + APEC model to the inner belt spectra. The first APEC has a temperature fixed to the best-fit value measured from the outer belt fit, and its normalisation is set to accommodate the outer gas assuming a disk geometry. The second APEC, corresponding to only the inner material is then fitted to a temperature of $0.62^{+0.12}_{-0.10}$ keV, somewhat lower than before. Once I established the temperatures of the two gas components, I performed a second APEC + APEC fit, this time to the entire gas belt. In this fit the temperatures were fixed at the inner and outer component values. This allowed better understanding of the spatial extent of each temperature component, as discussed further in Section b).

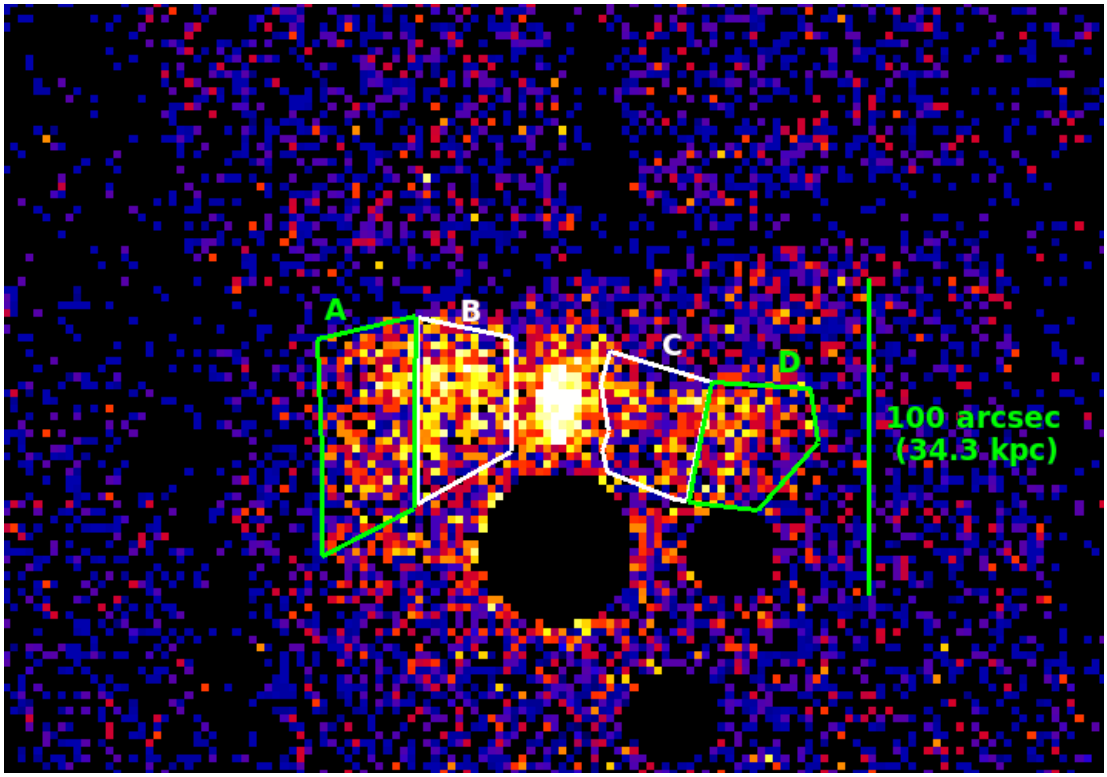

Figure 3.5: Image of 3C 386 with native 2.5 arcsec pixels, highlighting the extraction regions for the inner (B & C) and outer (A & D) regions of the gas belt.

Each subdivision of the belt can alternatively be fitted to an absorbed power law, with $\Gamma = 2.70^{+0.37}_{-0.28}$ for the inner gas belt, and $\Gamma = 2.10^{+0.17}_{-0.16}$ for the outer gas belt. A combination of an absorbed APEC and a power law finds the temperature of the inner gas belt $0.67^{+0.10}_{-0.09}$ keV and the outer gas belt $1.56^{+0.41}_{-0.18}$ keV, and the power law 1 keV normalisations are an order of magnitude smaller than those of the thermal components. Each fit described above has a fixed metal abundance with respect to solar of $Z_{\odot} = 0.3$. Further details can be found in Table 3.3.

I also performed a second APEC fit on the inner and outer gas belts, this time allowing the metal abundances in each region to vary along with the other parameters. I find no significant change in temperature, with metal abundance of $Z_{\odot} = 0.12^{+0.12}_{-0.05}$ and $Z_{\odot} = 0.68 \pm 0.49$ in the inner and outer regions respectively.

For the discussion, I assume that the gas belt is entirely of thermal origin, since any power law contribution is small.

The volume of the gas belt was estimated as 49×10^3 kpc^3, by assuming it is part of a disk of radius 83 arcsec ($\sim$ 30 kpc) and thickness 50 arcsec ($\sim$ 18 kpc). The radius and thickness of the disk were estimated assuming that the disk is seen edge-on.

b) Physical properties of the gas belt

The gas belt of 3C 386 is well described by a thermal model. Using the fitted parameter values along with the estimated volume I calculate the density, pressure, entropy index and total mass of the gas belt following the methods described in Section 2.4.2. A summary of results for the gas belt are given in Table 3.4. The densities and pressures in the gas belt correspond to the average density and average pressure over the region of the spectral extraction.

The masses calculated in Table 3.4 for the inner and outer belt were found using the APEC + APEC fit for the inner region and the APEC fit for the outer region. The distinction between the inner and outer belt was made at approximately the mid-point in the belt on either side of the core. I tested that this distribution of gas is roughly correct, by fitting an APEC + APEC to the entire belt with each APEC fixed at the inner and outer temperature. When doing this, I find a mass for the inner belt of $\log(M/M_{\odot}) = 8.8 \pm 0.1$ and a mass for the outer belt of $\log(M/M_{\odot}) = 9.1 \pm 0.1$. These masses are similar to those in Table 3.4, supporting the choice of the relative spatial extents of the inner and outer belt regions.

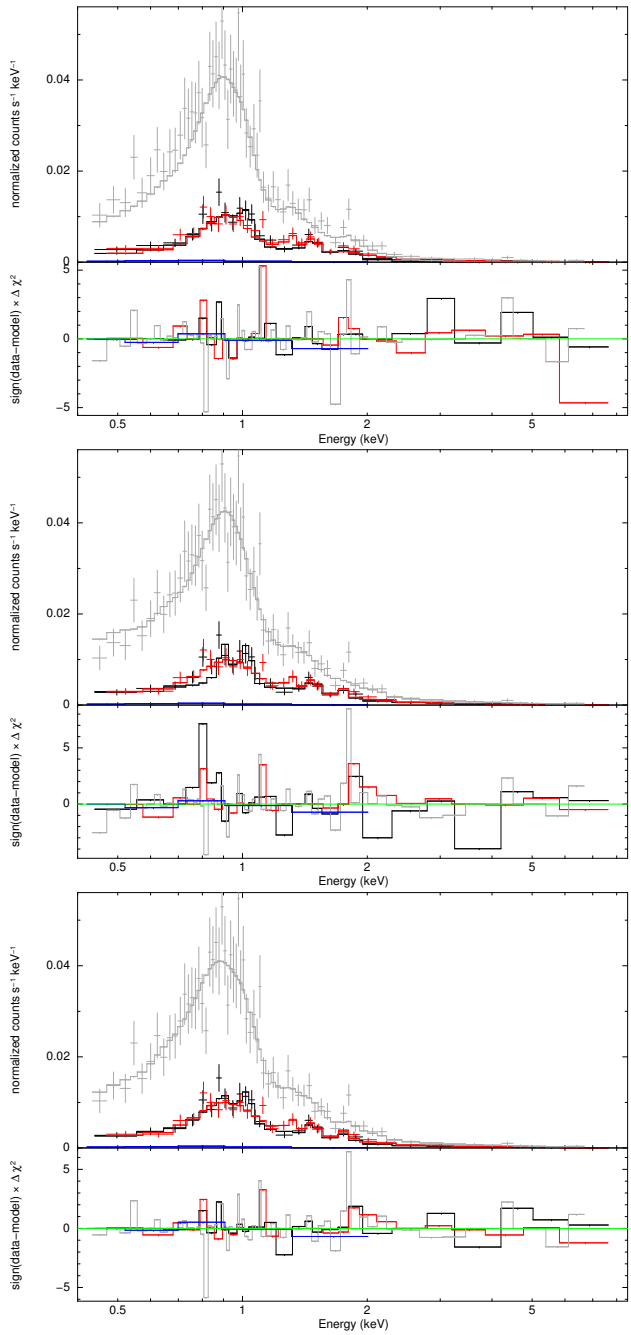

Figure 3.6: *XMM-Newton* spectra extracted from the whole gas belt, fitted to the background model plus an APEC component in the top panel, an absorbed power law in the middle panel and an APEC + power-law model in the bottom panel. The lower panel in each fit show the χ^2 residuals. In each panel, black, red, and grey correspond to MOS1, MOS2, and pn data, respectively.

Model parameter	Whole gas belt	Inner belt	Outer belt
APEC			
kT (keV)	$0.94^{+0.04}_{-0.05}$	$0.73^{+0.08}_{-0.11}$	$1.72^{+0.56}_{-0.36}$
$10^{14}N$ (10^9 cm^{-5})	$3.83^{+0.63}_{-0.62}$	$1.78^{+0.43}_{-0.42}$	2.22 ± 0.70
χ^2/dof	95.0/98	75.6/82	70.4/80
APEC + APEC			
kT_1 (keV)	1.72 (fixed)	1.72 (fixed)	-
$10^{14}N_1$ (10^9 cm^{-5})	3.92 ± 0.56	1.04 (fixed)	-
kT_2 (keV)	0.62 (fixed)	$0.62^{+0.12}_{-0.10}$	-
$10^{14}N_2$ (10^9 cm^{-5})	1.83 ± 0.32	$1.01^{+0.47}_{-0.46}$	-
χ^2/dof	95.8/101	75.2/78	-
power law			
Γ	2.33±0.11	$2.70^{+0.37}_{-0.28}$	$2.10^{+0.17}_{-0.16}$
$S_{1\ \mathrm{keV}}$ (nJy)	$10.49^{+1.57}_{-1.55}$	$5.01^{+1.37}_{-1.34}$	$4.20^{+1.20}_{-1.14}$
χ^2/dof	112.6/106	93.0/90	85.5/88
APEC + power law			
kT (keV)	$0.90^{+0.06}_{-0.10}$	$0.67^{+0.10}_{-0.09}$	$1.56^{+0.41}_{-0.18}$
$10^{14}N_{\mathrm{apec}}$ (10^9 cm^{-5})	$3.47^{+0.64}_{-0.39}$	$1.78^{+0.33}_{-0.34}$	$2.40^{+0.70}_{-0.88}$
Γ	$1.34^{+0.32}_{-0.39}$	$1.24^{+0.63}_{-0.20}$	$1.07^{+1.06}_{-0.43}$
$N_{\mathrm{power\ law}}$ (10^{-5}cm^{-2}s^{-1}keV^{-1})	$0.38^{+0.32}_{-0.30}$	$0.22^{+0.13}_{-0.11}$	$0.04^{+0.26}_{-0.04}$
χ^2/dof	84.5/95	94.5/79	75.0/77

Table 3.3: Best fit parameters of the emission from across the whole gas belt, the inner gas belt and the outer gas belt of 3C 386. Models fit are an absorbed APEC, power law and APEC plus power law. Metal abundances in the APEC, APEC + APEC and APEC + power law fits are fixed at $Z_\odot = 0.3$. Errors are quoted for a 90% confidence range.

Parameter	Gas belt	Inner belt	Outer belt
kT (keV)	$0.94^{+0.04}_{-0.05}$	$0.62^{+0.12}_{-0.10}$	$1.72^{+0.56}_{-0.36}$
Volume (kpc^3)	49×10^3	13×10^3	36×10^3
n_{p} (m^{-3})	1250 ± 200	1200 ± 100	1300 ± 100
P (10^{-13} Pa)	4.1 ± 0.2	$2.8^{+0.8}_{-0.9}$	$8.2^{+2.8}_{-1.8}$
$\log(M/M_\odot)$	9.2 ± 0.1	8.6 ± 0.1	9.0 ± 0.1
$\bar{r}$ (kpc)	15	10	21

Table 3.4: Temperature, density, and mass of the X-ray emission for the belt estimated from the *XMM-Newton* observations. $\bar{r}$ corresponds to the average distance from the core for regions of the gas belt.

Model parameter	North lobe	South lobe
$N_{\rm H}$ (10^{21} cm^{-2})	1.81 (fixed)	1.81 (fixed)
Γ	$2.02^{+0.23}_{-0.21}$	$1.57^{+0.12}_{-0.11}$
$S_{1\ \rm keV}$ (nJy)	$7.05^{+1.40}_{-1.39}$	$6.28^{+0.76}_{-0.82}$
χ^2/dof	227.5/268	295.0/310
1.4 GHz Radio flux density (Jy)	2.97 ± 0.31	1.39 ± 0.21

Table 3.5: Summary of the power law model fitting to the north and south lobes of 3C 386, along with measured radio flux densities. The Galactic neutral hydrogen column density is frozen for all fits. Errors are quoted for a 90% confidence range.

3.4.3 Lobes

The *XMM-Newton* spectra for the radio lobes were extracted from two elliptical regions north and south of the gas belt. Contaminating sources (holes seen in Figure 3.3) are excluded. Also in Figure 3.3, there is some excess flux visible from the wings of the PSF of an excluded bright GALEX source. These remaining counts contribute a small fraction of the total counts in the southern lobe, and have no significant impact on the spectral fits. The net count rates for each detector for each lobe are given in Table 3.2. The lobes were fitted separately. I performed a combined fit of the MOS and pn spectra. The source emission in both lobes is best fitted by a power law with fixed Galactic absorption. These fits find a photon index of $\Gamma = 2.02^{+0.23}_{-0.21}$ ($\alpha_X = 1.02^{+0.23}_{-0.21}$) for the northern lobe and $\Gamma = 1.57^{+0.12}_{-0.11}$ ($\alpha_X = 0.57^{+0.12}_{-0.11}$) for the southern lobe. See Table 3.5 for details. The difference in the spectral indices of these lobes is probably caused by different amounts of foreground and background gas along the line of sight. When both lobes are fit together I find $\alpha_X = 0.73^{+0.11}_{-0.07}$. Using measurements of flux density from the lobes of 3C 386 between 178 and 5000 MHz collected from the NASA/IPAC Extragalactic Database (NED), I find a spectral index $\alpha_{\rm r} = 0.72 \pm 0.16$. The X-ray and radio indices agree within measurement errors.

The lobes were also fitted to APEC models. With a fixed abundance of $0.3 Z_\odot$, the temperatures are found to be 3.3 $\pm$ 0.8 keV for the northern lobe and 6.2 $\pm$ 1.3 keV for the southern lobe. These temperatures are unrealistically high for 3C 386, as they are more consistent with those expected in a cluster environment. No evidence from either the X-ray surface brightness or the galaxy's environment suggests that 3C 386 resides in a cluster. I therefore conclude that the emission in the lobes is non-thermal, even though the χ^2 values for the thermal fits are acceptable.

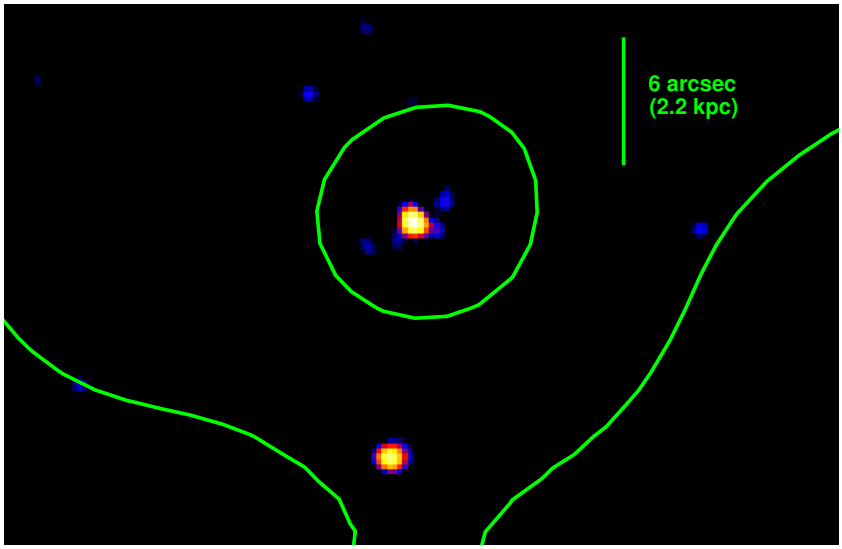

Figure 3.7: 0.5-7.0 keV *Chandra* image of the core of 3C 386 with 0.246 arcsec pixels, smoothed with a Gaussian of standard deviation 0.37 arcsec. Contours are of a 1.4 GHz VLA map 10, 15 mJy/beam (5.8 arcsec beam). The northern X-ray component within the radio map's centre corresponds to the radio nucleus, while the component to the south corresponds to stellar emission. These two components are confused in the *XMM-Newton* images.

Approximating oblate ellipsoids for the northern and southern lobes, I estimate the volumes corresponding to X-ray emission to be 81×10^3 kpc^3 and 42×10^3 kpc^3, respectively. The volume for the southern lobe has been corrected down to account for the excised regions. The 1.4 GHz VLA radio flux density was measured to be 2.97 ± 0.31 Jy for the northern lobe and 1.39 ± 0.21 Jy for the southern lobe over the same areas used for the X-ray spectral extraction.

3.4.4 The Core

The core is a superposition of the radio nucleus and an F7-type Galactic star. These two components can be seen in the *Chandra* observation of 3C 386 (see Figure 3.7), with a northern component corresponding to the radio nucleus, and a separate southern component corresponding to emission from the star. Despite this, the spectrum of the core was extracted from a circular region with radius 12.5 arcsec. The spectral data from the core were fitted to an absorbed power law with fixed Galactic absorption of $N_{\rm H} = 1.81 \times 10^{21}$ cm^{-2}. The best-fit photon index was found to be $\Gamma = 2.11^{+0.26}_{-0.25}$ and the best-fit 1 keV flux density corresponds to $S_{1\ \rm keV} = 3.01^{+0.82}_{-0.85}$ nJy, with $\chi^2/{\rm dof} = 126.1/133$. The spectral fit shows some indication of structured residuals

Model parameter	Group gas
kT (keV)	1.4 (fixed)
$10^{14}N$ (10^9 cm^{-5})	$5.68^{+1.68}_{-1.89}$
χ^2/dof	713.0/707

Table 3.6: Summary of the APEC fitting to the group gas surrounding 3C 386. The Galactic neutral hydrogen column density is frozen for all fits. Metallicity is fixed to $0.3Z_{\odot}$. Errors are quoted for a 90% confidence range.

between 0.6 and 0.9 keV. There is no evidence of excess absorption and results are consistent with the cores of other FRI radio galaxies (Evans et al., 2006). The 2-10 keV X-ray luminosity of the core is 6.54×10^{39} ergs s^{-1}, which is roughly consistent with the value obtained by Ogle et al. (2010). The derived X-ray luminosity is an upper limit because of contaminating emission from the star.

3.4.5 Extended Group Gas

Group-scale gas is evident in the *XMM-Newton* data, although was not necessarily expected given what is known of the galaxy environment (Section 3.1.1). The spectrum of this component was first extracted from an annulus surrounding the galaxy, extending between 100 arcsec to 230 arcsec from the core, and so beyond the belt and mostly beyond the radio lobes. To check the consistency of the results I also extracted a spectrum from a small rectangular region of less than 6% of the whole area (2.1 square arcmin, 2 arcmin to the southwest of the core) which had good coverage on all three EPIC detectors. The results of the fit from the smaller rectangular region are used as a method of testing the reliability of the fit from the larger annulus, as there is often difficulty in consistently modelling the *XMM-Newton* background over large detector areas. The background in both of the extracted regions was modelled as described in Section 2.2.3. The data were fitted to an APEC model. For the annulus extraction, the temperature of the group is poorly constrained, with the best-fit temperature too high for the X-ray luminosity and inferred richness of the group. I therefore fixed the temperature at 1.4 keV, which is roughly the 1σ lower bound. How this model fits the data for the group gas is shown in Figure 3.8, with parameter values given in Table 3.6. The rectangular region produces a temperature of $1.72^{+4.59}_{-0.94}$ keV, which is consistent with the temperature choice for the entire annulus. Although the errors on the measured temperatures are large, the *XMM-Newton* data support the existence of a component of extended emission of group scale and temperature.

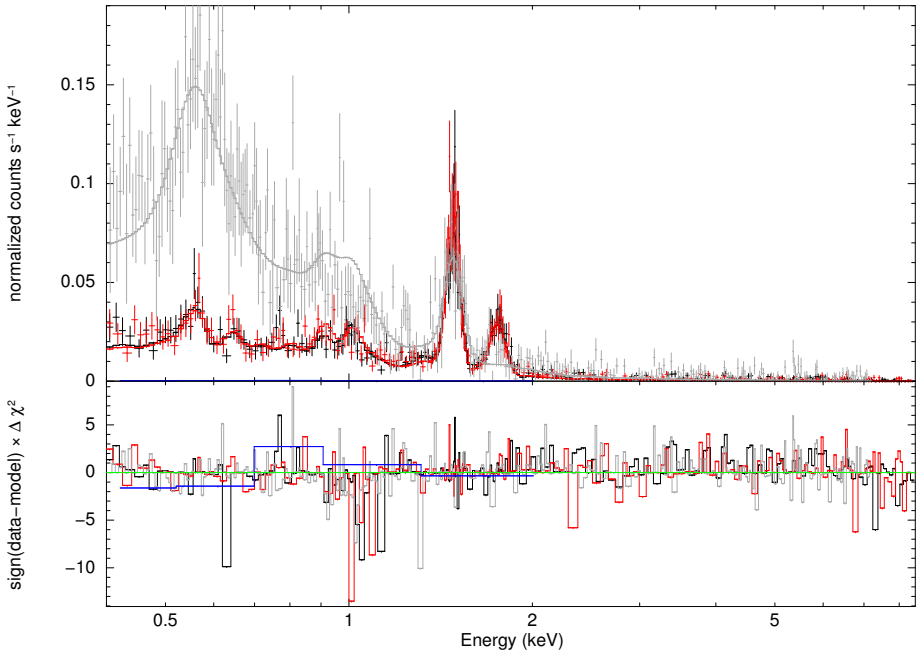

Figure 3.8: *XMM-Newton* spectra extracted from an annulus of group gas lying between 100 arcsec and 230 arcsec from the core of 3C386, fitted with an APEC + background model. The lower panel shows the χ^2 residuals. Black, red, and grey correspond to MOS1, MOS2, and pn data, respectively.

To investigate the radial profile of the group emission, counts were extracted from the pn detector from annuli of width 25 arcsec. I found a profile that decreased with increasing radius out to about 3.8 arcmin, at which point it flattened. This was taken to indicate the point at which the group emission falls significantly below the background. I used this information to subtract a background from each of the inner bins. The lobes and any additional point sources inside the annuli were masked so that only counts from group emission were counted. The resulting background-subtracted vignetting-corrected radial profile of X-ray gas surrounding 3C 386 is shown in Figure 3.9. Vignetting refers to the reduction of the *XMM-Newton*'s effective area with radial distance from its axis. This is a well defined function for off-axis angles of up to more than 10 arcmin, and is a standard correction applied when making radial profiles.

The radial profile can be a fitted with a β-model. I used χ^2 fitting to establish the best fit to the model, with β limited between 0.4 and 1.2 and find a best fit with $\beta = 1.2^{+\mathrm{unknown}}_{-0.8}$, core radius, $r_{\mathrm{cx}} = 91^{+56}_{-82}$ kpc and central counts, $B_o = 140^{+460}_{-65}$. The best fit $\chi^2_{\mathrm{min}} = 0.8$, with errors on each interesting parameter calculated to 90% confidence within $\chi^2_{\mathrm{min}} + 2.7$ allowing the other parameters to vary. If I fix $\beta = 0.5$, which is a value typical of groups of galaxies, the fitted core radius is $r_{\mathrm{cx}} = 30$ kpc. This is similar to the length of the gas belt, and so while group gas is detected out to 80 kpc, the gas belt lies within its core radius. Using equation 10 from Birkinshaw and Worrall (1993), the central proton density in cm^{-3} from this model profile can be calculated.

$$\eta_{po} = \frac{2.45(1+z)^3}{a^{\frac{3}{2}}} \sqrt{\frac{B_o f \Gamma(3\beta)}{t\theta_{\mathrm{cx}} D_{\mathrm{L}} \Gamma(3\beta - 0.5)}} \tag{3.1}$$

where B_o is the central brightness in count arcmin^{-2}, a is the number of radians per arcmin, f is a calibration quantity equivalent to 1 ct/s in cm^{-5} for a fitted XSPEC normalisation, t is the exposure time, θ_{cx} is the core radius in arcmin and D_{L} is the luminosity distance in cm.

Using this central proton density, the gas mass contained within multiples of the core radius can be calculated using the following equation:

$$M(r \leq kr_{\mathrm{cx}}) = \frac{4k^3 \pi m_{\mathrm{H}} \eta_{\mathrm{po}} r^3_{\mathrm{cx}}}{X} \int_0^1 dx\, x^2 (1 + k^2 x^2)^{-\frac{3\beta}{2}} \tag{3.2}$$

where $x = r/kr_{\mathrm{cx}}$ is used as a substitution, k is a multiple of the core radius, m_{H} is the mass of a hydrogen atom and X is the cosmic abundance of hydrogen by mass. Using this integral I find the gas mass contained within r_{cx} is $3.0^{+4.5}_{-2.9} \times 10^{10} M_{\odot}$ and the gas mass contained within $2r_{\mathrm{cx}}$

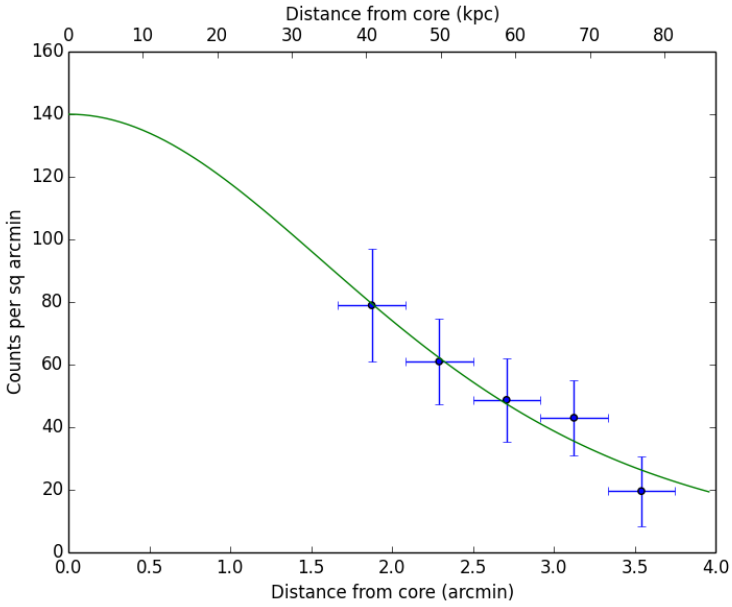

Figure 3.9: Vignetting-corrected, background subtracted radial profile of extended emission from the pn detector from 35 to 80 kpc from the core of 3C 386. Data have been filtered between 0.4-7.2 keV. The lobes and any additional point sources were masked in each annulus. The green line indicates a β-model where $\beta = 1.2$ and $r_{\rm cx} = 91$ kpc.

is $8.1^{+12.0}_{-8.0} \times 10^{11} M_{\odot}$.

3.5 Discussion

Assuming that the belt is of constant density, I estimate the mass of gas it contains as $\log(M/M_{\odot}) = 9.2 \pm 0.1$. When calculating the belt mass, I have continued to exclude the core from the volume. Were the core included, there would be an additional 4% of mass, which is less than the error quoted. This mass is similar to the average gas mass contained within 50 kpc of early-type galaxies (Anderson et al., 2013), despite being contained within a radius roughly half that distance. Furthermore, K-band measurements from 2MASS give $L_{\rm K} = 1.6 \times 10^{10} L_{\odot}$ for 3C 386. This is below the average range for early-type galaxies in Table 4 of Anderson et al. (2013), and so I would expect even less gas mass in 3C 386, around $2 \times 10^{8} M_{\odot}$ (based on Su et al. 2015). The results suggest that 3C 386's gas mass has been enhanced, presumably by gas originating in the group.

In Table 3.7 I estimate some physical parameters extrapolated from the observed group gas at

r (kpc)	$n_{\rm p}$ (m^{-3})	P (10^{-13} Pa)	$M(<r)\,(M_\odot)$	S (keV cm^2)	$S_{\rm belt}$ (keV cm^2)
0	610^{+2000}_{-260}	$3.1^{+13}_{-1.3}$	-	190^{+600}_{-50}	-
10	600^{+2000}_{-250}	$3.0^{+13}_{-1.3}$	$1.5^{+2.3}_{-1.4} \times 10^8$	200^{+600}_{-50}	50^{+10}_{-15}
21	560^{+1800}_{-240}	$2.8^{+12}_{-1.2}$	$1.4^{+2.1}_{-1.3} \times 10^9$	200^{+600}_{-40}	130^{+40}_{-30}
60	320^{+1100}_{-140}	$1.6^{+6.9}_{-0.7}$	$2.3^{+3.5}_{-2.2} \times 10^{10}$	300^{+1000}_{-70}	-

Table 3.7: Density, pressure and entropy index (estimated using $kT/n_{\rm p}^{2/3}$) of the group gas extrapolated to radii appropriate for the inner belt (10 kpc) and outer belt (21 kpc). The inner and outer gas belt entropy index are also given.

roughly the distances of the inner and outer belt. These values are derived from an extrapolation to small radii using parameters from the radial profile discussed in Section 3.4.5.

Using density and temperature I can estimate cooling timescales, $\tau_{\rm cool}$. Based on the cooling curves calculated by Worrall and Birkinshaw (2006, their Figure 5), I estimate $\tau_{\rm cool} \sim 5$ Gyr for the gas belt in 3C 386.

3.5.1 Physical parameters of the lobes

The spectra of the X-ray lobes are well described by an absorbed power law (Table 3.5). As described in Section 3.4.3 the agreement between the X-ray and radio spectral indices is consistent with the interpretation of the X-ray power-law component originating from inverse-Compton (IC) emission from a population of electrons which are also producing synchrotron radio emission.

Using the volumes estimated in Section 3.4.3 and referring to Worrall and Birkinshaw (2006), I find a minimum energy magnetic field $B_{\rm me} = 0.67$ nT for the northern lobe, and $B_{\rm me} = 0.65$ nT for the southern lobe. These were estimated assuming a filling factor of unity, no relativistic protons and no relativistic bulk motions. Minimum-energy pressure, $P_{\rm me}$, is also given in Table 3.8.

I also calculate the magnetic field and pressures in the lobes assuming all X-ray emission from the region is produced by the IC mechanism. Using this method I find lower magnetic fields in the lobes, with $B_{\rm iC} = 0.27$ nT in the north lobe and $B_{\rm iC} = 0.18$ nT in the south lobe. The pressures, P, in the lobes are found to be 3 and 5 times larger than those implied by the minimum-energy assumption. A discrepancy of a factor ~ 3 between $B_{\rm me}$ and $B_{\rm iC}$ for IC-emitting radio lobes is common (Croston et al., 2005).

Parameter	North lobe	South lobe
$B_{\rm me}$ (10^{-10} T)	6.7	6.5
$P_{\rm me}$ (10^{-13} Pa)	1.3	1.2
$B_{\rm iC}$ (10^{-10} T)	2.7	1.8
P (10^{-13} Pa)	3.5	5.9
$u_{\rm B}$ (10^{-13} J m^{-3})	0.3	0.1
$u_{\rm p}$ (10^{-13} J m^{-3})	10.3	17.6

Table 3.8: Physical parameters calculated based on the X-ray emission from the lobes of 3C 386. $u_{\rm B}$ and $u_{\rm p}$ correspond to the energy density in the magnetic field and the energy density in particles respectively.

3.5.2 Model

I have argued that there is too much gas in the belt for it to have originated entirely in the host galaxy. I suggest instead that it is being formed by a buoyancy-driven inflow from the gas atmosphere of the group on to a surviving cold core remnant of the pre-AGN atmosphere.

When the AGN of 3C 386 was at the height of its activity, it would have been feeding the radio lobes with jets, causing the lobes to expand into the intragroup gas. The AGN now appears to be driving no significant jets into the lobes, although it continues to show a low level of activity. The lobes are now rising buoyantly through the group medium away from the host galaxy, at a fraction of the sound speed in the group gas ($c_{\rm s}$ $\sim$600 km s^{-1}). As the lobes rise, gas from the group atmosphere must flow back between the lobes, and I interpret the outer gas belt as the re-accumulated group atmosphere that has been developed by this flow. This is illustrated in Figure 3.10.

The temperature structure of the belt supports this interpretation. The outer belt is hotter than the inner belt, with a temperature of about 1.7 keV, similar to that of the group gas. In the inner part of the belt the gas is cooler, at about 0.6 keV. The cooling time in the belt gas is far longer than the flow time from the edge to the centre of the belt (5 Gyr, compared to $\sim$50 Myr), so it is not cooling that causes the central temperature to be lower. It is possible that the inner belt gas is representative of the initial state of the group gas. Its low entropy index implies it is old, unheated group gas with a small ($\leq$10%) component of host galaxy gas. This is also supported by the morphology of the X-ray emission in the outer belt region. The density structure argues against the belt having arisen from the lobes acting on a pre-existing gas structure, as if this were the case, the inner belt would be denser than the outer.

Figure 3.3 seems to show that the gas belt has a sharp edge, which might not be expected

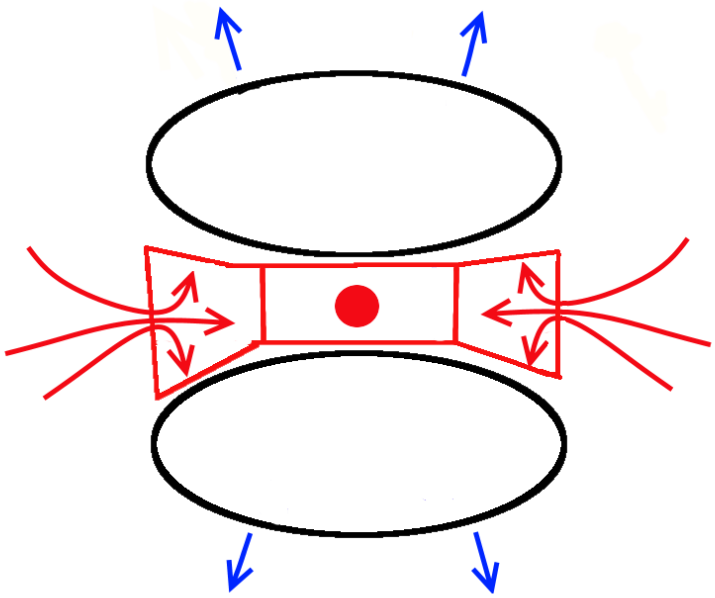

Figure 3.10: Once the radio source has become passive, the buoyant lobes rise through the ambient medium. Their motion through the group gas causes a 'buoyancy-driven inflow' of gas, which forms the outer gas belt. This inflow is directed towards the relic cool core of 3C 386.

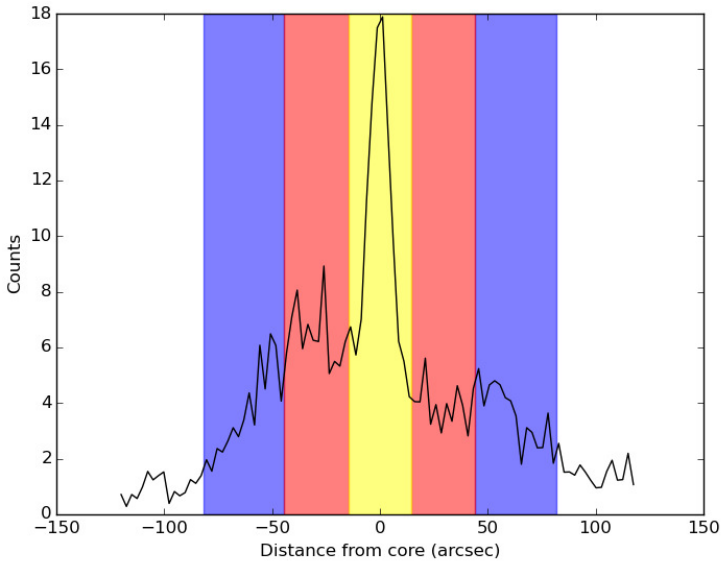

Figure 3.11: Background subtracted, exposure corrected counts as a function of distance from the core across a 20 arcsec slice of the gas belt and its surrounding group medium. Colored region indicates the extent of the gas belt region shown in Figure 3.3, where blue corresponds to the outer belt, red corresponds to the inner belt and yellow corresponds to the core.

from a buoyancy-driven inflow. However, a plot of the counts as a function of distance across the belt (Figure 3.11) reveals a more gradual change in the number of counts with distance from the core.

There are some remaining issues with this interpretation of the gas belt. First, the mass of gas in the belt $\sim 2 \times 10^9 M_\odot$, is about 10% of the total mass of the group gas within a sphere encompassing the radio lobes.

The efficiency of collection of group gas into the belt region is unexpectedly high, and would correspond to a high mass flow rate, $\sim 40 M_\odot$ yr^{-1}, into the belt. A redshift survey of 3C 386's group would be useful to help improve the understanding of the extent and composition of the group as currently little is known. This may help identify whether a merger in this group helped reshape the gas distribution.

Second, the entropy of gas in the inner belt is significantly lower than that of the group gas, but the cooling time for the belt gas is too long for it to have cooled significantly over the lifetime of the radio source. The cold gas must therefore predate the radio activity, and the high mass

means that it must be residual cool gas from the group. The group is poor in galaxies, consistent with the low gas temperature in the inner belt. The higher present temperature of the group gas and outer belt can then be interpreted as resulting from drastic heating driven by 3C 386 - the temperature difference between the inner belt and group roughly matches the heating that the lobes can provide. At the new temperature of the group, much of the gas should escape. The system was previously in hydrostatic equilibrium at ~ 0.7 keV and is now at a temperature of at least 1.4 keV which could result in the group scale atmosphere being blown away. To test this, I calculate the total mass of the group contained within a specified radius using the following equation (Worrall and Birkinshaw, 2006):

$$M_{\rm tot}(<r) = \frac{3\beta kTr^3}{G\mu m_{\rm H}(r^2+r_{\rm cx}^2)} \tag{3.3}$$

To a radius of 80 kpc, this gives a total group mass of $6.5^{+18}_{-6.4} \times 10^{12} M_{\odot}$. This is typical for galaxy groups (Mulchaey, 2000). I then find a gas mass fraction of $0.01^{+0.02}_{-0.005}$. This is much smaller than an expected cosmological value of about 0.17 (Planck Collaboration et al., 2015). Based on the size of the lobes and the sound speed in the group atmosphere, the age of the current outburst is 50 Myr. The sound speed of the gas is roughly equal to the escape velocity of the group, and it would take around 100 Myr for all the gas to flow out of the group. From these numbers, it is possible that a substantial fraction of the gas in the group has escaped due to heating by the radio source. It is also possible that multiple outbursts have been involved. Traces of a previous outburst may be sought in a low-frequency spectral index map, though I note that existing low frequency data show a relatively flat radio spectrum. Alternatively, the total mass of the 3C 386 group could be overestimated. Equation 3.3 applies only if the system is in hydrostatic equilibrium, whereas the 3C 386 system could be far from equilibrium if an inflow is present. If the total mass of the group is 10 times lower, so that the baryonic mass fraction is more normal, the total mass becomes of order a single galaxy mass, presumably the 3C 386 host galaxy itself.

Considering the work done by the lobes and calculating the bubble enthalpy ($4PV \approx 6 \times 10^{51}$ J) and comparing this to the thermal energy of all the gas out to the radius of the lobes ($E = 1.5^{+4.7}_{-1.4} \times 10^{52}$ J), show that within errors, the values are equal. This provides a lower limit to the total energy of the outburst, although an extended supersonic phase could increase this substantially.

Finally, the outer belt appears overpressured relative to the inner belt and the radio lobes,

although its entropy index is close to that of the group gas. A high pressure in this region is unexpected, since the buoyant motion of the lobes should generate only small pressure imbalances and slow gas flows back towards the 3C 386 galaxy. The geometry of the belt is uncertain. I have assumed that the belt is a flat disk of constant height. However, looking at Figure 3.5, it is apparent that the outer belt splays outwards from the inner belt. This splaying could lead to the volume of the outer belt increasing by a factor of 2. The pressure in the outer belt would then fall to $5.8^{+1.5}_{-1.4} \times 10^{-13}$ Pa, bringing the outer belt closer to pressure balance with the inner belt, with any remaining imbalance attributable to the dynamics in the system.

Additionally, I am limited by the current fit of the group gas temperature, having had to fix this parameter at the lower bound of its fitted range. Current X-ray missions are unlikely to be able to improve the observational situation. Future missions, such as *ATHENA*, with its significantly improved sensitivity, may be needed to constrain better the properties of the group gas.

3.6 Conclusion

I have reported measurements of the extended X-ray emission in the low-excitation radio galaxy 3C 386. I find that emission from the lobes is consistent with the interpretation of the X-ray power-law component originating from IC emission. The implied departure from equipartition of the lobes is comparable to the range seen in other sources.

I find that the X-ray emission from the gas belt in 3C 386 is most likely thermal, with an average temperature of $0.94^{+0.04}_{-0.05}$ keV across the whole of the belt. I find that the belt displays a clear temperature structure, with the gas closer to the core cooler than the gas closer to the surrounding group medium. I interpret this temperature structure as indicating that the belt was likely formed by a combination of gas components. In the outer belt a 'buoyancy-driven inflow' of part of the group-gas atmosphere, caused by the buoyant rising of the radio lobes through the ambient medium once the radio source became passive, is causing hot group gas to flow towards a relic cool core. This relic cool core is formed of old group gas, predating the radio activity in 3C 386.

It is possible that this inflow could lead to a resupply of fuel to the AGN, caused by gas reaching the parsec-scale regions surrounding the central black hole, which would lead to 3C 386 resuming a high level of radio activity in the future.

4

X-ray gas belts in low-redshift 3CRR radio galaxies

In this chapter, I expand the application of the analysis used on 3C 386 to *Chandra* observations of other belted sources in the low-redshift 3CRR sample. I begin by describing some general properties and statistics of the sample as a whole, before moving on to the X-ray spectroscopy.

4.1 The Low-redshift 3CRR Sample

4.1.1 Observations

A number of *Chandra* observations are used in this chapter. These observations vary significantly in both length and the date on which they were taken; over a 17 year period between May 2000 and December 2017. A summary of the *Chandra* observations of the belted sources is given in Table 5.1. The data were reprocessed and flare cleaned as described in Section 2.3.1 using software versions no earlier than CIAO 4.8 software with CALDB 4.7.2. This cleaning removed a significant fraction of time for only one source, NGC 6109.

Source	ObsID	Instrument	Date	Duration (ks)	Net Exposure (ks)
3C 35*	10240	ACIS-I	2009-03-08	25.6	24.3
3C 76.1	9298	ACIS-S	2007-12-09	8.1	7.3
3C 98	10234	ACIS-I	2008-12-24	31.7	31.2
3C 192	9270	ACIS-S	2007-12-18	10.0	9.5
	19496	ACIS-S	2017-12-18	69.2	67.8
	20888	ACIS-S	2017-12-21	9.9	9.7
	20889	ACIS-S	2017-12-21	32.7	32.7
	20890	ACIS-S	2017-12-24	21.1	19.3
	20891	ACIS-S	2017-12-22	35.3	34.8
3C 285	6911	ACIS-S	2006-03-18	39.6	36.0
3C 272.1	803	ACIS-S	2000-05-19	28.5	26.9
	5908	ACIS-S	2005-05-01	46.1	44.3
	6131	ACIS-S	2005-11-07	40.9	36.6
3C 296	3968	ACIS-S	2003-08-31	49.4	45.1
3C 305	12797	ACIS-S	2011-01-03	28.7	27.1
	13211	ACIS-S	2011-01-06	28.7	26.6
3C 310	11845	ACIS-S	2010-04-09	57.6	57.1
3C 386*	10232	ACIS-I	2008-11-29	29.3	29.0
3C 442A	5635	ACIS-I	2005-07-27	27.0	26.8
	6353	ACIS-I	2005-07-28	14.0	14.0
	6359	ACIS-I	2005-10-07	19.9	19.4
	6392	ACIS-I	2006-01-12	32.7	32.2
3C 388	5295	ACIS-I	2004-01-29	30.7	30.2
4C 73.08	10239	ACIS-I	2009-07-01	28.5	27.9
NGC 6109	3985	ACIS-S	2003-09-28	19.4	10.7
NGC 7385	10233	ACIS-I	2009-08-15	39.3	38.8

Table 4.1: Table of *Chandra* data used in this paper. Sources marked with a '*' are better described with *XMM-Newton* data as previously published, and so are not spectroscopically analysed in this paper.

4.1.2 Gas Scales

Before moving on to consider individual belted sources, firstly I consider the 3CRR sample as a whole. Table 4.2 lists all its members and details the scale of the X-ray structure seen in each source, along with the X-ray environment in which that source lies. The X-ray environment is classified based on nearby galaxy numbers and the temperature of the surrounding ambient medium of the source. Table 4.2 also indicates whether the sources have an X-ray bright gas belt in the system, along with an estimate of the scale of the gas belt and the largest projected linear size (LLS) of the radio source at 178 MHz in kpc. The belt scale is based on the length of the longest axis of the gas belt identified by eye.

The gas belts vary greatly in size, from galactic scales of a few kiloparsecs seen in sources such as 3C 272.1 (M84) and 3C 305 to group scales of hundreds of kiloparsecs seen in sources such as 3C 35 and 4C 73.08, although the size of the belt is closely matched to the LLS of the radio source. This suggests that these objects may have different origins, with the smaller belts perhaps arriving from X-ray coronae, i.e. galaxy gas which is believed to originate from stellar mass loss and be largely unaffected by the radio jets (Forman et al., 1985; Mathews, 1990), whilst the larger belts may form via gas stripping from mergers or other members of the group.

4.1.3 Histograms

As a rudimentary test of whether the belt sample is biased by observational factors, I plotted histograms and used a two-sample Kolmogorv-Smirnov (KS) test to examine the significance of the difference in distributions between the full sample and the belted subsample. The first of these displays the redshift distribution of the entire low-redshift 3CRR sample, along with the distribution of the belted sources. As shown in Figure 4.1, the distribution of belts in the 3CRR sample seems independent of the source's redshift. Almost all the bins in Figure 4.1 contain a belted source, with the redshift bin containing the most sources also containing the most belted sources. The KS test statistic, D, is 0.11 and the p-value is 0.998. This suggests that the null hypothesis that the two samples are drawn from the same distribution cannot be rejected, and that consequently the redshift distribution of the belted sources is only as biased as the sample from which it is drawn.

I also tested whether there was any bias in the distribution of belted sources as a function of total flare-cleaned exposure time for each source. Again, Figure 4.2 shows that the belted sources

Name of source	FR Class	X-ray Structure	Belt	Belt type, max scale (kpc)	LLS (kpc)	Smoothing radius of Gaussian (arcsec)
3C 192	II	Group	Y	Group (61 kpc)	231	2.46
3C 236	II	Galaxy	N	-	4530	-
3C 264	I	Cluster	N	-	173	-
3C 272.1	I	Cluster	Y	Galaxy (3.5 kpc)	11	0.98
3C 274	I	Cluster	N	-	71	-
3C 285	II	Group	Y	Group (106 kpc)	270	1.48
3C 293	I	Galaxy	N	-	228	-
3C 296	I	Group	Y	Group (32 kpc)	209	1.23
3C 305	I/II	Galaxy	Y	Galaxy (6.7 kpc)	11.2	0.74
3C 31	I	Group	N	-	917	
3C 310	I/II	Group	Y	Group (80 kpc)	320	1.97
3C 321	II	Pair	N	-	550	-
3C 326	II	Group	N	-	2010	-
3C 33	II	Group	N	-	293	-
3C 338	I/II	Cluster	N	-	71	-
3C 35	II	Galaxy	Y	Group (345 kpc)	972	1.97
3C 382	II	Galaxy	N	-	207	-
3C 386	I	Group	Y	Group (60 kpc)	105	2.46
3C 388	II	Cluster	Y	Group (43 kpc)	85	1.23
3C 390.3	II	Galaxy	N	-	253	-
3C 442A	I/II	Group	Y	Group (101 kpc)	320	1.48
3C 449	I	Group	N	-	522	-
3C 452	II	Galaxy	N	-	428	-
3C 465	I/II	Cluster	N	-	354	-
3C 66B	I	Group	N	-	304	-
3C 76.1	I/II	Galaxy	Y	Group (101 kpc)	129	3.2
3C 83.1B	I	Cluster	N	-	624	-
3C 84	I	Galaxy	N	-	486	-
3C 98	II	Galaxy	Y	Group (94 kpc)	190	1.23
4C 73.08	II	Group	Y	Group (334 kpc)	1130	5.9
DA 240	II	Group	N	-	1490	-
NGC 6109	I	Group, Cluster	Y	Galaxy (13 kpc)	528	0.492
NGC 6251	I/II	Group	N	-	1900	-
NGC 7385	I	Group, Cluster	Y	Galaxy (21 kpc)	437	0.74
PKS 1227+119	I	Galaxy	N	-	264	-

Table 4.2: Table detailing members of the low-redshift 3CRR catalogue and their Fanaroff-Riley classification, the scale of the X-ray environment in their observations, whether the source exhibits an X-ray bright gas belt and the scale size of the belt, based on measurements of its longest axis. LLS corresponds to the largest projected linear size in the radio at 178 MHz. Smoothing radius of Gaussian in arcsec applied to images in Figure 4.4.

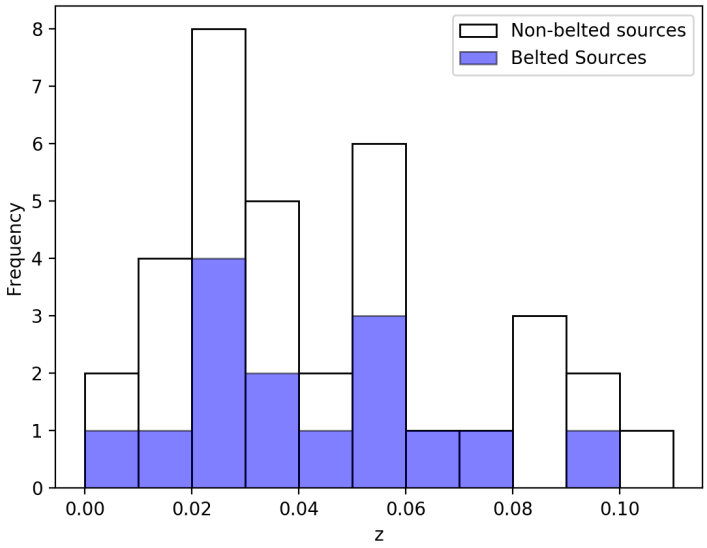

Figure 4.1: Histogram showing the redshift distribution of the whole low-redshift 3CRR sample (shown in white) along with the redshift distribution of the belted sources within the sample (highlighted in blue).

seem to be fairly well distributed across the entire range of exposure times in the sample. Again, I performed a two-sample KS test to determine the significance of the difference between the two distributions. In this instance $D = 0.21$ and the p-value is 0.693, suggesting that the two samples are drawn from the same distribution.

Finally, I tested if the 178 MHz radio luminosity had any bearing on the presence of a gas belt in the sources. The KS test returned a test statistic of $D = 0.12$ and a p-value of 0.994, again indicating that the sample of belted sources is no more biased to radio power than the complete sample from which it is drawn.

The results of these KS tests show that redshift and exposure time are not biasing the detection of gas belts any more than the sample from which they are drawn. Additionally, the 178 MHz radio luminosity of a source has no bearing on the detection of a belt in sources in the low-redshift 3CRR sample.

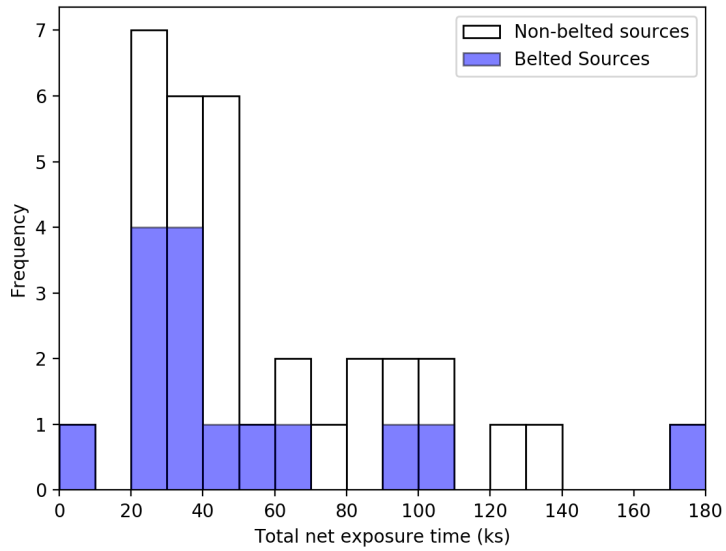

Figure 4.2: Histogram showing the total flare-cleaned exposure time of the whole low-redshift 3CRR sample (shown in white) along with the total flare-cleaned exposure time of the belted sources within the sample (highlighted in blue). I note that there are two sources with no belts with 400+ ks of exposure which are not displayed in the figure.

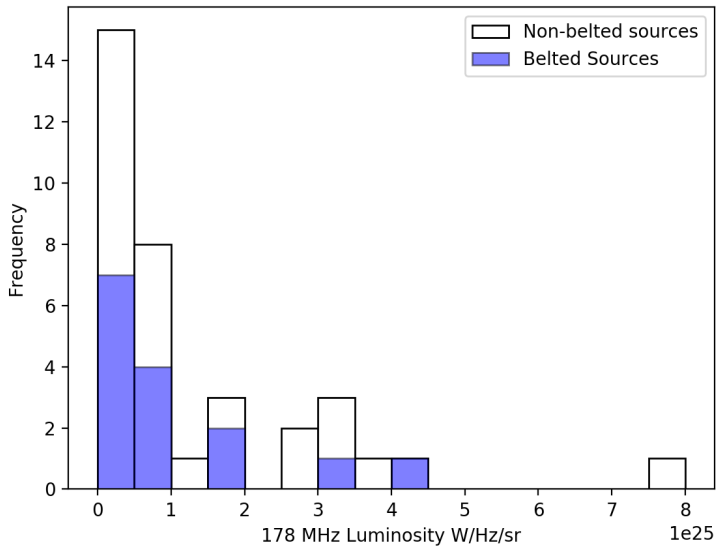

Figure 4.3: Histogram showing the 178 MHz radio luminosity of the whole low-redshift 3CRR sample (shown in white) along with the 178 MHz radio luminosity of the belted sources within the sample (highlighted in blue).

	I	II	Row total
A	a	d	a+d
B	b	e	b+e
C	c	f	c+f
Column total	a+b+c	d+e+f	n

Table 4.3: Example 3x2 contingency table.

4.2 Contingency Tables

In this section I calculate the statistical significance of the relationship between the 178-MHz radio power of members of the 3CRR sample and the appearance of various X-ray structures. I reprocessed, merged and exposure corrected the *Chandra* data for each of the galaxies in the sample as described in Section 2.3.2 and checked each image to identify whether the relevant X-ray structure was present. The sources were then divided into three separate groups based on the 178-MHz power of the relevant radio galaxy. The lowest power group contains 11 sources, and the middle and high power groups contain 12 sources each.

To test the statistical significance of the appearance of X-ray structure and the radio power of sources, I used Fisher's Exact Test. Fisher's Exact Test is used to examine the significance of the association between two different kinds of classification. It is preferred to χ^2 fitting in this instance as many of the contingency tables contain low frequency cells. When calculating χ^2, an approximation is made to the χ^2 distribution, and low frequency cells cause this approximation to break down and produce inaccurate results.

The most frequently used table in the analysis is a 3x2 contingency table, an example of which is shown in Table 4.3.

The p-value for this particular table is calculated using Equation 4.1, where each letter corresponds to the count in that particular cell.

$$p = \frac{(a+d)!(b+e)!(c+f)!(a+b+c)!(d+e+f)!}{a!b!c!d!e!f!n!} \tag{4.1}$$

Occasionally a 3x3 contingency table is used in the analysis (Table 4.4).

To calculate the p-value of Table 4.4, I use Equation 4.2.

$$p = \frac{(a+b+c)!(d+e+f)!(g+h+i)!(a+d+g)!(b+e+h)!(c+f+i)!}{a!b!c!d!e!f!g!h!n!} \tag{4.2}$$

In order to calculate the significance of the observed data, I have to calculate the probability of observing data as extreme or more extreme as the observed table. To do this I sum the p-value

	I	II	III	Row total
A	a	d	g	a+d+g
B	b	e	h	b+e+h
C	c	f	i	c+f+i
Column total	a+b+c	d+e+f	g+h+i	n

Table 4.4: Example 3x3 contingency table.

	FRI	FRI/II	FRII
low P	9	2	0
med P	4	4	4
high P	1	1	10

Table 4.5: Contingency table detailing the observed distribution of FR types in different radio power groups.

of the observed table along with the p-values of those tables with sets of values more extreme than those observed, whilst maintaining the row and column totals. I do this using the statistical software package R's FISHER.TEST function. The sum of these probabilities is the result of Fisher's Exact Test and provides the p-value of the data, or the probability of observing data as extreme or more extreme assuming that the null hypothesis of independence holds. I require a p-value of < 0.1 to reject the null hypothesis, and claim a relationship between radio power and the appearance of X-ray structure.

As a test of the method, I first calculated the relationship between radio power and Fanaroff-Riley (FR) classification. The observed table for the 3CRR sample is shown in Table 4.5, with the classifications taken from Table 4.2. Sources classified as FR I/II are either of intermediate radio luminosity or display the features of both FR I and FR II sources.

The total p-value for Table 4.5 is 1.6×10^{-4}. This indicates that the low-power source group is more likely to contain FRI sources and the high power group is more likely to contain FRII sources. This makes sense as the FRII sources are more high powered than the FRI sources and thus this provides an effective test of the method.

I next tested the relationship between radio power and the appearance of an X-ray jet in the *Chandra* observations. The observed table from this test is shown in Table 4.6.

The total p-value for Table 4.6 is 0.099, just below the cut off needed to reject the null hypothesis. This indicates that X-ray jets are more commonly a feature in low-power radio galaxies. It is possible that there is an observational bias in this sample. X-ray jets are often short, low surface brightness features and the high-power group contains the sources at higher

	X-ray jet	No X-ray jet
low P	7	4
med P	8	4
high P	3	9

Table 4.6: Contingency table indicating whether members of the low-redshift 3CRR sample in three different radio power groups have a visible X-ray jet or not.

	X-ray jet	No X-ray jet
low P	11	6
high P	7	11

Table 4.7: Contingency table indicating whether the members of the low-redshift 3CRR sample in two different radio power groups have a visible X-ray jet or not.

redshifts. It is possible that these high-power sources also have visible X-ray jets, but a longer observation is required in order to detect them.

Due to the proximity of the p-value to the cut-off, I performed the test again, this time with only two power groups to see if there is a more extreme relationship if the sample is divided this way. The 17 lowest power and the 18 highest power radio sources form the groups displayed in Table 4.7.

The total p-value for Table 4.7 is 0.18, which is above the cut-off needed to reject the null hypothesis. This indicates that there is no relationship between the radio power and a visible X-ray jet.

I next tested the relationship between power and the appearance of X-ray hotspots. The observed table is shown in Table 4.8. The total p-value for Table 4.8 is 4.6×10^{-4}. This shows a very strong relationship between power of the source and whether the source has hotspots, with hotspots more likely to appear in sources belonging to the high-power group. This again makes sense as hotspots tend to be a feature of the more high powered, edge-brightened FRII sources. It is also possible this relationship could be even stronger, given that the X-rays from the radio

	X-ray hot spots	No X-ray hotspots
low P	0	11
med P	4	8
high P	9	3

Table 4.8: Contingency table indicating whether members of the low-redshift 3CRR sample in different radio power groups have X-ray hot spots or not.

	iC lobes	No iC lobes
low P	2	9
med P	4	8
high P	6	6

Table 4.9: Contingency table indicating whether the X-ray emission in the lobes of members of the low-redshift 3CRR sample is caused by inverse-Compton scattering or not for different AGN power groups.

	Obvious X-ray gas at LAS	No obvious X-ray gas at LAS
low P	1	10
med P	3	9
high P	3	9

Table 4.10: Contingency table indicating whether members of the low-redshift 3CRR sample in different radio power groups have obvious X-ray gas at their largest angular scale in the radio.

hotspots are not always detected in shorter observations.

I next tested whether there is a relationship between radio power and inverse-Compton (iC) X-ray emission in the lobes (Table 4.9). The p-value of Table 4.9 is 0.37. This shows no evidence of a strong relationship between the power of the radio galaxy and the presence of iC emission in its lobes. This is interesting as it is expected that this is a feature of mostly FRII sources, which tend to have a higher power. Whilst the table does show that slightly more high powered sources show evidence of iC lobes, it is not strong enough to claim a relationship in this sample.

I next tested whether the radio power of an object has an impact on whether you can detect X-ray gas at the largest angular scale (LAS) of the source's radio emission. The sources are placed in the left column of Table 4.10 only if there is group/cluster emission above the background level obvious to the eye. Frequently, there is no X-ray gas at these extents, unless the LAS of the source is small or the object lies in a region with dense cluster gas. The total p-value of Fisher's Exact Test for Table 4.10 is 0.66, indicating no relationship between radio power and the presence of obvious X-ray gas at the source's LAS. It is difficult to make much comment on this table due to the low frequency with which gas at these distances is observed.

The next test I performed was between radio power and the appearance of cavities in the X-ray gas. The total p-value of Table 4.11 is 0.75. This is well above the limit for a statistically significant relationship between power and thus shows no evidence of a relationship between power of the source and detection of cavities. This is interesting as it would be expected that

	Cavities	No cavities
low P	4	7
med P	5	7
high P	3	9

Table 4.11: Contingency table indicating whether members of the low-redshift 3CRR sample in different power groups have cavities or not.

	Cluster env	Group env	Isolated galaxy
low P	8	2	1
med P	5	3	4
high P	3	5	4

Table 4.12: Contingency table indicating the optical environment of radio sources in low-redshift 3CRR sample in different radio power groups. Optical environment classifications are taken from Prestage and Peacock (1988) and Miller et al. (1999).

cavities would be a feature of the high-power sources, as these would be more effective at clearing gas from where the lobes are expanding. Observational limitations could again be a factor in this, as a lot of the sources show little evidence of extended group or cluster atmospheres, and thus identifying a feature characterised by its low surface brightness would be difficult.

I next tested the relationship between the optical classification of the environment of the sources and their radio power. The p-value of Table 4.12 is 0.24. This shows that there is no relationship between the optical classification of a source's environment and its radio power. Despite the lack of a strong mathematical relationship, cluster environments are more prevalent in low power than high power, probably due to the difficulty in detecting lower magnitude sources in surveys at higher redshifts.

The p-value of Table 4.13 is 0.63. This shows no evidence of a relationship between radio power and the detection of an X-ray bright gas belt in the source. Once again, they are more difficult to detect in high redshift sources. Belts seem common among radio galaxies, and may be a feature of all of them.

	Belt	No belt
low P	6	5
med P	5	7
high P	4	8

Table 4.13: Contingency table indicating whether members of the low-redshift 3CRR sample in different power groups have an X-ray belt or not.

	FR I	FR I/II	FR II
low SB	1	1	5
high SB	4	3	1

Table 4.14: Contingency table comparing the surface brightness of X-ray bright gas belts to the Fanaroff-Riley classification of its host galaxy.

	Obvious X-ray gas at LAS	No obvious X-ray gas at LAS
low SB	1	6
high SB	3	5

Table 4.15: Contingency table comparing the surface brightness of X-ray bright gas belts and the presence of X-ray gas at the largest angular scale of the radio emission.

4.2.1 Gas Belt Contingency Tables

I took a subsample of the 15 radio galaxies which contain an X-ray bright gas belt and calculated the surface brightness of the gas belt in the galaxy. To do this I took exposure-corrected images of each of the sources and then divided them by their areas in square arcseconds. These were then arranged in order of surface brightness and separated into only two groups due to the lower number of sources in this subsample. The low surface brightness group contains 7 gas belts, and the high surface brightness group contains 8 gas belts. As in Section 4.2 I then used Fisher's Exact Test to calculate the p-value of Tables 4.14-4.16 to test whether there was a significant relationship between the X-ray surface brightness of these belts and various properties of its host galaxy. Once again, p-values of less than 0.1 are required to disprove the null hypothesis of independence.

The first test performed investigates whether the surface brightness of X-ray gas belts is related to the FR classification of the radio source. The observed table from the data is shown in Table 4.14. The total p-value from Fisher's Exact Test of Table 4.14 is 0.096. This is just below the cut-off and therefore shows that high surface brightness belts are more likely to be FRI sources, and low surface brightness belts are more likely to be in FRII sources. This could be an observational effect, as the belts would be harder to detect in FRII sources, which tend to be at higher redshifts. If belts are detected in FRII sources, they would therefore obviously be weaker in the image, and have a lower surface brightness as shown in this table.

Secondly, I tested whether the appearance of X-ray gas at the LAS in the radio is related to the surface brightness of the gas belts. The observed table from the sample is shown in Table

	Cluster env	Group env	Isolated galaxy
low SB	2	3	2
high SB	5	2	1

Table 4.16: Contingency table comparing the surface brightness of X-ray bright gas belts to the optical environment of its host galaxy.

4.15. The total p-value from Fisher's Exact Test of Table 4.15 is 0.34. This shows no relationship between the presence of X-ray gas at the radio source's LAS and the surface brightness of X-ray gas belts. This may again, be due to the relatively low frequency at which X-ray gas is observed at the LAS throughout the sample. Interestingly, over half the sources with gas at the LAS have X-ray gas belts.

Finally, I tested whether the optical environment of the radio galaxy resides in effects the surface brightness of its X-ray gas belt. The table observed from the data is shown in Table 4.16. The p-value of Table 4.16 is 0.51. This shows no evidence of a relationship between the surface brightness of an X-ray bright gas belt and the optical classification of the environment in which its host galaxy resides in. A relationship between these is expected, as it is possible the ICM/IGM plays a crucial role in the formation of these gas belts, along with the merging of galaxies. It would make sense for richer environments to show stronger X-ray gas belts.

4.3 Notes on Individual Sources

Here I discuss previous research for each of the belted sources in the sample.

4.3.1 Sources with Previous Belt Discussion

Some of the observations used in this work have been used previously to discuss the X-ray source properties, touching on the belt gas, in dedicated publications. I summarise those findings here.

I investigated a prominent gas belt in 3C 386 in Chapter 3. This gas belt exhibits a strong temperature structure with the outer material in the belt being much hotter (roughly the same temperature as the group medium) and the inner belt material, closer to the core, being cooler. I determined that the gas belt likely formed as a result of a buoyancy-driven inflow of part of the group gas atmosphere towards a relic cold core of old group gas. The buoyant motion of the lobes through the ambient medium causes group gas to flow back between the lobes and on to an inner belt composed of old, unheated group gas.

3C 35 is an FR II radio galaxy with an elliptical host. It hosts a gas belt which Mannering et al. (2013) interpret as hot, fossil-group gas originating in galaxies which merged over a Gyr ago, which was driven outwards by the expanding radio lobes before continuing to expand at its own sound speed. Fossil groups are a class of system, with an extended hot, gaseous halo encompassing a single giant elliptical galaxy, but with the gravitating mass of a galaxy group (Hess et al., 2012). They are believed to be merger remnants of galaxy groups whose galaxies have coalesced (Dariush et al., 2007).

3C 272.1, also known as M84, is hosted by an elliptical galaxy within the core of the Virgo Cluster. It is an FRI galaxy and radio observations clearly show both jet and lobe emission, although these are quite small, comparable in size with the observed optical and X-ray diameters of the host. Finoguenov et al. (2008) identifies the gas belt as 'bubble walls' shaped by the expansion of the radio lobes. The belt coincides with regions of higher pressure and lower entropy, and this low entropy gas originates from entrained gas from the central regions of 3C 272.1.

3C 285 is an FR II radio galaxy with weak hotspots and fat lobes. The host galaxy is the brightest member of a small optical group. Hardcastle et al. (2007) note a 'ridge' of thermal gas, which is aligned orthogonal to the radio lobes of 3C 285. They suggest that it is possible that the ridge (or gas belt) was present before radio activity in the source began, although it is possible that some of the gas that forms the belt was stripped from galaxies which merged to the current 3C 285. They suggest that the lobes would have had limited impact on the gas belt throughout their history, as ram-pressure would initially cause the lobes to expand into the lower density group medium, while later, once the pressure in the lobes had dropped, the belt material would push lobe material out of the centre of the group.

3C 442A is a low-excitation radio galaxy which contains no active jet (Birkinshaw et al., 1981), so the dynamical state of the radio structure is able to be influenced by its surrounding medium. Worrall et al. (2007) conclude that an active merger is causing the gas of merging galaxies to align orthogonal to, and do work on, the radio lobes. In this system, the belt is over-pressured and driving the lobes apart, with some of the energy going into particle acceleration.

3C 305 is a small, unusual source with a relatively isolated host galaxy, that lies on the FR I/FR II power boundary. Hardcastle et al. (2012) discuss extended emission which lies perpendicular to the jet axis, which they call 'wings'. The pressure in the wings (or belt) in this system is very similar, within errors, to the minimum lobe pressure. As a result of this, the

authors suggest that it is possible that the belt is shocked material that has been driven back towards the centre of the source by the expanding radio lobes.

4.3.2 Sources without previous belt discussion

NGC 7385 is a low-excitation radio galaxy with an elliptical host (de Koff et al., 1996). It is an FR I head-tail source with the tail extending about 510 kpc (Schilizzi and Ekers, 1975), which resides in a poor cluster (Zwicky 2247.3+1107). The source has an optical and X-ray jet, which is undergoing a strong-jet cloud interaction which appears to be deflecting the counter-jet, causing a reversal in its direction (Rawes et al., 2015).

NGC 6109 is an FR I-type head-tail radio galaxy located in a poor cluster (Wegner et al., 1999). Feretti et al. (1995) observed NGC 6109 in X-rays with *ROSAT* and report point-source emission associated with the radio nucleus, consistent with a jet-base origin. They also note diffuse X-ray emission lying between NGC 6109 and another nearby radio galaxy, NGC 6107. The temperature and luminosity of this gas are lower than typically found for rich clusters, suggesting NGC 6109 belongs to a poor group of galaxies within a large supercluster.

3C 98 is an isolated (Prestage and Peacock, 1988), FR II radio galaxy with an elliptical host (Zirbel, 1996). It has previously been observed in X-rays with both *ROSAT* (Hardcastle and Worrall, 1999), revealing faint extended emission associated with its radio lobes and *XMM-Newton*, in which Isobe et al. (2005) report diffuse iC emission associated with the lobes, along with a bright X-ray nucleus.

3C 192 is a high-excitation radio galaxy with an elliptical host (Cheung, 2007). It has been identified as a winged or X-shaped radio galaxy (Cheung, 2007). It is the brightest member of a small group of galaxies (Prestage and Peacock, 1988); its closest companion is roughly 1 arcmin away with no evidence of an interaction (Baum et al., 1988). The gas belt in this source coincides with a region of low-surface brightness in radio observations. Hodges-Kluck et al. (2010) favours an enhancement in this region as originating from a bounding shock or having been influenced by the radio galaxy. 3C 192 is also a 'superdisk' radio galaxy, which are characterised by a wide, elongated emission gap with fairly sharp and straight edges between the radio lobes (Gopal-Krishna and Wiita, 2000). Gopal-Krishna and Wiita (2009) proposes that this type of radio galaxy forms through the merger of a small elliptical galaxy with the massive host, in which the gas attached to the infalling galaxy deposits its angular momentum into the host's circumgalactic gas, causing it flatten into a disk-like shape.

4C 73.08 is a giant radio galaxy with an elliptical host (Saunders et al., 1989), with an unusual X-shaped morphology, and lies on the boundary between FR I and FR II sources in radio power (Mayer, 1979). Chen et al. (2012) examine the optical field of 4C 73.08 and find that the radio source is accompanied by nine galaxies. Strom et al. (2013) identify three of the members of the group to be radio sources with flux densities less than 0.4 mJy.

3C 388 is an FR II low-excitation radio galaxy. *Chandra* observations of 3C 388 (Kraft et al., 2006) reveal the source lies in a cluster environment which extends roughly 400 kpc from the source. The inflation of radio lobes has created cavities in the gas, with coincident deficits in the X-ray surface brightness, and also caused the quenching of a cluster cooling flow.

3C 310 is an FR I, fat double radio galaxy in a moderately rich environment, well known for a bright radio ring positioned in the centre of its southern lobe (van Breugel and Fomalont, 1984; Gizani et al., 2002). Kraft et al. (2012) finds that the supersonic inflation of the lobes has driven a shock into the gas outside the southern radio lobe.

3C 76.1 is an FR I radio galaxy, with an unusually isolated environment. Early studies of its environment found no detectable hot gas, via X-ray emission (Miller et al., 1999) or Faraday rotation (Vallee, 1982). *XMM-Newton* observations revealed a very weak environment, elongated in the north-south direction (Croston et al., 2008a), which I claim is gas belt emission.

3C 296 is an FR I radio galaxy, hosted by a large elliptical galaxy (Martel et al., 1999). It has a moderate X-ray surface brightness group environment (Croston et al., 2008a).

4.4 Spectroscopy

4.4.1 Gas belts

In this section, I describe spectral analysis of the *Chandra* data of individual sources with belts. This does not include 3C 35 and 3C 386, as these sources are both better described with *XMM-Newton* data. As a result of this, relevant parameters will be taken from Chapter 3 for 3C 386 and Mannering et al. (2013) for 3C 35, unless otherwise specified. For each source, the region in which the gas belt lies is identified by eye. These regions then define the extent of the belts. The presence and extent of a belt in a source is subjective, but for the purposes of this thesis all analysed sources are assumed to feature belts. I also used the regions (Figure 4.4) for spectral extractions. In each case, the belt lies broadly orthogonal to and between the radio lobes. I initially considered the emission from each belt as a whole (excluding the cores and other point sources)

to measure the average temperature, density and pressure across the extent of the belt and also to identify where it might be possible to fit a temperature structure. I utilised SPECEXTRACT to extract source and local background spectra from each observation. The local background counts were subtracted and the remaining source spectral counts are binned differently for each source. Where possible, I attempted to retain at least 20 counts per bin to enable use of χ^2 as a measure of the goodness of fit. When a large number of counts are present in each bin in a binned dataset, the probability distribution for a fitted parameter can be assumed to be a Gaussian. However, this is not the case for datasets in which many bins have low counts. Where several bins in a dataset have less than 20 counts, I instead model the probability distribution of the parameter as a Poisson distribution, using cstat statistics in XSPEC (Cash, 1979). If a source has multiple observations, as is the case for 3C 272.1 and 3C 192, the observations are summed before fitting.

I fitted the extracted belt emission for each source separately to an absorbed APEC plasma model (Smith et al., 2001), an absorbed power-law model, and an APEC + power-law model. The Galactic neutral hydrogen densities were obtained with the *Chandra* COLDEN tool with the data of Dickey and Lockman (1990) and are fixed at these values through fitting. The metal abundance for each source is fixed at $Z_{\odot} = 0.3$. In almost all cases, the best-fit model to the belt emission, was an APEC model. The results from the best-fit spectral fitting are shown in Table 4.17 and example spectra are show in Figure 4.5. Three cases are exceptions: 3C 35 (Mannering et al., 2013), 3C 192 and 3C 272.1 where the best-fit model was found to be an APEC + power-law model. From the power-law component of the 3C 272.1 fit, the best-fit photon index was found to be $\Gamma = 2.08^{+0.45}_{-0.69}$ and the best-fit 1 keV flux density corresponds to $S_{1\,\mathrm{keV}} = 7.62^{+3.33}_{-3.99}$ nJy. For 3C 192, the spectral index is frozen at $\Gamma = 1.8$ and the best-fit 1 keV flux density corresponds to $S_{1\,\mathrm{keV}} = 1.49 \pm 0.76$ nJy.

As can be seen in Table 4.17, the average temperature across the population of gas belts ranges between 0.6 and 2.5 keV. The relation between belt and environment temperatures is represented graphically in Figure 4.6. The belt temperature is higher than the external temperature in some cases, meanwhile the opposite is true in other cases suggesting different belt origins. Where the external medium is hotter than the belt, this may suggest a galactic origin for the gas, as is the case in 3C 442A where cool gas is being stripped from merging galaxies to form the belt. It may also suggest a significant cool core component, which is the case for 3C 386. Belts hotter than their external medium, may indicate that the gas has been heated, presumably by an interaction with the radio source or a poor detection of the external medium.

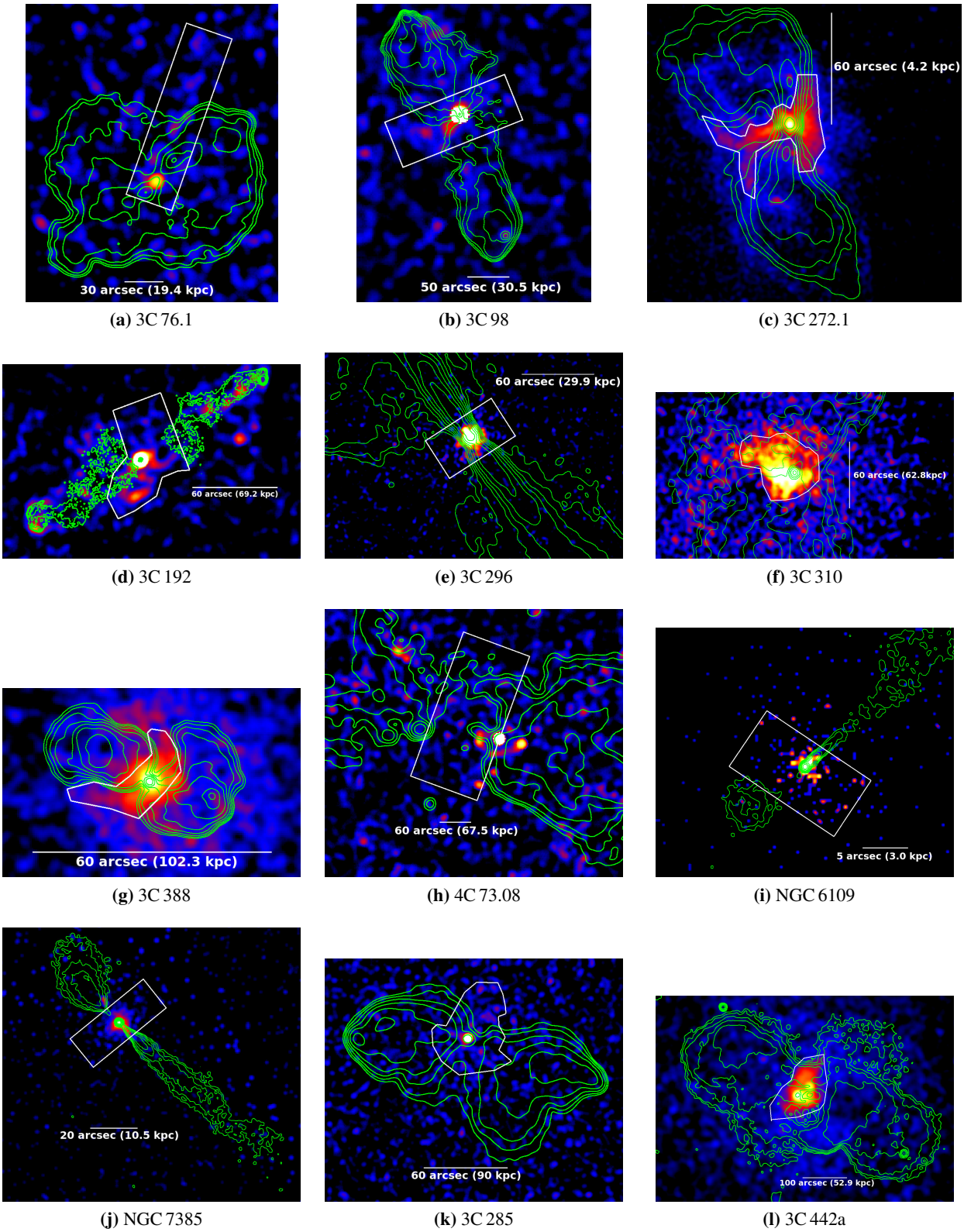

(a) 3C 76.1 **(b)** 3C 98 **(c)** 3C 272.1

(d) 3C 192 **(e)** 3C 296 **(f)** 3C 310

(g) 3C 388 **(h)** 4C 73.08 **(i)** NGC 6109

(j) NGC 7385 **(k)** 3C 285 **(l)** 3C 442a

Figure 4.4: Smoothed *Chandra* images of the sources in the low-redshift 3CRR sample containing belts (marked in white) studied in this thesis, with Gaussian smoothing radii given in Table 4.2. Point sources excluding the AGN have been excised and smoothed over. The contours are of VLA maps of angular resolution roughly matched to the X-rays, at different frequencies as given in Table 4.21.

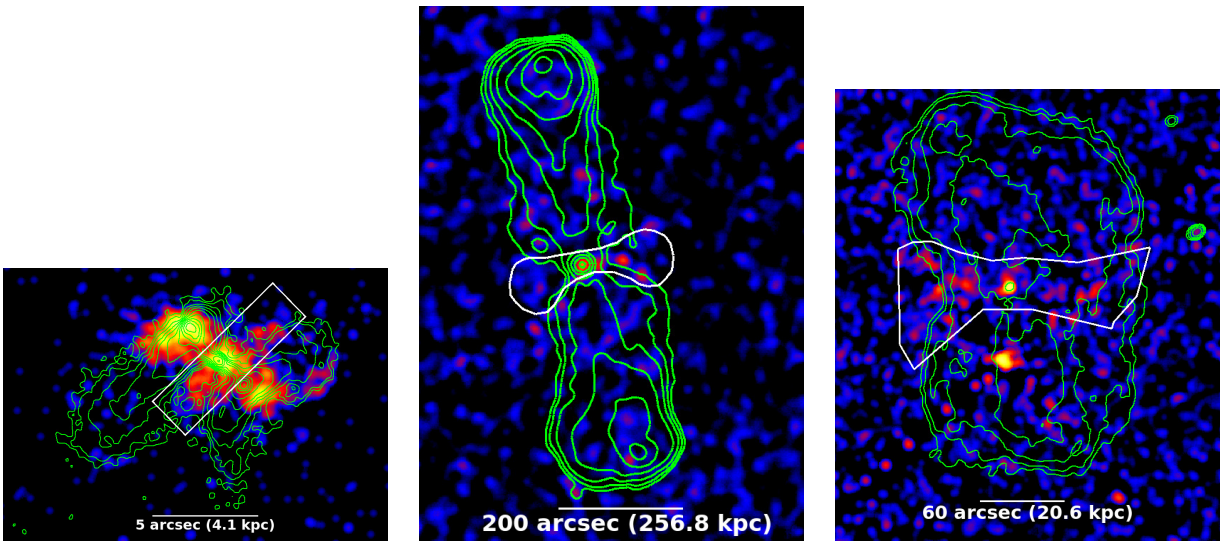

(a) 3C 305 **(b)** 3C 35 **(c)** 3C 386

Figure 4.4: (continued).

Source	kT (keV)	$10^{14}N$ (10^9 cm^{-5})	χ^2/dof
3C 76.1	$2.52^{+1.91}_{-1.18}$	$4.02^{+1.45}_{-1.27}$	cstat
3C 98	$0.98^{+0.54}_{-0.29}$	$1.99^{+0.67}_{-0.59}$	cstat
3C 192	$1.04^{+0.26}_{-0.16}$	1.13 ± 0.36	37.4/34
3C 272.1	0.64 ± 0.01	30.8 ± 1.2	273.8/225
3C 285	0.95 ± 0.04	$1.75^{+0.34}_{-0.31}$	cstat
3C 296	0.96 ± 0.04	$8.31^{+0.79}_{-0.88}$	55.6/58
3C 305	$1.54^{+0.14}_{-0.3}$	$2.52^{+0.29}_{-0.27}$	cstat
3C 310	1.45 ± 0.06	27.3 ± 1.0	160.7/112
3C 388	$2.04^{+0.30}_{-0.19}$	20.4 ± 1.4	40.8/35
3C 442A	1.06 ± 0.02	50.3 ± 4.9	233.8/123
4C 73.08	$1.01^{+0.34}_{-0.24}$	3.56 ± 0.97	43.2/60
NGC 6109	$0.90^{+0.09}_{-0.12}$	$3.47^{+0.62}_{-0.55}$	cstat
NGC 7385	$0.94^{+0.07}_{-0.09}$	$4.76^{+0.58}_{-0.54}$	cstat

Table 4.17: Best-fit parameters of the APEC plasma model fits to all sources (excluding 3C 192 and 3C 272.1 where this shows the APEC component of an APEC + power-law model). All metal abundances are fixed at $Z_\odot = 0.3$. Errors are quoted for a 90% confidence range.

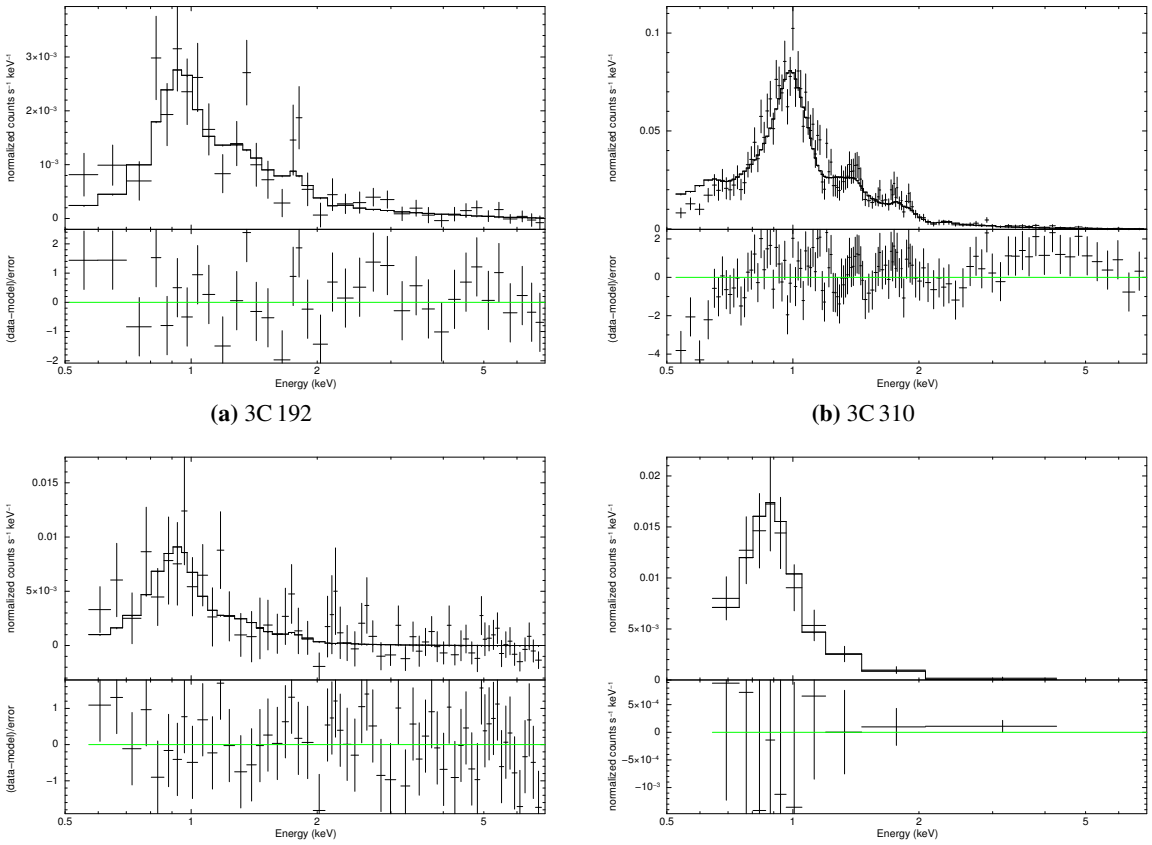

(a) 3C 192 **(b)** 3C 310

(c) 4C 73.08 **(d)** NGC 6109

Figure 4.5: Sample of the best-fit models to the gas belts in the sample. An APEC model is fit in all cases shown here, excluding 3C 192 which is fit with APEC+power-law, where the power-law emission likely originates in the lobes.

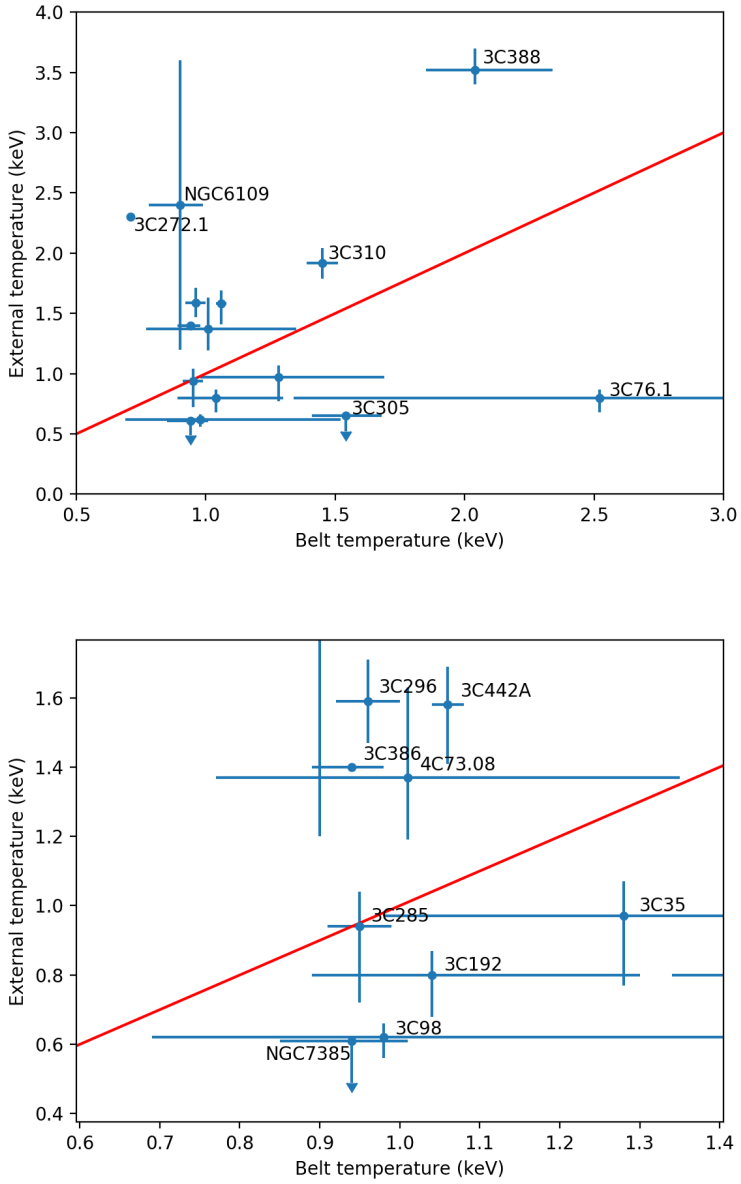

Figure 4.6: kT in the external medium of each of the sources, plotted against kT of each of the gas belts. The red line shows where the two temperatures are equal. Temperatures in the external medium are taken from Ineson et al. (2015), Urban et al. (2011) for the Virgo Cluster surrounding 3C 272.1 and Feretti et al. (1995) for NGC 6109.

a) Temperature structure in the gas belts

Using the spectral fits shown in Table 4.19, I selected three sources from which I thought it would be possible to measure a temperature structure in the belt. The sources selected were 3C 272.1, 3C 296 and 4C 73.08. 3C 310 was previously shown to have a temperature structure in Kraft et al. (2012), although I have also performed an independent fit over the region I identify as the belt to confirm this. For 3C 388, Kraft et al. (2006) found that errors on the temperature measurement were too large to establish whether a temperature structure were present in the belt. Due to the low counts and use of cstat in the other sources, it is impossible to make a reliable test.

To study temperature structure I split the belts into inner and outer regions. This division was performed by eye, based on the concentration of counts in the region or a noticeable morphological change in the X-ray gas. The divisions between the inner and outer regions for each source can be seen in Figure 4.7. The spectra were generated using SPECEXTRACT. The cores and any other point sources were excluded from the extraction.

Due to the morphology of the radio structure, I assume that the gas belts in 3C 296 and 4C 73.08 are disks that are viewed side on. This would result in some outer belt material in front of and behind the inner belt along the line of sight to the belt. To compensate for this, and hopefully gain a more accurate measurement of the temperature in different regions of the belt in these cases, I fitted an APEC + APEC model to the inner belt spectra. The first APEC in this model is fixed at the temperature obtained from fitting an APEC model to the outer belt material, and its normalisation is also fixed to accommodate the outer gas belt assuming a disk geometry. In 3C 272.1 the belt geometry is different, with the outer regions of the gas belt extending in filamentary arms away from the main, disk-like inner belt structure (see Figure 4.7a) so this correction was not used. In 3C 310, the inner section I have selected extends across almost the entirety of the width of a section of a cylinder. Therefore, I assume that any outer belt will have a negligible effect on the fitting of the inner belt material. The results for each spectral fit are shown in Table 4.18.

A pattern is found in 3C 272.1, 3C 296 and 3C 310, where the temperature in the outer belt is hotter than the inner belt. This is a significant result in the case of 3C 272.1 and 3C 310, but in the case of 3C 296 the large errors on the outer belt temperature make the result less clear. Such temperature structure was also seen in the belt of 3C 386 (Duffy et al., 2016), where the difference between outer and inner belt temperature is almost a factor of three, far more

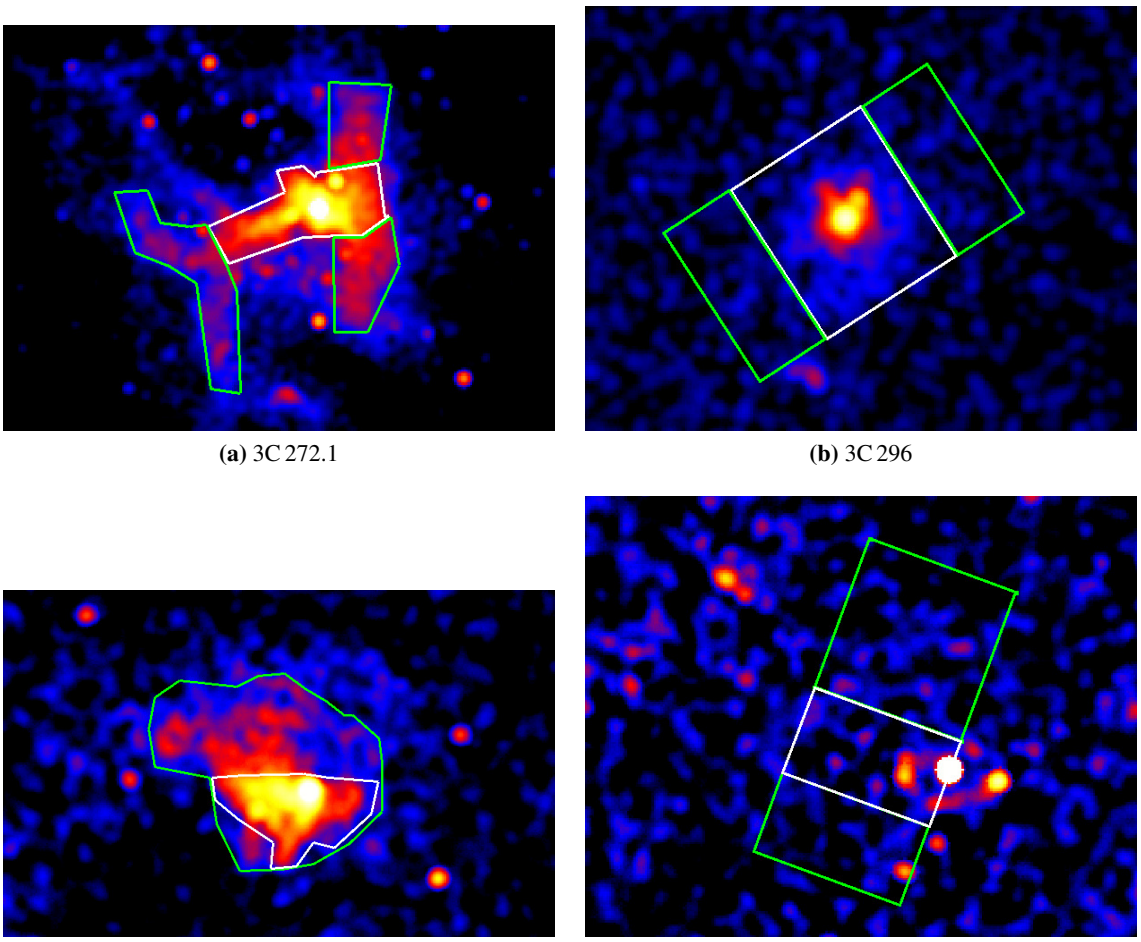

(a) 3C 272.1 **(b)** 3C 296

(c) 3C 310 **(d)** 4C 73.08

Figure 4.7: Smoothed *Chandra* images of 3C 272.1, 3C 296, 3C 310 and 4C 73.08, highlighting the extraction regions of the inner and outer regions of the gas belt. The inner regions of each belt are bounded in white, while the outer regions in each belt are bounded in green.

Source/ Model Parameter	Inner Belt	Outer Belt
3C 272.1		
kT (keV)	0.66 ± 0.01	0.74 ± 0.01
$10^{14}N$ (10^9 cm^{-5})	32.7 ± 0.6	23.2 ± 0.5
χ^2/dof	366.7/227	259.6/206
3C 296		
kT_1 (keV)	$0.93^{+0.04}_{-0.05}$	$1.22^{+0.29}_{-0.18}$
$10^{14}N_1$ (10^9 cm^{-5})	$6.69^{+0.70}_{-0.78}$	0.97 ± 0.26
kT_2 (keV)	1.22 (fixed)	-
$10^{14}N_2$ (10^9 cm^{-5})	1.14 (fixed)	-
χ^2/dof	55.9/51	7.4/10
3C 310		
kT (keV)	1.33 ± 0.04	$1.58^{+0.07}_{-0.08}$
$10^{14}N$ (10^9 cm^{-5})	11.7 ± 0.7	15.4 ± 0.8
χ^2/dof	81.7/59	105.9/79
4C 73.08		
kT (keV)	$0.54^{+0.99}_{-0.54}$	$1.20^{+0.45}_{-0.27}$
$10^{14}N$ (10^9 cm^{-5})	$1.38^{+2.81}_{-1.32}$	$2.90^{+1.17}_{-1.03}$
kT_2 (keV)	1.20 (fixed)	-
$10^{14}N_2$ (10^9 cm^{-5})	$0.30^{+1.08}_{-0.30}$	-
χ^2/dof	7.6/13	39.8/46

Table 4.18: Best fit parameters from the inner and outer belt of 3C 272.1, 3C 296, 3C 310 and 4C 73.08. The outer belts are fit to an absorbed APEC model, whilst the inner belts are fit to an absorbed APEC + APEC model. Metal abundances are fixed at $Z_\odot = 0.3$. Errors are quoted for a 90% confidence range.

substantial than any of the sources here.

In 4C 73.08 the temperatures overlap within errors, so it is not possible to claim a temperature structure with the current data. Unlike the other belts, the normalisation of the outer component of gas in the inner fit of 4C 73.08 had to be allowed to vary. When this value was fixed, it was not possible to obtain an acceptable fit for the inner component. However, the value of the outer component of normalisation calculated to accommodate the geometry lies within the 90% confidence range of the fitted value. While the errors are large, the best fit values are in the same direction as the other sources, with the outer belt hotter than the inner belt.

b) Physical parameters of the gas belts

The gas belt of each of the sources in the sample is well fit to models which contain a thermal APEC component. Using the fitted parameter values along with an estimated volume I calculate the density, pressure, total mass and entropy index of each gas belt following Section 2.4.2.

A summary of results for the gas belts in the sample is given in Table 4.19. The densities, pressures and entropies given in Table 4.19 correspond to the average density and average pressure over the entire belt. Most of the belts have gas masses between a few $10^8 M_\odot$ and a few $10^{10} M_\odot$.

I also apply the same equations to the belts I fitted in two spatial regions in order to probe their distribution of mass and pressure. The results of these calculations are shown in Table 4.20.

4.4.2 Lobes and plumes

The X-ray emission contained within the radio lobes and plumes was also extracted and fitted for each source. I used two elliptical extraction regions with extents defined using the VLA radio observations described in Table 4.21. These regions were also applied to the radio data to measure the radio flux density. Emission from contaminating point sources and belt gas was excluded from the X-ray extractions. The two lobes extracted from each source were initially fitted together, as in a number of cases a low number of counts made it difficult to obtain a reasonable fit to single lobes, although where possible I fitted the lobes separately. I performed calculations using these fits to test for possible inverse-Compton emission. I used a local background close to the lobes for each source in order to reduce the contribution of external medium as much as possible. For several sources, there were issues which resulted in the exclusion of one of the lobes. 3C 98 S crosses 4 chip boundaries in the X-ray observation, 3C 296 S, 3C 310 N and

Source	kT (keV)	$10^{14}N$ (10^9 cm^{-5})	$n_{\rm p}$ (m^{-3})	P (10^{-13} Pa)	$M(M_\odot)$	S (keV cm^{-2})
3C 35*	$1.28^{+0.41}_{-0.30}$	$2.28^{+1.78}_{-1.20}$	440 ± 190	$2.0^{+1.1}_{-1.0}$	$3.0 \pm 2.0 \times 10^{10}$	$220^{+95.0}_{-82.0}$
3C 76.1	$2.52^{+1.91}_{-1.18}$	$4.02^{+1.45}_{-1.27}$	800 ± 100	$7.2^{+5.6}_{-3.4}$	$5.4 \pm 0.9 \times 10^9$	290^{+230}_{-140}
3C 98	$0.98^{+0.54}_{-0.29}$	$1.99^{+0.67}_{-0.59}$	700^{+70}_{-60}	$2.5^{+1.4}_{-0.8}$	$4.0^{+0.6}_{-0.5} \times 10^9$	120^{+70}_{-40}
3C 192	$1.04^{+0.26}_{-0.15}$	1.13 ± 0.36	1600 ± 250	$5.8^{+1.7}_{-1.3}$	$3.9 \pm 0.6 \times 10^9$	80^{+20}_{-10}
3C 272.1	0.71 ± 0.01	48.4 ± 0.78	62000 ± 4700	160 ± 13	$1.4 \pm 0.2 \times 10^7$	4.5 ± 0.1
3C 285	$0.95^{+0.04}_{-0.04}$	$1.75^{+0.34}_{-0.31}$	1400 ± 100	4.9 ± 0.1	$8.6 \pm 1.1 \times 10^9$	75^{+6}_{-5}
3C 296	0.96 ± 0.04	$8.31^{+0.79}_{-0.88}$	4600^{+220}_{-240}	15.9 ± 1.0	$1.7 \pm 0.1 \times 10^9$	35 ± 2
3C 305	$1.54^{+0.14}_{-0.3}$	$2.52^{+0.29}_{-0.27}$	32000^{+1400}_{-1400}	180^{+20}_{-40}	$2.0 \pm 0.22 \times 10^8$	15 ± 1
3C 310	1.45 ± 0.06	27.3 ± 1.0	5300 ± 600	27.4 ± 2.0	$2.3 \pm 0.3 \times 10^{10}$	50 ± 2
3C 386*	$0.94^{+0.04}_{-0.05}$	$3.83^{+0.63}_{-0.62}$	1250 ± 200	4.1 ± 0.2	$1.6^{+0.4}_{-0.3} \times 10^9$	80 ± 10.0
3C 388	$2.04^{+0.30}_{-0.19}$	20.4 ± 1.4	21000 ± 1600	150^{+25}_{-18}	$1.2 \pm 0.2 \times 10^{10}$	14^{+2}_{-1}
3C 442A	1.06 ± 0.02	50.3 ± 4.9	2800 ± 150	10.7 ± 1.2	$1.9 \pm 0.2 \times 10^{10}$	53 ± 2
4C 73.08	$1.01^{+0.34}_{-0.24}$	3.56 ± 0.97	230 ± 20	$0.84^{+0.29}_{-0.21}$	$7.9 \pm 1.1 \times 10^{10}$	270^{+90}_{-70}
NGC 6109	$0.90^{+0.09}_{-0.12}$	$3.47^{+0.62}_{-0.55}$	13400^{+1300}_{-1200}	$43.4^{+6.1}_{-7.0}$	$3.5 \pm 0.5 \times 10^8$	10^{+1}_{-2}
NGC 7385	$0.94^{+0.07}_{-0.09}$	$4.76^{+0.58}_{-0.54}$	870 ± 50	$29.3^{+3.0}_{-3.3}$	$5.8 \pm 0.7 \times 10^8$	20 ± 2

Table 4.19: Results of fitting APEC models to each source along with the average temperature, density, pressure and mass of the X-ray emission calculated across the extent of each belt. Results for 3C 35 and 3C 386 are taken from Mannering et al. (2013) and Duffy et al. (2016) respectively. Errors are quoted for a 90% confidence range.

Source	kT (keV)	$10^{14}N$ (10^9 cm^{-5})	$n_{\rm p}$ (m^{-3})	P (10^{-13} Pa)	$M(M_\odot)$	S (keV cm^2)
3C 272.1 (inner)	0.65 ± 0.01	30.3 ± 0.6	77000 ± 5800	180 ± 14	$7.1 \pm 1.8 \times 10^6$	3.6 ± 0.1
3C 272.1 (outer)	0.74 ± 0.02	18.5 ± 0.05	50000 ± 11000	133 ± 30	$6.7 \pm 1.7 \times 10^6$	5.5 ± 0.2
3C 296 (inner)	$0.93^{+0.04}_{-0.05}$	$6.69^{+0.70}_{-0.78}$	8300^{+430}_{-480}	$27.7^{+1.8}_{-2.2}$	$7.6 \pm 0.9 \times 10^8$	23^{+1}_{-2}
3C 296 (outer)	$1.22^{+0.29}_{-0.18}$	2.11 ± 0.5	2700 ± 280	$11.8^{+3.1}_{-2.1}$	$7.4 \pm 1.0 \times 10^8$	63^{+15}_{-11}
3C 310 (inner)	1.33 ± 0.04	11.7 ± 0.07	7100 ± 1100	34.1 ± 5.2	$7.2 \pm 1.3 \times 10^9$	36 ± 1
3C 310 (outer)	$1.58^{+0.07}_{-0.08}$	15.4 ± 0.8	4500 ± 500	25.4 ± 3.1	$1.5 \pm 0.2 \times 10^{10}$	58 ± 3
3C 386 (inner)	$0.62^{+0.12}_{-0.10}$	$1.01^{+0.47}_{-0.46}$	1200 ± 100	$2.8^{+0.8}_{-0.9}$	$4.0 \pm 1.0 \times 10^8$	50^{+10}_{-15}
3C 386 (outer)	$1.72^{+0.56}_{-0.36}$	2.22 ± 0.70	1300 ± 100	$8.2^{+2.8}_{-1.8}$	$1.0^{+0.3}_{-0.2} \times 10^9$	130^{+40}_{-30}

Table 4.20: Results of fitting APEC models to each source along with the average temperature, density, pressure and mass of the X-ray emission calculated across the extent of the inner and outer region of each belt. Results for 3C 386 taken from Duffy et al. (2016). Only belts with a detected temperature difference between the inner and outer regions are shown in the table. Errors are quoted for a 90% confidence range.

NGC 7385 N cross chip boundaries and 4C 73.08 E is positioned such that part of the lobe falls off the edge of the detector. These lobes were omitted in fitting. As was the case with the belts, where possible the extracted counts are grouped into bins of 20 in order to use χ^2 as a measure of the goodness of fit. Where this was not possible cstat was used.

Much like the belts, I fitted the lobes and plumes with absorbed power-law, absorbed APEC and APEC + power-law models. In most cases, the best fits are to an absorbed power-law model. Some cases are also well fit to APEC and APEC + power-law models, however for these either the best-fit temperature was unlikely on the basis of the environment of the source or the APEC + power-law models produced an unphysical power-law spectral index. In 3C 272.1 and 3C 305, no power law component could be found, and the lobe emission was best described with an APEC model. No acceptable fit could be found to the lobe emission of 3C 442A. The results from the spectral fitting of the power law component for the lobes are shown in Table 4.21.

a) Physical parameters of the lobes and plumes

The spectra of the X-ray lobes and plumes are generally well described by an absorbed power law. Using parameters measured from the radio emission I estimated the minimum energy magnetic field, $B_{\rm me}$, assuming that all the lobes and plumes in the sample were prolate ellipsoids. I used the radio spectral indices given in Table 4.21 and assumed the electron spectra extends to a minimum Lorentz factor of $\gamma_{\rm min} = 10$. I assume a filling factor of unity, and that the lobes and plumes contain no relativistic protons and have no relativistic bulk motions. The minimum energy pressure, $P_{\rm me}$, is also given in Table 4.22.

The X-ray power law component FRII lobes of 3CRR sources has previously been shown to originate from iC emission (Hardcastle and Worrall, 1999). Combining the radio and X-ray data allows the calculation of the magnetic field, $B_{\rm iC}$, and pressure in the lobes, $P_{\rm iC}$, assuming the X-ray emission from the region (Table 4.21) is produced by the iC mechanism. Sources in which acceptable power-law fits could not be found were excluded. The ratios of $B_{\rm iC}$ to $B_{\rm me}$ are consistent with the range found by Croston et al. (2005) for FRII lobes in most cases. For 3C 388, the X-ray spectral index differed from the radio when allowed to vary. As it is an FRII source, where iC emission is expected to be detected in the lobes, I repeated the fitting with X-ray spectral index fixed at the value of the radio's. The results from this process are also shown in Table 4.22.

[1] `http://3crr.extragalactic.info/`

Source	$\Gamma_{\rm X}$	$\Gamma_{\rm R}$	$S_{\rm 1keV}$ (nJy)	χ^2/dof	Radio frequency (GHz)	Radio flux density (Jy)	VLA programme	Restoring beam (arcsec^2)
3C 76.1	$2.67^{+0.90}_{-0.76}$	1.77	$13.8^{+4.4}_{-4.0}$	cstat	1.46	2.11	AS604	5.3×4.6
3C 98 N	$2.20^{+0.81}_{-0.60}$	1.78	$10.1^{+3.17}_{-2.90}$	20.8/16	1.4	4.87	AR440	4.4×4.3
3C 192 W	$2.07^{+0.50}_{-0.43}$	1.79	$3.01^{+0.70}_{-0.68}$	25.4/30	8.35	0.29	AB534	1.4×1.2
3C 192 E	$2.56^{+0.47}_{-0.42}$	1.79	$4.18^{+0.76}_{-0.77}$	23.9/32	8.35	0.31	AB534	1.4×1.2
3C 272.1 N	-	1.6	-	-	4.86	0.95	AW530A	4.5×4.5
3C 272.1 S	-	1.6	-	-	4.86	0.91	AW530A	4.5×4.5
3C 285 W	$2.70^{+2.62}_{-1.73}$	1.95	$0.8^{+0.6}_{-0.5}$	cstat	4.87	0.31	AV127	1.0×1.0
3C 285 E	$2.25^{+1.12}_{-0.86}$	1.95	$1.7^{+0.7}_{-0.6}$	cstat	4.87	0.38	AV127	1.0×1.0
3C 296 N	-	1.63	-	-	1.48	1.2	AL146	7.3×5.5
3C 305 W	-	1.85	-	-	8.5	0.06	AH982	0.7×0.6
3C 305 E	-	1.85	-	-	8.5	0.08	AH982	0.7×0.6
3C 310 S	1.89 ± 0.16	1.92	26.4 ± 2.4	153.5/169	1.45	2.49	VANB	4.7×4.5
3C 442A W	-	1.96	-	-	1.4	1.34	AC131	8.8×7.7
3C 442A E	-	1.96	-	-	1.4	1.42	AC131	8.8×7.7
3C 388 W	1.7 (fixed)	1.7	16.9 ± 1.5	35.8/23	1.48	2.36	AC149	1.4×1.2
3C 388 E	1.7 (fixed)	1.7	15.1 ± 1.5	29.6/20	1.48	2.67	AC149	1.4×1.2
4C 73.08 W	$2.44^{+0.78}_{-0.68}$	1.85	$20.3^{+5.90}_{-5.93}$	145.6/148	0.33	7.14	AO185	20×17
NGC 6109	$2.47^{+7.51}_{-1.75}$	1.76	$2.8^{+2.7}_{-2.1}$	cstat	4.86	0.15	AH766	15×15
NGC 7385 S	$1.64^{+0.98}_{-0.76}$	1.75	$1.18^{+0.85}_{-0.58}$	cstat	4.99	0.24	BT018	1.4×1.4

Table 4.21: Summary of the power law model fitting to the lobes and plumes of sources with belts in the low-redshift 3CRR sample, along with the radio frequency of the VLA observation and the measured radio flux densities. $\Gamma_{\rm R}$ denotes the radio spectral index between 178 and 750 MHz and are taken from the online 3CRR catalogue[1]. The plumes of 3C 272.1 and 3C 305 are best fit to thermal APEC models, and show no indication of power law components. The plumes of 3C 442A do not fit any tested model. The plumes of 3C 296 do not show significant excess emission once background has been subtracted. The table gives the power-law component only. $\Gamma_{\rm X} = \alpha_{\rm X} + 1$ and $\Gamma_{\rm R} = \alpha_{\rm R} + 1$. The Galactic neutral hydrogen column density is frozen for all fits. Errors are quoted to the 90% confidence range.

Source	$B_{\rm me}$ (10^{-10} T)	$P_{\rm me}$ (10^{-13} Pa)	$B_{\rm iC}$ (10^{-10} T)	$P_{\rm iC}$ (10^{-13} Pa)	$P_{\rm belt}$ (10^{-13} Pa)
3C 35*	1.58 ± 0.04	0.072 ± 0.004	0.87 ± 0.10	$0.12^{+0.03}_{-0.02}$	$2.0^{+1.1}_{-1.0}$
3C 76.1	6.5	1.2	$1.8^{+0.6}_{-0.5}$	$6.1^{+1.9}_{-1.8}$	$7.2^{+5.6}_{-3.4}$
3C 98 N	10.6	3.2	$3.5^{+1.1}_{-1.0}$	$12.4^{+3.9}_{-3.6}$	$2.5^{+1.4}_{-0.8}$
3C 192 W	12.1	4.1	3.5 ± 0.8	20.0 ± 5.0	$5.8^{+1.7}_{-1.3}$
3C 192 E	9.3	2.5	2.8 ± 0.5	22.0 ± 4.0	$5.8^{+1.7}_{-1.3}$
3C 272.1 N	13.1	5.1	-	-	150 ± 12
3C 272.1 S	12.7	4.8	-	-	150 ± 12
3C 285 W	12.9	4.5	$9.3^{+7.0}_{-5.8}$	$5.5^{+4.1}_{-3.4}$	4.9 ± 0.1
3C 285 E	14.6	5.7	$7.1^{+2.9}_{-2.5}$	$12.4^{+5.1}_{-4.4}$	4.9 ± 0.1
3C 296 N	4.1	0.5	-	-	15.9 ± 1.0
3C 305 W	71.6	142	-	-	180^{+20}_{-40}
3C 305 E	73.6	150	-	-	180^{+20}_{-40}
3C 310 S	10.5	3.0	2.2 ± 0.2	31.2 ± 3.1	27.4 ± 2.0
3C386 N*	6.7	1.3	2.7 ± 0.5	3.5 ± 0.7	4.1 ± 0.2
3C 386 S*	6.5	1.2	1.8 ± 0.2	$5.9^{+0.7}_{-0.8}$	4.1 ± 0.2
3C 388 W	19.0	10.0	1.6 ± 0.1	350 ± 20	$150^{+25.0}_{-18.0}$
3C 388 E	20.0	12.0	1.8 ± 0.2	370 ± 40	$150^{+25.0}_{-18.0}$
3C 442A W	7.6	1.5	-	-	10.7 ± 1.2
3C 442A E	7.7	1.6	-	-	10.7 ± 1.2
4C 73.08 W	2.7	0.2	1.2 ± 0.3	0.47 ± 0.14	$0.84^{+0.29}_{-0.21}$
NGC 6109	9.3	2.5	$1.7^{+1.6}_{-1.3}$	$26.2^{+24.7}_{-20.0}$	$43.4^{+6.1}_{-7.0}$
NGC 7385 S	18.7	9.9	$3.3^{+2.4}_{-1.7}$	110^{+80}_{-60}	$29.3^{+3.0}_{-3.3}$

Table 4.22: Physical parameters of the lobes and plumes calculated based on the X-ray emission from the lobes of sources with belts in the low-redshift 3CRR sample. When the lobes are considered on an individual basis (when they are followed by a compass direction), individual lobes in the same source often have different volumes. The results for 3C 35 and 3C 386 are taken from Mannering et al. (2013) and Duffy et al. (2016) respectively.

IC emission is detected in the lobes of each of the FRII sources in the sample. Results are roughly consistent with those found by Isobe et al. (2005) for 3C 98 and Ineson et al. (2017) in all other cases excluding 3C 285. Interestingly, I am able to measure a component of iC emission in several FRI sources: 3C 76.1, 3C 310, 3C 386, NGC 6109 and NGC 7385. Croston et al. (2018) claim that there is a difference between the internal energy conditions in FRI and FRII lobes, which is best explained by the presence of an energetically dominant proton population in the FRI, but not the FRII radio galaxies. I find that the distribution of magnetic field relative to minimum energy (assuming for the latter electrons only) is similar for FRIs and FRIIs. This contradicts the idea that FRI plumes and FRII lobes are composed of physically different plasmas.

4.4.3 Extended group medium

I used the β model and temperature fits obtained in Ineson et al. (2015) to probe the properties of the extended group media of all the sources in the sample, excluding 3C 272.1. Table 5 in Ineson et al. (2015) contains $n_{0.1R_{500}}$, the density of the gas in each source at $0.1R_{500}$. I use this value along with the core radius $r_{\rm cx}$, and the β of the surface brightness profile to calculate the central density, $n_{\rm p0}$, using:

$$n_{\rm p0} = n_{0.1R_{500}} \left(1 + \frac{(0.1R_{500})^2}{r_{\rm cx}^2}\right)^{\frac{3\beta}{2}} \tag{4.3}$$

I then used the obtained central density to calculate the density of the gas at the base of the lobes in each source using:

$$n(r) = n_{\rm p0} \left(1 + \frac{r^2}{r_{\rm cx}^2}\right)^{\frac{-3\beta}{2}} \tag{4.4}$$

Ineson et al. (2015) states that some of the sources in the sample require a two-component β profile to acceptably model the gas in the system, with an inner to model the host galaxy gas and an outer to model the ICM. I assume that at the distances I am interested in, only the parameters from the outer component of the model apply.

To calculate the pressure and entropy index of the outer atmospheres I used the ICM temperatures from Table 6 of Ineson et al. (2015) and the same equations applied to the belts. For 3C 386, I use the model obtained in Chapter 3. For their fits, Ineson et al. (2015) do not consider

Source	β	$r_{\rm cx}$ (kpc)	kT (keV)	$n_{\rm p0}$ (m^{-3})	$n_{\rm p}$(base lobes) (m^{-3})	P(base lobes) (10^{-13} Pa)	S (base lobes) (keV cm^2)
3C 35	1.17 (0.30 - 1.20)	134.53 (2.08 - 384.43)	$0.97^{+0.10}_{-0.20}$	910^{+120}_{-110}	890^{+120}_{-110}	3.1 ± 0.4	110^{+10}_{-20}
3C 76.1	0.46 (0.3 - 1.20)	9.84 (0.82 - 64.56)	$0.80^{+0.07}_{-0.12}$	3400^{+970}_{-780}	3400^{+970}_{-780}	$9.7^{+2.8}_{-2.2}$	36^{+10}_{-8}
3C 98	0.42 (0.3 - 1.20)	1.79 (1.00 - 58.13)	$0.62^{+0.04}_{-0.06}$	$1.6^{+0.83}_{-0.77} \times 10^4$	1800^{+930}_{-870}	$3.9^{+2.0}_{-1.9}$	43^{+22}_{-21}
3C 192	0.41 (0.3 - 0.91)	1.02 (1.00 - 10.63)	$0.80^{+0.07}_{-0.12}$	$5.6^{+1.0}_{-0.6} \times 10^4$	5100^{+870}_{-560}	$14.6^{+2.2}_{-1.3}$	27^{+4}_{-5}
3C 285	0.36 (0.32 - 0.70)	14.63 (5.98 - 82.47)	$0.94^{+0.10}_{-0.22}$	2900^{+200}_{-210}	1900 ± 130	$6.4^{+0.1}_{-1.6}$	61^{+7}_{-14}
3C 296	0.70 (0.3 - 1.20)	188.61 (58.28 - 338.58)	1.59 ± 0.12	540^{+20}_{-19}	540^{+20}_{-19}	3.1 ± 0.2	240 ± 20
3C 305	< 0.47	< 40.39	< 0.65	< 410	< 410	< 1.0	< 120
3C 310	0.50 (0.46 - 0.54)	41.34 (32.67 - 53.09)	$1.92^{+0.12}_{-0.13}$	4700 ± 65	4200 ± 58	$28.7^{+1.9}_{-1.8}$	74 ± 5
3C 386*	$1.2^{+\rm unknown}_{-0.8}$	91^{+56}_{-82}	1.4 (fixed)	-	-	$3.0^{+13.0}_{-1.3}$	$200.0^{+600.0}_{-50.0}$
3C 388	0.52 (0.49 - 0.56)	40.39 (31.04 - 52.38)	$3.52^{+0.18}_{-0.15}$	9700^{+100}_{-90}	9500 ± 94	$120.0^{+5.1}_{-6.1}$	78^{+4}_{-3}
3C 442A	1.11 (0.58 - 1.20)	212.86 (101.64 - 251.01)	$1.58^{+0.11}_{-0.17}$	740 ± 20	720 ± 20	$4.1^{+0.3}_{-0.5}$	200^{+14}_{-20}
4C 73.08	0.42 (0.31 - 1.20)	1.01 (1.00 - 68.33)	$1.37^{+0.26}_{-0.18}$	$3.7^{+2.2}_{-1.3} \times 10^4$	1100^{+650}_{-390}	$5.4^{+3.2}_{-1.9}$	130^{+77}_{-46}
NGC 6109	1.20 (0.30 - 1.20)	167.46 (24.80 - 579.03)	$0.91^{+0.11}_{-0.24}$	640 ± 45	640 ± 45	$2.1^{+0.3}_{-0.6}$	120^{+16}_{-33}
NGC 7385	< 0.47	< 40.89	< 0.61	< 520	< 510	< 1.1	< 95.3

Table 4.23: Table detailing the results of fitting β-profiles to the ICM of galaxies with belts from Ineson et al. (2015) along with extrapolations of density, pressure and entropy index at the base of the lobes in each of these sources. Results for 3C 386 taken from Duffy et al. (2016).

the existence of the gas belts, although their modelling of inner components in some of these profiles may mitigate this. In cases without an inner component, such as 3C 192 and 3C 386, this may result in biases in these fits as the gas belt is included as ambient medium, reducing the core radius in particular. For example, fitting only the ambient medium outside the belt emission, I find $r_{\rm cx} = 91.0^{+56.0}_{-41.0}$ kpc for 3C 386, whereas Ineson et al. (2015) finds $r_{\rm cx} = 1.01^{+3.16}_{-0.01}$ kpc. Results for the external gas are shown in Table 4.23.

For 3C 272.1, which is not included in the sample from Ineson et al. (2015), I measured the physical parameters of the extended medium using a similar method to that applied to the belts (Section b)). Taken from Worrall et al. (2012), the equation to calculate the density in terms of observables for the extended media is

$$\begin{aligned}(n_{\rm p}/{\rm m}^{-3}) &= 8.5 \times 10^8 (1+z)^2 \sqrt{\frac{(N/{\rm cm}^{-5})}{f(D_L/{\rm Mpc})}} \\ &\quad \times \left[\left(\theta_{\rm t}^2 - \theta_1^2\right)^{3/2} - \left(\theta_{\rm t}^2 - \theta_2^2\right)^{3/2} \right]^{-1/2} \end{aligned} \tag{4.5}$$

where f is the fraction of a circle in degrees (for a $250^{\rm o}$ arc $f = 250/360$), θ_1 and θ_2 correspond to the inner and outer radii of the annulus in arcseconds and θ_t is the true radius of the emission centred on the nucleus. I adopt $\theta_t = \theta_2$ as the extended emission is often extremely faint beyond this radius. This assumes uniform density of the gas in the region between θ_1 and θ_2.

Model parameter	3C 272.1 Group gas
kT (keV)	0.81 ± 0.03
N (cm^{-5})	$7.94 \pm 0.35 \times 10^{-6}$
χ^2/dof	781.5/442
$n_{\rm p}$ (m^{-3})	$1.1 \pm 0.3 \times 10^{5}$
$P(10^{-13}$ Pa)	320 ± 90
S (keV cm^2)	3.5 ± 0.7

Table 4.24: Summary of the APEC fitting to the group gas surrounding 3C 272.1. The Galactic neutral hydrogen column density is frozen for all fits. Metallicity is fixed at 0.3 $Z_{\odot}$. Errors are quoted for a 90% confidence range.

The spectrum of the galaxy atmosphere near 3C 272.1 was extracted from an annulus between 40 and 65 arcseconds from the core. The lobes and any additional point sources within the annulus were excluded from the spectral extraction. Before performing the spectral fit, counts were subtracted from a local background. The galaxy medium of 3C 272.1 is reasonably well fit to an APEC model. The results from this process are given in Table 4.24.

4.5 Discussion

4.5.1 Pressures

The pressures in the various parts of a radio source and its environment provide some insight to its dynamical situation. Through use of the β-profiles and spectroscopy, I have calculated the pressures in the gas belts, external media and the lobes of each of the sources in the sample. In the following section I test how the gas belt pressure compares to the pressure in the external medium and the pressure in the lobes. I am confident based on Figure 4.8, where the lowest and highest redshift sources are found near each other, that there is no redshift bias in the conclusion.

Figure 4.8 shows the pressure of the ambient medium of each source plotted against the pressure contained within the belt, along with a line showing where $P_{\rm env} = P_{\rm belt}$. $P_{\rm env}$ are the pressures calculated for the external medium at the base of the lobes (Table 4.23). Sources above the line have higher environmental pressures than belt pressures, while sources below the line show the opposite. In the majority of cases the gas belt and environment are in approximate pressure balance. Given the geometric uncertainties, it is reasonable to assume that in the majority of cases, the belts are in pressure balance with their external environments.

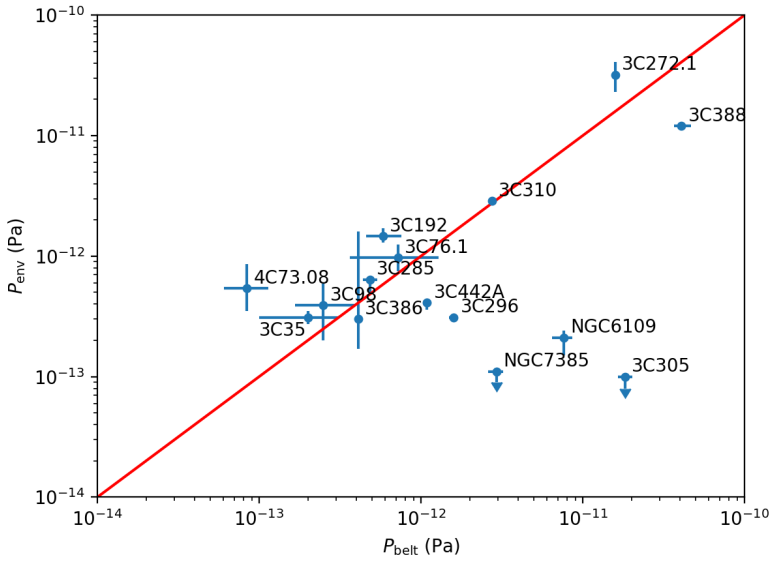

Figure 4.8: Pressure of the ambient medium against the pressure of the gas belt. The red line indicates where the environment and the gas belt would be in pressure balance.

The gas belts in NGC 6109, NGC 7385 and 3C 305 are significantly overpressured in comparison to their environments. This may suggest that the belt gas is a result of gas expanding outwards from the centre of the sources. However, it is also possible that the parameters used to model the external medium from Ineson et al. (2015) are causing an underestimate of the pressure in the environment. In 3C 305, the X-ray gas in the lobes was found to be thermal, and could provide the additional pressure required to contain the belt. The pressure contained within the gas in the eastern lobe is $440 \pm 40 \times 10^{-13}$ Pa, within a factor of two of the belt pressure. This is likely in pressure balance with the belt, once geometric uncertainties are included. NGC 7385 lies in a poor cluster (Zwicky 2247.3+1107) and NGC 6109 resides in a poor group at the edge of a cluster. These clusters could potentially provide the additional pressure required to contain the belts, but do not seem to be included in the modelling of Ineson et al. (2015).

Figure 4.9 shows the minimum energy pressure in the lobes versus the pressure contained in the gas belt, along with a line showing where $P_{\rm me} = P_{\rm belt}$. In the majority of cases the belt is overpressured compared to the minimum energy pressure of the lobes: the typical overpressure is by a factor of ~ 10.

Figure 4.10 shows the pressure calculated from iC X-rays in the lobes against the pressure

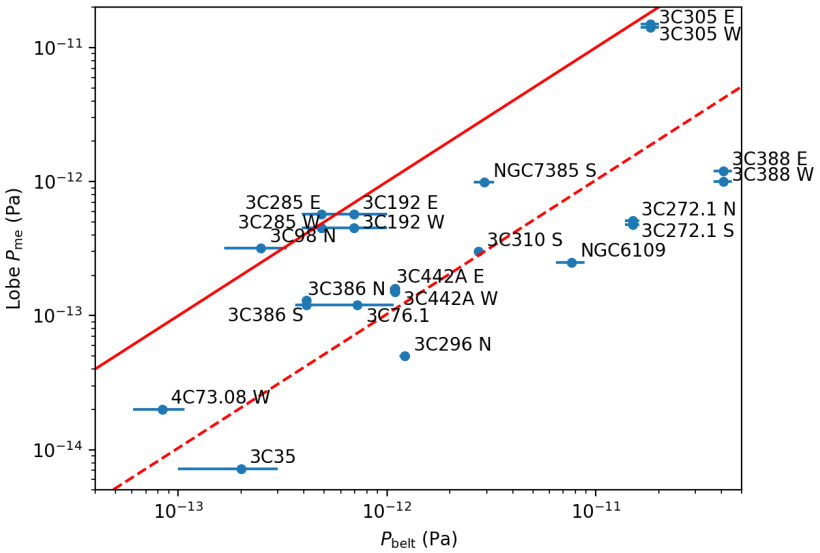

Figure 4.9: Minimum energy pressure of the lobes versus the pressure in the gas belt. The red line indicates where the minimum energy pressure of the lobes and the gas belt would be in pressure balance. The dashed red line indicates where the belt pressure is ten times that of the minimum lobes pressures. The majority of the sources are clustered here.

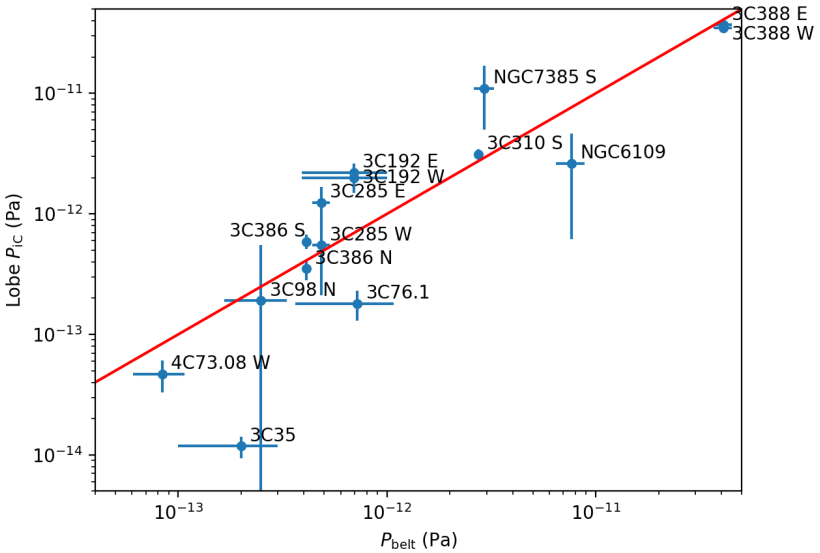

Figure 4.10: Pressure from iC X-rays of the lobes versus the pressure in the gas belt. The red line indicates where the IC pressure of the lobes and the gas belt would be in pressure balance.

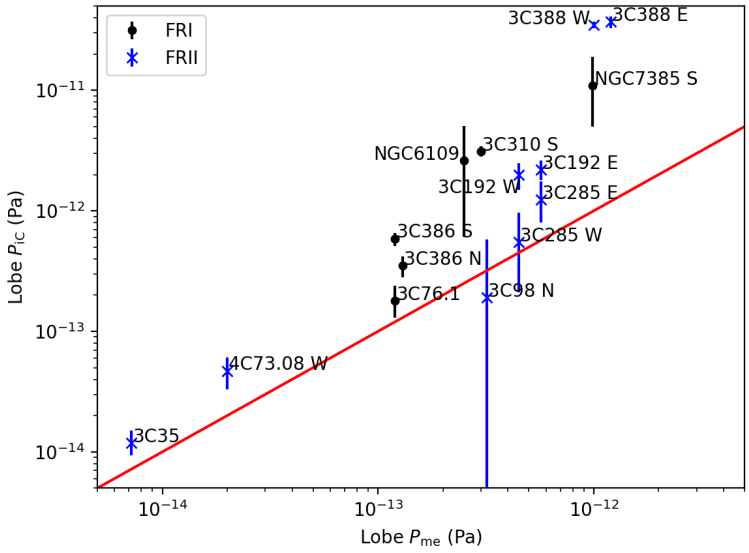

Figure 4.11: Pressure from iC X-rays of the lobes versus the minimum energy pressure of the lobes. The red line indicates where the pressures would be equal. FR I sources are shown by black circles, with FR II sources shown with blue crosses.

contained in the gas belt, along with a line showing where $P_{\rm iC} = P_{\rm belt}$. For sources below the line, a belt is overpressured in comparison to the radio lobes. In almost all cases, the lobes are in approximate pressure balance with the gas belt. This excludes 3C 35, where the gas belt is significantly overpressured compared to the lobe pressure as also noted by Mannering et al. (2013).

Figure 4.11 shows pressure from iC X-rays in the lobes against the minimum energy pressure in the lobes. The pressure from iC X-rays is found to be roughly one order of magnitude larger than the minimum energy pressures, as has been seen in previous studies of FR II lobes (Croston et al., 2005; Ineson et al., 2017). For the first time this also shown to be the case for a sample for FR Is.

4.5.2 Entropy Index

The measured entropies give context to the thermal history of the gas in the belts and also the surrounding external medium.

Figure 4.12 shows the entropy index in the external environment plotted against the average entropy index of the gas belt. The graphs shows a wide range of belt entropies, in comparison

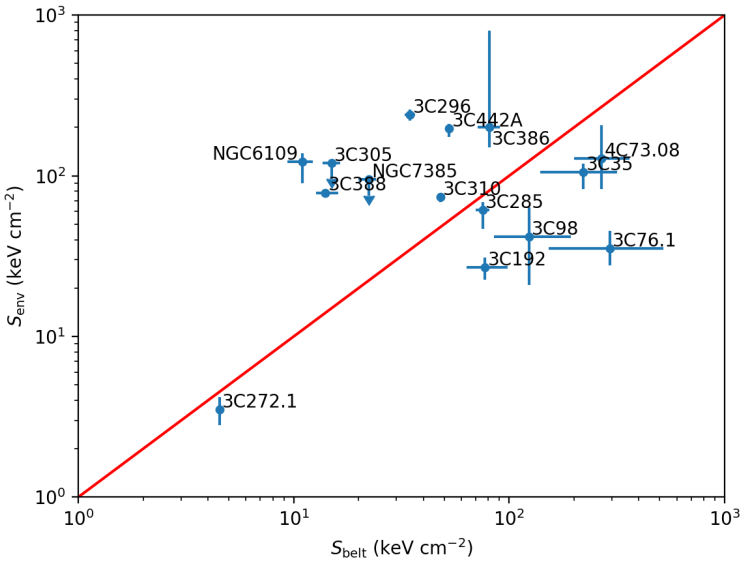

Figure 4.12: Entropy index of the external medium against the entropy index of the belt. The red line indicates where the entropies are equal.

to a relatively narrow range of environmental entropies. For 3C 272.1 and 3C 285, the entropies within the gas belt and the external medium are approximately equal. This suggests that the material in the gas belt may originate from the same gas which composes the atmosphere. In the case of 3C 272.1 this would be galaxy gas, due to the small linear scales involved. In 3C 285, this may suggest gas stripped from the galaxies which coalesced to form the host galaxy of the radio source as discussed by Hardcastle et al. (2007) for this source. The very low entropy in the belt of 3C 272.1 could also result from radiative loss however, as the gas has a cooling time of around 10^8 years.

The entropy index in the belts is slightly higher than that of the environments in 3C 35, 4C 73.08, 3C 98, 3C 192, and the entropy index in the belt of 3C 76.1 is about an order of magnitude higher than in the external environment. It is these sources in which the radio source is more likely to have had an effect on the gas.

The entropy index in the environment is higher than in the belt in 3C 272.1, 3C 296, 3C 310, 3C 386, 3C 388, 3C 442A and NGC 6109. This makes sense in 3C 388 which resides in a dense, disturbed cluster environment. This grouping of sources also contains belts formed from galaxies undergoing an active merger, such as 3C 310 and 3C 442A. These sources have lower entropies

than their environments as galaxy gas is usually cooler and denser than the surrounding ambient medium. The belt gas in 3C 272.1, 3C 296 and NGC 6109 is likely also to have a galactic origin, but from within the host galaxies alone. Curiously, 3C 386 also lies in this group, despite its gas belt originating at least partially from inflow. The gas which forms the inner belt of 3C 386 is so much cooler than the outer belt, that it brings the average entropy of the belt into this section of the graph. This could be true for other sources with multiple temperature components.

Despite these groupings, it is also possible that there is no obvious relation between the entropy index of the belt and its environment. The entropy is mostly defined by the large-scale properties of the group, with some variable amount of modification by the radio source. Therefore, over several duty cycles, the sources would likely move across the parameter space of the figure. Some of the belts could have radiated heat away, while others could still be forming.

4.5.3 Masses and Environments

The gas belt in 3C 98 has a gas mass of $4.0^{+0.6}_{-0.5} \times 10^9 M_\odot$ (Table 4.19). Previous studies of its environment have suggested that it is an isolated elliptical galaxy (Prestage and Peacock, 1988; Miller et al., 1999), or is accompanied by a smaller elliptical galaxy (Floyd et al., 2008). The K-band luminosity from 2MASS of 3C 98 is $L_K \sim 2.2 \times 10^{10} M_\odot$. Using the correlations of Su et al. (2015), this corresponds to an X-ray gas mass of $\sim 8.5 \times 10^6 M_\odot$, far less than is calculated to be within the gas belt. It is possible that this is fossil group gas given the relative lack of galaxies in the field of 3C 98. 3C 76.1 also has an isolated environment (Sandage, 1972), along with a weak X-ray environment (Croston et al., 2008b). Its mass also exceeds that likely to originate from within the galaxy, although it lacks a K-band magnitude measurement to check this against. Its relative isolation and fairly large mass also suggest that this may be fossil group gas. The entropies of the belts in these sources are also fairly similar, with the belt entropy higher than the environment's, as is the case for 3C 35 which was previously interpreted as fossil group gas (Mannering et al., 2013).

Hubble data (Kraft et al., 2012) shows the presence of three interacting galaxies near the host galaxy of 3C 310. The temperature in both subregions of the belt is lower than the surrounding medium, suggesting that the gas originates from cooler galaxy gas stripped during the ongoing interaction. The temperature structure seen in the belt suggests that the outer gas has begun to mix slightly with the hotter ambient medium.

Chen et al. (2012) and Strom et al. (2013) identified that 4C 73.08 is a member of a group

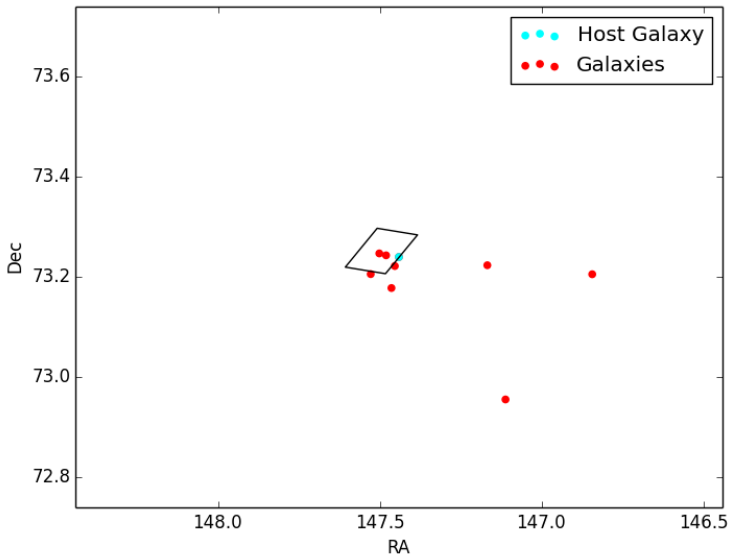

Figure 4.13: The environment of 4C 73.08 in the region of its gas belt. The gas belt is outlined in black, with the host galaxy marked in cyan and confirmed group members from Chen et al. (2012) shown in red.

of nine galaxies, three of which lie within the boundaries of the gas belt, with another two close to the boundary, as can be seen in Figure 4.13. 3C 192 has an elliptical host (Cheung, 2007) and resides in a small group of galaxies (Sandage, 1972; Prestage and Peacock, 1988), in which it is the brightest. Both their masses exceed what is expected from the host galaxy alone. Two of these galaxies appear within the selected boundaries of the gas belt. *HST* data for both 3C 192 (Chiaberge et al., 2000) and 4C 73.08 show no evidence of a current active merger in either of the systems. It is possible that the belts in these sources are formed of gas stripped from old merging galaxies. 3C 442A has a similar sort of belt with an active merger ongoing, showing interaction with the radio lobes. 3C 285 may be an older example of this type of source, wherein the gas belt formed prior to the beginning of radio activity and was able to influence the formation of the lobes, which would preferentially expand into the lower density group medium. Hogbom (1979) estimate the age of 3C 192 to be $\lesssim 10$ Gyr, so a similar scenario could be present here, causing the radio surface brightness deficit coincident with the belt.

The 2MASS K-band luminosities and the correlations of Su et al. (2015) show that the 3C 272.1 and NGC 6109 belts have gas masses which could potentially be sourced from within

their own galaxies. I assume the same for NGC 7385 given its similarities to NGC 6109. Morphologically, these belts differ significantly, with NGC 6109 and NGC 7385 appearing relatively flat and disk-like, while 3C 272.1's belt is more 'H' shaped and traces the edges of the radio lobes. NGC 7385 resides within a group which presents as a poor cluster (White et al., 1999), 3C 272.1 resides in the atmosphere of the Virgo cluster and NGC 6109 resides within a poor group within a supercluster. NGC 6109 and NGC 7385 are significantly overpressured when compared to their ambient medium, although are in pressure balance with the lobes. Their small scale, mass and low entropies in the belt argue for a galactic origin for the gas in these sources. The typical X-ray gas mass of galactic coronae is between $10^{6.5} - 10^{8}\,M_{\odot}$ for coronae of radius 1.5–4 kpc, with some of the most massive found to be $\approx 10^{9}\,M_{\odot}$ (Sun et al., 2007). Coronae have also been seen to have been disrupted into belt-like shapes by the expansion of the radio lobes (O'Sullivan et al., 2011). The temperatures of NGC 6109 and NGC 7385 are also expected for galactic coronae. It is therefore possible that the gas belts in these objects are disrupted galactic coronae.

The host galaxy of the radio source in 3C 296 is NGC 5532, a large elliptical galaxy. Optical observations of the galaxy with radio contours overlaid, show that the dimensions of the galaxy itself could account for what is interpreted as gas belt emission, although the galaxy is oriented peculiarly with respect to its radio source. Additionally, previous work by Hardcastle et al. (2005) and Croston et al. (2008b) show galaxy gas is detected up to 60 arcsec from the source, suggesting that the belt in this source is likely of galactic origin.

3C 305 is described in Jackson et al. (2003) and Floyd et al. (2008) as a merger remnant. Using the 2MASS K-band luminosity for IC 1065, the host of 3C 305, and the correlations of (Su et al., 2015) shows an expected X-ray gas mass of $\sim 4.5 \times 10^{7} M_{\odot}$. Given the large errors associated with the assumed geometry it is possible for this amount of mass to originate within the host galaxy.

For 3C 388, the gas mass is larger than could be provided from the host galaxy alone, which makes sense given its position in a dense cluster. The local galaxy environment for 3C 388 is dense, comparable to that of the Abell cluster (Prestage and Peacock, 1988).

a) Cooling Time and Age of the Radio Source

Figure 4.14 compares the cooling time in the belt gas with the radio source age. The cooling times are estimated based on the cooling curves calculated by Worrall and Birkinshaw (2006,

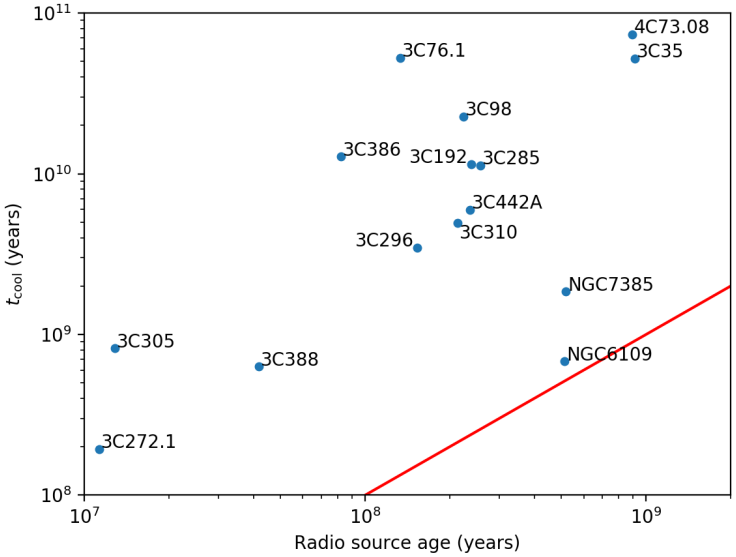

Figure 4.14: Cooling time of the gas belt against radio source age. The red line indicates where the cooling time is equal to the age of the radio source.

their Figure 5), and the radio source age is inferred from half the LLS scales (see Table 4.2) divided by the sound speed of the gas in the external medium.

If the cooling time in the belt is long compared to the radio source age, then it suggests that the belt is not responsible for fuelling the radio source, as the belt gas has not cooled fast enough to fuel the AGN. If the radio source age is long compared to the cooling time of the belt however, it implies a direct feedback process. Figure 4.14 shows that in all cases the cooling time of the belt gas is longer than age of the radio source.

4.5.4 Inflow and Outflow

One way to test inflowing and outflowing gas models is finding the temperature structure in the gas belts. Gas belts which exhibit hotter outer belts, close to the temperature of the external medium, with cooler inner belts are indicative of an inflow model. Gas which has flowed outwards from the centre of the host galaxy would typically exhibit a roughly constant temperature, with the entire structure cooler than the surrounding external medium.

The sources studied in this sample all exhibit hotter outer belts than inner belts, where measuring a temperature structure is possible. In 3C 272.1 the inner and outer belt temperatures are

similar, and are far cooler than the surrounding Virgo cluster atmosphere, which has an average of temperature of ~ 2.3 keV (Urban et al., 2011). This supports an outflow interpretation, as has already been suggested in Finoguenov et al. (2008).

3C 310 exhibits a similar temperature structure to 3C 272.1, with the temperature in the external medium hotter than the outer belt, which itself is hotter than the inner belt. Three galaxies within the gas belt are currently undergoing an active merger (Kraft et al., 2012), with the belt formed of this gas. This material is outflowing from these galaxies during the mergers.

The temperature in the outer belt of 3C 296 is hotter than its inner belt, but is equal within errors to the temperature of the external medium. This is more likely to indicate an inflow model, although the pressure structure of 3C 296, where the pressure in the external medium is lower by an order of magnitude, argues against this. Equally, the belt in 3C 296 aligns well with previous detections of galaxy gas (Hardcastle et al., 2005; Croston et al., 2008b), which suggests the gas could also be stagnant. The pressure in 3C 388 suggests outflow, although there will be significant mixing with the surrounding dense ICM.

3C 98 and 3C 76.1 may result from the outflowing of fossil group gas driven outwards by the expanding radio lobes, much like 3C 35 (Mannering et al., 2013), although the belt pressure being equal to the environmental pressure argues against this, as higher belt pressures would be expected. If it is assumed that the mass of X-ray gas is being ejected away from the central galaxy, then to overcome an escape velocity of 300 km s^{-1} (the average central velocity dispersion for fossil groups (Eigenthaler and Zeilinger, 2013)), the 3C 98 and 3C 76.1 gas belts must each be given a kinetic energy of $\sim 10^{52}$ J. Estimating the total energy from the current episode of radio activity as $4PV$, where P is the pressure in the lobes from the X-ray data and V is the total lobe volume, shows that they can easily provide enough energy to lift the belt gas in both systems. It is, however, difficult to confirm the presence of an outflow without measurement of the temperature structure within the belts.

4.5.5 Summary and Conclusions

15 of the 35 radio galaxies in the low-redshift 3CRR sample exhibit an excess of X-ray emitting counts between the lobes but away from the active nucleus, which are not likely to be normal undistorted group or galaxy atmospheres. This shows that belts of this nature are a common feature of radio galaxies, at least among low-redshift sources.

There is no single origin for the belts, with evidence of inflow driven by the lobes, outflow

driven by the AGN and mergers and stagnant gas seen amongst the sources in the sample.

In each of these sources, the belts are in approximate pressure balance with the pressure calculated from inverse-Compton X-rays in the lobes. The majority of sources are also seen to be in rough pressure balance with their surrounding external medium.

I find that the amount by which magnetic field strength tends to be lower than the minimum energy value is similar for FR I and FR II sources, if minimum energy is calculated assuming no protons. Since FR Is in clusters are known to need protons for pressure support with the external medium, the results provide the first evidence that magnetic field strengths are largely oblivious to non-radiating particles in radio galaxy plumes and lobes.

5

The X-ray ribs within the cocoon shock of Cygnus A

In this chapter I investigate the non-axisymmetric gas around the core of the powerful FRII radio galaxy Cygnus A. This gas aligns similarly to the belts seen in the 3CRR sources in previous chapters. This chapter has been published and is largely reproduced from Duffy et al. (2018).

5.1 Introduction

Cygnus A is the best known and nearest example of a powerful FRII radio galaxy. The galaxy which hosts Cygnus A is also the dominant galaxy of a 6 keV cluster with mass within 500 kpc in excess of $\sim 2 \times 10^{14} M_{\odot}$ (Arnaud et al., 1984; Smith et al., 2002). The proximity and power of Cygnus A allows in-depth study of interactions between the expanding radio lobes of Cygnus A and the surrounding X-ray gas.

The host galaxy of Cygnus A resides within an elliptical cocoon shock, which extends about 60 arcsec (65 kpc) from north to south of the AGN and about 120 arcsec (130 kpc) from west to east (Nulsen et al., 2015; Snios et al., 2018). Within the projected extent of the cocoon shock, surrounding the radio core, lies a region of enhanced X-ray emission with a complex rib-like structure. Previous studies of this have revealed it to be thermal emission from gas with

an average temperature of about 4 keV (Smith et al., 2002; Wilson et al., 2006). The X-ray emitting ribs lie predominantly between the high-frequency radio lobes, their long axes mostly perpendicular to the radio axis of Cygnus A. I call this structure 'rib-like' as its appearance suggests a hollow structure, with the filaments lying in the surrounding envelope, so that they are seen projected on to the core from in front or behind, rather than lying within it. It is conceivable that the origin of the gas may be similar to that of belt-like emission seen in other local radio galaxies (Worrall et al., 2007; Hardcastle et al., 2007; Mannering et al., 2013; Duffy et al., 2016), and enhanced central gas distributions showing interactions with the base of the lobes are a common feature of numerical models of radio galaxies (Hardcastle and Krause, 2013, 2014).

Despite spectral studies of the gas, no firm conclusions have been drawn as to its origin. One possibility suggested by Smith et al. (2002) is that the rib-like structure represents a large-scale accretion disk with gas flowing into the Cygnus A nucleus. Alternatively, Mathews and Guo (2010) suggest that the X-ray emission may be the expanded remnant of denser gas formerly located near the centre of Cygnus A, which has been shocked and heated by the AGN during the early stages of FRII development.

Using archival and new *Chandra* data, totalling over 1.9 Ms of observation, I investigate the physical properties of the gas interior to the cocoon shock of Cygnus A, specifically focussing on the rib-like structure which surrounds the core.

5.2 Chandra Observations

Cygnus A has been observed numerous times using *Chandra's* Advanced CCD Imaging Spectrometer (ACIS), with the source centred on either the S3 or I3 chip, mostly as part of the Chandra Visionary Project (Wise et al., prep). I opted to include only observations where Cygnus A is centred on the I3 chip, as these form the vast majority of observations. I did not include any observations where Cygnus A's northwest subcluster was the target, or ObsIDs 17145 and 17505 where the PSF near Cygnus A's core is very broad. A list of the *Chandra* observations used in the present work is given in Table 5.1.

The data were reprocessed using CHANDRA_REPRO from CIAO 4.8 or 4.9 with CALDB 4.7.2 or 4.7.4 (later versions used for 2017 observations) and were then cleaned using the routine DEFLARE in its *lc_clean* mode to remove the small contribution from background flaring, with

ObsID	Date	t_{exp}	ObsID	Date	t_{exp}
05830	2005-05-26	23.5	17518	2016-07-16	49.4
05831	2005-02-16	51.1	17519	2016-12-19	29.7
06225	2005-02-15	24.3	17520	2016-12-06	26.8
06226	2005-02-19	23.8	17521	2016-07-20	24.7
06228	2005-02-25	16.0	17522	2017-04-08	49.4
06229	2005-02-23	22.8	17523	2016-08-31	49.4
06250	2005-02-21	7.0	17524	2015-09-08	23.0
06252	2005-09-07	29.7	17525	2017-04-22	24.7
17133	2016-06-18	30.2	17526	2015-09-20	49.4
17134	2017-05-20	29.4	17527	2015-10-11	26.7
17135	2017-01-20	19.8	17528	2015-08-30	49.3
17136	2017-01-26	22.2	17529	2016-12-15	35.1
17137	2017-03-29	25.2	17530	2015-04-19	21.3
17138	2016-07-25	26.4	17650	2015-04-22	28.2
17139	2016-09-16	39.5	17710	2015-08-07	19.8
17140	2016-10-02	34.6	18441	2015-09-14	24.6
17141	2015-08-01	29.7	18641	2015-10-15	22.4
17142	2017-04-20	23.3	18682	2015-10-14	22.8
17143	2015-09-04	27.1	18683	2015-10-18	14.1
17144	2015-05-03	49.4	18688	2015-11-01	34.6
17507	2016-11-12	32.6	18871	2016-06-13	21.8
17508	2015-10-28	14.8	18886	2016-07-23	21.7
17509	2016-07-10	51.4	19888	2016-10-01	19.5
17510	2016-06-26	37.5	19956	2016-12-10	54.3
17511	2017-05-11	15.9	19989	2017-02-12	41.5
17512	2016-09-25	66.8	19996	2017-01-28	28.9
17513	2016-08-15	49.4	20043	2017-03-25	29.6
17514	2016-12-13	49.4	20044	2017-03-27	14.8
17515	2017-03-22	39.5	20048	2017-05-19	22.8
17516	2016-08-18	49.0	20077	2017-05-13	27.7
17517	2016-09-17	26.7	20079	2017-05-21	23.8
				Total:	1919.8 ks

Table 5.1: List of *Chandra* observations used in this work, with observation identification number, start date of the observation and net exposure time after background flare corrections, t_{exp}, in ks.

applied GTIs removing no more than 1 ks of exposure time in any observation. To account for astrometric errors ObsID 5831 was chosen as a reference due to its high total counts. Following Snios et al. (2018), 0.5 - 7.0 keV images in 0.492-arcsec pixels were made of a region 160 arcsec by 120 arcsec centred on Cygnus A, with the events from other ObsIDs reprojected into the same sky frame as ObsID 5831. The cross correlations between each ObsID's image and the image from ObsID 5831 were then fitted with a Lorentzian profile to determine the offsets between them. These offsets of order 0.5 arcsec or less constitute the astrometric shifts required to align the data sets with ObsID 5831. The offsets were applied to the event and aspect solution files using the WCS_UPDATE command in CIAO. Aligned exposure corrected images were then merged together using MERGE_OBS for image analysis.

5.3 X-ray Morphology

Figure 5.1 shows an exposure-corrected image made using all the observations listed in Table 5.1. The edges of the cocoon shock are clearly visible at the lower brightness limit of the scale selected, as well as hotspots at the extremities of the lobes. Visible in both lobes is a broad X-ray jet-like feature, which is roughly aligned with the radio jet axis close to the AGN, but becomes misaligned in the outer part of the jet (Steenbrugge et al., 2008). The bright eastern X-ray jet-like feature can be seen extending almost the full length towards the eastern hot spots, while the western X-ray jet-like feature can only be seen extending roughly half way along the length of the western lobe in this particular image. The core can be seen between the lobes at the centre of the bright rib-like emission. The ribs occupy a region between high-brightness parts of the radio lobes, although radio emission extends across the centre of the lobes and down to the south of the ribs and is more uniform at lower radio frequencies. There is no obvious relation between the X-ray brightness enhancements associated with the ribs and the radio emission. The brightest part of the X-ray rib structure is seen extending immediately to the south of the core, with another bright filament to the west of this at the boundary of the ribs. The north-south axis of the ribs measures roughly 42 arcsec (45 kpc) in length, while the east-west axis measures roughly 29 arcsec (32 kpc). To the south of the brightest rib structure and contours on Figure 5.1 is a roughly elliptical region of low surface brightness representing the cavity previously studied by Chon et al. (2012).

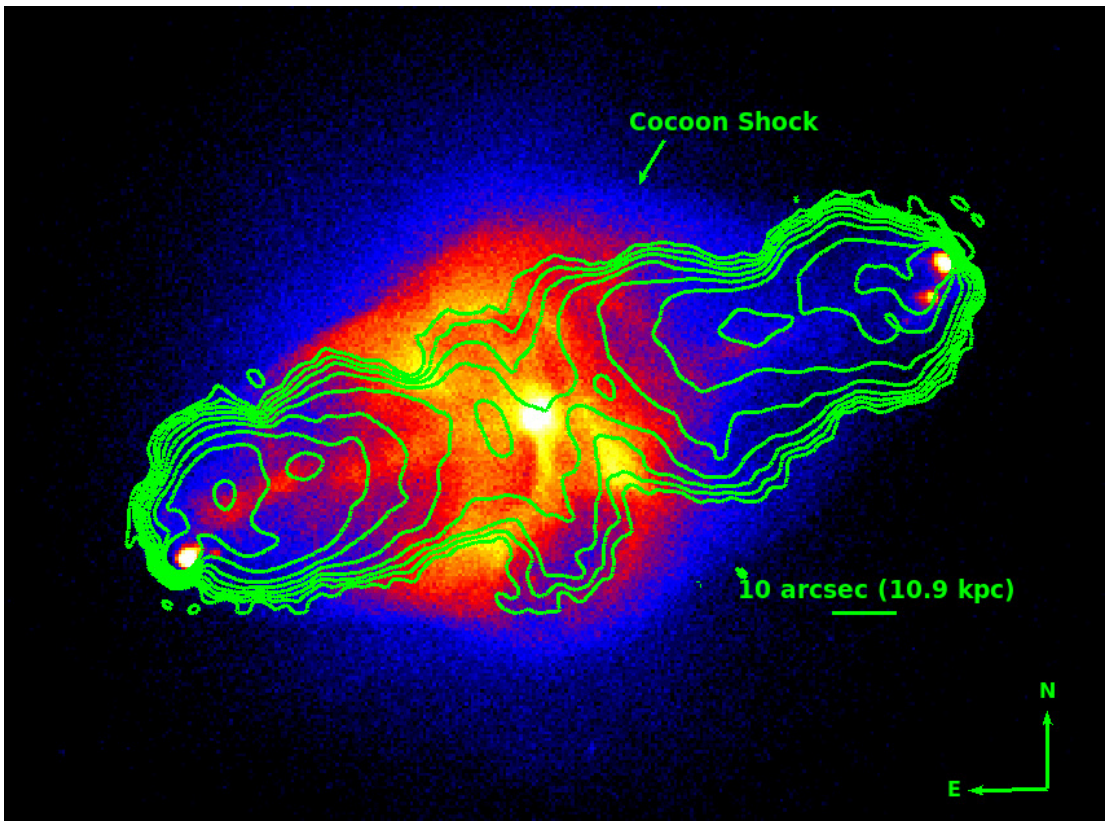

Figure 5.1: Merged *Chandra* exposure-corrected 0.5-7.0 keV image of Cygnus A observations listed in Table 5.1. with native 0.492 arcsec pixels. Contours are of a 327 MHz VLA radio map with restoring beam of size 2.75 arcsec from program AK570, and are shown at brightness levels of $1.434\times(0.2, 0.5, 1.0, 2.0, 5.0, 7.5, 15, 20, 25)$ Jy beam^{-1}.

5.3.1 Unsharp Mask Images

The merged X-ray image was used to create unsharp mask images of Cygnus A. Firstly the image was binned into soft (0.5 - 2.0 keV) and hard (2.0 - 7.0 keV) energy bands. The core to a radius of 3 arcsec and the hotspots were excised. The hard and soft images were then smoothed on two different length scales and these images were subtracted to produce the unsharp mask images. Figure 5.2 shows the result after using Gaussian smoothings of 2 arcsec and 10 arcsec.

In both panels of Figure 5.2 the rib structure is clearly visible. The rib to the south is unusual in that it appears to terminate at the AGN, unlike any of the others, although this is possibly an effect of projection. There appear to be several holes, corresponding to regions of low surface brightness, not only visible within the rib structure, but also extending beyond the position where the south rib bends. The unsharp mask images also clearly show X-ray jet-like features of Cygnus A to both the east and the west.

5.4 Spectroscopy

5.4.1 Region Selection

The structure of the X-ray emission from the region lying between the bright radio lobes is complex and clearly inhomogeneous. I first divided it into related regions for spectral analysis by applying the CONTBIN 1.4 software (Sanders, 2006) on the merged data. CONTBIN employs an algorithm for spatially binning X-ray data using contours on an adaptively smoothed map and defining regions of matched signal-to-noise ratio (SNR). The regions closely match the surface brightness structure, allowing one to examine whether different populations of gas are found in different ribs of Cygnus A.

I tested CONTBIN with several different settings, before settling on a SNR of 200 after the image had been adaptively smoothed with a SNR of 15. The resulting regions aligned well with the surface brightness features identifiable by eye. The region within 5 arcsec of the AGN and a broad rectangular region around the eastern jet-like emission were excluded from all analysis. No background was used in defining the regions, as the features I am studying are much brighter than their surroundings. CONTBIN identified 28 regions across a 60 arcsec by 63 arcsec field.

Whilst the CONTBIN regions were interesting in helping us to define appropriately sized and located regions for selection, this selection misses several potentially interesting structures.

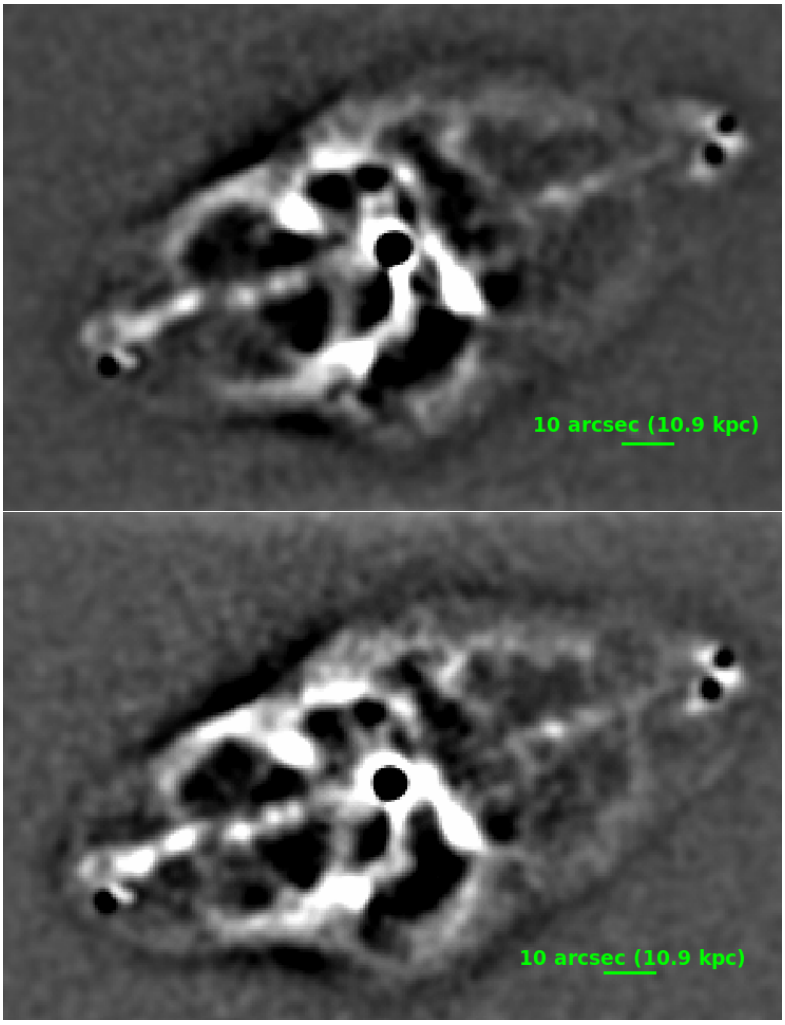

Figure 5.2: *Top:* Unsharp mask image made from the soft 0.5-2.0 keV band by subtracting an image smoothed with a Gaussian dispersion of 10 arcsec from one smoothed by 2 arcsec. *Bottom:* Unsharp mask image made from the hard 2.0-7.0 keV band by subtracting an image smoothed with a Gaussian dispersion of 10 arcsec from one smoothed by 2 arcsec. Black circular regions correspond to excised core and hotspots.

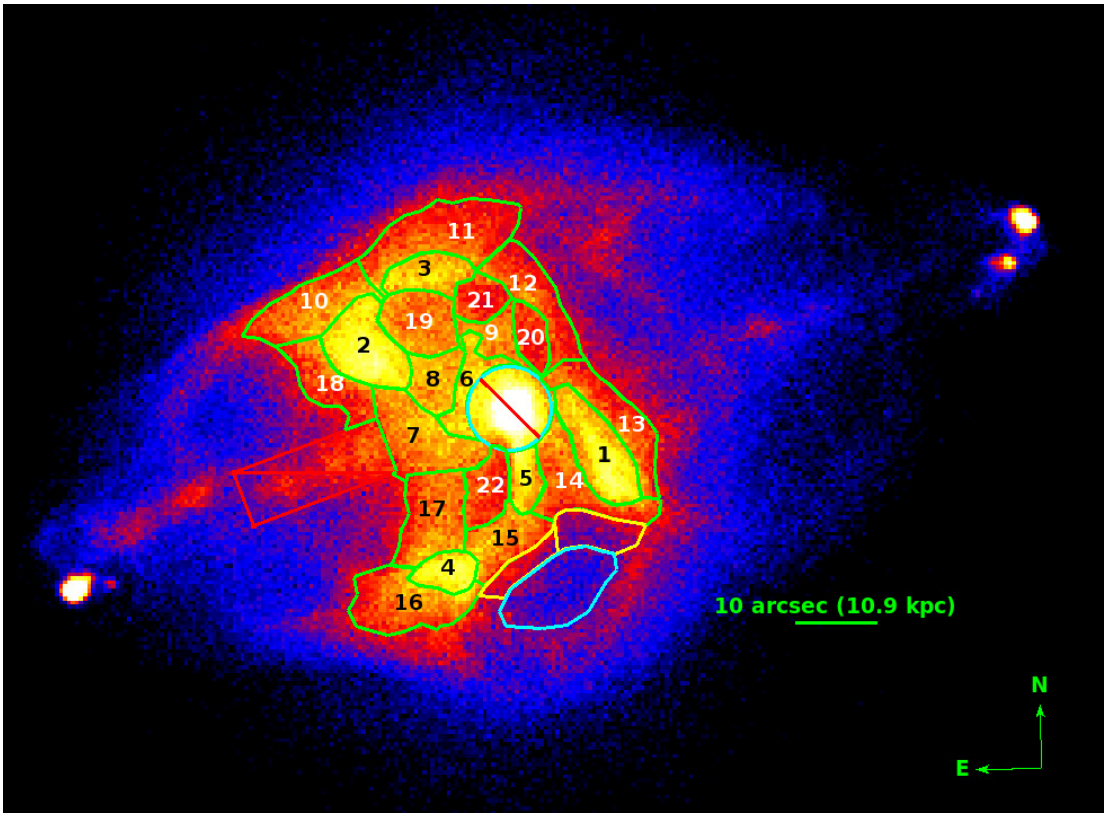

Figure 5.3: Map identifying spectral extraction regions across the rib-like structure of Cygnus A. The unnumbered cyan region to the south corresponds to the position of the Chon et al. (2012) cavity, while the yellow regions correspond to regions between the ribs and cavity. A rectangular region coincident with the jet-like feature and a 5 arcsec region are excluded and not used in spectral analysis.

This applies mostly to regions of low surface brightness, which are amalgamated into other larger regions in order for CONTBIN's selection to reach the appropriate SNR. To prevent this, I adjusted the regions suggested by CONTBIN to make the connected regions more contiguous and to create smoother boundaries with the regions of lower surface brightness while roughly retaining the signal to noise. This identified 22 regions on which to perform spectral extraction, across a smaller area than that used in the initial CONTBIN selection. The 22 regions are shown in Figure 5.3.

5.4.2 Spectral Fitting

I utilised SPECEXTRACT to extract source and local background spectra for each of the 22 regions from the 50 included observations. The local background is taken from a square annulus outside the area of interest, with width 15 arcsec (see Figure 5.4). CIAO's COMBINE_SPECTRA was used to sum the spectra from individual observations and combine the calibration files, with the counts binned to retain at least 20 counts per bin to allow the use of χ^2 fitting. Combining data with very different observation times had no significant impact on the fits, and results were consistent between early and late data. I applied READOUT_BKG to each observation to estimate the contribution of out-of-time (OOT) events to each spectrum and remove it, although the rib region is sufficiently bright that the OOT contribution is negligible.

Each of the 22 regions was fitted in XSPEC (Arnaud, 1996) with a PHABS$\times$APEC model (Smith et al., 2001) between 0.5 and 7.0 keV with z=0.056075 and Galactic $N_H = 3.1 \times 10^{21}$ cm^{-2} based on an average of results from Dickey and Lockman (1990) and Kalberla et al. (2005). The abundance was left free in the fitting and was scaled to the solar abundances of Anders and Grevesse (1989). Freeing the PHABS component of the model showed that $N_H = 3.1 \times 10^{21}$ cm^{-2} is an underestimate of the absorption in the region of the ribs. To account for absorption associated with the host galaxy of Cygnus A, I added a second absorption component to the model, ZPHABS. The ZPHABS component increases the value of N_H in almost all regions by at least 10 per cent. The highest absorption is in the north ribs, with a map shown in Figure 5.5. A broadly acceptable fit could be found for each region using just this model, suggesting that each region is dominated by single-temperature thermal emission.

The origin of excess photoelectric absorption in brightest cluster galaxies (BCG) is a topic of current debate, with suggested origins including gas condensing from lower entropy gas which is lifted outwards from the cluster core by X-ray bubbles (McNamara et al., 2016) or gravitational attraction from the BCG moving through a region with a short cooling time focussing cooling in its wake (Fabian et al., 2001). The excess absorption I detect is similar to the column densities of molecular gas seen in other BCGs (Vantyghem et al., 2016). Wilman et al. (2000) detect molecular hydrogen extending some 6 kpc from the centre of Cygnus A, although the highest absorption columns I measure are found at around 20 kpc from the core.

It is reasonable to expect some systematic uncertainties in combining 62 data sets, but as a goal I have defined an acceptable fit from the χ^2 fitting as one with a null hypothesis probability $\geq$0.01. The majority of the selected regions fit acceptably by these criteria while modelled as an

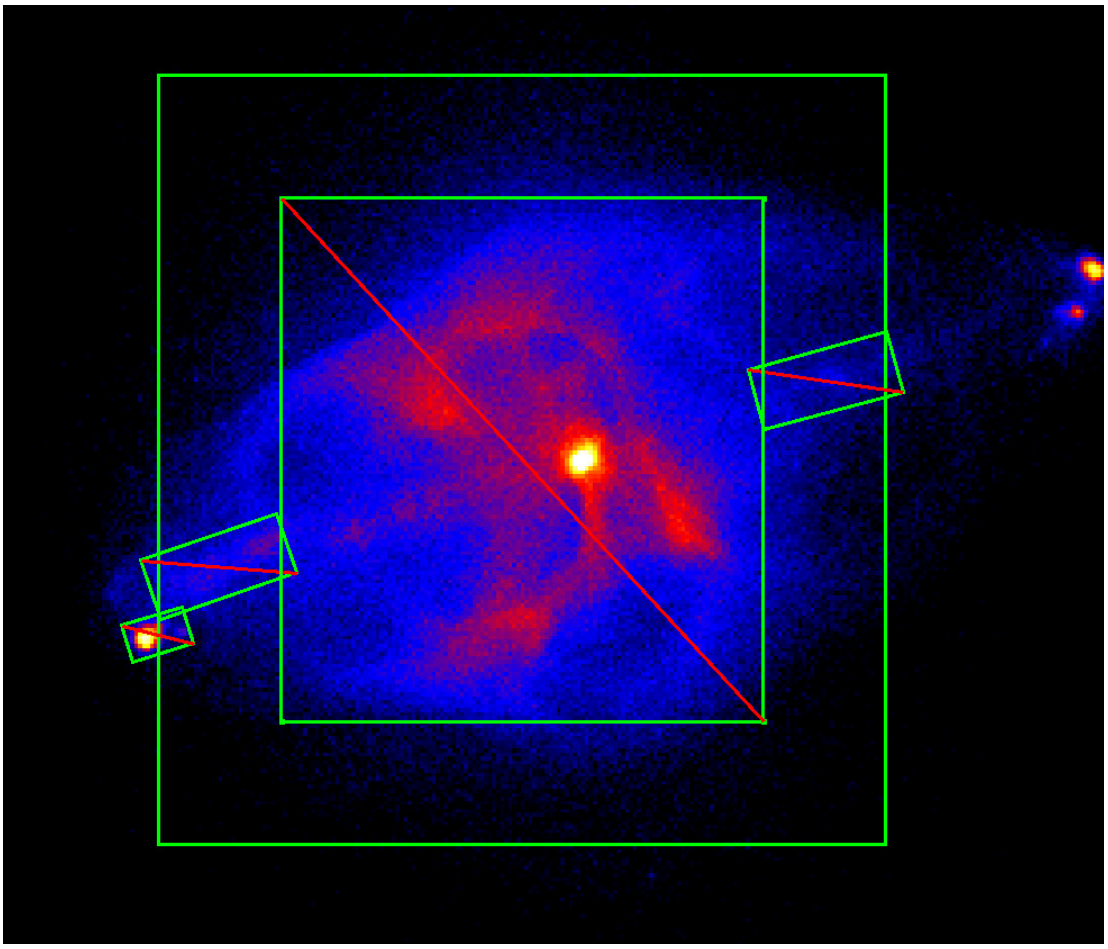

Figure 5.4: Merged *Chandra* image of Cygnus A. The 'square annulus' local background extraction region is overlaid.

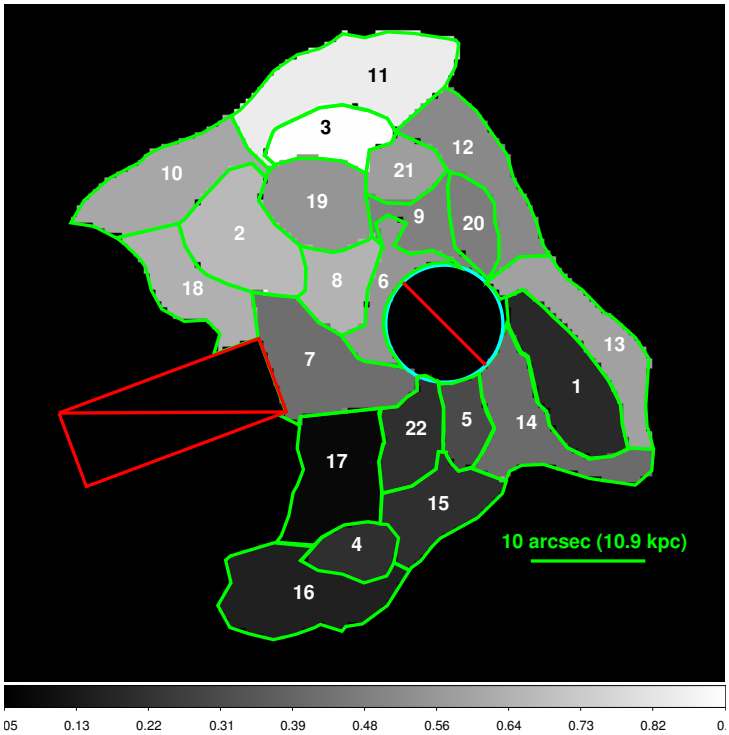

Figure 5.5: Absorption at the redshift of Cygnus A across the rib-like structure. The colourbar corresponds to the best-fit ZPHABS component in 10^{21} cm^{-2}. The black circle at the centre of the sources corresponds to an excised circle of radius 5 arcsec, representing the core.

absorbed APEC model (see Table 5.2). It is possible that some of these regions are contaminated with non-thermal core AGN emission. In the extraction regions, the region near the AGN was excised with a circle of radius 5 arcsec. However, comparison of the PSF (for the ACIS-S image, ObsID 1707, which has a 0.4 s frame time to mitigate the effect of pileup) with a radial profile suggests that significant core emission may be found up to 8 arcsec from the core. I therefore included the spectral model of the nucleus from Young et al. (2002) (see their Table 2, Model 1) in the poorly fit regions close to the core. I included both the hard and soft model components, and their relative normalisations were fixed. I also used the absorption column suggested in Young et al. (2002), although this is likely to have varied across the timescale of the various observations (Reynolds et al., 2015). The core model is necessary as a simple power law does not improve the fits, and the data show a preference for a spectrum that rises with increasing energy. The shape of the core model is very different from a single-component power law and its inclusion causes a significant improvement for several regions.

Adding the core component brought the fits of regions 1, 5, 6 and 13 to an acceptable level and improved the fit of region 14. F-test probabilities are $\leq 10^{-7}$ for each region, showing that the addition of the core components is very strongly favoured. Poorly fitted regions 2 and 11 are too far from the core to justify the inclusion of this model. I tested for multi-temperature components in regions still giving a poor fit, but could find no evidence of a second component. Radio maps at 327 MHz, 1345 MHz and 146 MHz show Cygnus A is bright at low radio frequencies across the centre and much of the southern ribs (Lazio et al., 2006; Steenbrugge et al., 2010; McKean et al., 2016) and inverse-Compton X-ray emission at some level is expected, so I tested for an extra single power-law component. I again found no evidence for this component, although regions 2 and 11 occupy the northern part of the ribs away from the brightest radio emission. Inverse-Compton emission has been plausibly detected in the lobes of Cygnus A in the past (Hardcastle and Croston, 2010; Yaji et al., 2010), although these detections are where the radio emission is brightest at GHz frequencies, to the east and west of the ribs. The poor fits in regions 2 and 11 are possibly explained by mixing of gases, but it seems the mixing is sufficiently complicated that the spectral fitting does not cope well. Example spectra and the fits of regions 3, 6 and 11 are shown in Figure 5.6.

The best fit APEC components are given in Table 5.2. Regions marked with a '*' are those where additional components were added to the absorbed APEC model to improve the fits.

Region 7 has a particularly poor fit to the APEC model, which is not improved to acceptable

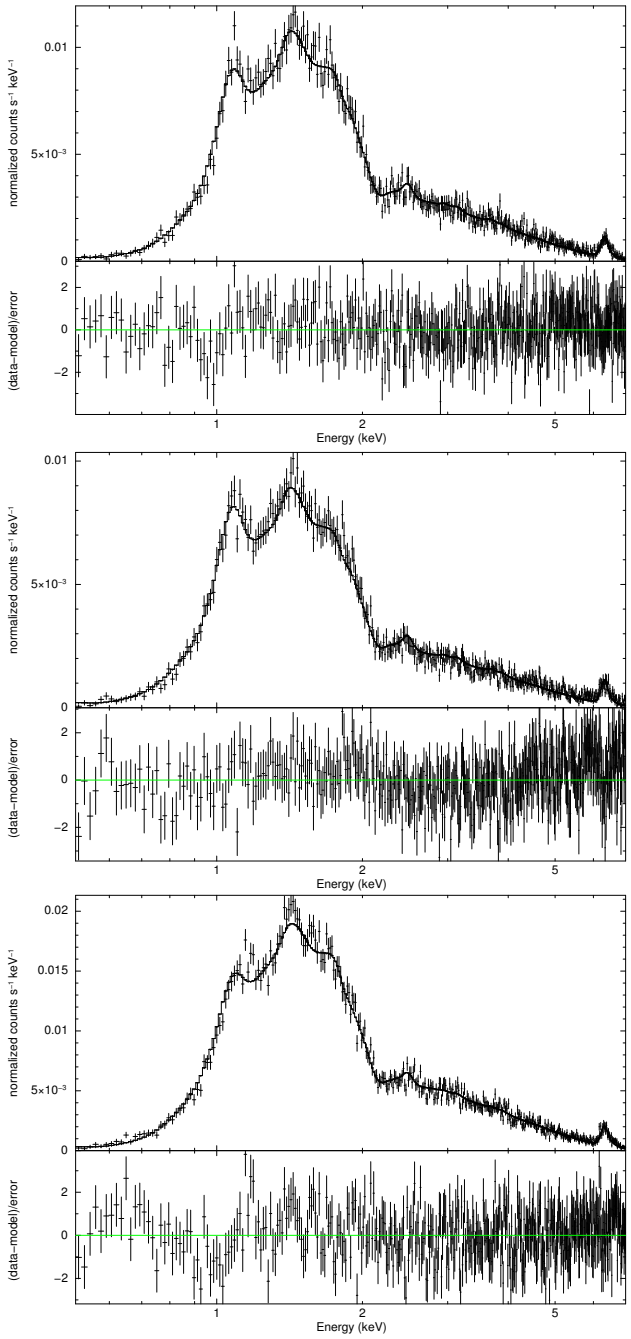

Figure 5.6: *Chandra* spectra extracted regions 3 (top), 6 (middle) and 11 (bottom) fitted to an absorbed APEC model (3 and 11) and an absorbed APEC plus core component model (6).

Region	Source N_H (10^{21} cm^{-2})	kT (keV)	Z ($Z_\odot$)	$N_{\rm APEC}$	$N_{\rm hard\,core}$	χ^2/dof	Probability
*Region 1	$0.19^{+0.16}_{-0.15}$	$3.22^{+0.10}_{-0.11}$	0.78 ± 0.06	$5.23^{+0.15}_{-0.14}$	0.20 ± 0.05	510.3/439	0.01
Region 2	$0.67^{+0.16}_{-0.15}$	3.94 ± 0.10	0.72 ± 0.05	5.92 ± 0.13	-	481.6/396	0.002
Region 3	0.95 ± 0.20	$3.76^{+0.14}_{-0.13}$	$0.77^{+0.08}_{-0.07}$	2.68 ± 0.08	-	443.8/440	0.44
Region 4	$0.21^{+0.22}_{-0.21}$	$3.50^{+0.15}_{-0.13}$	0.59 ± 0.07	$2.29^{+0.08}_{-0.07}$	-	510.2/440	0.01
*Region 5	$0.30^{+0.31}_{-0.29}$	$2.61^{+0.14}_{-0.15}$	$0.69^{+0.11}_{-0.10}$	$1.84^{+0.12}_{-0.11}$	0.12 ± 0.03	505.5/439	0.02
*Region 6	$0.55^{+0.29}_{-0.27}$	$3.26^{+0.18}_{-0.19}$	$0.81^{+0.11}_{-0.10}$	$2.15^{+0.11}_{-0.10}$	0.19 ± 0.04	436.3/439	0.53
Region 7	0.42 ± 0.16	4.90 ± 0.17	0.78 ± 0.06	4.46 ± 0.10	-	568.6/440	3.3×10^{-5}
Region 8	$0.65^{+0.23}_{-0.21}$	$3.83^{+0.15}_{-0.14}$	0.80 ± 0.08	2.41 ± 0.08	-	485.5/440	0.07
Region 9	$0.48^{+0.27}_{-0.26}$	$3.69^{+0.17}_{-0.16}$	0.88 ± 0.10	1.62 ± 0.06	-	508.9/440	0.01
Region 10	$0.61^{+0.19}_{-0.18}$	4.73 ± 0.19	0.76 ± 0.07	3.74 ± 0.10	-	477.7/440	0.10
Region 11	$0.84^{+0.18}_{-0.17}$	$4.23^{+0.13}_{-0.12}$	0.65 ± 0.05	4.89 ± 0.11	-	528.9/440	0.002
Region 12	$0.51^{+0.21}_{-0.20}$	4.55 ± 0.21	0.74 ± 0.07	2.80 ± 0.08	-	497.1/440	0.03
*Region 13	$0.59^{+0.25}_{-0.23}$	$3.44^{+0.25}_{-0.17}$	0.61 ± 0.07	$3.21^{+0.13}_{-0.12}$	$0.21^{+0.05}_{-0.06}$	476.1/439	0.11
*Region 14	$0.41^{+0.22}_{-0.21}$	$3.02^{+0.14}_{-0.15}$	0.81 ± 0.08	3.47 ± 0.13	0.28 ± 0.05	529.2/439	0.002
Region 15	0.21 ± 0.20	3.31 ± 0.09	0.74 ± 0.07	2.86 ± 0.09	-	483.4/440	0.07
Region 16	$0.16^{+0.18}_{-0.16}$	$4.27^{+0.15}_{-0.13}$	0.64 ± 0.06	4.01 ± 0.10	-	478.7/440	0.10
Region 17	$0.08^{+0.17}_{-0.08}$	4.44 ± 0.17	$0.78^{+0.07}_{-0.06}$	3.65 ± 0.09	-	475.2/440	0.12
Region 18	$0.64^{+0.26}_{-0.25}$	$4.63^{+0.25}_{-0.24}$	$0.75^{+0.09}_{-0.08}$	$2.44^{+0.09}_{-0.08}$	-	473.9/440	0.13
Region 19	$0.55^{+0.21}_{-0.20}$	4.09 ± 0.14	0.75 ± 0.07	3.27 ± 0.09	-	510.2/440	0.01
Region 20	$0.47^{+0.33}_{-0.31}$	4.63 ± 0.32	$0.97^{+0.14}_{-0.13}$	1.05 ± 0.05	-	433.4/440	0.58
Region 21	$0.58^{+0.34}_{-0.33}$	$4.22^{+0.28}_{-0.21}$	0.87 ± 0.12	$1.21^{+0.06}_{-0.05}$	-	280.4/268	0.29
Region 22	$0.21^{+0.26}_{-0.21}$	$4.10^{+0.18}_{-0.17}$	0.81 ± 0.10	1.66 ± 0.06	-	471.2/440	0.15

Table 5.2: Results from spectral fits to each region. Regions 1, 5, 6, 13 and 14 have additional components ($N_{\rm APEC}$, $N_{\rm hard\,core}$) representing the core emission from Young et al. (2002) to make their fits acceptable. Column 1 is the absorption column at the source, obtained from the ZPHABS component of the model. All normalisations have units 10^{10} cm^{-5}. Errors are given for a 90% confidence limit.

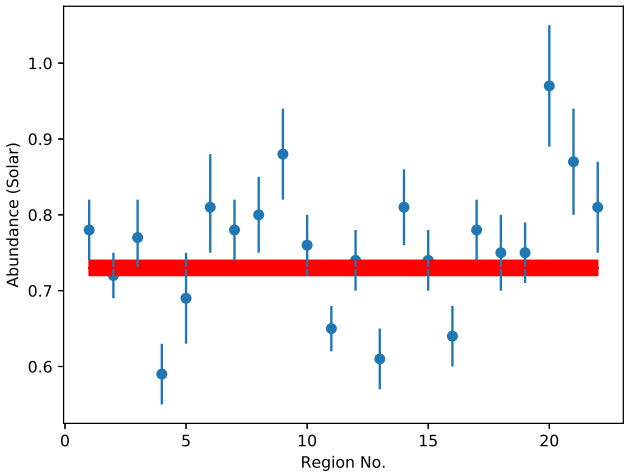

Figure 5.7: The abundance in $Z_\odot$ in each region of the ribs. The weighted average of the metallicity with errors of these regions is shown in red. This shows that the metallicity is not constant across the whole rib structure.

levels by the inclusion of core or power-law components. This is likely to be because there is emission associated with the X-ray jet-like feature within this region. A fit including this is beyond the scope of this work (but see de Vries et al. prep). For this reason, region 7 is not included in any analysis beyond the temperature mapping in Section 5.6.1.

The abundance in each region is plotted in Figure 5.8. A χ^2 test to compare the abundances with a constant (each with 1σ errors as compared with the 90% values given in Table 5.2) finds an unacceptable fit with χ^2/dof = 67.4/21. This suggests some changes in metallicity across the rib structure. There appear to be no systematic trends as can be seen in Figure 5.8, although regions of higher and lower metallicity are clustered together. The range in metallicities is consistent with the abundances seen in new radial profiles of the cluster gas up to 20 arcseconds beyond the cocoon shock(Snios et al., 2018). A fit to the cavity identified in Chon et al. (2012), immediately south of the ribs gives a temperature of $4.39^{+0.31}_{-0.26}$ keV and an abundance of $0.62^{+0.11}_{-0.10} Z_\odot$.

Regions 1, 2, 3 and 4 are similar to those defined in other studies of the rib-like structure and can be compared with them. The temperatures I find tend to match those found by Smith et al. (2002) and are between 0.3 and 0.8 keV cooler than those found by Wilson et al. (2006) and Chon et al. (2012). This is likely because I have used local background to remove the hot cluster component in the foreground and background, whereas the studies with which the results

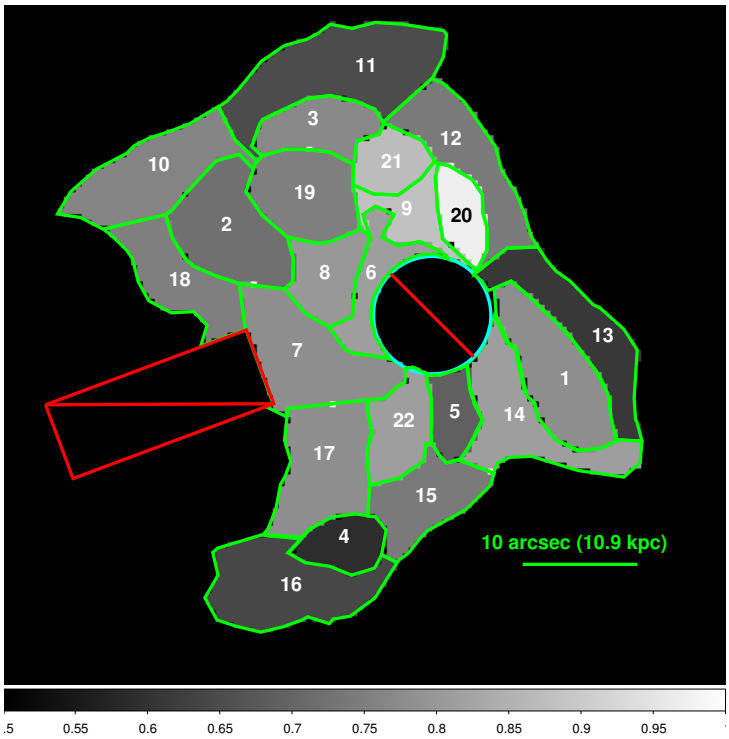

Figure 5.8: Map of the metal abundance across the rib-like structure. The colourbar corresponds to the best-fit abundance in $Z_{\odot}$. The black circle at the centre of the sources corresponds to an excised circle of radius 5 arcsec, representing the core.

are discrepant were conducted using blank-sky backgrounds.

The metallicities and temperatures in two regions in the gap between the ribs and the cavity (shown in yellow in Figure 5.3) are the same ($kT = 3.90 \pm 0.20$ keV and $Z = 0.66^{+0.15}_{-0.14} Z_{\odot}$), and are consistent with the metallicity of the cavity and of region 16. It is therefore plausible that region 16 and the cavity are composed of gas forming a continuous structure.

The location of the local background is an important consideration. I opted to use the square annulus seen in Figure 5.4 in order to border the area given to identify spectral extraction regions using *contbin*. The disadvantage of using this region is that instead of completely isolating the spectrum of the rib structures, some emission from the shocked cocoon gas is included. This could potentially affect both temperatures and normalisations of the fits. To test the impact of the shocked rims on the spectral fits, I used the Chon et al. (2012) cavity as a local background on some of the best defined regions in the ribs. I opted to use the cavity as it lies within the cocoon shock so should contain foreground and background emission from the shocked rims, is close to the ribs, but does not form a part of the rib structure. The resulting fits in regions 1, 2 and 5 show no change in temperature and a reduction in normalisation of a factor of less than 1.5. This has a very small impact on calculation of the physical parameters, with pressures dropping by (0.1 - 0.2) $\times$ 10^{-10} Pa in the selected regions.

5.5 Physical Parameters of the Regions

The regions of the ribs are well described by thermal models, which return the temperatures and abundances within each. I therefore calculated the density, pressure and entropy of each region, using the methods described in Section 2.4.2.

I calculated the volumes of the regions within the ribs in two different ways. Firstly, I assumed the regions were cylinders or spheres represented by their projected volumes. Whether a region is circular or spherical is dependent on its 2D appearance. For example, region 19 is considered spherical, while region 1 is considered cylindrical. For cylinders, the volume was calculated assuming the longest axis of the region corresponds to the height of the cylinder and half the length of the shortest axis corresponds to the radius. The results using this method are shown in Table 5.3. Secondly, I assume the rib structures each fill a cylinder of radius 39 arcsec (the semi-minor axis of the cocoon), lying in the plane of the sky, whose axis lies coincident with the radio axis. The surface areas of the regions are then multiplied by a depth representing

Cylinders/spheres geometry				
Region	n_p (10^{-1} cm^{-3})	P (10^{-10} Pa)	$M(10^9 M_\odot)$	S (keV cm^2)
Region 1	1.40 ± 0.02	1.6 ± 0.1	1.8 ± 0.1	11.9 ± 0.4
Region 2	1.41 ± 0.01	2.0 ± 0.1	2.0 ± 0.1	14.5 ± 0.4
Region 3	1.83 ± 0.01	2.5 ± 0.1	0.7 ± 0.1	$11.7^{+0.5}_{-0.4}$
Region 4	1.68 ± 0.03	2.1 ± 0.1	0.7 ± 0.1	$11.5^{+0.5}_{-0.4}$
Region 5	$1.83^{+0.06}_{-0.50}$	1.7 ± 0.1	0.5 ± 0.1	8.1 ± 0.5
Region 6	$2.29^{+0.06}_{-0.05}$	2.7 ± 0.2	0.5 ± 0.1	8.7 ± 0.5
Region 8	1.54 ± 0.03	2.1 ± 0.1	0.8 ± 0.1	13.3 ± 0.5
Region 9	1.33 ± 0.02	1.8 ± 0.1	0.6 ± 0.1	$14.1^{+0.7}_{-0.6}$
Region 10	1.34 ± 0.02	2.3 ± 0.1	1.3 ± 0.1	18.0 ± 0.7
Region 11	1.22 ± 0.01	1.9 ± 0.1	1.9 ± 0.1	17.2 ± 0.5
Region 12	1.61 ± 0.02	2.6 ± 0.1	0.8 ± 0.1	15.4 ± 0.7
Region 13	$1.75^{+0.04}_{-0.03}$	$2.2^{+0.2}_{-0.1}$	0.9 ± 0.1	$11.0^{+0.8}_{-0.6}$
Region 14	1.64 ± 0.03	1.8 ± 0.2	1.0 ± 0.1	10.1 ± 0.5
Region 15	1.73 ± 0.03	2.1 ± 0.1	0.8 ± 0.1	10.7 ± 0.3
Region 16	1.16 ± 0.01	1.8 ± 0.1	1.7 ± 0.1	18.0 ± 0.6
Region 17	1.28 ± 0.02	2.0 ± 0.1	1.4 ± 0.1	17.5 ± 0.7
Region 18	1.18 ± 0.02	2.0 ± 0.1	1.0 ± 0.1	19.2 ± 1.0
Region 19	1.15 ± 0.02	1.7 ± 0.1	1.4 ± 0.2	17.3 ± 0.6
Region 20	1.23 ± 0.03	2.0 ± 0.2	0.4 ± 0.1	18.7 ± 1.3
Region 21	1.21 ± 0.03	1.8 ± 0.1	0.5 ± 0.1	$17.2^{+1.2}_{-0.9}$
Region 22	1.23 ± 0.02	1.8 ± 0.1	0.7 ± 0.1	$16.6^{+0.8}_{-0.7}$
		Total mass:	21.0 ± 1.0	

Table 5.3: Density, pressure, mass and entropy index of the X-ray emission in the various regions within the rib structure of Cygnus A. Errors are quoted for 90% confidence range. These were calculated assuming a spherical or cylindrical volume for each region.

the line of sight contained within the cylinder. The results using this method are shown in Table 5.4.

A comparison between the pressures for each volume assumption can be seen in Figure 5.9. Fitting a constant to these data gives an average pressure $\overline{P} = (2.0 \pm 0.1) \times 10^{-10}$ Pa with χ^2 = 246.4 for the cylinders and spheres and $\overline{P} = (4.7 \pm 0.2) \times 10^{-11}$ Pa with χ^2 = 234.7 assuming the ribs fill a cylinder. This fitting shows no significant preference for either model. The clear difference in pressure between the two volume models suggests that the ribs are not composed of a mixture of cylinders and spheres and regions which fill a cylinder. This suggests that all structures within the ribs are likely to have a similar geometry and similar dynamical origins. The poor χ^2 and deviations from the mean are possibly caused by inhomogeneities in the density of the various rib structures. For both geometries the total mass of rib gas is substantial at a few

Filled cylinder geometry				
Region	n_p (10^{-2} cm^{-3})	P (10^{-11} Pa)	$M(10^9 M_\odot)$	S (keV cm^2)
Region 1	3.73 ± 0.05	$4.3^{+0.1}_{-0.2}$	6.7 ± 0.1	$28.8^{+0.9}_{-1.0}$
Region 2	4.29 ± 0.04	6.1 ± 0.2	6.6 ± 0.1	32.2 ± 0.9
Region 3	3.78 ± 0.06	5.1 ± 0.2	3.4 ± 0.1	$33.4^{+1.3}_{-1.2}$
Region 4	$4.20^{+0.07}_{-0.06}$	5.3 ± 0.2	2.6 ± 0.1	$28.9^{+1.3}_{-1.1}$
Region 5	3.63 ± 0.01	3.4 ± 0.2	2.4 ± 0.1	23.8 ± 1.4
Region 6	$3.51^{+0.09}_{-0.08}$	4.1 ± 0.3	2.9 ± 0.1	30.4 ± 1.8
Region 8	3.76 ± 0.06	5.2 ± 0.2	3.1 ± 0.1	$34.2^{+1.4}_{-1.3}$
Region 9	3.19 ± 0.06	4.2 ± 0.2	2.4 ± 0.1	$36.7^{+1.8}_{-1.7}$
Region 10	3.56 ± 0.05	6.1 ± 0.3	5.0 ± 0.1	43.7 ± 1.8
Region 11	3.25 ± 0.04	4.9 ± 0.2	7.2 ± 0.1	$41.6^{+1.3}_{-1.2}$
Region 12	3.02 ± 0.04	4.9 ± 0.2	4.5 ± 0.1	47.0 ± 2.2
Region 13	3.10 ± 0.06	$3.8^{+0.3}_{-0.2}$	5.0 ± 0.1	$34.8^{+2.6}_{-1.8}$
Region 14	3.34 ± 0.06	$3.6^{\pm}0.2$	5.0 ± 0.1	$29.1^{+1.4}_{-1.5}$
Region 15	3.37 ± 0.05	4.0 ± 0.1	4.1 ± 0.1	31.7 ± 0.9
Region 16	3.53 ± 0.04	5.4 ± 0.2	5.4 ± 0.1	$39.7^{+1.4}_{-1.3}$
Region 17	3.29 ± 0.04	5.3 ± 0.1	5.3 ± 0.1	43.2 ± 1.7
Region 18	$3.22^{+0.06}_{-0.05}$	5.4 ± 0.3	3.6 ± 0.1	$45.8^{+2.5}_{-2.4}$
Region 19	3.32 ± 0.05	4.9 ± 0.2	4.7 ± 0.1	39.6 ± 1.4
Region 20	2.81 ± 0.07	4.7 ± 0.3	1.8 ± 0.1	50.1 ± 3.6
Region 21	$2.92^{+0.07}_{-0.06}$	$4.4^{+0.3}_{-0.2}$	2.0 ± 0.1	$44.5^{+3.0}_{-2.3}$
Region 22	3.04 ± 0.06	4.5 ± 0.2	2.6 ± 0.1	$42.1^{+1.9}_{-1.8}$
		Total mass:	86.0 ± 1.0	

Table 5.4: Density, pressure, mass and entropy index of the X-ray emission in the various regions within the rib structure of Cygnus A. Errors are quoted for 90% confidence range. These were calculated assuming that ribs are contained to fill a cylinder of radius 39 arcsec.

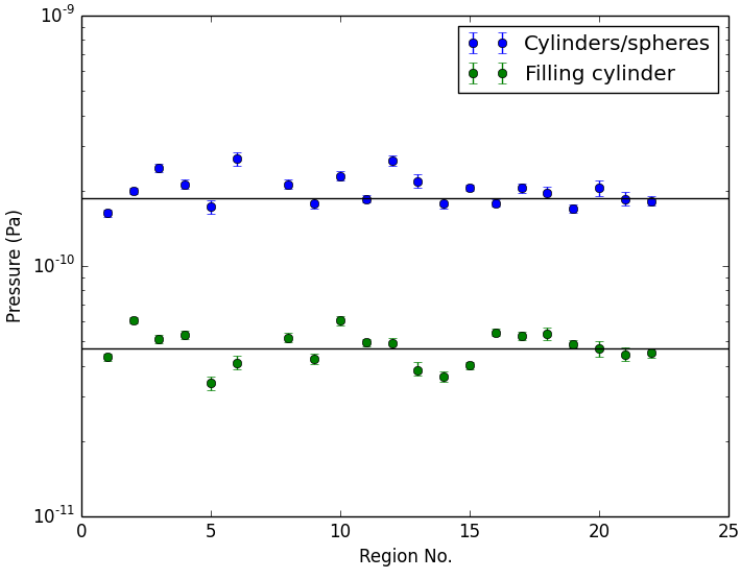

Figure 5.9: Pressure in each region calculated for the two different geometries. Lines of best fit indicate the mean for each pressure group.

times $10^{10} M_{\odot}$.

Snios et al. (2018) have determined the pressure of the lobes to be $(1.0 \pm 0.4) \times 10^{-10}$ Pa in the east lobe and $(8.4 \pm 0.2) \times 10^{-11}$ Pa in the west lobe using spectra for the thin rim of gas between the shock and the radio lobes. This is an order of magnitude larger than the 1.3×10^{-11} Pa minimum energy field of lobes closest to the centre of the source found by Carilli et al. (1991). The mean pressures I find in the two configurations fall either side of the Snios et al. estimates.

5.5.1 Dynamical timescales of the ribs

The sound speed, c_s, of the gas in each region is found using Equation 5.1 (Worrall et al., 2012), where T is the temperature of the regions obtained from the spectral fits.

$$c_s(\mathrm{kpc\,Myr^{-1}}) = 0.54(kT/\mathrm{keV})^{0.5} \tag{5.1}$$

An estimate of the dynamical timescale of each region can be found by taking the length of the shortest two-dimensional axis and dividing it by the calculated sound speed. If the source is older than this timescale the gas in each region is likely to be in pressure balance. The results for c_s and the dynamical timescale are given in Table 5.5. The timescales vary between 3.1 and

Region	c_s (kpc Myr^{-1})	Dynamical timescale (Myr)
Region 1	0.97 ± 0.02	6.3 ± 0.1
Region 2	1.07 ± 0.02	9.7 ± 0.1
Region 3	1.05 ± 0.02	3.9 ± 0.1
Region 4	1.01 ± 0.01	6.6 ± 0.1
Region 5	0.87 ± 0.02	4.7 ± 0.2
Region 6	0.98 ± 0.03	3.1 ± 0.1
Region 8	1.06 ± 0.02	6.8 ± 0.1
Region 9	1.04 ± 0.02	6.7 ± 0.1
Region 10	1.17 ± 0.02	4.8 ± 0.1
Region 11	1.11 ± 0.01	5.7 ± 0.1
Region 12	1.15 ± 0.03	3.4 ± 0.1
Region 13	$1.00^{+0.04}_{-0.02}$	3.7 ± 0.1
Region 14	0.94 ± 0.02	5.3 ± 0.1
Region 15	0.98 ± 0.01	5.3 ± 0.1
Region 16	$1.12^{+0.02}_{-0.01}$	7.6 ± 0.1
Region 17	1.14 ± 0.01	6.3 ± 0.1
Region 18	1.16 ± 0.03	4.9 ± 0.1
Region 19	1.09 ± 0.02	8.9 ± 0.1
Region 20	1.16 ± 0.04	5.5 ± 0.2
Region 21	$1.11^{+0.04}_{-0.03}$	$6.1^{+0.2}_{-0.1}$
Region 22	1.09 ± 0.02	6.8 ± 0.1

Table 5.5: Sound speed and age of the X-ray gas contained within each region of the rib structure in Cygnus A.

9.7 Myr, and are somewhat less than the 18.7 Myr estimated age of the shock front (Snios et al., 2018) implying that the structure has largely reached local pressure equilibrium.

5.6 Mapping

5.6.1 Temperature Mapping

The best-fit temperature map in the rib gas is shown in Figure 5.10. Interestingly, there is a clear range in temperature within the structure, with regions in the southwestern corner of the ribs cooler than those in the remainder, although the temperatures in regions 6 and 13 have been reduced by 0.5 and 0.4 keV respectively (more than 10 per cent) by the inclusion of the core component.

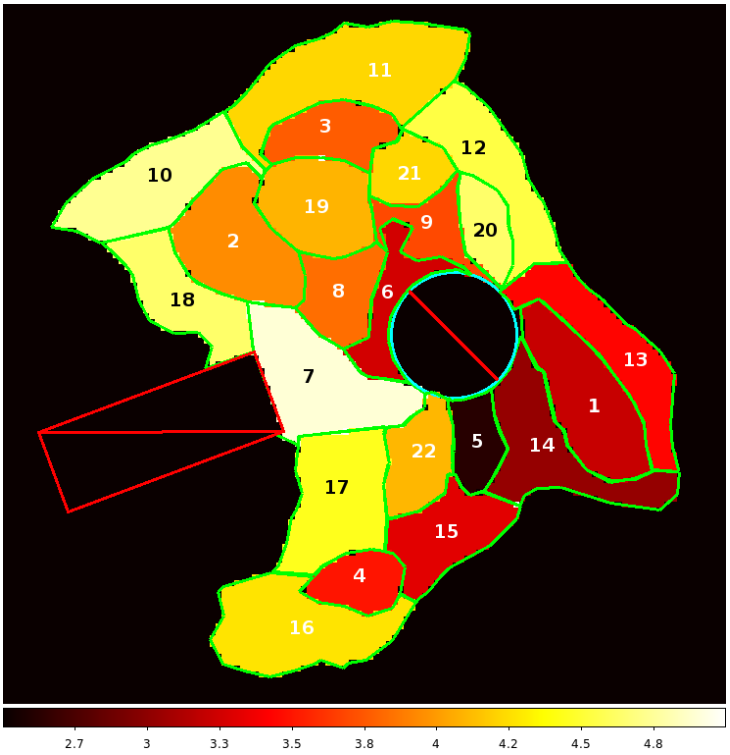

Figure 5.10: Temperature map of the rib-like structure of Cygnus A. The colourbar corresponds to the best-fit temperature of each region in keV. The black circle at the centre of the sources corresponds to an excised circle of radius 5 arcsec, representing the core.

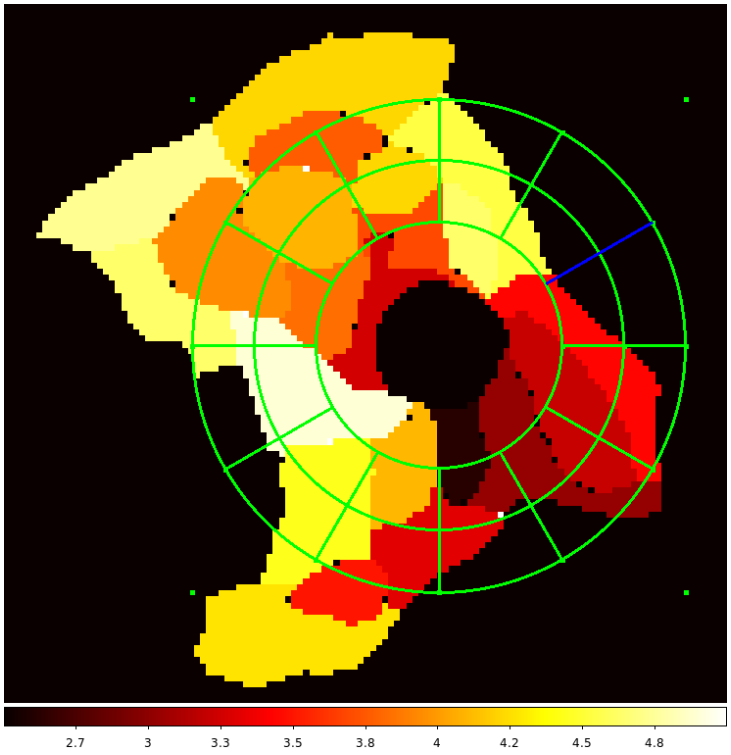

Figure 5.11: Temperature map of the ribs showing the pie slices used to model the temperature at various angles and radii. The blue line indicates the 0 degree line.

To obtain a measure of the range in temperature, I placed annuli of width 5 arcseconds centred on the core and calculated the average temperature in 30 degree annular sectors (see Figure 5.11). The results for annuli at 5-10 arcseconds and 10-15 arcseconds can be seen in Figure 5.12. The difference between the hottest and coolest regions is about 2 keV. The temperature difference is compensated by an opposing density asymmetry that causes the pressure to be roughly constant in the ribs.

5.6.2 Pressure and Entropy Index Maps

Assuming that the ribs are composed of cylinders and spheres, there is no discernible systematic structure in the pressure map (see Figure 5.13). However, in Figure 5.14 (ribs filling cylinder) the regions in the eastern half of the ribs contain somewhat higher pressure when compared to the western half, which is a pattern also identified for the lobes (Snios et al., 2018). The average pressures of the eastern half of the ribs, for this geometry, is $(5.5 \pm 0.2) \times 10^{-11}$ Pa and the average pressure of the western half is $(4.4 \pm 0.2) \times 10^{-11}$ Pa, which is 10 per cent lower. While

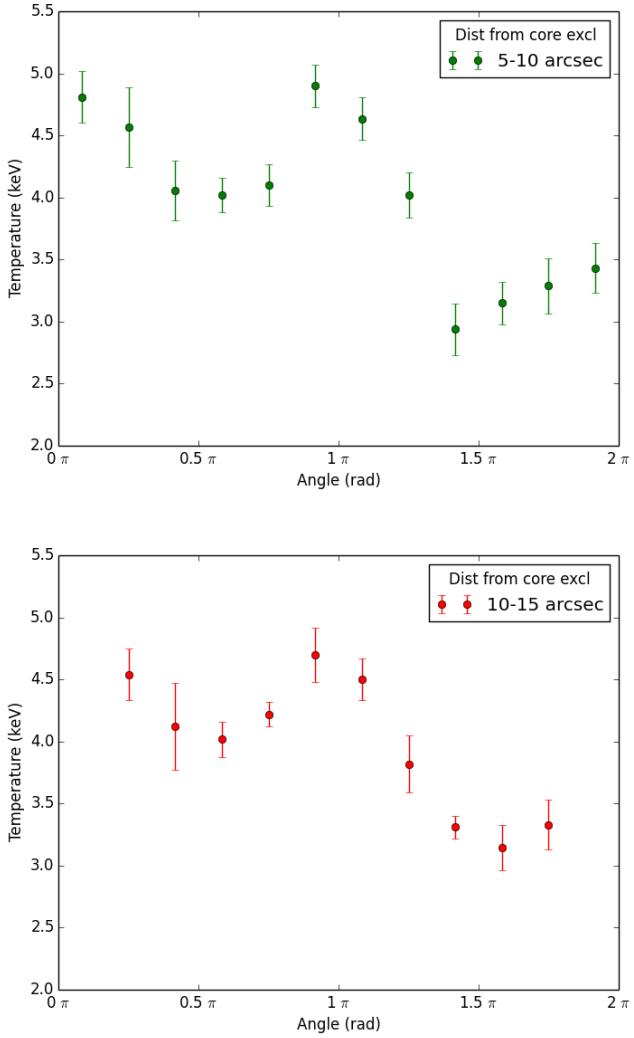

Figure 5.12: Temperature versus angle across the rib-like structure in Cygnus A between 5-10 arcseconds from the core exclusion (middle) and 10-15 arcseconds from the core exclusion (bottom). The first and final wedges of the 10-15 arcsecond plot are missing as there is no rib structure in these segments at this radius.

less significant than the roughly 20 per cent difference seen by Snios et al., it is interesting that it an east-west pressure difference may be present closer to the nucleus. However, pressures in the east and west of the cylinders and spheres configuration are the same within errors.

I also investigate the entropy index of the ribs, which is of interest as the entropy structure contains information about the thermal history of the gas in clusters, especially with regard to the effect of feedback on the intracluster medium (ICM). In general, the entropies across the ribs are uniform, with the highest entropy index for both geometries (lower images, Figures 5.13 and 5.14) found at the extremities of the rib structure. The exception to this is the southwestern corner and entropies here are similar to those seen in regions 2 and 3. Interestingly, the entropies in regions 5, 15 and 4, which arguably belong to the same rib, are similar but increase with angle from the core. Perhaps unsurprisingly, the entropies measured for the filled cylinder geometry are closer to the central entropy of Cygnus A found by Cavagnolo et al. (2009), assuming spherical symmetry.

Although I have discussed differences in pressure and entropy in the rib structure, within each geometry the pressures and entropies measured are similar across regions. There is less than a factor of 2 difference between the lowest and highest pressures and entropies within each geometry. As it is unlikely the two geometries are mixed (see Figure 5.9), and because of the suggested origin for the ribs (see Section 5.8) I prefer the cylinder and spheres geometry for the following sections.

5.7 Rayleigh-Taylor Instabilities

The gas extending to the south of the core is one of the more striking parts of Cygnus A's ribs. The eastern edge of region 5 (Figure 5.3) is a particularly sharp boundary. This is remarkable since it appears that X-ray emitting gas is decelerating the low-density plasma from a part of the Cygnus A lobe system, and so this interface should be subject to the Rayleigh-Taylor (RT) instability. In this Section I discuss this edge of region 5 as an exemplar of other sharp features in Cygnus A (Figure 5.2).

RT instabilities develop where a higher-density gas lies above a lower-density gas in a gravitational field, or, equivalently, where the higher-density gas is decelerating the expansion of the lower-density gas. Bubbles and fingers of the fluids then disturb the interface and cause mixing.

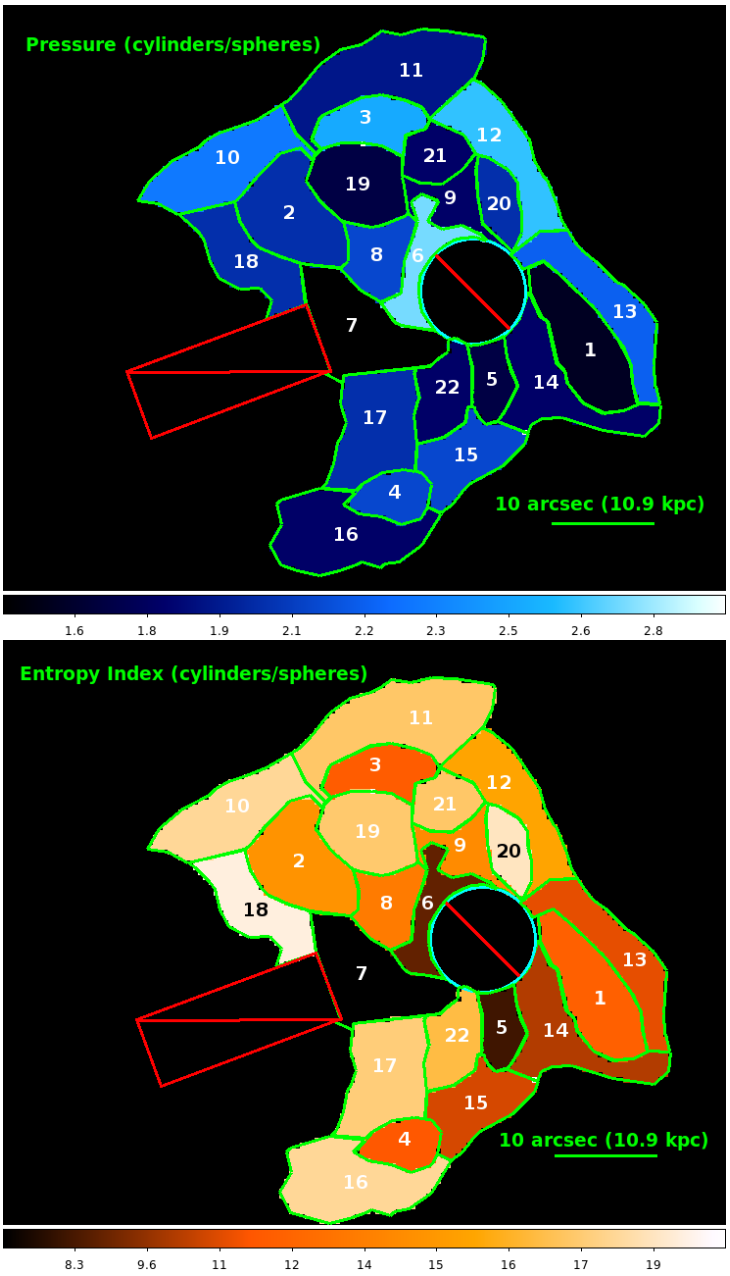

Figure 5.13: *Top:* Pressure map of the rib-like structure of Cygnus A, where volumes are calculated using cylinders and spheres representing the regions. The colourbar corresponds to the best-fit pressure of each region in 10^{-10} Pa. The black circle at the centre of the sources corresponds to an excision of radius 5 arcsec, representing the core. *Bottom:* Entropy index map of the rib-like structure of Cygnus A, where volumes are calculated using cylinders and spheres representing the regions. The colourbar corresponds to the entropy index of each region in keV cm^2. The black circle at the centre of the sources corresponds to an excision of radius 5 arcsec, representing the core.

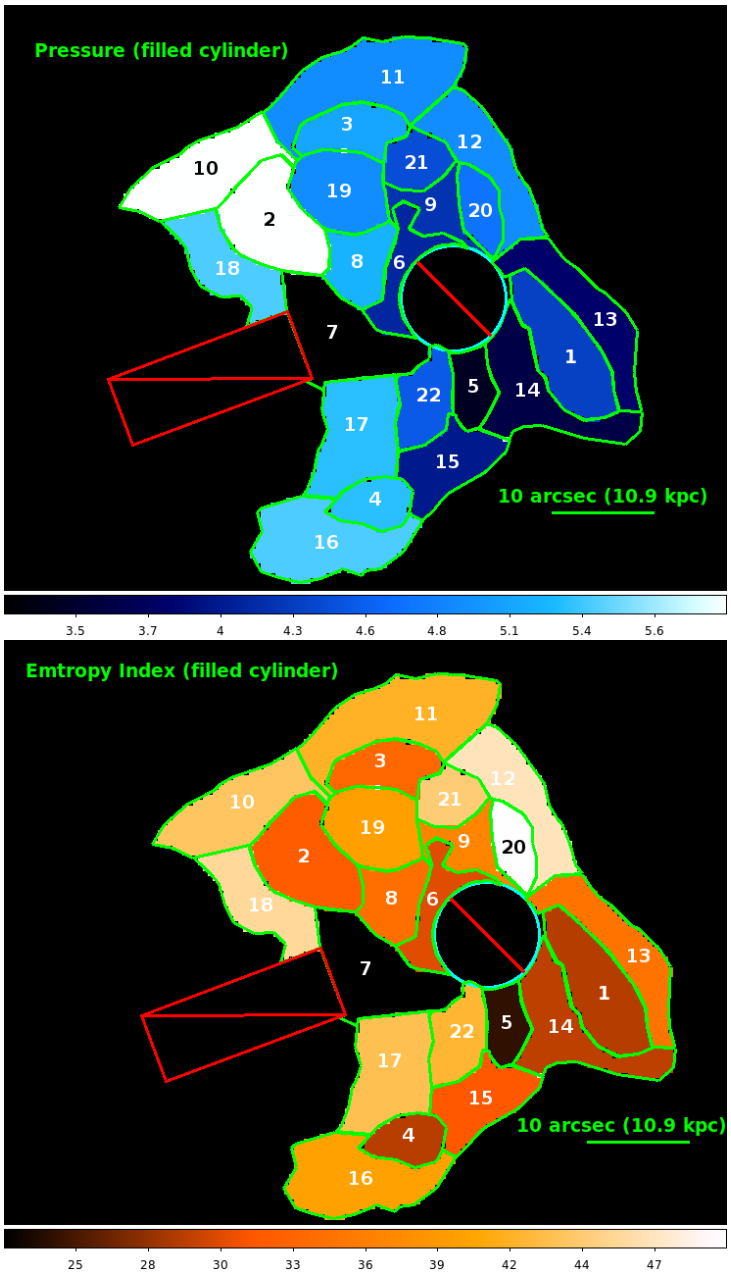

Figure 5.14: *Top:* Pressure map of the rib-like structure of Cygnus A, where volumes are calculated assuming the ribs fill a cylinder defined by the cocoon shock. The colourbar corresponds to the best-fit pressure of each region in 10^{-11} Pa. The black circle at the centre of the sources corresponds to an excision of radius 5 arcsec, representing the core. *Bottom:* Entropy index map of the rib-like structure of Cygnus A, where volumes are calculated assuming the ribs fill a cylinder defined by the cocoon shock. The colourbar corresponds to the entropy index of each region in keV cm^2. The black circle at the centre of the sources corresponds to an excision of radius 5 arcsec, representing the core.

If the lower-density gas lies over the higher-density gas, or if the higher-density gas is accelerating the lower-density gas, then there are no RT instabilities. In the context of Cygnus A, RT instabilities should be apparent where the radio plasma is encountering denser external gas.

In the absence of dynamically-important magnetic fields the growth rate of the RT instability is (Chandrasekhar, 1961)

$$\Gamma = \left(2\pi \frac{g}{\lambda} \frac{\rho_{\rm a} - \rho_{\rm b}}{\rho_{\rm a} + \rho_{\rm b}} \right)^{1/2} \tag{5.2}$$

where g is the deceleration, ρ_a and ρ_b are the densities of the two gases ($\rho_a > \rho_b$), and λ is the horizontal (parallel to the interface) wavelength of a mode. RT instabilities grow at all wavelengths, but faster at shorter λ.

The density of the radio-emitting plasma in Cygnus A is much lower than the density of the external rib gas, $\rho_{\rm a} \gg \rho_{\rm b}$, so the growth rate of the instability simplifies to

$$\Gamma = \left(2\pi \frac{g}{\lambda} \right)^{1/2} \quad . \tag{5.3}$$

If the instabilities have been growing for time, τ, then any initial perturbations in the interface will grow by a factor $\exp(\Gamma\tau)$ which should be < 1 for the perturbations still to be in the linear regime. If the radio plasma has been interacting with the X-ray plasma for the same time τ, during which the lobe has expanded to scale R, then g will be of order R/τ^2 (e.g., for self-similar expansion), and

$$\exp(\Gamma\tau) \approx \exp\left(2.5 \left(\lambda / R \right)^{-1/2} \right) \quad . \tag{5.4}$$

Perturbations on scales smaller than the radio structure should therefore have grown to the non-linear regime and blurred the interface, unless the radio lobe lies over the thermal plasma, or the thermal plasma is accelerating the radio lobe.

However, such a conclusion is premature, since the result (5.4) is unrealistic. The magnetic fields in the radio plasma and thermal gas are expected to become concentrated and ordered near the interface and the magnetic layer should inhibit the RT instability (e.g., Carlyle and Hillier 2017). A full treatment of the RT instability then requires a model for the magnetic structure. Since the magnetic field is expected to lie predominantly parallel to the interface, but with no consistent direction on the large scale, and with the field strength decreasing away from the interface, no analytic or numerical calculation to date provides a sufficient treatment of the growth of the instability. However, an approximate result (validated by a comparison with simpler field models, such as that of Goldston and Rutherford 1995) can be obtained by

modelling the field as providing surface energy that mimics surface tension. Surface tension, σ_T, introduces a wavelength of maximum instability

$$\lambda_* = 2\pi \left(\frac{3\sigma_T}{(\rho_a - \rho_b)g} \right)^{1/2} \tag{5.5}$$

and suppresses the RT instability completely for modes with $\lambda < \lambda_*/\sqrt{3}$. The rate of growth of the RT instability is modified to

$$\Gamma = \left[2\pi \frac{g}{\lambda} \left\{ \frac{\rho_a - \rho_b}{\rho_a + \rho_b} - \frac{4\pi^2 \sigma_T}{g\lambda^2(\rho_a + \rho_b)} \right\} \right]^{1/2} \tag{5.6}$$

and takes a maximum value of

$$\Gamma_* = \left[\frac{4g^3(\rho_a - \rho_b)^3}{27\sigma_T(\rho_a + \rho_b)^2} \right]^{1/4} \tag{5.7}$$

at $\lambda = \lambda_*$.

The model quantity σ_T is taken as arising from magnetic field energy density u_B concentrated in a layer of thickness d at the edge of the radio lobe. d could be the vertical scale on which the RT instability causes field bunching, or some scale established by the dynamics of the expansion of the radio lobe. The effective surface tension is then

$$\sigma_T = u_B d \quad . \tag{5.8}$$

I take the value of u_B as some multiple, f_B, of the minimum-energy pressure in the lobes of Cygnus A, so that $u_B = 3f_B \times 10^{-10}$ J m^{-3}. The gas in region 5 has $\rho_a \approx 3 \times 10^{-22}$ kg m^{-3} (Table 3). Equation (5.5) then gives a scale of maximum instability

$$\lambda_* \approx 40 f_B^{1/2} \, (d/\mathrm{kpc})^{1/2} \ \mathrm{kpc} \tag{5.9}$$

which exceeds the radius $R \sim 30$ kpc of Cygnus A's cocoon shock unless the magnetic layer is thin or f_B is small. That is, a magnetic layer of thickness > 0.1 kpc at the edge of the radio plasma bubble east of region 5, can fully stabilise the interface against RT instabilities with local magnetic field enhancements of less than a factor of 3 ($f_B \lesssim 10$). The field is then less than 90 nT.

I quantified the sharpness of the interface at region 5 by measuring the width of count profiles perpendicular to the interface at four positions along its length (see Fig. 5.15). I specified the interface width as the distance between counts corresponding to 0.25 and 0.75 of the maximum

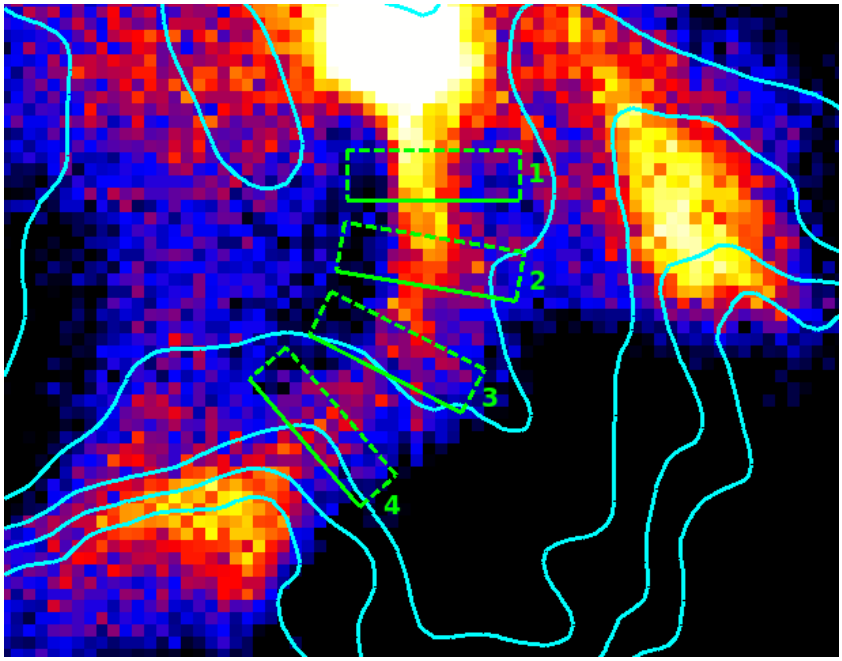

Figure 5.15: Merged *Chandra* event file image of Cygnus A observations listed in Table 5.1. with native 0.492 arcsec pixels, zoomed in on the south rib and associated arm with radio contours from Figure 5.1 overlaid in cyan. Each box indicates the position of extracted counts profiles. Boxes are of width 2 arcseconds with counts in the profiles averaged over the thickness of the box.

above the surrounding background. This measured width, $\sigma_{\rm obs}$, is where $\sigma^2_{\rm obs} = \sigma^2_{\rm intrinsic} + \sigma^2_{\rm PSF}$. I found $\sigma_{\rm PSF}$ based on a simulated PSF generated using the *Chandra* software `ChaRT` and `MARX`. I defined the spectrum using the data for region 5, and projected the ray tracings onto the ACIS-I detector at the centre of region 5 on ObsID 5831. The PSF is a sum of 100 simulated PSFs giving a total exposure of over 5 Ms. $\sigma_{\rm PSF}$, the width between 0.25 and 0.75 of the maximum counts of the PSF, is measured to be 0.43 arcsec (470 kpc).

The count profiles from each of the projection boxes are shown in Figure 5.16, along with the estimated upper limit on $\sigma_{\rm intrinsic}$, and show a typical PSF-corrected interface width of around 400 pc.

For a mode of $\lambda \approx 400$ pc to be unstable, $d < 0.2 f_B^{-1}$ pc. Such a small scale for a magnetic layer seems implausible. Thus I expect that the RT instability at the edge of region 5, and by extension at the other sharp edges in Cygnus A, will be suppressed by the effective surface tension of magnetised layers at the edge of the radio lobe, even if the plasmas are in an RT-unstable configuration.

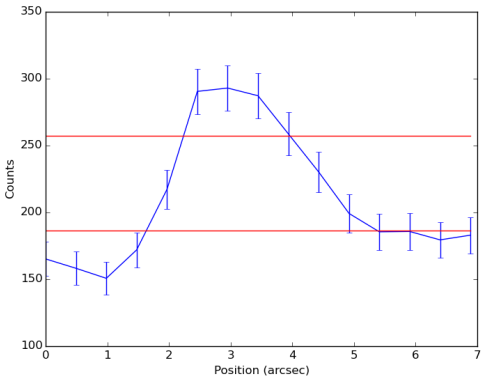

(a) Profile 1; After PSF correction, $\sigma_{\rm intrinsic} < 460$ pc (0.42 arcsec)

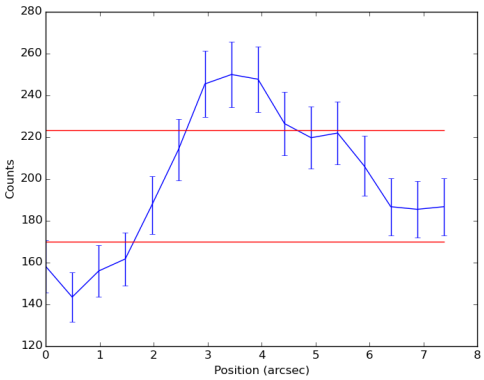

(b) Profile 2; After PSF correction, $\sigma_{\rm intrinsic} < 880$ pc (0.81 arcsec)

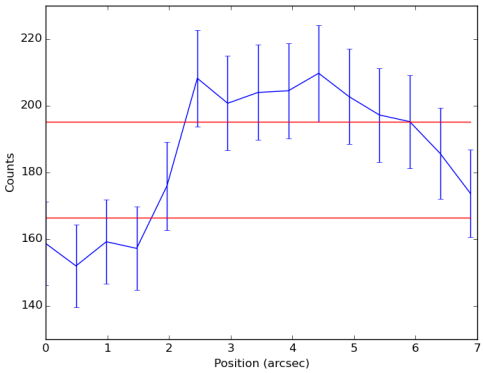

(c) Profile 3; After PSF correction $\sigma_{\rm intrinsic} < 400$ pc (0.37 arcsec)

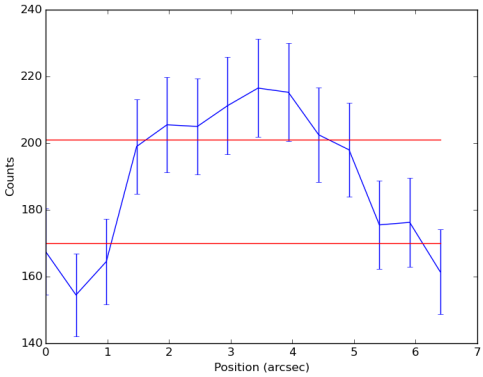

(d) Profile 4; After PSF correction, $\sigma_{\rm intrinsic} < 370$ pc (0.34 arcsec)

Figure 5.16: Count profiles of the various regions along the south rib. Red lines indicate the 0.25 and 0.75 of the maximum counts above the background.

It should be noted that adding a surface-tension-like energy in magnetic field to the edges of the radio lobes in this way has little effect on the estimated lobe pressure since the pressure differential introduced is a factor $2f_B d/R$ less than the minimum energy pressure, and this factor is small for any plausible magnetic layer.

5.8 An Origin for the Ribs

It is unlikely that the ribs are formed from a large-scale accretion event with gas flowing into the Cygnus A nucleus as suggested by Smith et al. (2002). The amount of mass calculated in the ribs is of order $10^{10} M_{\odot}$, which is much larger than expected in accretion disks. Mathews and Guo (2010) suggest that the ribs may be the expanded remnant of denser gas formerly located near the centre of Cygnus A, which has been shocked and heated by the AGN during the early stages of FRII development. The uniform low entropies seen across the rib structure imply that not a lot of strong shock heating has occurred within the structure.

Because of the total mass, morphology and dynamical ages of the ribs, I suggest that they result from the destruction of the cool core of the Cygnus A cluster during the early stages of jet propagation. After the radio outburst was triggered, the radio jets would have passed through the cool core, heating the gas and perhaps causing it to fragment and expand if the break out is slow. Backflow antiparallel to the jet's motion after the jets exit the cool core could cause the fragments to roll up into the cylindrical filaments, as is seen in simulations with cylindrical symmetry (Mathews and Guo, 2010, 2012). The ribs are then lifted to the central inside surface of the cocoon rim by the pressure of the underlying structure.

It is possible that a minor merger between the Cygnus A host galaxy and another galaxy had some impact in shaping the ribs. The favoured explanation for a transient detected in both K-band observations from Keck II (Canalizo et al., 2003) and new JVLA observations (Perley et al., 2017) is that it represents a secondary supermassive black hole in orbit around the Cygnus A primary. It is speculated that this merger delivered the gas which caused the ignition of the radio source in Cygnus A, and is also the origin of the transient. However, while it is possible that a merger had some impact on the shaping of ribs, it is not the overall origin of the gas, the large mass I measure argues against the ribs originating as gas stripped from the interstellar medium (ISM).

This interpretation suggests that the volume of the ribs is more likely to be represented by

the projected cylinders and spheres, than a geometry that fills the cocoon. This gives a total mass in the structure of $(2.1 \pm 0.1) \times 10^{10} M_{\odot}$, which matches well with the gas masses found in the cool cores of other clusters (Vikhlinin et al., 2006; Hogan et al., 2017). The rib structure is a similar size to the cool cores of other clusters, measuring around 50 kpc across along its north-south axis (Vikhlinin et al., 2006; Pratt et al., 2007). This model suggests that the pressures and entropies across the rib structure should vary by only modest functions (as seen across smoother structures in other cluster cool cores by Panagoulia et al. 2014), and those which I measure vary only by a factor of 2. Pressure equilibrium with the lobes means that the ribs are no longer undergoing local expansion and will expand and contract with the cocoon.

The southwestern temperature deficit seen in Figure 5.10 could result if the host galaxy of Cygnus A was a few kpc to the northeast of the cluster centre at the start of the radio outburst. BCGs are frequently found to be off-centre as a result of mergers (Martel et al., 2014) and Cygnus A is thought to be undergoing a merger currently with a sub-cluster to its northwest (Wise et al., prep).

Parts of this explanation and the lack of gas mass transport to outer regions seen here are similar to results of simulations of GHz-peak spectrum objects undertaken by Sutherland and Bicknell (2007). Obviously, those sources are far smaller than Cygnus A (around 60 times) and have disrupted their ISMs rather than a cluster cool core as is inferred for Cygnus A.

The rib filaments may be associated with enhanced magnetic fields. This, in combination with the already clear density variations in the region, suggests there would be rotation measure structures present across the central region. Unfortunately, the rotation measure maps of Dreher et al. (1987), which find a RMs of up to a few thousand rad m^{-2}, do not cover the central regions containing the ribs. There is a significant amount of gas in the region, indicating the rotation measure could be large, perhaps up to 10,000 rad m^{-2} depending on the degree of magnetic ordering in the interfaces. Radio telescopes such as LOFAR and JVLA could provide measurements of such high RMs and RM gradients near the ribs, but these measurements will be challenging: they must be done at low frequencies so that synchrotron emission in these regions is bright; at high angular resolution to resolve the cavity edges; at high spectral resolution to avoid depolarisation; and at high dynamic range. The question of whether the thermal gas associated with the ribs is in the interior regions of the radio lobes should also be answered by radio polarimetry.

5.9 Summary

I have used X-ray spectroscopy from very deep *Chandra* observations to investigate the rib-like structure within the cocoon shock of Cygnus A and have confirmed it to be dominated by thermal emission with an average temperature of about 4 keV (Section 5.4.2, Table 5.2).

Dynamical timescales for the ribs are somewhat less than the estimated age of the shock front, suggesting that the gas is in local pressure equilibrium with its surroundings and expanding with the cocoon (Section 5.5.1, Table 5.5). Similarities in the pressures across the rib structure suggest that it is a coherent structure with a single dynamical origin (Sections 5.5 and 5.6.2).

The clumpy, filamentary, rib-like structure is likely debris resulting from disintegration of the cool core of the Cygnus A cluster during the early stages of the current epoch of activity (Section 5.8). The gas now lies on the central inside surface of the cocoon rim (Section 5.8). The pressure across the ribs is roughly constant if the filaments are modelled as structures lying within a sheath; this is not the case if some are elongated structures projected to fill the radio lobes.

I have discovered that the gas exhibits a temperature structure, with the southwestern part of the ribs cooler than the rest (Figure 5.10). Plotting the temperature as a function of angle 5-10 arcseconds and 10-15 arcseconds from the core shows an oscillatory pattern with an amplitude of about 1 keV providing a quantitative measure of the temperature gradient (Figure 5.12). I suggest that the X-ray gas in the southwest region is cooler and the AGN was a few kpc northeast of the cluster centre at the start of the outburst.

RT instabilities are not active in the sharp edge measured in detail for one of the gas filaments. I show that they could have been suppressed by magnetised layers at the edge of the radio lobe (Section 5.7).

6

Conclusion

In this thesis, I have studied the interactions between the radio plasma and X-ray gas in local radio galaxies, with specific emphasis on understanding the occurrence, morphologies and origins of X-ray gas belts, and their impact upon AGN feedback and fuelling. Here, I review the key results of this work, along with suggesting further interesting studies which could be undertaken.

6.1 Summary of results

In Chapter 3, I reported measurements of an X-ray gas belt in 3C 386, establishing that it is thermal emission, and displays a temperature structure where the gas closer to the core is cooler than the outer part of the belt, which itself has a temperature similar to the external medium. I interpret this structure as indicating that the belt is likely formed of a combination of gas components. The outer belt is formed of a 'buoyancy-driven inflow' of part of the group gas atmosphere, caused by the buoyant rising of the radio lobes through the ambient medium away from the core. This hot group gas is flowing towards a relic cool core, composed of old, unheated group gas which predates the radio activity in 3C 386. It is possible that in the future, this inflow could lead to a resupply of fuel to the central AGN, caused by the gas reaching the parsec-scale regions surrounding the central black hole, which would lead to 3C 386, which currently shows no evidence of relativistic particle acceleration, resuming a high level of radio activity. This

provides an example of a direct feedback loop, in which the radio source responds to its large scale environment on scales of hundreds of kpc.

I expand this study in Chapter 4, to a total of 15 sources with gas belts in the low-redshift 3CRR sample, showing that belts are a common feature, at least among low-redshift radio galaxies. The gas belts are again found to be dominated by thermal emission. In the cases where the measurement could be made, the outer belt is hotter than the inner belt. However, unlike in 3C 386, the outer belt is also cooler than the external medium of the sources. I find that the origins of the gas belts in this sample are diverse, with evidence of inflow on large scales driven by the radio lobe, outflow driven by the expanding radio lobes, gas stripped from merging galaxies and relatively stagnant gas from either galactic coronae or old merging galaxies. Across the sample, the belts are in approximate pressure balance with the lobe pressure calculated from inverse-Compton X-rays. The majority of sources are also found to be in rough pressure balance with their immediate external medium.

Throughout the sample, inverse-Compton emission is detected in the lobes of all FRII sources, and unusually in the plumes of five of the nine FRI radio galaxies. From this I find that the amount by which the magnetic field strength tends to be lower than the minimum energy value is similar for FRIs and FRIIs, if minimum energy for both is calculated assuming no protons. FRIs in clusters are assumed to need protons to provide pressure support with the external medium, this result provides the first evidence that magnetic field strengths are largely oblivious to non-radiating particles in radio galaxy plumes and lobes.

In Chapter 5, I use X-ray spectroscopy from very deep *Chandra* observations to investigate the rib-like structure within the cocoon shock of Cygnus A. This structure is dominated by thermal emission, with an average temperature of about 4 keV. The gas exhibits a temperature structure, with the southwestern part of the ribs cooler than the rest. Plotting the temperature as a function of angle 5-10 arcsec and 10-15 arcsec from the core shows an oscillatory pattern with an amplitude of about 1 keV, providing a quantitative measure of the temperature gradient. This temperature difference is possible if the AGN was a few kpc northeast of the cluster centre at the start of the outburst. I find that Rayleigh-Taylor instabilities are not active in the sharp edge measured in detail for one of the gas filaments, showing that they could have been suppressed by magnetised layers at the edge of the radio lobe. Dynamical timescales for the ribs are somewhat less than the estimated age of the shock front, which suggests that the gas is in local pressure equilibrium with its surroundings and expanding with the cocoon. The similarities in pressure

across the rib structure suggest it is a coherent structure with a single dynamical origin. The filamentary, rib-like structure is likely debris resulting from the fragmentation of the cool core of the Cygnus A cluster during the early stages of the current epoch of radio activity. The gas now likely lies on the central inside surface of the cocoon rim, after being lifted by the pressure of the underlying structure.

6.2 Further Work

The interpretation of some of the belts is limited, due to a lack of robust temperature structure information. Without this, it is difficult to state with complete confidence whether sources such as 3C 35, 3C 98 and 3C 76.1 have outflow or inflow origins. The study of the ambient medium in some of the sources is limited by weak detections or a lack of detection of the IGM/ICM. In these instances, current X-ray missions are unlikely to be able improve on what is currently measured. Future missions, such as *ATHENA*, with its significantly improved sensitivity, may be able to place better constraints on the properties of weak group and cluster gas.

It would be interesting to study whether the ribs in Cygnus A are associated with enhanced magnetic fields, as, in combination with the clear density variations across the ribs, there should be large rotation measure structures across the central region. Current generation radio telescopes such as LOFAR and JVLA could provide measurements of these rotation measures, although the measurements would be challenging. It is currently unclear whether the thermal gas associated with the ribs is in the interior regions of the radio lobes, or sitting on the outside of the cocoon. This question could be answered with radio polarimetry. With regard to Cygnus A, but not entirely related to the investigation of the ribs, I am also interested in using a Bayesian deconvolution (Stein et al., 2015; McKeough et al., 2016) to test whether it is possible to detect what appears to be a secondary AGN detected in the radio (Perley et al., 2017) in the X-rays, although given the complexities of the central regions of Cygnus A, this would be incredibly difficult.

This work is mostly focussed on the investigation of low-redshift sources. It would be interesting to investigate a sample of sources at higher redshift, perhaps up to redshifts of 0.5, and see if gas belts remain in a large fraction of sources at earlier epochs. There is evidence of some X-ray belt emission in sources up to $z \sim 0.2$ such as 3C 401 (Reynolds et al., 2005) and 3C 444 (Croston et al., 2011). I would also be interested in investigating whether rib-like disrupted cool

cores are a feature of other high power FR II sources, with 3C 444 seeming to host a similar structure. Gopal-Krishna and Wiita (2009) identifies a number of radio galaxies, which they call 'superdisks', which are characterised by wide, elongated emission gaps between the two radio lobes. The optically-identified superdisks have similar dimensions to the belts in this sample, and even includes 3C 192 which was studied in this thesis. A targeted follow-up of some of the higher redshift sources in the sample of superdisks could provide evidence for higher redshift X-ray gas belts.

Bibliography

Allen, L. R., B. Anderson, R. G. Conway, H. P. Palmer, V. C. Reddish, and B. Rowson

1962. Observations of 384 radio sources at a frequency of 158 Mc/s with a long baseline interferometer. MNRAS, 124:477.

Allen, S. W., R. J. H. Dunn, A. C. Fabian, G. B. Taylor, and C. S. Reynolds

2006. The relation between accretion rate and jet power in X-ray luminous elliptical galaxies. MNRAS, 372:21–30.

Anders, E. and N. Grevesse

1989. Abundances of the elements - Meteoritic and solar. Geochim. Cosmochim. Acta, 53:197–214.

Anderson, M. E., J. N. Bregman, and X. Dai

2013. Extended Hot Halos around Isolated Galaxies Observed in the ROSAT All-Sky Survey. *ApJ*, 762:106.

Arnaud, K. A.

1996. XSPEC: The First Ten Years. In *Astronomical Data Analysis Software and Systems V*, G. H. Jacoby and J. Barnes, eds., volume 101 of *Astronomical Society of the Pacific Conference Series*, P. 17.

Arnaud, K. A., A. C. Fabian, S. A. Eales, C. Jones, and W. Forman

1984. The intracluster gas around Cygnus-A. MNRAS, 211:981–989.

Baum, S. A., T. M. Heckman, A. Bridle, W. J. M. van Breugel, and G. K. Miley

1988. Extended optical-line-emitting gas in radio galaxies - Broad-band optical, narrow-band optical, and radio imaging of a representative sample. ApJS, 68:643–714.

Beckmann, V. and C. R. Shrader

2012. *Active Galactic Nuclei*.

Belsole, E., D. M. Worrall, M. J. Hardcastle, M. Birkinshaw, and C. R. Lawrence

2004. XMM-Newton observations of three high-redshift radio galaxies. MNRAS, 352:924–938.

Belsole, E., D. M. Worrall, M. J. Hardcastle, and J. H. Croston

2007. High-redshift Fanaroff-Riley type II radio sources: large-scale X-ray environment. MNRAS, 381:1109–1126.

Bennett, A. S.

1962. The revised 3C catalogue of radio sources. MmRAS, 68:163.

Best, P. N. and T. M. Heckman

2012. On the fundamental dichotomy in the local radio-AGN population: accretion, evolution and host galaxy properties. MNRAS, 421:1569–1582.

Bieri, R., Y. Dubois, J. Silk, G. A. Mamon, and V. Gaibler

2016. External pressure-triggering of star formation in a disc galaxy: a template for positive feedback. MNRAS, 455:4166–4182.

Birkinshaw, M., R. A. Laing, and J. A. Peacock

1981. Radio synthesis observations of 3C 296, 3C 442A and 3C 449 at 0.4, 1.4 and 2.7 GHz. MNRAS, 197:253–263.

Birkinshaw, M. and D. M. Worrall

1993. The X-ray structure and spectrum of NGC 6251. ApJ, 412:568–585.

Bîrzan, L., B. R. McNamara, P. E. J. Nulsen, C. L. Carilli, and M. W. Wise

2008. Radiative Efficiency and Content of Extragalactic Radio Sources: Toward a Universal Scaling Relation between Jet Power and Radio Power. *ApJ*, 686:859–880.

Bîrzan, L., D. A. Rafferty, M. Brüggen, and H. T. Intema

2017. A study of high-redshift AGN feedback in SZ cluster samples. MNRAS, 471:1766–1787.

Bîrzan, L., D. A. Rafferty, B. R. McNamara, M. W. Wise, and P. E. J. Nulsen

2004. A Systematic Study of Radio-induced X-Ray Cavities in Clusters, Groups, and Galaxies. ApJ, 607:800–809.

Blandford, R. D. and D. G. Payne

1982. Hydromagnetic flows from accretion discs and the production of radio jets. MNRAS, 199:883–903.

Blandford, R. D. and R. L. Znajek

1977. Electromagnetic extraction of energy from Kerr black holes. MNRAS, 179:433–456.

Bondi, H.

1952. On spherically symmetrical accretion. MNRAS, 112:195.

Bowyer, C. S., M. Lampton, J. Mack, and F. de Mendonca

1970. Detection of X-Ray Emission from 3c 273 and NGC 5128. ApJ, 161:L1.

Brunetti, G., M. Bondi, A. Comastri, and G. Setti

2002. Chandra discovery of extended non-thermal emission in 3C 207 and the spectrum of the relativistic electrons. A&A, 381:795–809.

Burbidge, G. R.

1956. On Synchrotron Radiation from Messier 87. ApJ, 124:416.

Buttiglione, S., A. Capetti, A. Celotti, D. J. Axon, M. Chiaberge, F. D. Macchetto, and W. B. Sparks

2009. An optical spectroscopic survey of the 3CR sample of radio galaxies with z ¡ 0.3. I. Presentation of the data. *AAP*, 495:1033–1060.

Byram, E. T., T. A. Chubb, and H. Friedman

1966. Cosmic X-Ray Sources-Galactic and Extragalactic. AJ, 71:379.

Canalizo, G., C. Max, D. Whysong, R. Antonucci, and S. E. Dahm

2003. Adaptive Optics Imaging and Spectroscopy of Cygnus A. I. Evidence for a Minor Merger. ApJ, 597:823–831.

Carilli, C. L., R. A. Perley, J. W. Dreher, and J. P. Leahy

1991. Multifrequency radio observations of Cygnus A - Spectral aging in powerful radio galaxies. ApJ, 383:554–573.

Carlyle, J. and A. Hillier

2017. The non-linear growth of the magnetic Rayleigh-Taylor instability. A&A, 605:A101.

Cash, W.

1979. Parameter estimation in astronomy through application of the likelihood ratio. ApJ, 228:939–947.

Cavagnolo, K. W., M. Donahue, G. M. Voit, and M. Sun

2009. Intracluster Medium Entropy Profiles for a Chandra Archival Sample of Galaxy Clusters. ApJS, 182:12–32.

Cavaliere, A. and R. Fusco-Femiano

1978. The Distribution of Hot Gas in Clusters of Galaxies. A&A, 70:677.

Chandrasekhar, S.

1961. *Hydrodynamic and hydromagnetic stability*.

Chen, R., B. Peng, R. G. Strom, and J. Wei

2012. Group of galaxies around the giant radio galaxy 4C 73.08. MNRAS, 422:3004–3009.

Cheung, C. C.

2007. FIRST "Winged" and X-Shaped Radio Source Candidates. AJ, 133:2097–2121.

Chiaberge, M., A. Capetti, and A. Celotti

2000. The HST view of the FR I / FR II dichotomy. A&A, 355:873–879.

Chiu, I., J. Mohr, M. McDonald, S. Bocquet, M. L. N. Ashby, M. Bayliss, B. A. Benson, L. E. Bleem, M. Brodwin, S. Desai, J. P. Dietrich, W. R. Forman, C. Gangkofner, A. H. Gonzalez, C. Hennig, J. Liu, C. L. Reichardt, A. Saro, B. Stalder, S. A. Stanford, J. Song, T. Schrabback, R. Šuhada, V. Strazzullo, and A. Zenteno

2016. Baryon content of massive galaxy clusters at $0.57 < z < 1.33$. MNRAS, 455:258–275.

Chon, G., H. Böhringer, M. Krause, and J. Trümper

2012. Discovery of an X-ray cavity near the radio lobes of Cygnus A indicating previous AGN activity. A&A, 545:L3.

Cowie, L. L. and J. Binney

1977. Radiative regulation of gas flow within clusters of galaxies - A model for cluster X-ray sources. ApJ, 215:723–732.

Croston, J. H., M. Birkinshaw, M. J. Hardcastle, and D. M. Worrall

2004. X-ray emission from the nuclei, lobes and hot-gas environments of two FR II radio galaxies. MNRAS, 353:879–889.

Croston, J. H., M. J. Hardcastle, M. Birkinshaw, and D. M. Worrall

2003. XMM-Newton observations of the hot-gas atmospheres of 3C 66B and 3C 449. MNRAS, 346:1041–1054.

Croston, J. H., M. J. Hardcastle, M. Birkinshaw, D. M. Worrall, and R. A. Laing

2008a. An XMM-Newton study of the environments, particle content and impact of low-power radio galaxies. MNRAS, 386:1709–1728.

Croston, J. H., M. J. Hardcastle, D. E. Harris, E. Belsole, M. Birkinshaw, and D. M. Worrall

2005. An X-Ray Study of Magnetic Field Strengths and Particle Content in the Lobes of FR II Radio Sources. *ApJ*, 626:733–747.

Croston, J. H., M. J. Hardcastle, B. Mingo, D. A. Evans, D. Dicken, R. Morganti, and C. N. Tadhunter

2011. A Large-scale Shock Surrounding a Powerful Radio Galaxy? ApJ, 734:L28.

Croston, J. H., J. Ineson, and M. Hardcastle

2018. Particle content, radio-galaxy morphology and jet power: all radio-loud AGN are not equal. MNRAS.

Croston, J. H., G. W. Pratt, H. Böhringer, M. Arnaud, E. Pointecouteau, T. J. Ponman, A. J. R. Sanderson, R. F. Temple, R. G. Bower, and M. Donahue

2008b. Galaxy-cluster gas-density distributions of the representative XMM-Newton cluster structure survey (REXCESS). A&A, 487:431–443.

Croton, D. J., V. Springel, S. D. M. White, G. De Lucia, C. S. Frenk, L. Gao, A. Jenkins, G. Kauffmann, J. F. Navarro, and N. Yoshida

2006. The many lives of active galactic nuclei: cooling flows, black holes and the luminosities and colours of galaxies. MNRAS, 365:11–28.

Curtis, H. D.

1918. Descriptions of 762 Nebulae and Clusters Photographed with the Crossley Reflector. *Publications of Lick Observatory*, 13:9–42.

Dariush, A., H. G. Khosroshahi, T. J. Ponman, F. Pearce, S. Raychaudhury, and W. Hartley

2007. The mass assembly of fossil groups of galaxies in the Millennium simulation. MNRAS,

382:433–442.

de Koff, S., S. A. Baum, W. B. Sparks, J. Biretta, D. Golombek, F. Macchetto, P. McCarthy, and G. K. Miley

1996. HST Snapshot Survey of 3CR Radio Source Counterparts. I. Intermediate Redshifts. ApJS, 107:621.

de Vries, M. N., M. W. Wise, D. Huppenkothen, P. E. J. Nulsen, B. Snios, M. J. Hardcastle, et al. in prep. Thermal and Non-thermal X-ray Emission in the Environment Surrounding the Powerful Radio Galaxy Cygnus A.

Dickey, J. M. and F. J. Lockman

1990. H I in the Galaxy. ARA&A, 28:215–261.

Dreher, J. W., C. L. Carilli, and R. A. Perley

1987. The Faraday rotation of Cygnus A - Magnetic fields in cluster gas. ApJ, 316:611–625.

Dubois, Y., S. Peirani, C. Pichon, J. Devriendt, R. Gavazzi, C. Welker, and M. Volonteri

2016. The HORIZON-AGN simulation: morphological diversity of galaxies promoted by AGN feedback. MNRAS, 463:3948–3964.

Duffy, R. T., D. M. Worrall, M. Birkinshaw, and R. P. Kraft

2016. Buoyancy-driven inflow to a relic cold core: the gas belt in radio galaxy 3C 386. MNRAS, 459:4508–4517.

Duffy, R. T., D. M. Worrall, M. Birkinshaw, P. E. J. Nulsen, M. W. Wise, M. N. de Vries, B. Snios, W. G. Mathews, R. A. Perley, M. J. Hardcastle, D. A. Rafferty, B. R. McNamara, A. C. Edge, J. P. McKean, C. L. Carilli, J. H. Croston, L. E. H. Godfrey, and R. A. Laing

2018. The X-ray Ribs Within the Cocoon Shock of Cygnus A. MNRAS.

Dunn, R. J. H., A. C. Fabian, and G. B. Taylor

2005. Radio bubbles in clusters of galaxies. MNRAS, 364:1343–1353.

Edge, D. O., J. R. Shakeshaft, W. B. McAdam, J. E. Baldwin, and S. Archer

1959. A survey of radio sources at a frequency of 159 Mc/s. MmRAS, 68:37–60.

Eigenthaler, P. and W. W. Zeilinger

2013. Age and metallicity gradients in fossil ellipticals. A&A, 553:A99.

Evans, D. A., D. M. Worrall, M. J. Hardcastle, R. P. Kraft, and M. Birkinshaw

2006. Chandra and XMM-Newton Observations of a Sample of Low-Redshift FR I and FR II Radio Galaxy Nuclei. *ApJ*, 642:96–112.

Fabian, A. C.

1994. Cooling Flows in Clusters of Galaxies. ARA&A, 32:277–318.

Fabian, A. C. and P. E. J. Nulsen

1977. Subsonic accretion of cooling gas in clusters of galaxies. MNRAS, 180:479–484.

Fabian, A. C., J. S. Sanders, S. Ettori, G. B. Taylor, S. W. Allen, C. S. Crawford, K. Iwasawa, and R. M. Johnstone

2001. Chandra imaging of the X-ray core of Abell 1795. MNRAS, 321:L33–L36.

Fabian, A. C., J. S. Sanders, G. B. Taylor, S. W. Allen, C. S. Crawford, R. M. Johnstone, and K. Iwasawa

2006. A very deep Chandra observation of the Perseus cluster: shocks, ripples and conduction. MNRAS, 366:417–428.

Fanaroff, B. L. and J. M. Riley

1974. The morphology of extragalactic radio sources of high and low luminosity. MNRAS, 167:31P–36P.

Faraday, M.

1846. Experimental Researches in Electricity. Nineteenth Series. *Philosophical Transactions of the Royal Society of London Series I*, 136:1–20.

Feigelson, E. D. and C. J. Berg

1983. X-ray observations of 20 3CR radio galaxies and their environs. *ApJ*, 269:400–415.

Feretti, L., R. Fanti, P. Parma, S. Massaglia, E. Trussoni, and W. Brinkmann

1995. ROSAT observations of the B2 radio galaxies 1615+35 and 1621+38: implications for the radio source confinement. A&A, 298:699.

Fernandes, C. A. C., M. J. Jarvis, A. Martínez-Sansigre, S. Rawlings, J. Afonso, M. J. Hardcastle, M. Lacy, J. A. Stevens, and E. Vardoulaki

2015. Black hole masses, accretion rates and hot- and cold-mode accretion in radio galaxies at z $\approx$ 1. MNRAS, 447:1184–1203.

Ferrari, A.

1998. Modeling Extragalactic Jets. ARA&A, 36:539–598.

Finoguenov, A., M. Ruszkowski, C. Jones, M. Brüggen, A. Vikhlinin, and E. Mandel

2008. In-Depth Chandra Study of the AGN Feedback in Virgo Elliptical Galaxy M84. ApJ, 686:911–917.

Floyd, D. J. E., D. Axon, S. Baum, A. Capetti, M. Chiaberge, D. Macchetto, J. Madrid, G. Miley, C. P. O'Dea, E. Perlman, A. Quillen, W. Sparks, and G. Tremblay

2008. Hubble Space Telescope Near-infrared Snapshot Survey of 3CR Radio Source Counterparts. II. An Atlas and Inventory of the Host Galaxies, Mergers, and Companions. *ApJS*, 177:148–173.

Forman, W. and C. Jones

1982. X-ray-imaging observations of clusters of galaxies. ARA&A, 20:547–585.

Forman, W., C. Jones, and W. Tucker

1985. Hot coronae around early-type galaxies. ApJ, 293:102–119.

Gerwin, R. A.

1968. Stability of the Interface between Two Fluids in Relative Motion. *Reviews of Modern Physics*, 40:652–658.

Gilkis, A. and N. Soker

2012. Heating the intra-cluster medium perpendicular to the jets axis. MNRAS, 427:1482–1489.

Gizani, N. A. B., M. A. Garrett, and J. P. Leahy

2002. The Multiwavelength Study of Two Unique Radio Galaxies. *Journal of Astrophysics and Astronomy*, 23:89.

Goldston, R. J. and P. H. Rutherford

1995. *Introduction to Plasma Physics*, Plasma Physics Series. Institute of Physics Pub.

Gonzalez, A. H., S. Sivanandam, A. I. Zabludoff, and D. Zaritsky

2013. Galaxy Cluster Baryon Fractions Revisited. ApJ, 778:14.

Gopal-Krishna and P. J. Wiita

2000. Superdisks in Radio Galaxies. ApJ, 529:189–200.

Gopal-Krishna and P. J. Wiita

2009. Superdisks and the structural asymmetry of radio galaxies. New A, 14:51–58.

Hanbury Brown, R., R. C. Jennison, and M. K. D. Gupta

1952. Apparent Angular Sizes of Discrete Radio Sources: Observations at Jodrell Bank, Manchester. Nature, 170:1061–1063.

Hardcastle, M. J., M. Birkinshaw, R. A. Cameron, D. E. Harris, L. W. Looney, and D. M. Worrall

2002. Magnetic Field Strengths in the Hot Spots and Lobes of Three Powerful Fanaroff-Riley Type II Radio Sources. ApJ, 581:948–973.

Hardcastle, M. J. and J. H. Croston

2010. Searching for the inverse-Compton emission from bright cluster-centre radio galaxies.

MNRAS, 404:2018–2027.

Hardcastle, M. J., D. E. Harris, D. M. Worrall, and M. Birkinshaw

2004. The Origins of X-Ray Emission from the Hot Spots of FR II Radio Sources. ApJ, 612:729–748.

Hardcastle, M. J., R. P. Kraft, D. M. Worrall, J. H. Croston, D. A. Evans, M. Birkinshaw, and S. S. Murray

2007. The Interaction between Radio Lobes and Hot Gas in the Nearby Radio Galaxies 3C 285 and 3C 442A. *ApJ*, 662:166–181.

Hardcastle, M. J. and M. G. H. Krause

2013. Numerical modelling of the lobes of radio galaxies in cluster environments. MNRAS, 430:174–196.

Hardcastle, M. J. and M. G. H. Krause

2014. Numerical modelling of the lobes of radio galaxies in cluster environments - II. Magnetic field configuration and observability. MNRAS, 443:1482–1499.

Hardcastle, M. J., F. Massaro, D. E. Harris, S. A. Baum, S. Bianchi, M. Chiaberge, R. Morganti, C. P. O'Dea, and A. Siemiginowska

2012. The nature of the jet-driven outflow in the radio galaxy 3C 305. MNRAS, 424:1774–1789.

Hardcastle, M. J. and D. M. Worrall

1999. ROSAT X-ray observations of 3CRR radio sources. MNRAS, 309:969–990.

Hardcastle, M. J. and D. M. Worrall

2000. The environments of FRII radio sources. MNRAS, 319:562–572.

Hardcastle, M. J., D. M. Worrall, and M. Birkinshaw

1998. Dynamics of the radio galaxy 3C449. MNRAS, 296:1098–1104.

Hardcastle, M. J., D. M. Worrall, M. Birkinshaw, R. A. Laing, and A. H. Bridle

2005. A Chandra observation of the X-ray environment and jet of 3C 296. MNRAS, 358:843–850.

Harris, D. E., C. L. Carilli, and R. A. Perley

1994. X-ray emission from the radio hotspots of Cygnus A. Nature, 367:713–716.

Harris, D. E. and J. E. Grindlay

1979. The prospects for X-ray detection of inverse-Compton emission from radio source electrons and photons of the microwave background. MNRAS, 188:25–37.

Hess, K. M., E. M. Wilcots, and V. L. Hartwick

2012. Fresh Activity in Old Systems: Radio AGNs in Fossil Groups of Galaxies. AJ, 144:48.

Hillel, S. and N. Soker

2016. Heating the intracluster medium by jet-inflated bubbles. MNRAS, 455:2139–2148.

Hlavacek-Larrondo, J., A. C. Fabian, A. C. Edge, H. Ebeling, J. S. Sanders, M. T. Hogan, and G. B. Taylor

2012. Extreme AGN feedback in the MAssive Cluster Survey: a detailed study of X-ray cavities at z>0.3. MNRAS, 421:1360–1384.

Hodges-Kluck, E. J., C. S. Reynolds, C. C. Cheung, and M. C. Miller

2010. The Chandra View of Nearby X-Shaped Radio Galaxies. *ApJ*, 710:1205–1227.

Hogan, M. T., B. R. McNamara, F. Pulido, P. E. J. Nulsen, H. R. Russell, A. N. Vantyghem, A. C. Edge, and R. A. Main

2017. Mass Distribution in Galaxy Cluster Cores. ApJ, 837:51.

Hogbom, J. A.

1979. A study of the radio galaxies 3C111, 192, 219, 223, 315 and 452. A&AS, 36:173–192.

Hopkins, P. F., L. Hernquist, T. J. Cox, T. Di Matteo, B. Robertson, and V. Springel

2006. A Unified, Merger-driven Model of the Origin of Starbursts, Quasars, the Cosmic X-Ray Background, Supermassive Black Holes, and Galaxy Spheroids. ApJS, 163:1–49.

Hopkins, P. F., P. Torrey, C.-A. Faucher-Giguère, E. Quataert, and N. Murray

2016. Stellar and quasar feedback in concert: effects on AGN accretion, obscuration, and outflows. MNRAS, 458:816–831.

Hudson, D. S., R. Mittal, T. H. Reiprich, P. E. J. Nulsen, H. Andernach, and C. L. Sarazin

2010. What is a cool-core cluster? a detailed analysis of the cores of the X-ray flux-limited HIFLUGCS cluster sample. A&A, 513:A37.

Ineson, J., J. H. Croston, M. J. Hardcastle, R. P. Kraft, D. A. Evans, and M. Jarvis

2015. The link between accretion mode and environment in radio-loud active galaxies. MNRAS, 453:2682–2706.

Ineson, J., J. H. Croston, M. J. Hardcastle, and B. Mingo

2017. A representative survey of the dynamics and energetics of FR II radio galaxies. MNRAS, 467:1586–1607.

Isobe, H., H. Takasaki, and K. Shibata

2005. Measurement of the Energy Release Rate and the Reconnection Rate in Solar Flares. ApJ, 632:1184–1195.

Jackson, N., R. Beswick, A. Pedlar, G. H. Cole, W. B. Sparks, J. P. Leahy, D. J. Axon, and A. J. Holloway

2003. Observations of the neutral gas and dust in the radio galaxy 3C 305. MNRAS, 338:643–654.

Jennison, R. C. and M. K. Das Gupta

1953. Fine Structure of the Extra-terrestrial Radio Source Cygnus I. Nature, 172:996–997.

Kalberla, P. M. W., W. B. Burton, D. Hartmann, E. M. Arnal, E. Bajaja, R. Morras, and W. G. L.

Pöppel

2005. The Leiden/Argentine/Bonn (LAB) Survey of Galactic HI. Final data release of the combined LDS and IAR surveys with improved stray-radiation corrections. A&A, 440:775–782.

Kataoka, J. and Ł. Stawarz

2005. X-Ray Emission Properties of Large-Scale Jets, Hot Spots, and Lobes in Active Galactic Nuclei. ApJ, 622:797–810.

Kauffmann, G., T. M. Heckman, C. Tremonti, J. Brinchmann, S. Charlot, S. D. M. White, S. E. Ridgway, J. Brinkmann, M. Fukugita, P. B. Hall, Ž. Ivezić, G. T. Richards, and D. P. Schneider

2003. The host galaxies of active galactic nuclei. MNRAS, 346:1055–1077.

Kewley, L. J., B. Groves, G. Kauffmann, and T. Heckman

2006. The host galaxies and classification of active galactic nuclei. MNRAS, 372:961–976.

Konar, C., M. J. Hardcastle, J. H. Croston, and D. J. Saikia

2009. The dynamics of the giant radio galaxy 3C457. MNRAS, 400:480–491.

Kraft, R. P., J. Azcona, W. R. Forman, M. J. Hardcastle, C. Jones, and S. S. Murray

2006. The Hot Gas Environment of the Radio Galaxy 3C 388: Quenching the Accumulation of Cool Gas in a Cluster Core by a Nuclear Outburst. ApJ, 639:753–760.

Kraft, R. P., M. Birkinshaw, P. E. J. Nulsen, D. M. Worrall, J. H. Croston, W. R. Forman, M. J. Hardcastle, C. Jones, and S. S. Murray

2012. An Active Galactic Nucleus Driven Shock in the Intracluster Medium around the Radio Galaxy 3C 310. ApJ, 749:19.

Laing, R. A. and A. H. Bridle

2002. Dynamical models for jet deceleration in the radio galaxy 3C 31. MNRAS, 336:1161–1180.

Laing, R. A., J. M. Riley, and M. S. Longair

1983. Bright radio sources at 178 MHz - Flux densities, optical identifications and the cosmological evolution of powerful radio galaxies. *MNRAS*, 204:151–187.

Lazio, T. J. W., A. S. Cohen, N. E. Kassim, R. A. Perley, W. C. Erickson, C. L. Carilli, and P. C. Crane

2006. Cygnus A: A Long-Wavelength Resolution of the Hot Spots. ApJ, 642:L33–L36.

Leahy, J. P. and R. A. Perley

1991. VLA images of 23 extragalactic radio sources. *AJ*, 102:537–561.

Ledlow, M. J. and F. N. Owen

1996. 20 CM VLA Survey of Abell Clusters of Galaxies. VI. Radio/Optical Luminosity Functions. AJ, 112:9.

Leung, G. C. K., A. L. Coil, M. Azadi, J. Aird, A. Shapley, M. Kriek, B. Mobasher, N. Reddy, B. Siana, W. R. Freeman, S. H. Price, R. L. Sanders, and I. Shivaei

2017. The MOSDEF Survey: The Prevalence and Properties of Galaxy-wide AGN-driven Outflows at z $\approx$ 2. ApJ, 849:48.

Limber, D. N.

1959. Effects of Intracluster Gas and Duct upon the Virial Theorem. ApJ, 130:414.

Longair, M. S.

2011. *High Energy Astrophysics*.

Lynds, R.

1971. ON the Nature of the Galaxy Identified with 3c 386. *ApJL*, 168:L87.

Madrid, J. P., M. Chiaberge, D. Floyd, W. B. Sparks, D. Macchetto, G. K. Miley, D. Axon,

A. Capetti, C. P. O'Dea, S. Baum, E. Perlman, and A. Quillen

2006. Hubble Space Telescope Near-Infrared Snapshot Survey of 3CR Radio Source Counterparts at Low Redshift. *ApJS*, 164:307–333.

Mannering, E.

2013. A Multi-Wavelength Study of Radio-loud Active Galactic Nuclei. *Unpublished PhD thesis, University of Bristol*.

Mannering, E., D. M. Worrall, and M. Birkinshaw

2013. Galaxy gas ejection in radio galaxies: the case of 3C 35. *MNRAS*, 431:858–873.

Martel, A. R., S. A. Baum, W. B. Sparks, E. Wyckoff, J. A. Biretta, D. Golombek, F. D. Macchetto, S. de Koff, P. J. McCarthy, and G. K. Miley

1999. Hubble Space Telescope Snapshot Survey of 3CR Radio Source Counterparts. III. Radio Galaxies with z<0.1. ApJS, 122:81–108.

Martel, H., F. Robichaud, and P. Barai

2014. Major Cluster Mergers and the Location of the Brightest Cluster Galaxy. ApJ, 786:79.

Mathews, W. G.

1990. Interstellar events in elliptical galaxies. ApJ, 354:468–482.

Mathews, W. G. and F. Guo

2010. Self-consistent Evolution of Gas and Cosmic Rays in Cygnus A and Similar FR II Classical Double Radio Sources. ApJ, 725:1440–1451.

Mathews, W. G. and F. Guo

2012. Dynamics inside the Radio and X-Ray Cluster Cavities of Cygnus A and Similar FRII Sources. ApJ, 755:13.

Mayer, C. J.

1979. Multifrequency observations of 4C 73.08 - A new addition to the 3CR 'complete sample'. MNRAS, 186:99–106.

McKean, J. P. et al.

2016. LOFAR imaging of Cygnus A - direct detection of a turnover in the hotspot radio spectra. MNRAS, 463:3143–3150.

McKeough, K., A. Siemiginowska, C. C. Cheung, Ł. Stawarz, V. L. Kashyap, N. Stein, V. Stampoulis, D. A. van Dyk, J. F. C. Wardle, N. P. Lee, D. E. Harris, D. A. Schwartz, D. Donato, L. Maraschi, and F. Tavecchio

2016. Detecting Relativistic X-Ray Jets in High-redshift Quasars. ApJ, 833:123.

McNamara, B. R. and P. E. J. Nulsen

2007. Heating Hot Atmospheres with Active Galactic Nuclei. *ARAA*, 45:117–175.

McNamara, B. R., H. R. Russell, P. E. J. Nulsen, M. T. Hogan, A. C. Fabian, F. Pulido, and A. C. Edge

2016. A Mechanism for Stimulating AGN Feedback by Lifting Gas in Massive Galaxies. ApJ, 830:79.

Miller, N. A., M. J. Ledlow, F. N. Owen, and J. M. Hill

2002. Redshifts for a Sample of Radio-selected Poor Clusters. AJ, 123:3018–3040.

Miller, N. A., F. N. Owen, J. O. Burns, M. J. Ledlow, and W. Voges

1999. An X-Ray and Optical Investigation of the Environments around Nearby Radio Galaxies. *AJ*, 118:1988–2001.

Mingo, B., M. J. Hardcastle, J. H. Croston, D. Dicken, D. A. Evans, R. Morganti, and C. Tadhunter

2014. An X-ray survey of the 2 Jy sample - I. Is there an accretion mode dichotomy in radio-loud AGN? MNRAS, 440:269–297.

Morganti, R., T. A. Oosterloo, R. A. E. Fosbury, and C. N. Tadhunter

1995. Investigating beaming and orientation effects using a complete sample of radio sources. MNRAS, 274:393–406.

Mulchaey, J. S.

2000. X-ray Properties of Groups of Galaxies. ARA&A, 38:289–335.

Narayan, R. and I. Yi

1994. Advection-dominated accretion: A self-similar solution. ApJ, 428:L13–L16.

Nulsen, P. E. J., A. J. Young, R. P. Kraft, B. R. McNamara, and M. W. Wise

2015. Interaction of Cygnus A with its environment. In *Extragalactic Jets from Every Angle*, F. Massaro, C. C. Cheung, E. Lopez, and A. Siemiginowska, eds., volume 313 of *IAU Symposium*, Pp. 236–241.

O'Dea, C. P., S. A. Baum, G. Privon, J. Noel-Storr, A. C. Quillen, N. Zufelt, J. Park, A. Edge, H. Russell, A. C. Fabian, M. Donahue, C. L. Sarazin, B. McNamara, J. N. Bregman, and E. Egami

2008. An Infrared Survey of Brightest Cluster Galaxies. II. Why are Some Brightest Cluster Galaxies Forming Stars? ApJ, 681:1035–1045.

Ogle, P., F. Boulanger, P. Guillard, D. A. Evans, R. Antonucci, P. N. Appleton, N. Nesvadba, and C. Leipski

2010. Jet-powered Molecular Hydrogen Emission from Radio Galaxies. *ApJ*, 724:1193–1217.

O'Sullivan, E., D. M. Worrall, M. Birkinshaw, G. Trinchieri, A. Wolter, A. Zezas, and S. Giacintucci

2011. Interaction between the intergalactic medium and central radio source in the NGC 4261 group of galaxies. MNRAS, 416:2916–2931.

Pacholczyk, A. G.

1970. *Radio astrophysics. Nonthermal processes in galactic and extragalactic sources*.

Panagoulia, E. K., A. C. Fabian, and J. S. Sanders

2014. A volume-limited sample of X-ray galaxy groups and clusters - I. Radial entropy and cooling time profiles. MNRAS, 438:2341–2354.

Perley, D. A., R. A. Perley, V. Dhawan, and C. L. Carilli

2017. Discovery of a Luminous Radio Transient 460 pc from the Central Supermassive Black Hole in Cygnus A. ApJ, 841:117.

Peterson, J. R., S. M. Kahn, F. B. S. Paerels, J. S. Kaastra, T. Tamura, J. A. M. Bleeker, C. Ferrigno, and J. G. Jernigan

2003. High-Resolution X-Ray Spectroscopic Constraints on Cooling-Flow Models for Clusters of Galaxies. ApJ, 590:207–224.

Peterson, J. R., F. B. S. Paerels, J. S. Kaastra, M. Arnaud, T. H. Reiprich, A. C. Fabian, R. F. Mushotzky, J. G. Jernigan, and I. Sakelliou

2001. X-ray imaging-spectroscopy of Abell 1835. A&A, 365:L104–L109.

Pizzolato, F. and N. Soker

2006. On the Rayleigh-Taylor instability of radio bubbles in galaxy clusters. MNRAS, 371:1835–1848.

Planck Collaboration, P. A. R. Ade, N. Aghanim, M. Arnaud, M. Ashdown, J. Aumont, C. Baccigalupi, A. J. Banday, R. B. Barreiro, J. G. Bartlett, and et al.

2015. Planck 2015 results. XIII. Cosmological parameters. *ArXiv e-prints*.

Ponman, T. J., D. B. Cannon, and J. F. Navarro

1999. The thermal imprint of galaxy formation on X-ray clusters. Nature, 397:135–137.

Pontzen, A., M. Tremmel, N. Roth, H. V. Peiris, A. Saintonge, M. Volonteri, T. Quinn, and F. Governato

2017. How to quench a galaxy. MNRAS, 465:547–558.

Pratt, G. W., H. Böhringer, J. H. Croston, M. Arnaud, S. Borgani, A. Finoguenov, and R. F. Temple

2007. Temperature profiles of a representative sample of nearby X-ray galaxy clusters. A&A, 461:71–80.

Prestage, R. M. and J. A. Peacock

1988. The cluster environments of powerful radio galaxies. *MNRAS*, 230:131–160.

Rafferty, D. A., B. R. McNamara, P. E. J. Nulsen, and M. W. Wise

2006. The Feedback-regulated Growth of Black Holes and Bulges through Gas Accretion and Starbursts in Cluster Central Dominant Galaxies. ApJ, 652:216–231.

Rawes, J., D. M. Worrall, and M. Birkinshaw

2015. Discovery of an optical and X-ray synchrotron jet in NGC 7385. MNRAS, 452:3064–3072.

Reynolds, C. S., L. W. Brenneman, and J. T. Stocke

2005. The interaction of 3C 401 with the surrounding intracluster medium. MNRAS, 357:381–386.

Reynolds, C. S., A. M. Lohfink, P. M. Ogle, F. A. Harrison, K. K. Madsen, A. C. Fabian, et al.

2015. NuSTAR Observations of the Powerful Radio Galaxy Cygnus A. ApJ, 808:154.

Sandage, A.

1972. The Redshift-Distance Relation. 111. Photometry and the Hubble Diagram for Radio Sources and the Possible Turn-On Time for QSOS. ApJ, 178:25–44.

Sanders, J. S.

2006. Contour binning: a new technique for spatially resolved X-ray spectroscopy applied to Cassiopeia A. MNRAS, 371:829–842.

Sanders, J. S. and A. C. Fabian

2007. A deeper X-ray study of the core of the Perseus galaxy cluster: the power of sound waves and the distribution of metals and cosmic rays. MNRAS, 381:1381–1399.

Sarazin, C. L.

1986. X-ray emission from clusters of galaxies. *Reviews of Modern Physics*, 58:1–115.

Saunders, R., J. E. Baldwin, S. Rawlings, P. J. Warner, and L. Miller

1989. Spectrophotometry of FRII radiogalaxies in an unbiased, low-redshift sample. MNRAS, 238:777–790.

Scheuer, P. A. G.

1974. Models of extragalactic radio sources with a continuous energy supply from a central object. *MNRAS*, 166:513–528.

Schilizzi, R. T. and R. D. Ekers

1975. Radio tail source associated with NGC 7385. A&A, 40:221–224.

Schmidt, M.

1963. 3C 273 : A Star-Like Object with Large Red-Shift. Nature, 197:1040.

Seyfert, C. K.

1943. Nuclear Emission in Spiral Nebulae. ApJ, 97:28.

Shakura, N. I. and R. A. Sunyaev

1973. Black holes in binary systems. Observational appearance. A&A, 24:337–355.

Smith, D. A., A. S. Wilson, K. A. Arnaud, Y. Terashima, and A. J. Young

2002. A Chandra X-Ray Study of Cygnus A. III. The Cluster of Galaxies. ApJ, 565:195–207.

Smith, R. K., N. S. Brickhouse, D. A. Liedahl, and J. C. Raymond

2001. Collisional Plasma Models with APEC/APED: Emission-Line Diagnostics of Hydrogen-like and Helium-like Ions. ApJ, 556:L91–L95.

Snios, B., P. E. J. Nulsen, M. W. Wise, M. de Vries, M. Birkinshaw, D. M. Worrall, R. T. Duffy, R. P. Kraft, B. R. McNamara, C. Carilli, J. H. Croston, A. C. Edge, L. E. H. Godfrey, M. J. Hardcastle, D. E. Harris, R. A. Laing, W. G. Mathews, J. P. McKean, R. A. Perley, D. A. Rafferty, and A. J. Young

2018. The Cocoon Shocks of Cygnus A: Pressures and Their Implications for the Jets and Lobes. ApJ, 855:71.

Snowden, S. L. and K. D. Kuntz

2011. Cookbook for Analysis Procedures for XMM-Newton EPIC MOS Observations of Extended Objects and the Diffuse Background. *Cookbook for Analysis Procedures for XMM-Newton EPIC MOS Observations of Extended Objects and the Diffuse Background (ftp://xmm.esac.esa.int/pub/xmm-esas/xmm-esas.pdf)*.

Steenbrugge, K. C., K. M. Blundell, and P. Duffy

2008. Multiwavelength study of Cygnus A - II. X-ray inverse-Compton emission from a relic counterjet and implications for jet duty cycles. MNRAS, 388:1465–1472.

Steenbrugge, K. C., I. Heywood, and K. M. Blundell

2010. Multiwavelength study of Cygnus A - III. Evidence for relic lobe plasma. MNRAS, 401:67–76.

Stein, N. M., D. A. van Dyk, V. L. Kashyap, and A. Siemiginowska

2015. Detecting Unspecified Structure in Low-count Images. ApJ, 813:66.

Strom, R. G., R. Chen, J. Yang, and B. Peng

2013. Structure and environment of the giant radio galaxy 4C 73.08. MNRAS, 430:2090–2096.

Strom, R. G., A. G. Willis, and A. S. Wilson

1978. Two-frequency high resolution observations of 3C 382 and 3C 386. *AAP*, 68:367–379.

Su, Y., J. A. Irwin, R. E. White, III, and M. C. Cooper

2015. The Scatter in the Hot Gas Content of Early-type Galaxies. ApJ, 806:156.

Sun, M., C. Jones, W. Forman, A. Vikhlinin, M. Donahue, and M. Voit

2007. X-Ray Thermal Coronae of Galaxies in Hot Clusters: Ubiquity of Embedded Mini-Cooling Cores. ApJ, 657:197–231.

Sunyaev, R. A. and Y. B. Zeldovich

1972. The Observations of Relic Radiation as a Test of the Nature of X-Ray Radiation from the Clusters of Galaxies. *Comments on Astrophysics and Space Physics*, 4:173.

Sutherland, R. S. and G. V. Bicknell

2007. Interactions of a Light Hypersonic Jet with a Nonuniform Interstellar Medium. ApJS, 173:37–69.

Urban, O., N. Werner, A. Simionescu, S. W. Allen, and H. Böhringer

2011. X-ray spectroscopy of the Virgo Cluster out to the virial radius. MNRAS, 414:2101–2111.

Urry, C. M. and P. Padovani

1995. Unified Schemes for Radio-Loud Active Galactic Nuclei. PASP, 107:803.

Vallee, J. P.

1982. The highly polarized galaxy 3C 76.1. AJ, 87:486–493.

van Breugel, W. and E. B. Fomalont

1984. Is 3C 310 blowing bubbles? ApJ, 282:L55–L58.

Vantyghem, A. N. et al.

2016. Molecular Gas Along a Bright Hα Filament in 2A 0335+096 Revealed by ALMA. ApJ, 832:148.

Veilleux, S., G. Cecil, and J. Bland-Hawthorn

2005. Galactic Winds. ARA&A, 43:769–826.

Vikhlinin, A., A. Kravtsov, W. Forman, C. Jones, M. Markevitch, S. S. Murray, and L. Van Speybroeck

2006. Chandra Sample of Nearby Relaxed Galaxy Clusters: Mass, Gas Fraction, and Mass-Temperature Relation. ApJ, 640:691–709.

Voit, G. M.

2005. Tracing cosmic evolution with clusters of galaxies. *Reviews of Modern Physics*, 77:207–258.

Wagner, A. Y., M. Umemura, and G. V. Bicknell

2013. Ultrafast Outflows: Galaxy-scale Active Galactic Nucleus Feedback. ApJ, 763:L18.

Wegner, G., M. Colless, R. P. Saglia, R. K. McMahan, R. L. Davies, D. Burstein, and G. Baggley

1999. The peculiar motions of early-type galaxies in two distant regions - II. The spectroscopic data. MNRAS, 305:259–296.

White, R. A., M. Bliton, S. P. Bhavsar, P. Bornmann, J. O. Burns, M. J. Ledlow, and C. Loken

1999. A Catalog of Nearby Poor Clusters of Galaxies. AJ, 118:2014–2037.

Wilman, R. J., A. C. Edge, R. M. Johnstone, C. S. Crawford, and A. C. Fabian

2000. Molecular hydrogen emission in Cygnus A. MNRAS, 318:1232–1240.

Wilson, A. S., D. A. Smith, and A. J. Young

2006. The Cavity of Cygnus A. ApJ, 644:L9–L12.

Wing, J. D. and E. L. Blanton

2011. Galaxy Cluster Environments of Radio Sources. AJ, 141:88.

Wise, M. W., M. N. de Vries, J. P. McKean, D. A. Rafferty, et al.

in prep. Persistent AGN Activity in the Merging Cluster Cygnus A.

Worrall, D. M. and M. Birkinshaw

2000. X-Ray-emitting Atmospheres of B2 Radio Galaxies. ApJ, 530:719–732.

Worrall, D. M. and M. Birkinshaw

2006. Multiwavelength Evidence of the Physical Processes in Radio Jets. In *Physics of Active Galactic Nuclei at all Scales*, D. Alloin, ed., volume 693 of *Lecture Notes in Physics, Berlin Springer Verlag*, P. 39.

Worrall, D. M., M. Birkinshaw, R. P. Kraft, and M. J. Hardcastle

2007. The Effect of a Chandra-measured Merger-related Gas Component on the Lobes of a Dead Radio Galaxy. *ApJL*, 658:L79–L82.

Worrall, D. M., M. Birkinshaw, A. J. Young, K. Momtahan, R. A. E. Fosbury, R. Morganti, C. N. Tadhunter, and G. Verdoes Kleijn

2012. The jet-cloud interacting radio galaxy PKS B2152-699 - I. Structures revealed in new deep radio and X-ray observations. *MNRAS*, 424:1346–1362.

Yaji, Y., M. S. Tashiro, N. Isobe, M. Kino, K. Asada, H. Nagai, S. Koyama, and M. Kusunose

2010. Evidence of Non-thermal X-ray Emission from Radio Lobes of Cygnus A. ApJ, 714:37–44.

Young, A., L. Rudnick, D. Katz, T. DeLaney, N. E. Kassim, and K. Makishima

2005. Canonical Particle Acceleration in FR I Radio Galaxies. *ApJ*, 626:748–766.

Young, A. J., A. S. Wilson, Y. Terashima, K. A. Arnaud, and D. A. Smith

2002. A Chandra X-Ray Study of Cygnus A. II. The Nucleus. ApJ, 564:176–189.

Zirbel, E. L.

1996. Properties of Host Galaxies of Powerful Radio Sources. ApJ, 473:713.

Zirbel, E. L.

1997. The Megaparsec Environments of Radio Galaxies. ApJ, 476:489–509.